An infrared absorption study of surface stimulated species conversion in low and atmospheric pressure plasmas

INAUGURALDISSERTATION

zur

Erlangung des akademischen Grades

doctor rerum naturalium (Dr. rer. nat.)

an der Mathematisch-Naturwissenschaftlichen Fakultät

der

Ernst-Moritz-Arndt-Universität Greifswald

vorgelegt von
Marko Hübner
geboren am 29. Mai 1978
in Berlin

Greifswald, 28. März 2012

Dekan: Prof. Klaus Fesser

1. Gutachter :   Prof. Jürgen Röpcke

2. Gutachter :   Prof. Antoine Rousseau

Tag der Promotion: 23. August 2012

Contents

Abstract

In the framework of the current work has been the plasma initiated and surface catalysed species conversion studied in low pressure and atmospheric plasmas. The aim of the work is to improve the understanding of the internal processes in order to increase the energy efficiency as well as the selectivity of the reaction products of future plasma devices. Beside many technical applications of plasmas, air purification shows great potential. Over the last decades, plasma based pollution control has proofed its ability to remove harmful contaminants or annoying odours from an air stream. However, the energy efficiency and the selectivity of the products are a remaining challenge.

Motivated by these issues, a multi stage packed-bed reactor has been applied to remove admixed pollutions from an air stream. The performance has been studied removing one aliphatic, ethylene, and one aromatic, toluene, species. Glass beads served as packing material. The destruction of toluene has been found to be between 20 and 60%. The ethylene concentration has been reduced below the detection limit. According to the applied diagnostics, Fourier Transform Infrared spectroscopy, FTIR spectroscopy, combined with an optical long path cell, the remaining ethylene concentration has been below $10ppm$ which corresponds to nearly complete ethylene destruction. The specific energy β has been between 300 and $1600JL^{-1}$ for toluene and between 120 and $900JL^{-1}$ for ethylene. In total, 10 reaction products have been identified and quantified. Beside H_2O and CO_2, it has been possible to detect CO, O_3, HNO_3, HCN, CH_2O, CH_2O_2 and the nitrous oxides N_2O and NO_2. However, none of these experiments led to the detection of NO which means that the NO concentration has always been below $30ppm$.

The diversity of the high number of reaction products implies a very complex chemistry which can not be studied as a whole. Additionally, beside volume processes, surface processes can have an increased influence. For example, sorption processes can influence the reaction rate of single surface processes.

For an improved understanding of those surface effects, a simplified plasma geometry has been used. The inner side of a tube reactor, made of Pyrex, served as the surface under study and has been exposed to a rf plasma for $1h$. Four different precursors were used, namely Ar, O_2, N_2 or synthetic air. The surface effects of the plasma treatment have been investigated indirectly by studying the oxidation of NO into NO_2. After the plasma exposure, the reactor has been evacuated and filled with a gas mixture of 1% NO in N_2 / Ar, up to a pressure of $5.3mbar$. At low pressure conditions, the influence of volume processes is reduced. Afterwards, for a closed reactor, the concentrations of NO and NO_2 have been measured using quantum cascade laser absorption spectroscopy, QCLAS, for the next $120min$.

The results show that, depending on the precursor, the NO_2 concentration varied. For a

N_2 or Ar pre-treatment, the NO_2 concentration remains below the detection limit whereas the NO_2 concentration has been $5.3 \times 10^{14} molecules\, cm^{-3}$ after an O_2 plasma treatment and $1.05 \times 10^{14} molecules\, cm^{-3}$ after an air plasma treatment. This difference corresponds to the reduced O_2 concentration in air. These results led to the conclusion that oxygen containing plasmas are able to deposit oxygen atoms on the surface. The filling with NO leads to the NO oxidation via the Eley-Rideal mechanism including the deposited oxygen atoms. Modelling, including physisorption, chemisorption, thermal desorption, surface diffusion, and both Eley-Rideal and Langmuir-Hinshelwood recombination mechanism, showed that the NO concentration in the gas phase decreases due to the surface oxidation but also due to NO adsorption or production of other N_xO_y molecules.

The investigation of surface processes can not be done without knowledge of the kinetics of the surrounding gas phase and plasma chemistry. The start phase of a plasma influences the chemistry of the volume and, therefore, influences the species interacting with the surface. In the past, it has been relatively difficult to study the first milliseconds of a plasma using infrared absorption spectroscopy. However, since one decade, a new type of laser, quantum cascade laser, QCL, became commercially available. These lasers provide narrow band laser radiation in the mid infrared. A spectrometer based on this technique allows high time resolved absorption spectroscopy in the μs-range to be performed.

For a more comfortable application of this measurement technology, especially in an industrial environment, a compact multi channel spectrometer has been developed, TRIPLE Q. It combines the high time resolution with the possibility to measure the concentration of at least three infrared active species simultaneously. Due to the high time resolution, a huge number of spectra have to be analysed. Depending on the setup, several thousands spectra can be recorded for one experiment. In order to calculate absolute number densities, an algorithm has been developed which automatically treats typical phenomena like pulse jitter, rapid passage effect or variations of the intensity of the laser pulses.

The performance of the spectrometer has been validated in experiments studying the kinetics of nitrous oxides, N_xO_y, in pulsed dc low pressure plasmas. The duration of the plasma pulses has been between $1ms$ and $10ms$. A gas mixture of 1% N_2O, 1% NO or 1% NO_2 in N_2 / synthetic air at a pressure of $1.3mbar$ served as a precursor. From the time evolution of the intensities of the absorption structures during the plasma pulse and in its afterglow, the degree of dissociation and the NO production have been determined.

Using the TRIPLE Q system, it has been found that all three nitrous oxides, N_xO_y, admixed in N_2 have been fully fragmented for a mean plasma current of about $150ms$ after $2ms$. For this example, the applied voltage has reached its maximum after $5\mu s$.

The gas temperature is an important parameter in plasma physics. Using the TRIPLE Q system, the gas temperature has been determined for pulsed dc plasmas. A gas mixture of 1% NO in air at a pressure of $1.3mbar$ served as a precursor. For this case, NO has been used as a probe gas. From the spectra, the temperature has been calculated using the line ratio method. The relative intensity of the absorption structures of NO at $1900.5cm^{-1}$ and $1900.08cm^{-1}$ depend on the temperature. Therefore, the ratio has been used to calculate the gas temperature. The influence of the rapid passage effect to the spectra has been compensated with the help of a spectra simulation. The ability of this approach has been validated using a heated gas cell,

$T_{max} = 600K$, without plasma ignition. For example, the temperature of pulsed dc plasma with a mean plasma current of $150mA$ is $500K$.

Few *ms* after the plasma pulse, the temporally evolution of the NO and NO_2 concentrations show stable conditions. On the contrary, the N_2O concentration reached a stable condition about $100ms$ after the plasma pulse. Neither a temperature effect nor the production of N_2O can explain such a discrepancy. During the plasma pulse and in the after glow, new absorption structures have been identified in the spectra. They belong to a hot band of an asymmetric stretch vibration of the N_2O molecule. Therefore, it has been concluded, that the relatively long relaxation time of the N_2O molecule is caused by a resonant vibration-vibration coupling between vibrationally exited N2 and N_2O. The method allows one to study the relaxation of vibrationally excited N_2. Using this method, molecules, which are not infrared active, can be monitored. This approach extends the field of scientific and commercial applications of the QCLAS.

Kurzfassung

Im Rahmen der vorliegenden Arbeit fand die Untersuchung der Stoffwandlung in Niederdruck- und Atmosphärendruckplasmen statt, die durch ein Plasma initiiert und durch Oberflächenprozesse katalysiert wurden. Von einem verbesserten Verständnis derartiger Vorgänge wird eine Steigerung der Effizienz als auch eine gezielte Steuerung der Selektivität der Stoffwandlung zukünftiger Entladungsapparaturen erwartet. Neben einer Vielzahl technischer Anwendungen von Plasmen zeigt die Abgasreinigung ein hohes Entwicklungspotential. Nach heutigem Kenntnisstand ist ein Plasma prinzipiell geeignet, Schadstoffe oder unangenehme Gerüche aus einem Abluftstrom zu entfernen. Als Herausforderung muss jedoch die Energieeffizienz und die Produktselektivität angesehen werden.

Motiviert durch diese Herausforderungen wurde ein mehrstufiger Schüttgutreaktor verwendet, um synthetische Luft bei Atmosphärendruck von beigemischten Verunreinigungen zu säubern. Als Testschadstoff kamen das Aliphat Ethylen und das Aromat Toluol zum Einsatz. Die Schüttung bestand aus Glaskugeln. Die Konzentration von Toluol konnte um 20 bis 60% und die Konzentration von Ethylen unter die Nachweisgrenze reduziert werden. Bei der hier verwendeten Messmethode, Fourier-Transformations-Infrarotspektroskopie, FTIR-Spektroskopie, kombiniert mit einer optischen Langwegzelle, entspricht das einer Konzentration kleiner $10 ppm$. Die spezifische Energie β lag dabei zwischen 300 und $1600 JL^{-1}$ für Toluol und zwischen 120 und $900 JL^{-1}$ für Ethylen. Die bereits erwähnte Problematik der Produktselektivität zeigte sich dadurch, dass insgesamt 10 Reaktionsprodukte identifiziert werden konnten. Neben H_2O und CO_2 konnten auch CO, O_3, HNO_3, HCN, CH_2O, CH_2O_2 und die Stickoxide N_2O sowie NO_2 nachgewiesen werden. Allerdings wurde bei keinem Versuch NO identifiziert, was einer NO Konzentration kleiner $30 ppm$ entspricht.

Die hohe Anzahl verschiedener Reaktionsprodukte impliziert eine äußerst komplexe Reaktionschemie, die als Ganzes nur sehr schwer einer praktischen Analyse zugänglich ist. Neben den Gasphasenreaktionen treten bei einem Schüttgutreaktor verstärkt Oberflächeneffekte in den Vordergrund. So können beispielsweise Sorptionsvorgänge die Reaktionsraten einzelner Reaktionen beeinflussen.

Um einen verbesserter Zugang zu solchen Oberflächeneffekten zu ermöglichen, wurde eine stark vereinfachte Entladungsgeometrie verwendet. Die Innenseite eines Rohrreaktors aus Pyrex stellte dabei die Oberfläche dar, die für $1h$ einem RF Plasma ausgesetzt war. Als Precursor fanden Ar, O_2, N_2 oder synthetische Luft Anwendung. Die Auswirkungen der Plasmabehandlung wurden indirekt durch die Oxidation von NO in NO_2 untersucht. Dazu wurde der Reaktor nach der Plasmabehandlung evakuiert und anschließend mit einem Messgas, 1% NO in N_2/Ar, gefüllt, wobei der Enddruck $5.3 mbar$ betrug. Der Wechsel in den Niederdruckbe-

reich reduziert die Einflüsse eventueller Volumenprozesse. Anschließend wurde für die nächsten 120min die NO und NO$_2$ Konzentration in der Gasphase mit Quantenkaskadenlaserabsorptionsspektroskopie, QCLAS, bestimmt. Es zeigte sich, dass in Abhängigkeit des verwendeten Precursors die Menge produzierten NO$_2$ variierte. Während die NO$_2$ Konzentration nach einem N$_2$ bzw. Ar-Plasma unter der Nachweisgrenze blieb, betrug die NO$_2$ Konzentration nach einem O$_2$-Plasma ca. $5.3 \times 10^{14} Moleküle \, cm^{-3}$. Nachdem die Reaktorwand einem Luftplasma ausgesetzt war, wurde eine NO$_2$ Konzentration von $1.05 \times 10^{14} Moleküle \, cm^{-3}$ gemessen, was gerade genau der reduzierten Sauerstoffkonzentration in Luft entspricht. Die Ergebnisse führten zu der Schlussfolgerung, dass Sauerstoffatome durch die Plasmabehandlung an der Oberfläche adsorbieren und dort längere Zeit verbleiben können. Die anschließende Befüllung mit NO führt zu einer NO Oxidation via Eley-Rideal Mechanismus. Eine einfache Modellrechnung, in der Physisorption, Chemiesorption, thermische Desorption, Oberflächendiffusion, Eley-Rideal Mechanismus und Langmuir-Hinshelwood Mechanismus berücksichtigt wurden, zeigte, dass nicht nur die Oxidation von NO mit adsorbiertem Sauerstoff zum Abbau der NO-Konzentration in der Gasphase führt, sondern andere Verlustprozesse, wie z.B. die Adsorption von NO an der Wand oder die Bildung weitere Stickoxide, berücksichtigt werden müssen.

Das Verständnis der Oberflächenprozesse ist ohne eine Kenntnis der Kinetik des angrenzenden Volumens nicht möglich. Die Anfangsphase einer Entladung beeinflusst die Reaktionschemie im Volumen und damit die mit der Oberfläche in Wechselwirkung tretenden Spezies. Diese Startphase einer Entladung ist bisher nur schwer durch Infrarotabsorptionsspektroskopie zugänglich. Abhilfe schafft hier die Verwendung der seit ca. einem Jahrzehnt kommerziell verfügbaren Quantenkaskadenlaser. Die auf dieser Technologie basierenden Spektrometer erlauben eine Zeitauflösung im μs-Bereich.

Zur Vereinfachung solcher Messungen und um deren Einsatz routinemäßig auch außerhalb einer Laborumgebung ermöglichen zu können, wurde ein kompakter industrietauglicher Mehrkanalspektrometer, TRIPLE Q, entwickelt, der die Vorteile der hohen Zeitauflösung mit der Möglichkeit vereint, die zeitliche Entwicklung der Konzentration von mindestens drei verschiedene IR-aktiven Spezies simultan nachzuweisen.Die hohe Zeitauflösung macht es erforderlich, eine entsprechend hohe Anzahl an Spektren auszuwerten. Je nach eingestellter Messdauer können dabei mehrere tausend Spektren aufgezeichnet werden. Zur Auswertung der einzelnen Spektren war die Entwicklung eines Algorithmus nötig, der vollautomatisch typische Phänomene wie Pulsejitter, *Rapid Passage Effect* oder Intensitätsschwankungen erkennt und bei der Bestimmung der absoluten Teilchenzahlen berücksichtigt.

Die Leistungsfähigkeit des Spektrometers wurde in Experimenten zur Kinetik von Stickoxiden in gepulsten DC Niederdruckentladungen nachgewiesen. Die Pulsdauer lag zwischen 1ms und 10ms. Ein Gasgemisch von 1% N$_2$O, 1% NO oder 1% NO$_2$ in N$_2$/synthetische Luft mit einem Druck von 1.3$mbar$ diente dabei als Precursor. Aus dem zeitlichen Verlauf der Absorptionsintensitäten während der Entladung als auch im Afterglow wurde der Grad der Dissoziation der Stickoxide und die NO Produktion ermittelt. Die Messungen mit dem TRIPLE Q System ergaben, dass alle drei Stickoxide, N$_x$O$_y$ gemischt in N$_2$, bei einem mittleren Entladungsstrom von 150mA bereits nach 2ms vollständig dissoziiert waren. Die angelegte Spannung erreichte dabei ihr Maximum bereits nach ca. 5μs.

Ein wichtiger Parameter bei der Beschreibung plasmachemischer Vorgänge ist die Gastem-

peratur. Diese wurde ebenfalls mit dem TRIPLE Q System am Beispiel der gepulsten DC Entladung bestimmt. In einem Gasgemisch aus 1% NO in N_2 fand die Verwendung von NO als Sondengas statt. Die Temperaturbestimmung erfolgte aus den Spektren nach der Linien-methode. Dazu wurde die relative Intensität der Absorptionslinie bei $1900.5 cm^{-1}$ mit der bei $1900.08 cm^{-1}$ gemessen. Aus deren relativen Intensitätsverhältnis zueinander konnte die Gas-temperatur bestimmt werden. Der Einfluss des *Rapid Passage Effects* auf das Spektrum ist mit Hilfe einer Spektrensimulation kompensiert worden. Die Eignung dieses Ansatzes konnte durch die Verwendung einer auf $600K$ geheizten Gaszelle bestätigt werden. Für das bereits angespro-chene Beispiel einer gepulsten DC Entladung mit einem mittleren Entladungsstrom von $150 mA$ wurde eine Gastemperatur von ca. $500K$ gemessen.

Der zeitliche Verlauf der NO und NO_2 Konzentrationen zeigte, das beide Spezies weni-ge *ms* nach dem Plasmapuls ein stabiles Niveau erreichten. Im Gegensatz dazu benötigte die N_2O Konzentration ca. $100 ms$ um in einen stabilen Zustand zu relaxieren. Diese Diskrepanz ist weder durch Temperatureffekte noch durch eine Produktion von N_2O erklärbar. Während der Dauer des Plasmas und im Afterglow konnten neue Absorptionslinien im N_2O-Spektrum iden-tifiziert werden. Diese gehören zu einem Hot Band der asymmetrischen Stretchschwingung des N_2O-Moleküls. Der Nachweis solcher Übergänge impliziert ein hohes Maß an vibratorisch an-geregten N_2O-Molekülen. Die relativ lange Relaxionszeit des N_2O-Moleküls von ca. $100 ms$ konnte durch eine resonante Vibration-Vibrationskopplung zwischen vibratorisch angeregtem N_2 und N_2O erklärte werden. Mit dieser Methode ist es möglich, Informationen von Molekülen zu erhalten, die nicht im IR aktiv sind. Der wissenschaftliche und kommerzielle Verwertungs-bereich der QCLAS wird durch diesen Ansatz erweitert.

Chapter 1

Plasma induced species conversion in the gas phase and at surfaces

1.1   Introduction

A plasma, sometimes called the fourth state of matter [1], is obtained, in general, in the follow way. If a sufficient amount of energy is coupled into solid state matter the state of matter changes from solid to liquid. If a sufficient increase of the energy transfer is applied the liquid becomes a gas and, finally, if the energy transfer is increased further then the gas becomes a plasma. A plasma can be understood as an ionized gas which consists of free electrons, ions, atoms or molecules [2]. Such a plasma is characterised by the parameters [3]

- particle density n $\left(cm^{-3}\right)$

- temperature T

- magnetic field B(T)

The temperature can be expressed in eV with $1eV = 11605K$. Concerning the temperature, each component can be assigned to its own temperature i.e. T_e: electron temperature, T_{ion}: ion temperature and T_{gas}: neutral gas temperature. These parameters are spread over several orders of magnitude. For example, the temperature of an intergalactic gas can be T $\approx 10^8 K$ with n $\approx 1m^{-3}$ and B $\approx 10^{-10}T$, technical plasmas: T $\approx 10^3 \ldots 10^5 K$ with n $\approx 15^{15} \ldots 10^{25} m^{-3}$ and B $\approx 10^{-2}$ or a neutron star T $\approx 10^4 K$ with n $\approx 10^{45} m^{-3}$ and B $\approx 10^8$ [2]. According to the temperature, plasmas can be distinguished into thermal and non-thermal plasmas [4]. For thermal plasmas, the conditions $T_e \approx T_{ion} \approx T_{gas} \approx 10^4 K$ have to be fulfilled where the last relations roughly accounts for low temperature plasmas. Such conditions are named Local Thermodynamic Equilibrium, LTE. On the contrary, a Partial Thermodynamic Equilibrium, PTE, is given if the condition $T_e \approx 10^4 K \gg T_{ion} \approx T_{gas} \approx 300K$, i.e. the electron temperature is much higher than the temperature of the ions and neutral gas particles. The formation of ions, radicals or the emission of radiation offers a huge field for technical applications. Indeed, since the American scientist Langmuir named it all plasma, many applications have been developed and improved. Nowadays, plasma technology is applied in fields like [5, 6]

- Pollution control

- Surface processing / modification

- Thin film deposition

- Sterilization / decontamination

- Lightning

- Ozone production

Beyond that, recent research activities are carried out combining a plasma and human skin in order to study potentially treatment of chronicle wounds [7, 8].

Especially the ability of a plasma to dissociate molecules and the formation of radicals have turned plasmas into the field of species conversion processes like destruction of contaminants admixed to a gas stream. The application of plasma technology to pollution control has been initiated by the destruction of military toxic gases [6] with the aim to neutralize the gases or at least to reduce the toxicology. Since than, the plasma induced species conversion, mainly pollutant destruction, has been studied further by many researcher groups worldwide. An overview can be found in [9] and references therein. This nice compilation provides an overview about fundamental aspects and the supporting technologies. The second volume deals about electron beam technologies and electrical discharge processing. Air plasma chemistry details can be found in Ref. [5] as well as an overview about current applications of atmospheric pressure air plasmas. Details about low temperature plasma aspects are compiled in Ref. [10]. The focus of this thesis is on the species conversion in the plasma volume and at surfaces.

The current thesis can be separated into three main topics.

First, the destruction of volatile organic compounds using a multi-stage packed bed reactor under atmospheric conditions. In the centre of the research activities has been the degree of destruction as a function of the number of active stages. Two different species, toluene and ethylene, have been tested.

Second, the quantum cascade laser absorption spectroscopy, QCLAS, has been developed further. A method is presented which extents the QCLAS for the measurement of the gas temperature despite the huge distortion of the recorded spectra. The applied line ratio method, known from conventional absorption spectroscopy, has been combined with simulated spectra. Additionally, based on QCLAS, a three channel spectrometer, TRIPLE Q, has been developed and validated.

Third, the ability of a low pressure RF plasma to create active sites on a Pyrex surface has been investigated. Furthermore, N_xO_y kinetic studies in a DC low pressure air-like plasma pulse are given. The formation and destruction of N_2O, NO and NO_2 has been studied. Additionally, vibrational excitation and the corresponding relaxcation kinetic have been detected using the developed TRIPLE Q system. A hypothesis is presented which correlates the degree of vibrationally excited N_2 to the detectable N_2O hot bands.

1.2   Outline of the thesis

In chapter 2, a literature study summaries the basics concepts and should allow the reader to follow the whole thesis. Further details can be found in the references given therein. Since in chapter 4 experiments are presented about the purification of an air stream contaminated with volatile organic compounds, VOC, the chapter 2 starts with a classification of the VOC and how they affect the human health. Emission sources are given, followed by a short overview about conventional destruction techniques. Furthermore, processes are described which the molecules can undergo in a plasma leading to e.g. vibration excitation or dissociation. Additionally, the two main dissociation channels, electron impact and radical production followed by radical VOC reaction, present in a plasma are discussed. Some parameters, allowing the comparability between the different types of plasma devices, all applied to VOC destruction, are presented. Preparing the reader for chapter 4, the concept of a packed-bed plasma reactor is introduced. Examples for the packing material, the treated gas mixtures and the different working parameters are presented. Finally, catalysis is repeated. The interaction of plasma and surfaces and the most important surface processes, i.e. Langmuir-Hinshelwood and Eley-Rideal, are explained and how they are related to plasma induced heterogeneous catalysis.

In chapter 3, the diagnostics used in the experiments are summarized. Starting with a short introduction of infra red absorption spectroscopy, IRAS, the measurement of absolute number density of species, present in the gas phase, is explained. For the experiments about VOC destruction in a packed-bed reactor, chapter 4, the broad band method Fourier Transform Infra-Red, FTIR, spectroscopy has been applied. It allows the simultaneous measurement of several species at a relatively low spectral resolution and slow time resolution. A description is given how the species corresponding to the measured spectra have been identified. Absolute species concentrations have been determined with the aid of databases. The experiments about N_xO_y kinetics, chapter 5, have been done using quantum cascade laser, QCL, absorption spectroscopy, AS. These relatively new class of lasers were driven in a pulsed regime scanning about $0.5 cm^{-1}$ of the spectrum within about $150 ns$ at a relatively high spectral intensity. Such a fast and high power scanning leads to a distortion of the measured spectra especially at low pressure conditions. In literature, this phenomenon has been named rapid passage effect. In order to obtain absolute number densities, the applied calibration routine is introduced. Applying QCLAS, time resolved measurement in the order of 10ths of μs are presented. Additionally, efforts are described which allow the calculation of the gas temperature from the measured spectra despite the strong disturbance of the spectra, i.e. rapid passage effect. The method applied uses the temperature depending absorption intensity, known as line ratio method. Thus, the ratio of two of these absorption structures has been used to determine the gas temperature. The line ratio method has been adapted to the QCLAS. Due to the spectral distortion, the method combines simulated spectra with the measured ones. A comparison with a conventionally heated reference gas cell is shown. The experiences working with QCLAS have been resulted into the development of a simple and compact three channel spectrometer. The principal arrangement and the optical subsystem are shown in detail. Additionally, an algorithm is presented which automatically calculates the absolute number density from the measured spectra. Inherent properties

of the QCLs lead to jitter phenomenon and variations in the pulse intensity. Both are regarded by the algorithm. The system performance has been validated for the measurements given in chapter 5.

In chapter 4, the destruction of toluene and ethylene using a multi stage packed-bed plasma reactor is described. Both species have been admixed to an air gas flow. There are a plenty of literature dealing with such an experimental arrangement. The application of several geometries, gas mixtures, gas flows or packing material has been reported in the literature. However, the focus of the work presented here has been the serial combination of several reactors, or stages, one after another. Of interest has been the question: how changes the destruction efficiency as the number of active stages increased? It has been reported that the destruction efficiency increases progressively but the supplied power increases linear. Such a phenomenon is interesting not only from a scientific point of view but also from a commercial one. Therefore, a special reactor has been designed in order to simple mount identical stages. The stages itself are commercially available. The measurements have been done varying parameters like gas flow, humidity level and applied voltage. The exhaust gas composition has been identified and quantified using a FTIR spectrometer coupled to an optical long path cell. The destruction of both toluene and ethylene is shown. The carbon balance as well as the formation of by-products are given. The lack of a closed dielectric barrier principally allows arcing to occur. Therefore, at pre discharge voltages, a current could flow over the surface of the packing material. This possibility has been studied for two state configurations by estimating power losses at pre discharge voltages. A comparison between power losses caused by polarization or by surface currents is discussed. The spatial appearance of the plasma around the embedded packing material has been illustrated by imaging. A normal photograph of a single beads and a double beads configuration is given. Additionally, a filament resolved imaging is also given combined with the corresponding voltage and current peak measurement.

In chapter 5, experiments are described which deal with the plasma surface/wall interaction induced by a RF plasma as well as with the N_xO_y kinetics present in a low pressure dc plasma pulse. At first, chapter 5.3, it is outlined how a Pyrex surface has been treated by a RF plasma using different precursors. Of special interest has been the ability of the plasma to deposit oxygen on the wall. The modification of the surface has been studied by measuring the time dependent oxidation of NO into NO_2 in the gas phase. Both concentrations have been measured using QCLAS. The oxidizing surface processes, the possibility of O_2, O_2^- or O atoms are discussed and oxidizing rates are calculated. Additionally, a simple kinetic surface modelling is presented. Time resolved measurements of the concentration of N_2O, NO and NO_2 in a DC plasma pulse are described. The foci have been to study the nitrous oxides kinetics and validating the functionality of the TRIPLE Q spectrometer. With the aid of the TRIPLE Q system, the temporally behaviour of the concentration of all three species could have been given simultaneously before, during and after the plasma pulse. Using these measurements, the degree of dissociation as a function of the supplied energy is presented. The chosen spectral region of the QCL used for N_2O detection principally allows the detection of hot band of the N_2O molecule. Indeed, the identification as well as temporally evolution of the hot band inten-

sity is given for periods before, during and after the dc plasma pulse. The reaction rate constant could be determined and is given as well. The detection and the temporally evolution of the hot band of N_2O is discussed. A hypothesis is formulated in order to correlate the relaxation of N_2O in the after glow period to a resonant coupling between vibrationally excited N_2 and the N_2O molecules. This method offers a new possibility to study properties of non-IR active molecules like vibrationally excited N_2. Therefore, the scientific and commercial return value of the QCLAS is improved. Finally, the NO production by N_2O dissociation is presented too.

Some parts of this work have been, fully or partly, published earlier. Chapter 3.6 in [11], chapter 5.3 in [12, 13] and chapter 5.3.3 in [14].

Bibliography

[1] A. Dinklage. *Plasma physics : confinement, transport and collective effects*. Lecture notes in physics,. Springer, (2005).

[2] U. Schumacher. Basics of plasma physics. In A. Dinklage, editor, *Plasma Physics*, Lecture Notes in Physics, page 3. Springer, (2005).

[3] P. M. Bellan. *Fundamentals of plasma physics*. Cambridge University Press, (2006).

[4] J. Meichsner. Low temperature plasmas. In A. Dinklage, editor, *Plasma Physics*, Lecture Notes in Physics, page 95. Springer, (2005).

[5] K. H. Becker. *Non-equilibrium air plasmas at atmospheric pressure*. Series in plasma physics. Institute of Physics, (2005).

[6] U. Kogelschatz and J. Salge. High-pressure plasmas: Dielectric-barrier and corona discharge - properties and technical applications. In R. Hippler, editor, *Low Temperature Plasmas*, page 439. Wiley-VCH, (2008).

[7] M. Laroussi. Low-temperature plasmas for medicine? *IEEE TRANSACTIONS ON PLASMA SCIENCE*, **37**:714, (2009).

[8] K.-D. Weltmann and T. von Woedtke. Basic requirements for plasma sources in medicine. *Eur. Phys. J. Appl. Phys.*, **55**:13807, (2011).

[9] B. M. Penetrante, S. E. Schultheis, and North Atlantic Treaty Organization. Scientific Affairs Division. *Non-thermal plasma techniques for pollution control*. NATO ASI series. Series G, Ecological sciences. Springer-Verlag, (1993).

[10] R. Hippler. *Low temperature plasmas : fundamentals, technologies and techniques*. Wiley-VCH ; [Chichester : John Wiley, distributor], 2nd rev. and enl. ed. edition, (2008).

[11] M. Hübner, S. Welzel, D. Marinov, O. Guaitella, S. Glitsch, A. Rousseau, and J. Röpcke. TRIPLE Q: A three channel quantum cascade laser absorption spectrometer for fast multiple species concentration measurements. *Rev. Sci. Instrum.*, **82**:093102, (2011).

[12] O. Guaitella, M. Hübner, S. Welzel, D. Marinov, J. Röpcke, and A. Rousseau. Evidence for surface oxidation on pyrex of NO into NO_2 by adsorbed o atoms. *Plasma Sources Science & Technology*, **19**, (2010).

[13] O. Guaitella, M. Hübner, D. Marinov, V. Guerra, C. D. Pintassilgo, S. Welzel, J. Röpcke, and A. Rousseau. Oxidation of NO into NO_2 by surface adsorbed O atoms. *Contributions to Plasma Physics*, **51**:176, (2011).

[14] V. Guerra, O. Guaitella, D. Marinov, C. D. Pintassilgo, M. Hübner, J. Röpcke, and A. Rousseau. A simple model of the surface oxidation of NO in NO_2. In 20*th European Conference on the Atomic and Molecular Physics of Ionized Gases*, Novi Sad, Serbien, 2010.

Chapter 2

Plasma induced Pollution Control

This chapter 2 presents a short literature study about VOC destruction by plasma technology. The descriptions should allow the reader to follow the main concepts. Extended information about a specific topic can be found the cited literature and the references therein.

2.1 Introduction

In this chapter, a short overview is given about the scientific details needed to follow the entire topic of the thesis. The details given herein are a summary of several literature sources. Precise references are given in the text. The increased understanding for a clean environment and the increased approval for a life friendly earth has increased research efforts in the field of the destruction of poisonous species as they could be present in the gas streams emitted from e.g. industrial activities, crude oil handling. Especially children and grandchildren, being the inheritors of the anthroposphere, are greatly interest in nature inspired cycle economy, i.e. any waste should be recycled or neutralised back to natural substances. One group of poisonous species are Volatile Organic Compounds, VOC. These are chemical substances with carbon hydrogen bounds. They are organic liquids or solids with a room temperature vapour pressure greater than $0.7mbar$ [1]. The atmospheric boiling point is defined to be $260°C$. Two main classes of VOC can be defined [1]: hydrocarbons and compounds. Hydrocarbons are Paraffin (e.g. propane), Olefins (e.g. ethylene), Acetylenes (e.g. acetylene) and aromatics (e.g. toluene). Compounds are alcohols (e.g. methanol), aldehydes (e.g. formaldehyde) or ketones (e.g. methyl) [1]. Because of their vapour pressure, they are easy evaporated into the ambient air and, when exhausted, are easy to breath by human beings. VOC present in the air can affect humans and animal health, vegetation, forest and damage physical materials. For example, VOC present in the air affects the skin, mucous membrane and the lungs followed by possible harms of other organs or systems [1]. In tab. 2.1, a short list is given which relates the damage of an organ by a specific agent. The strength of these effects depends on the exposure time as well as on the concentration. The Threshold Limit Value (TLV) for e.g benzene is $10ppm$, for toluene is $100ppm$ and for acetone is $750ppm$. These examples illustrate the sensitivity of humans to the concentration of pollution. Nowadays, two sources can be distinguished. First, natural sources e.g. wetlands, ruminants or rice agriculture. These emissions usually considered to be unprob-

Table 2.1: Potentially agents harmful to humans. The table list some examples of toxic agents, a specific example and the organ which can be damaged when the agent is accumulated in humans body [1].

Agent	Example	Affected Human Organ
heptatotoxic	carbon tetrachloride	liver
nephrotoxic	halogenated hydrocarbons	kidney
hematopoietic	aniline	blood
neurotoxic	methanol	nervous system
anesthetic	olefins	brain

lematic. The second sources are anthropogenic emissions caused by human activities. They can be roughly separated into industrial / outdoor pollutants, indoor air pollutants and odorous pollutants [1], epa]. Industrial / Outdoor pollutants covers the emission caused by mass activities which create emission potentially exhausted to the environment. Fig. 2.1 shows an overview of the VOC emission sorted by source sector [2]. Indoor pollutants describes the VOC emis-
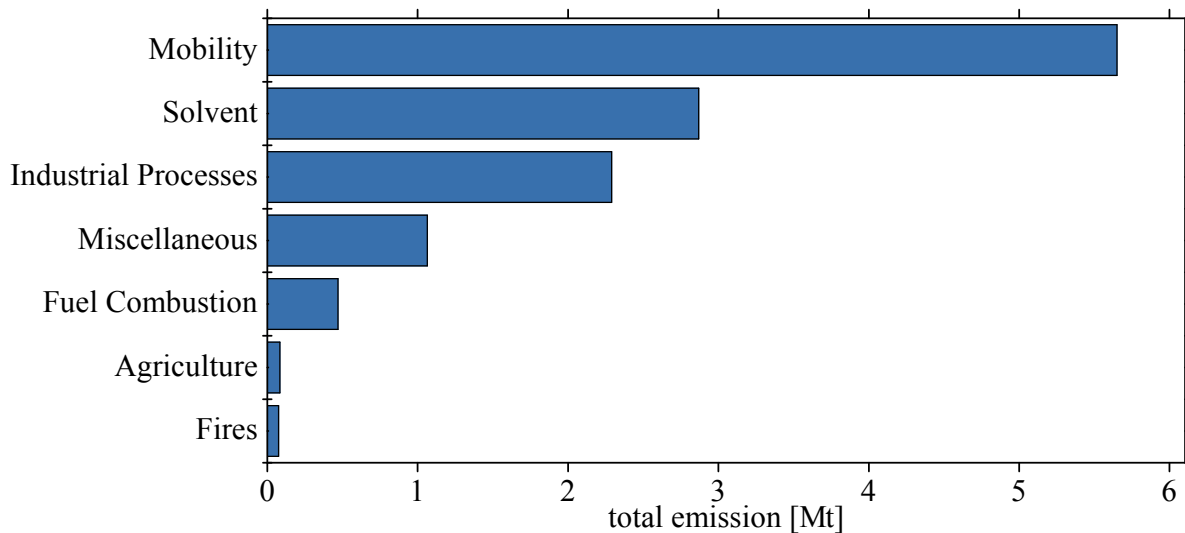
Figure 2.1: Total amount of VOC emission exemplarily shown for the United States of America in 2008 [2] sorted after emission source.

sion in houses. The sources are the combustion of oil wood or coal, furniture made of pressed wood products, products for household cleaning, combustion of tobacco products, solvents and paintings. The grade of harmfulness depends on the concentration, the species and the exposure time. Regular ventilation and the replacements of the products, e.g. paintings based on water instead of organic solver, can reduce the danger significantly [1, 3]. Odorous pollutants are a special kind of air pollutants. Usually, the emitted species are not primary harmful to humans but limit the comfort because of an irritating smell detection [1].

2.2 Conventional VOC destruction

The best method keeping the environment free from VOC is to avoid the production or emission at the source. This, of course, depends on the process itself and might be difficult to made for a certain processes. It can be easier to cover the emission and ventilate the contaminated gases to a subsequent cleaning installation. For some processes, however, it is relative difficult or impossible to maintain them under cover, e.g. painting or animal caring. Nevertheless, conventionally methods for VOC destruction from a gas stream have been developed and used in the past. The method best applicable depends on several parameters, e.g. temperature, pressure, concentration, flow, admixed amount of dust and species composition. Conventional methods especially used for VOC destruction are: condensation, adsorption, absorption / scrubbing, thermal incineration, catalytic incineration, flaring, biological treatment, odor modification, dilution, membrane separation, ultraviolet treatment and catalytic ozone oxidation [1]. Condensation uses the dew point of the species. The entire gas stream is cooled. Below the dew point temperature, species are transformed to a liquid which are easily extractable from the condenser. The method might be problematic in case the dew point of one species is higher than the melting point of another component. The accumulation of the solid material e.g. wax at the condenser can take place. As a consequence, the heat transfer can be reduced and, therefore, the performance of the entire system too [1]. Adsorption describes the trapping of VOC on the surface of an adsorbing material. Such a material is characterised by a high surface to mass ratio. Adsorption takes place onto the surface or interstitial parts of activated carbon or molecular sieve. For a continuous operation, the adsorber has to be regenerated by, e.g. heating or a counter gas flow. Adsorption is well suited for decontamination of low concentrated VOC density [1]. Absorption / Scrubbing can be used when the VOC shows a good solubility in a liquid. The contaminated air is mixed with a liquid. Due to concentration differences, the VOC diffuse into the liquid and is, on one side, enriched in the liquid and, on the other side, degraded in the gas stream. The process can be described using Henry's law. In case the VOC reacts with the liquid, the method is called wet scrubbing. This leads to a reduced reactivity. Therefore, the liquid has to be continuously regenerated. This may increase the cost for this method [1]. Thermal incineration directly burns the VOC contamination. Air, admixed with not more than 25% of the lower explosive limit (LEL) is guided around a flame. The heat of the exhausted is used to preheat the new contaminated air for energy saving purposes. The flame is sustained by an additional fuel source. This method is suitable for a multi component gas mixture since a broad sensitivity is given. Nowadays, destruction efficiencies up to 98% can be reached. Additionally, this method may created NO_x as an by-product, which has to be removed by an other technique [1]. Catalytic incineration describes the destruction of VOC using a combustion aided by catalyst. This reduces the activation energy compared to gas phase combustion. Basically, the oxidation takes place at a lower temperature and, therefore, higher cost efficiency. Special care has to be paid in order to avoid the poisoning of the catalyst by particulate matter of metal fumes present in the gas stream [1]. Flaring, like thermal incineration, directly burns the VOC. Usually additional fuel is needed to sustain the combustion. But, no combustion chamber is used. Therefore, flame temperature might be varying [1]. Biological treatment describes the application of microorganism to the VOC destruction in a air stream. Two principles are

used: (i) bio filtration, where the microorganism life on a substrate and (ii) bio scrubber, where the microorganism life in scrubber liquor. The method is well suitable for low contaminated gases. Due to biological life forms are used, the system has to maintained in working condition, e.g. temperature, food or gas flow, even between operations. The destruction of the poisoning species is accomplieched because the micro organisms break large molecules into smaller, less harmful molecules [1]. Odor modification describes the reduction of the uncomfortable smell detection in a gas stream. For this purpose, a chemical substance is added to the gas stream which either reduces the odor species by a chemical reaction or causes the odor to be covered for the nose [1]. Dilution is the simplest way. The contaminated air is given to the atmosphere. The emission is done far away from humans. Therefore, the local concentration in human living area is maintained below an acceptable value [1]. Membrane separation uses semi permeable membranes for VOC separation from a gas stream. The membrane allows the VOC molecules to pass the membrane preferentially, whereas the air molecules are blocked. This leads to a reduced concentration after the membrane. For a reliably operation, any particles, potentially filling the membrane, have to be removed by a filter [1]. Ultraviolet Treatment uses the photo catalytic effect of ultraviolet radiation. Under ultra violet radiation, a catalyst is used to create e.g. ozone from ambient oxygen. Afterwards, the VOC is oxidised and, therefore, destructed from the gas stream [1]. + paper Olivier lesen Catalytic ozone oxidation describes the destruction of VOC from a gas stream. Ozone is admixed to the contaminated gas stream. This mixture undergoes chemical reaction aided by a catalyst which is placed into the flow. Both, the oxidising reaction and the selectivity of the catalyst are combined. High flow rates with high or low concentrated VOC can be treated [1]. Technically, ozone can be produced using a dielectric barrier discharge, DBD. Nowadays, commercial solutions are available on the market for industrial applications [4] or for the private usage e.g. air purification for kitchens [1]. However, these devices mainly use air or pure oxygen for the ozone formation. The purification is done by a chemical reaction between the ozone and the pollutant. Alternatively, the contaminated air has been directly treated by the plasma devices. The destruction is done by the energetic electrons provided by the plasma or by the chemical substances which are also produced in the plasma volume. The plasma volume is energised by high energetic electrons, 1eV-10eV, whereas the heavy particles remain near room temperature. Thus, chemical reactions can be initialised at a relatively low energy cost because the heating of the entire mass flow can be avoided. Compared to e.g. conventional thermal incineration, such an approach shows the potential to decrease operation cost significantly. However, the energy, coupled due to electron impact, is not selective to a certain type of molecule. The electron impact basically interacts with all molecules. Therefore, for air, nitrogen can be activated leading to the formation of e.g. HNO_3. These two examples, non-selective energy coupling and the formation of other toxic by-products [5], limits the commercially throughput of plasma based pollution destruction to the commercial market. Consequently, efforts have been made in order to better control the kinetics of the chemical reaction. One approach towards a better ability to design chemical path ways is to combine plasma technology with catalysis. Here, surface effects are no longer considered to be neglectable as usually done in plasma physics experiment but are especially pronounced to take place. This has been done in two ways. First, the catalyst has been placed into the discharge volume. Second, the catalytic material has been placed in the afterglow region in order

to control the by-products formation. For example, Holzer et al. [5] has been shown that the oxidising of toluene into CO_x has been increased by a factor of about two using a $PbTiO_3$-$PbZrO_3$ packing.

2.3 Plasma based pollution destruction

The appearance of plasma in nature is known to humans since living memory, e.g. lightning, northern lights or St. Elms fire [6]. These phenomena have always been mystery to human beings and were not understood for a long time. Within the last century, the simple availability of electricity leads to the understanding of lighting arrestors or ozone production using plasma technology. Nowadays, since plasmas are sources for photons or charged particles, they are widely used in industry applications, e.g. fluorescent lamps, television screens, arc welders, IC manufacturing, surface treatment, ozonizers or arc furnaces [6]. The operation conditions of these applications vary strongly. The pressure ranges from 1Pa up to tens of bars, the dimension of the active volume can range from micrometers up to tens of meters and many different gases and gas mixtures have been studied [6]. The applied voltage has been either DC, AC with frequencies from 50Hz up to several GHz or pulse regimes. One focus of the thesis lies on VOC destruction using atmospheric plasmas at ambient air conditions, i.e. humidified synthetic air near atmospheric pressure. However, to find the most efficient method used for a application, competitive parameters have to be taken into account, such as capital investment, running cost, destruction efficiency or the formation of by-products [6]. The plasma used for VOC destruction appears as a filamented structure. This can be seen by the current peaks with a ns duration. For such a short time, only electrons can move whereas the heavy particles stay almost unchanged. Therefore, such a plasma can be called transient non-thermal discharge [6]. Pollutions are then destructed in two different ways. First, VOC can be destructed directly by electron impact. Second, the electrons create radical such as O or OH which lead to an increased oxidation of the pollutant. The simplest way of creating a discharge is a vessel filled with a sufficient gas surrounded by two electrodes [6]. An applied voltage, for atmospheric pressure it is in the order of $1kV/mm$, creates an electric field in the volume. Electrons, present in the volume, start to move. Theses electrons are usually assumed to be created as a consequence of electron-ion pair generation of the gas which is caused by cosmic radiations. On earth's surface, the cosmic radiations lead to an electron density of about 106 electrons m^{-3} in the gas volume. Due to their low mass, electrons travel for view ns range whereas the havier ions are accelerated in the μs range. Consequently, the movement of the ions can be neglected in the ignition phase. Free electrons might also be created by detachment of negative ions. This is influenced by gas composition and the history of the discharge volume and discharge vessel [6]. As time goes on, the electric field energises the electrons. Consequently, the electrons consume power from the power supply and accelerate. The second step is, that an electron will hit most probably an neutral gas molecule. This is because the particle density at atmospheric pressure is in the order of $10^{25}m^{-3}$. Because of the collision, the electrons energy as well as the direction might be changed. The particle hit by the electron consumes some parts of the energy and the following properties of a molecule can be affected [6]:

- translation

- rotation excitation

- vibration excitation

- electronic excitation

- dissociation

- ionisation

Translation describes the linear motion of a particle which can be changed in direction or speed. Principally, any energy value can be exchanged, but other processes are usually begun to be initiated below $1eV$. Rotational and vibrational excitation describes the population of higher rotational or vibrational orbits of the molecule. Rotational excitation is quantized of steps in the order of $0.1eV$ whereas vibrational excitation has energy steps in the order of $0.5eV$. Other processes can follow, e.g. de-excitation or quenching which means that the vibrational energy of a molecule can transfer into rotation or translation of another molecule, caused by collision. Electronic excitation describes the population of a higher orbit with outer electrons. This energy can be emitted by a photon and is called spontaneous emission. The energy can also be loss by collisional quenching, that is, the energy is transferred in a way which changes the vibrational or electronic state of another molecule. The energy can also ionise a molecule. Some excited states can not emit a photon, i.e. the transition to the ground state is forbidden. Such e state is called metastable state. The lifetime of such a state can be view ms but also several seconds are possible. Dissociation describes the process, when excited molecules break into fragments. As a consequence, radicals may be produced. This usually, requires energy in the order of $5eV$. Under atmospheric conditions, oxygen and water may be lead to the formation of O and OH respectively. These species create a very oxidising environment which leads to pollution destruction [6]. Ionisation is the process which leads to the extraction of, at least, one electron from a molecule into the gas volume. It requires usually energies in the order of $10eV$. Once a second electron is freed, two electrons are energised by the electric field. Each of them may react in the same way and can potentially create another electron. Now, four electrons are now moving in the gas volume undergoing the same reaction, each freeing a new electron.. Such an exponential increase of the number of electrons in the gas volume is called an avalanche and was first described by Townsend. The development of an avalanche requires two additional criterions to be fulfilled [6]l, these are: (i) inception field strength (critical field strength) and (ii) critical volume. For (i), under atmospheric conditions, the mean free path is in the order of about $1\mu m$, that is the distance between two collisions on average. As seen, the ionisation requires electron energies in the order of about 10eV. Consequently, the electric field strength has to be strong enough in order to energise the electrons within the mean free path. Therefore, a field strength of about $10^7 Vm^{-1}$ would be necessary is the gas volume. However, the field strength found in experiments is about 10 times less this value, i.e. $10^6 Vm^{-1}$. The discrepancy can be explained by the fact that the electron energy is a statistical value, a distribution. There are always electrons which are faster than the main velocity, so they are able to start at lower field

strengths. For (ii), under atmospheric conditions, the discharges appear as micro discharges with a duration of view *ns*. For such short period, the electrons move to the anode whereas the ions stay almost at their position. Once enough ions are created, a cloud of charges, so called space charge, creates its own electric field with the same field strength as the outer electric field. That means the space charge stops the development of the avalanche. Therefore, the discharge shout start at least one length of avalanche in front of the anode. A volume with this length is called critical volume. The exact dimension of such a critical volume depends on the geometry of the electrode but is, for atmospheric conditions, in the order of a fraction of a mm. The critical volume allows the definition of an inception time lag. That is, the time before at least one free electron appears in the critical volume. Under atmospheric conditions, the interception time lag is in the order of view tens of ns. As a consequence of the formation of an avalanche, a space charge is created which, at the same time, causes the avalanche to be stopped. That is when the space charge creates a field strength in the order of the outer field. On the way creating a space charge, the electrons create also high excited molecules which can emit a photon. Although, the space charge is above the inception value, the avalanche is stopped because there are not enough free electrons around the avalanche volume. Consequently, a second source for electrons must be available. It must have a higher electron production rate than the rate caused by cosmic radiation. This second source is photo ionisation. The avalanche creates not only ions but also excited molecules. Some of them de-excite into the ground state emitting a photon. The photon can be emitted into any direction, i.e. no preferred direction for the photon exists. This photon can be absorbed by the surrounding molecules. Two effects can be distinguished at this point. First, the photon ionised a molecule near the space charge region. The local electric field is below the inception field strength and no avalanche can be created. Second, a molecules is ionised which is sufficient far from the space charge region. That means, the freed electron fulfils the inception condition and, therefore, a new avalanche is created. This effect is caused by resonance radiation. For example, for N_2 and O_2, the wavelength of the resonant radiation is about $100nm$. Because the levels of N_2 are much higher than the one of O_2, these emitted photons can ionise O_2. Once such a photon is travelled a sufficient distance, a new electron is freed and a new avalanche can start leading to electrons travelling toward the anode. Due to the space charge, the electrons can also travel into the exciting space charge region creating quasi neutral plasma with a low electric field. No further charge separation in this region will happen. The creation of a second space charge region in front of the first space charge region leads the movement of the space charge region of the ion towards the cathode although the ions do not move. Once the electric field in front of the space charge region remains high enough the space charge region propagates through the gas volume. Such a phenomenon is usually called streamer. The space charge region moving towards the gas is called streamer head whereas the quasi neutral plasma channel behind the had is called the streamer channel [6]. Numerical simulations [6] have shown that the diameter of such a streamer channel is in the order of several 100 of μm. The production of ozone can be done by a plasma application [4, 7] or by UV light. The latter is a process in the troposphere. For pollution control, plasma applications are used for ozone production. A main application is the purification of water by ozone treatments [4]. For odour destruction in e.g. in kitchens, commercial devices are available which use atmospheric plasma both to direct destroy the pollutant and to enrich the contaminated air stream with ozone.

The main pollution destruction is done by a catalysed chemical reaction between the ozone and the pollutant. For this purpose, the air stream is guided over a catalyst. The destruction of pollution in a discharge has been widely studied. Many publications are available.

2.4   VOC destruction in plasmas

The decomposition of harmful species from a gas stream requires plasma physics and plasma chemistry to be considered [8]. In the active discharge volume, not only hot electrons are generated but also chemically active fragments such as free radicals or functional molecule groups. Therefore, for pollution destruction, two main destruction mechanisms can be distinguished [8]. First, direct electron impact in the VOC molecules leads to a dissociation of the VOC molecules and creates VOC fragments which may undergo other chemical reactions. This can be summarised by

$$ e + X \rightarrow \text{Product} \tag{2.1} $$

Second, the energised electrons create also radicals e.g. O and OH which can destroy VOC molecules by a chemical reaction. This is described by

$$ O, OH + X \rightarrow \text{Product} \tag{2.2} $$

Electron impact decomposition, (i), may be the dominating process at higher VOC concentration whereas the radical promoted decomposition, (ii), may dominate at lower VOC concentrations. Other mechanisms are reported in the literature, e.g. ion molecule reactions. A charge exchange can lead to the decomposition of methanol. Ion-neutral clustering can create aerosols which leads to an increases VOC destruction due to reactions at the surface of the aerosols. Such mechanism can also influence the final species. Table 2.2 shows some example reaction channels present in an air plasma. The destruction of VOC by plasma technology has been done by many different research groups world wide. Not only the type of discharge, e.g. corona, DBD or packed bed, has been studied. Also different voltages, ac or dc, at varying amplitudes. For ac, many frequencies have been studied as well as varying gas mixtures. For a better comparability of the different ways, certain parameters have been defined [8].

1. the yield of radical per unit energy, G-value

2. specific energy of a compound, β-value

3. energy cost per molecule, γ-value

The efficiency of radical production, i.e. the ratio between number of radicals produced divided by unit deposited plasma energy, depends on parameters such as gas composition, gas pressure and the average electron temperature. This is usually described by the G-Value which defines how many radical have been produced per $100 eV$ deposited plasma energy.

$$ G = G \left(\frac{k_{rad}}{V_d \cdot \frac{E}{N}} \right) \tag{2.3} $$

Table 2.2: Examples of formation mechanisms for the radical formation in air like plasma at atmospheric conditions [8].

Electron Impact	$e + O_2$	$\rightarrow$	$O + O^* + e$
	$e + O_2$	$\rightarrow$	$O + O + e$
	$e + N_2$	$\rightarrow$	$N + N + e$
	$e + O_2$	$\rightarrow$	$O_2^* + e$
	$e + N_2$	$\rightarrow$	$N_*^2 + e$
	$e + H_2 + O$	$\rightarrow$	$OH + H + e$
	$e + NO$	$\rightarrow$	$N + O + e$
	$e + NH_3$	$\rightarrow$	$NH + H_2 + e$
Quenching	$O^* + H_2O$	$\rightarrow$	$2OH$
	$N_2 + O_2$	$\rightarrow$	$N_2 + O + O$
Ionisation / Clusters	$e + O_2$	$\rightarrow$	$O_{2+} + e$
	$O_{2+} + H_2O$	$\rightarrow$	$O_2 + (H_2O)$
	$O_2 + (H_2O) + H_2O$	$\rightarrow$	$HO_3^+ + O_2 + OH$
	$O_2 + (H_2O) + H_2O$	$\rightarrow$	$HO_3 + (OH) + O_2$
	$HO_3 + (OH) + H_2O$	$\rightarrow$	$HO_3^+ + H_2O + OH$
Others	$H + O_3$	$\rightarrow$	$OH + O_2$
	$HO_2 + NO$	$\rightarrow$	$OH + NO_2$
	$H + O_2 + M$	$\rightarrow$	$HO_2 + M$
	$O + O_2 + M$	$\rightarrow$	$O_3 + M$

where k_{rad} is an effective rate constant for the production of radical, e.g. the rate constant of O production from dissociation of O_2, V_d electron drift velocity and E/N is the reduced electric field strength. Because k_{rad} and V_d are also a function of the reduced field strength, the G-value depends mainly on the reduced electric field strength E/N and the plasma chemical kinetics [8]. The specific energy β, or the plasma energy density, is another important plasma parameter especially for VOC destruction. Several experiments have shown that the pollution destruction can approximately be described by

$$[X] = [X]_0 \cdot exp\left(-\frac{E}{\beta}\right) \tag{2.4}$$

where $[X]_0$ is the initial pollutant concentration, $[X]$ is the pollutant concentration after plasma treatment and E is the deposited electrical energy density for a certain gas flow, unit: energy per standard litre i.e. J/l. The specific energy β can be used to characterise the pollutant destruction and is related to a certain pollutant, the carrier gas and the reduced electric field strength E/N. Therefore, the calculation of the β-value for two different plasma reactors working with the same initial composition of the carrier gas, the same pollutant concentration, supplied with the same energy allow simple comparison of the two reactors performances. Thus, β is independent of the reactor and the speed of the gas. The β-value has been determined in many experiments for several types of reactors and working conditions. Simple kinetic models have been used to

describe the pollutant decomposition induced by a radical pollutant reaction [6]. For the case that the degree of pollutant destruction is low, i.e. when , β can be expressed by

$$\beta = \frac{1}{G}\left([X]_0 + \frac{\sum_i k_{S_i} \cdot [S_i]}{k}\right) \tag{2.5}$$

where G is the radical production, k is the radical pollutant kinetic rate constant, $[S_i]$ is the concentration of the ith scavenger and k_{S_i} is the scavenging rate constant for the ith species. From eqn. 2.5, one can see that in case the radical scavenging $\sum_i k_{S_i} \cdot [S_i]$ is greater than the radical pollutant reaction rate k, β does not depend on the initial pollutant concentration $[X]_0$. Experimentally obtained destruction ratios plotted as a function of the deposited energy, therefore, allow to see weather the destruction ratio depends on the initial concentration or not. If the destruction ratio is independent on the initial concentration, the plot should show a straight line. If the destruction ratio depends on the initial concentration, more complex curves may appear. The cost of air stream purification from a pollutant is an important issue. The parameter used to compare different methods is the ratio between the consumed energy and the number of removed hazardous molecules [8]. This is

$$\gamma = \frac{E}{[X]_0 - [X]} = \frac{-\beta \cdot \ln\left(\frac{[X]}{[X]_0}\right)}{[X]_0 \cdot \left(1 - \frac{[X]}{[X]_0}\right)} \tag{2.6}$$

For the last part of the equation, the energy E has been substituted using eqn. 2.4.

## 2.5   The concept of a packed bed reactor

The concept of packed-bed reactor is widely used in chemical processes. A granulate or powder is situated in a chemical reactor [9]. Such an arrangement still allows a gas or liquate to flow through the packing material, although the flow residence might be increased. Doing so, the size of the interaction surface between the packed material and the liquate or gas is significantly increased. Therefore, this setup is suitable in, for example, adsorption or heterogeneous catalysis applications. In plasma technology, the embedment of a dielectric material between the two electrodes causes the packing material to be polarised. Depending on the relative dielectric constant ε_r, higher field strength can be reached near the surface of the packing material compared to the case no material is embedded. This is even stronger at sharp corners. Therefore, packed-bed reactors have been used for the creation of large, relatively homogenous plasma volumes at atmospheric pressure [10]. Additionally, the embedment of dielectric material can support heterogeneous catalysis. Fig. 2.2 shows two setups of a packed-bed reactor. First, the two electrodes are a plane meshes holding the packing material [11, 12]. The contaminated gas flows perpendicular through the setup. Both, the characteristic diameter of the electrodes, circle or rectangular, as well as the electrode distance have been in the order of several centimetre. Second, a cylindrical setup has been reported. For the electrodes, a metal wire or cylindrical rod serving as the inner electrode is surrounded by a metal tube or mesh holding the packing ma-

terial. The gas flows axially through the setup [5, 11–15]. The diameter of the inner electrode can be in the sub mm range but also some cm. Both setups have been driven with sinusoidal or sinusoidal like ac voltage. Depending on the electrode distance, the amplitude has been in the kV range. The frequency ranges from main, i.e. $50 Hz$ or $60 Hz$, up to several kHz. The gas flow ranges from some $10s$ of $cm^3 min^{-1}$ up to several $l min^{-1}$ for experiments under laboratory scale. The flow F is important because it determines the residence time of the gas mixture in the reactor. Usually, the volume of the reactor V_R is considered i.e. the part of the reactor which is filled with the packing material. The residence time t_{res} is than given by $t_{res} = V_R/F$. As mentioned above, the embedment of dielectric material has been done in order to locally increase the field strength between the electrodes. Consequently, materials with a high relatively dielectric constant ϵ_r have been used, for example BaTiO3. A systematic study of the influence of the relative dielectric constant to the decomposition of benzene in air can be found in Ref. [16]. Here, the main components of the packing material with a diameter of $2 mm$ have been: Mg_2TiO_4, $CaTiO_3$, $SrTiO_3$ and $BaTiO_3$. Other materials like for example TiO_2, Zeolithes [5], γ-Al_2O_3, α-Al_2O_3 [15] or just glass [17] have been applied as well. The embedment of zeoliths, however, has been done because these type of materials have a high surface. Therefore, adsorption and plasma based regeneration have been in the focus of the experiments. The shape of the packing material has also been investigated. Takaki used spheres, cylinder and hollow cylinder as packing material for the destruction of C_2F_6 contaminating exhaust gases of semi conductor processing [18]. It was found that the usage of hollow cylinders increases the destruction efficiency from $2.5 g/kWh$ using spheres up to $3.7 g/kWh$. Packed-bed reactors have been used to study the destruction efficiency of several gas mixtures. For example, benzene [16, 20], carbon tetrachloride [11], toluene [11, 15, 20], butane [14], o-xylene and trichloroethylene [11], methane [13], 1,1,1,2-tetrafloroethane and 1,1-difluoroethane [21], trichloromethane [22], C_2F_6 [18], methyl mercaptan and dimethyl sulphide [23], methylene chloride and trichlorotrifluoroethane [24], acetaldehyde [25] or NH_3 [19].

2.6 Plasma induced catalysis

The combination of plasma and catalytic active material has shown significant improvements of the absolute destruction of pollutants admixed to gas streams, e.g. [26–32] and references therein. They are either placed directly into the active plasma volume or into the afterglow region. In the after glow region, depending on the gas flow and pressure, the catalyst can mainly act on stable or long living species. For example, [26] has been shown that the degree of benzene removal can be increased applying MnO_2 into the afterglow region. From their conclusion, ozone, created into the plasma, can react with benzene on the MnO_2 surface leading to an advanced ozone destruction and benzene removal. Another example considers TiO_2. Its photocatalytic properties can create reactive oxygen species, OH, O_3^- and O^-, under UV radiation. This can be done by the light emission from excited nitrogen [30]. Both species are present in air-like mixtures. The embedment of catalytic active material directly into the active plasma region, e.g. packed-bed reactor, allows catalysed reaction between the transient fragments present only during the plasma. However, the embedment of a dielectric material
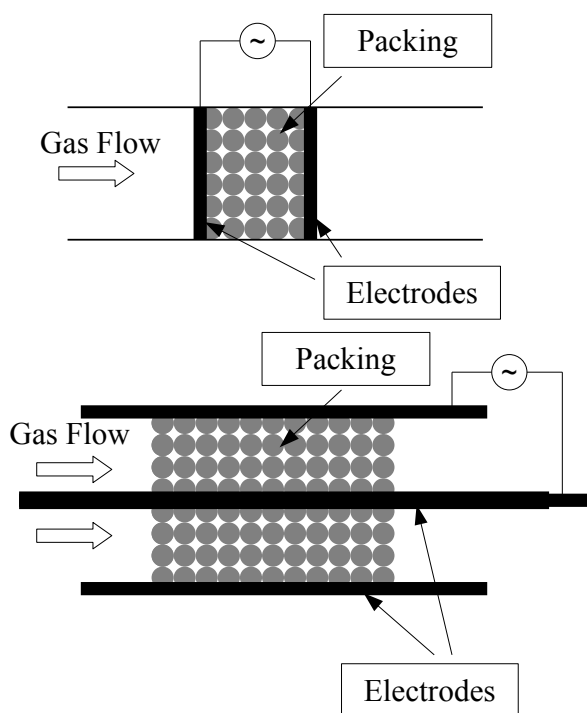
Figure 2.2: Two different setups of an packed bed plasma reactor [13, 19]. Two planar electrodes are separated by the packing material. The gas mixture flows perpendicular through the reactor, top. A cylindrical wire or rod is surrounded by a cylindrical tube, both acting as the electrodes. The contaminated gas flows axially through the packing material, bottom.

can change the local field strength as well as cause catalysed surface - gas phase reactions. In chapter 4, it is shown that the embedment of a glass sphere leads (i) to the plasma to be appear around the sphere, directly around the surface, and (ii) to an active volume near the surface. Consequently, at least for research purposes, two processes have to be distinguished: volume processes and surface processes. Indeed, already in [33] are examples discussed distinguishing between surface initiated and volume species conversion reaction. The importance of them is illustrated by the surface sensitised NO, NH_3 and hydrazine synthesis. Additionally, not only material can have an influence to the species conversion but also charged cheats near the surface. These cheats can be formed under plasma exposure and influence the diffusion of charged plasma fragments towards the wall. The combination of plasma and a catalytic material is usually called plasma catalysis. However, this term might be not the best choice. Historically, the term catalysis has been defined by chemistry and describes a process which can change the speed of a reaction, increasing (positive catalysis) or decreasing (negative catalysis). The catalysts can neither change the equilibrium of the reaction nor the equilibrium concentrations [33]. It is questionable weather these definitions do fit to a non-thermal, non-equilibrium plasma. Therefore, here it is preferred to use the term plasma induced catalysis indicating that at least one certain chemical reaction is influenced by the catalysis in a way the conversion of the target species is changed. In chemical text books, the term catalyst is defined to be a substance which

can change the rate of a chemical reaction being in contact with the reactants. It is not a product or reactant [34]. The following points characterise a catalyst in a classical manner [34].

1. A catalyst leads to an increased rate of reaction compared to the uncatalysed reaction.

2. A catalyst is not part of the stoichiometric of the reaction.

3. A catalyst is neither produced nor consumed by the reaction.

4. A catalyst does not change the chemical nature of the products.

5. A catalyst does not influence the thermodynamic affinity of the reaction. It can change the rate of a reaction but not the tendency. Neither the free energy change (δG) nor the equilibrium constant (K_{eq}) are affected.

6. From 5, it follows that a catalyst acts on both, forward and reverse reactions.

7. A catalyst, in general, leads to a reduction of the activation energy, E_A, of a chemical reaction. This leads to the formation of intermediates between the catalyst and the reactants. Finally, the products are created and the catalyst becomes regenerated.

The process changing the reaction rate is called catalysis. Nowadays, different types of catalysis are distinguished. The nomenclature mainly orientates on the species responsible of the catalytic activity [34].

- Molecular catalysis

- Surface catalysis

- Enzyme catalysis

- Autocatalysis

- Homogenous catalysis

- Heterogeneous catalysis

The term *heterogeneous catalysis* implies the fact that the species in the gas phase have to reach the surface of the catalyst. In the volume, this is mainly described by the mean free path of the gas particles and can be estimated to be in the sub micrometre range [35]. In order to emphasis surface processes compared to volume processes, the effective dimensions of the active volume should be equal or less the mean free path. Since one of the foci of this thesis lie on the plasma wall and the plasma induced wall interaction, the concept of *catalytic site* on a surface is discussed. The term *catalytic site* describes a little part of the surface where the catalysed reaction takes place. These small locations separate the extended surface into thousands of thousands of reaction zones. The non-ideal structure of most of the catalysts leads to a distribution of the properties of the *catalytic sites*. They may vary in e.g. reactivity or size. For example, metal catalysts are made of metal crystallites of different size. Additionally, the

number of catalytic active metal atoms on the surface varies from *catalytic site* to *catalytic site*. When a reactant reaches the surface of a catalytic active material, a bond between the reactant and the catalyst is formed. Thus, the energy of the system is decreased. On the surface, the bonded species can undergo surface diffusion and can react with each other. The product leafs the surface into the gas volume whereas the *catalytic site* becomes regenerated. In literature, two important mechanisms are distinguished [36]:

- Langmuir-Hinshelwood Reaction

- Eley-Rideal Reaction

Bibliography

[1] P. Hunter and S. T. Oyama. *Control of volatile organic compound emissions : conventional and emerging technologies*. John Wiley & Sons, (2000).

[2] EPA United States Environmental Protection Agency. http://www.epa.gov/cgi-bin/broker?_service=data&_debug=0&_program=dataprog.national_1.sas&polchoice=voc, 2011.

[3] EPA United States Environmental Protection Agency. http://www.epa.gov/iaq/ia-intro.html, 2011.

[4] U. Kogelschatz. Dielectric-barrier discharges: Their history, discharge physics, and industrial applications. *Plasma Chemistry and Plasma Processing*, **23**:1, (2003).

[5] F. Holzer. Oxidation von organischen Verbindungen unter Nutzung von porösen und unporösen Feststoffen im nichtthermischen Plasma, (2003).

[6] E. M. v. Veldhuizen. *Electrical discharges for environmental purposes : fundamentals and applications*. Nova Science Publishers, (2000).

[7] U. Kogelschatz and J. Salge. High-pressure plasmas: Dielectric-barrier and corona discharge - properties and technical applications. In R. Hippler, editor, *Low Temperature Plasmas*, page 439. Wiley-VCH, (2008).

[8] L. A. Rosocha. Removal of volatile organic compounds (VOCs) by atmospheric-pressure dielectric-barrier and pulsed-corona electrical discharges. In E.M. Velduizen, editor, *Electrical discharges for environmental purposes*. NOVA Science Publishers, Inc., (1999).

[9] J. Falbe and M. Regitz. *Chemie*. Georg Thieme Verlag, (1999).

[10] E. E. Kunhardt. Generation of large-volume, atmospheric-pressure, nonequilibrium plasmas. *IEEE Transactions on Plasma Science*, **28**:189, (2000).

[11] T. Yamamoto, K. Mizuno, I. Tamori, A. Ogata, M. Nifuku, M. Michalska, and G. Prieto. Catalysis-assisted plasma technology for carbon tetrachloride destruction. *IEEE Transactions on Industry Applications*, **32**:100, (1996).

[12] T. Yamamoto. Decomposition of toluene, o-xylene, trichloroethylene, and their mixture using a BaTiO$_3$ packed-bed plasma reactor. *J. Adv. Oxid. Technol.*, **1**, (1996).

[13] A. Ogata, K. Mizuno, S. Kushiyama, and T. Yamamoto. Methane decomposition in a barium titanate packed-bed nonthermal plasma reactor. *Plasma Chemistry and Plasma Processing*, **18**:363, (1998).

[14] S. Futamura, A. H. Zhang, G. Prieto, and T. Yamamoto. Factors and intermediates governing byproduct distribution for decomposition of butane in nonthermal plasma. *IEEE Transactions on Industry Applications*, **34**:967, (1998).

[15] T. Zhu, Y. D. Wan, H. R. Li, S. Chen, and Y. Fang. VOCs decomposition via modified ferroelectric packed bed dielectric barrier discharge plasma. *IEEE Transactions on Plasma Science*, **39**:1695, (2011).

[16] A. Ogata, N. Shintani, K. Mizuno, S. Kushiyama, and T. Yamamoto. Decomposition of benzene using a nonthermal plasma reactor packed with ferroelectric pellets. *IEEE Transactions on Industry Applications*, **35**:753, (1999).

[17] A. M. Harling, D. J. Glover, J. C. Whitehead, and K. Zhang. Novel method for enhancing the destruction of environmental pollutants by the combination of multiple plasma discharges. *Environmental Science & Technology*, **42**:4546, (2008).

[18] K. Takaki, K. Urashima, and J. S. Chang. Ferro-electric pellet shape effect on C_2F_6 removal by a packed-bed-type nonthermal plasma reactor. *IEEE Transactions on Plasma Science*, **32**:2175, (2004).

[19] R. H. Zhang, T. Yamamoto, and D. S. Bundy. Control of ammonia and odors in animal houses by a ferroelectric plasma reactor. *IEEE Transactions on Industry Applications*, **32**:113, (1996).

[20] A. M. Harling, H. H. Kim, S. Futamura, and J. C. Whitehead. Temperature dependence of plasma-catalysis using a nonthermal, atmospheric pressure packed bed; the destruction of benzene and toluene. *Journal of Physical Chemistry C*, **111**:5090, (2007).

[21] Y. S. Mok, V. Demidyuk, and J. C. Whitehead. Decomposition of hydrofluorocarbons in a dielectric-packed plasma reactor. *Journal of Physical Chemistry A*, **112**:6586, (2008).

[22] Y. S. Mok, S. B. Lee, J. H. Oh, K. S. Ra, and B. H. Sung. Abatement of trichloromethane by using nonthermal plasma reactors. *Plasma Chemistry and Plasma Processing*, **28**:663, (2008).

[23] I. K. Ahmad, A. E. Wallis, and J. C. Whitehead. The plasma destruction of odorous molecules: Organosulphur compounds. *High Temperature Material Processes*, **7**:487, (2003).

[24] T. Yamamoto, K. Ramanathan, P. A. Lawless, D. S. Ensor, J. R. Newsome, N. Plaks, and G. H. Ramsey. Control of volatile organic-compounds by an ac energized ferroelectric pellet reactor and a pulsed corona reactor. *IEEE Transactions on Industry Applications*, **28**:528, (1992).

[25] H. M. Lee and M. B. Chang. Gas-phase removal of acetaldehyde via packed-bed dielectric barrier discharge reactor. *Plasma Chemistry and Plasma Processing*, **21**:329, (2001).

[26] S. Futamura, A. H. Zhang, H. Einaga, and H. Kabashima. Involvement of catalyst materials in nonthermal plasma chemical processing of hazardous air pollutants. *Catalysis Today*, **72**:259, (2002).

[27] C. L. Gordon, L. L. Lobban, and R. G. Mallinson. Ethylene production using a Pd and Ag-Pd-Y-zeolite catalyst in a dc plasma reactor. *Catalysis Today*, **84**:51, (2003).

[28] R. X. Valenzuela, G. Bueno, V. C. Corberan, Y. D. Xu, and C. L. Chen. Selective oxidehydrogenation of ethane with CO_2 over CeO_2-based catalysts. *Catalysis Today*, **61**:43, (2000).

[29] S. Delagrange, L. Pinard, and J. M. Tatibouet. Combination of a non-thermal plasma and a catalyst for toluene removal from air: Manganese based oxide catalysts. *Applied Catalysis B-Environmental*, **68**:92, (2006).

[30] S. Futamura, H. Einaga, H. Kabashima, and L. Y. Hwan. Synergistic effect of silent discharge plasma and catalysts on benzene decomposition. *Catalysis Today*, **89**:89, (2004).

[31] A. Ogata, H. H. Kim, S. Futamura, S. Kushiyama, and K. Mizuno. Effects of catalysts and additives on fluorocarbon removal with surface discharge plasma. *Applied Catalysis B-Environmental*, **53**:175, (2004).

[32] Y. F. Guo, D. Q. Ye, K. F. Chen, and J. C. He. Toluene removal by a DBD-type plasma combined with metal oxides catalysts supported by nickel foam. *Catalysis Today*, **126**:328, (2007).

[33] H. Drost. *Plasmachemie*. Akademie-Verlag Berlin, (1978).

[34] R. W. Missen, C. A. Mims, and B. A. Saville. *Introduction to chemical reaction engineering and kinetics*. J. Wiley, (1999).

[35] B. N. Chapman. *Glow discharge processes : sputtering and plasma etching*. Wiley, (1980).

[36] G. Ertl, H. Knözinger, and J. Weitkamp. *Handbook of heterogeneous catalysis*. VCH, (1997).

Chapter 3

Diagnostics of the studied discharges

3.1 Introduction

The diagnostic of plasma applications is a fundamental demand in order to understand the internal processes. In the field of pollution destruction and plasma surface interaction studies, the plasma stimulated species transformation and their kinetics as well as surface interaction probabilities can be deduced from a precise and time resolved measurement of the gas phase species concentration. The methods used for plasma diagnostics can be classified into invasive and non-invasive methods as well as into in-situ and ex-situ measurements [1]. Invasive methods disturb the object of investigation significantly. For example, probe measurements developed by Langmuir [2] can change the local electric field due to the applied voltage [3]. The probe can be coated or sputtered probe material can contaminate the plasma volume. These phenomena can influence the probe measurement. Because the probe has to be inside the active plasma volume, this method can be considered to be an in-situ method. On the other hand, gas chromatography [4] and mass spectrometry [5] are two examples for non-invasive, ex-situ investigations of plasmas. For these methods, a gas sample is extracted from the discharge and investigated outside the plasma. For mass spectrometry, the mass to charge ratio of the extracted and afterwards ionised neutrals is studied. The sensitivity is usually quite high in the order of 10^{-4}. For gas chromatography, the gas components are also extracted from the discharge and analysed according to their specific travel time passing a separation column. The method is suitable for the investigation of more complex species. Due to the relatively slow velocity of the gas mixture inside the separation column, the time resolution is in the order of minutes and therefore rather low. Non-invasive investigations of plasmas can be performed using spectroscopic diagnostic techniques. Information about the atom, ion or molecule density in their exited or ground state can be achieved. Additionally, the rotational and vibrational temperature can be studied. In general, spectroscopic methods are line of sight methods. One example for a non-invasive, in-situ method is optical emission spectroscopy, OES. For this method, the emitted electromagnetic radiation is separated into its spectral intensities. The used spectrometers usually allow high spectral resolution. Sensitivities near the single photon detection are faceable. The time resolution can be in the order of ns. The measurement of absolute species concentration in their ground state might be difficult since a theoretical model considering (i) excitation

and de-excitation processes, (ii) cross-section, (iii) transition probabilities and (iv) the electron energy distribution function, EEDF [1] are necessary. These parameters are not easy to measure experimentally. Therefore, actinometry is often applied in practice which compares measured intensities with a known reference [1, 6–8]. Another example for a non-invasive method is absorption spectroscopy assuming that the excitation of the species can be neglected. This method allows the measurement of species concentration in their ground state as well as excited states. For the studies presented in this thesis, two infra red based absorption methods have been used, (i) Fourier Transformation Infrared (FT-IR) spectroscopy and (ii) Quantum Cascade Laser Absorption Spectroscopy (QCLAS). Both methods have been used to identify and quantify the gas mixture and are shortly summarised. The destruction of pollution, chapter 4, has been monitored using the FTIR system. It combines a wide spectral range sensitivity with a relatively sensitive detection limit which is in the order of ppm. For FTIR measurements, a gas sample has been extracted into a optical long path cell detecting the neutrals in their ground state. QCLAS has been used manifold, see also chapter 5. First, the species transformation stimulated by a plasma treated Pyrex surface, chapter 5.3. Second, the species conversion during and in the early after glow of a ms dc plasma pulse applied to low pressure air like mixture has been measured. The time resolution has been in the order of several μs. Third, the temperature during a ms dc plasma pulse at low pressure could be measured adapting a line ratio method [9], chapter 3.5 to the QCLAS. At low pressure, such spectra are highly distorted by non-linear absorption effect. Therefore, a calibration method has been applied to both the concentration as well as to the temperature measurements. In this third chapter, the diagnostics are described which have been used for the experiments. The following subchapter 3.2 contains a short introduction into absorption spectroscopy and how this method is used to obtain absolute number concentrations for both, FT-IR spectroscopy and QCLAS. In chapter 3.5, a method is presented which allows the measurement of the gas temperature despite the strong disturbance of the obtained absorption spectra usually present using QCLAS working in the *Intra Pulse Mode*. Additionally, a spectrometer that facilitates the investigation of transient phenomena in molecular plasmas has been developed based on QCLAS. It combines high time-resolution with high sensitivity to detect key species in the gas phase and the potential of (simultaneous) multi-species monitoring. Although in-situ experiments tackling all these three criteria are still challenging, a significant improvement of existing spectrometers has become feasible due to the aforementioned progress in mid-IR laser technology. In chapter 3.6, a relatively compact 3 channel QCL spectrometer has been developed. Its performance is described with special attention to the data treatment. A special trigger regime has been applied. The typical jitter of the lasers has been statistically investigated and allows estimating the influence to the data treatment algorithm.

3.2   Infrared absorption spectroscopy

The general concept of absorption applied to the investigation of matter describes the reduction of a physical quantity when passing an absorbing medium. In gas phase absorption spectroscopy, the intensity of an incident light beam can be reduced when it passes a volume filled with an absorbing species. These reductions, for example, depend on the wavelength of the

radiation, the number density of the absorber, the cross section and the absorbing length. The incident intensity of a light beam, I_0, reduced by dI after passing the distance dz can be expressed by [10, 11]

$$dI(v) = (j(v) - k(v)) \cdot I_0(v) \cdot dz \qquad (3.1)$$

where $j(v)$ is the emission coefficient and $k(v)$ is the absorption coefficient. The absorption coefficient $k(v)$ is the product of the number density n per unit volume and the corresponding absorption cross section $\sigma(v)$. In case several absorption features are involved, the absorption coefficient can be expressed by the sum over all k_i

$$k(v) = \sum_i k_i(v) = \sum_i n_i \sigma(v) \qquad (3.2)$$

Scattering can be neglected in the infrared region due to the dependency. In case no scattering or emission effects have to be included, eqn. 3.1 can be integrated over an effective absorption length L leading to Beer-Lambert law of linear absorption [11]

$$\ln\left(\frac{I_0(v)}{I(v)}\right) = k(v)L \qquad (3.3)$$

One important quantity obtained from the absorption spectroscopy measurements is the number
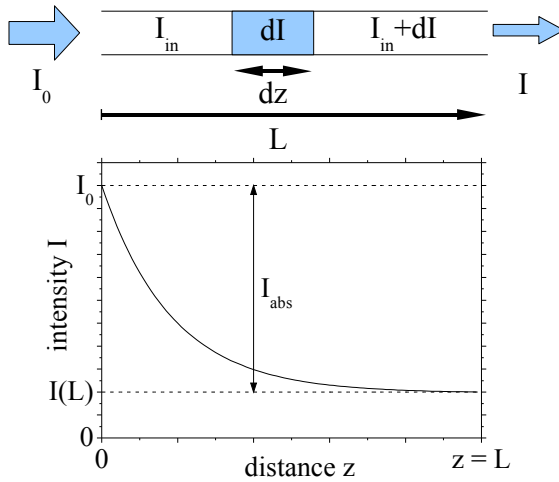
Figure 3.1: Schematic diagram of the variation of the intensity in a infinitesimal distance dz, upper [10] and a 1D representation of the decreasing intensity absorbed along the distance z, lower [11].
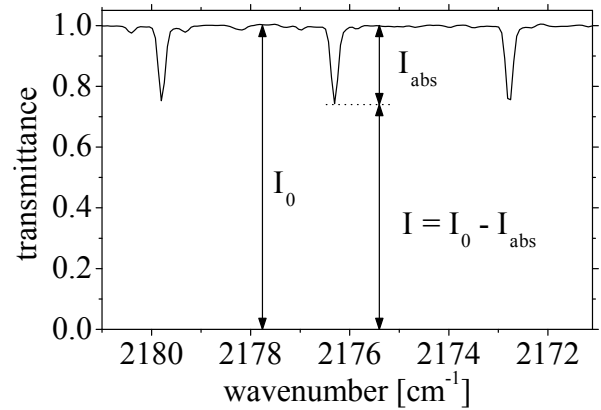
Figure 3.2: Transmission spectrum of CO at $2176cm^{-1}$ taken with a FTIR spectrometer with a resolution of $0.11cm^{-1}$. The definitions of the used symbols are shown.

density *n* of the gas components. Therefore, the integrated absorption coefficient *K* is defined

as

$$K(T) = \int_{Structure} k(v) \cdot dv = \frac{1}{L} \int_{Structure} \ln\left(\frac{I_0(v)}{I(v)}\right) dv = n \cdot S(T) \tag{3.4}$$

and associates the absorption coefficient to the number density n via the absorption strength S. The integration has to be done over the absorption structure. The eqn. 3.4 allows the determination of the number density n from measured quantities, i.e. I_0, I and L. In laser absorption spectroscopy with high spectral resolution, S is called the line strength since the absorption structures appear to have a line shape. For spectrometers where single absorption phenomena are not resolved, S might be named band strength. Nevertheless, S is a proportionality factor and can be found in databases. For this thesis, two different databases have been used. For the laser spectroscopy in chapter 3.4, the database HITRAN [12] has been used which lists the line strengths for single transitions. For the analyses of the FT-IR spectra, see next chapter, the PNNL [13] database has been used. It contains measured spectra normalised to $ppm^{-1}m^{-1}$. For sufficient narrow band sources where single absorption structures can be resolved, a line shape profile $\Phi(v - v_0)$ can be assigned to the absorption structure. The line strength S can then be treated as a scaling parameter describing the absorption cross section $\sigma(v - v_0)$ for a absorption line centred at v_0 [11]

$$\sigma(v - v_0) = S \cdot \Phi(v - v_0) \tag{3.5}$$

where the line shape profile $\Phi(v - v_0)$ has to be normalised.

$$\int_{line} = \Phi(v - v_0) \, dv = 1 \tag{3.6}$$

Several effects lead to a broadening of the line shape profile $\Phi(v - v_0)$ [14]

- natural broadening

- Doppler broadening

- pressure broadening

The first two broadenings are neglected here since the influence is about 10^{-9} for natural broadening and in the order of 10^{-3} for the Doppler broadening [15]. The pressure broadening ranges from about $10^{-4}cm^{-1}$ at low pressure, $< 5mbar$, up to $5 \times 10^2 cm^{-1}$ at atmospheric pressure. Parts of this work have been done, see chapter 4, using a FTIR spectrometer with a resolution of $0.11cm^{-1}$. The measurements have been done at $50mbar$ or $250mbar$, respectively. The database which has been used for species quantification is specified for a pressure of $1000mbar$ [13]. The possibly influence of the pressure broadening to the quantification can be neglected since the resolution of the FTIR spectrometer is much higher as the pressure broadening at atmospheric pressure. Therefore, the influence of spectral broadening to the spectra appearance is neglected throughout this thesis.

3.3 Fourier Transformation Infrared Spectroscopy

A Fourier Transform Infra Red (FTIR) spectrometer allows the spectroscopic investigation of matter, especially the identification and the quantification of a gas phase composition is a widely used application. The main components of a FTIR spectrometer are the light source, the interferometer and the detector unit. The light source is usually a broad band emitter. An Off Axis Ellipsoid (OAE) is used to focus the emitted light through a pin hole aperture. The beam is then parallelised by an Off Axis Paraboloid (OAP). Most of the FTIR spectrometers use a Michelson interferometer with a beam splitter [16, 17]. The parallel beam hits the beam splitter. For ideal conditions, 50% of the light is reflected at the beam splitter and 50% are transmitted. The reflected part is reflected by the fixed mirror whereas the transmitted part is reflected by a moveable mirror, fig. 3.3. Both reflected beams pass the beam splitter again in an opposite direction. The initially reflected beam is transmitted and the initially transmitted beam is reflected at the beam splitter. Right after the beam splitter, both beams are reunified interfering with each other and are passed to the detector. The intensity of each beam, because of interference, depends on the difference of the path length in the two arms of the interferometer. It is this variation of the intensity which yields the spectral information in a FTIR spectrometer. The
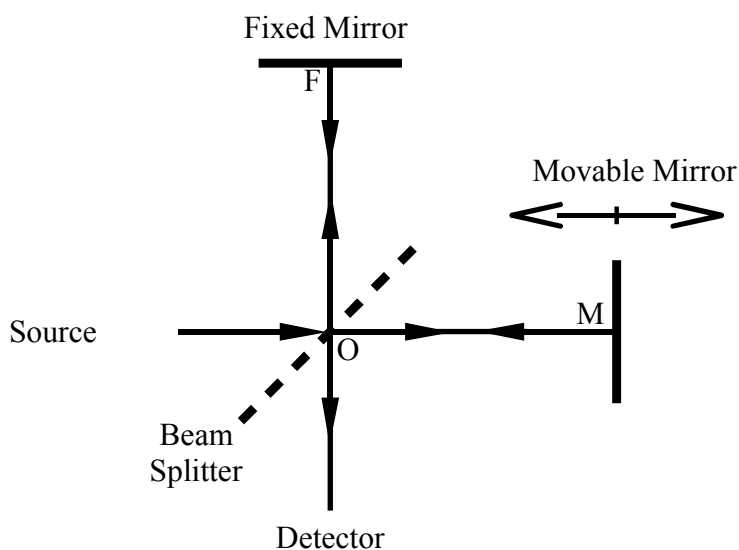
Figure 3.3: Principal sketch of a Michelson interferometer [16]. The incident parallel beam is split into two parts. One is reflected to the fixed mirror and the other one is transmitted to the moveable mirror. The returning beams are reunified after the beam splitter and passed to the detector. The interference depends on the retardation $\delta = 2\left(\overline{OM} - \overline{OF}\right)$.

difference of the path length of the two arms is usually called retardation δ and can be expressed by $\delta = 2\left(\overline{OM} - \overline{OF}\right)$ in fig. 3.3. For a continuing emitting source, the interferogram I as a

function of the path length difference δ can be represented by the integral [16]

$$I(\delta) = \int_{-\infty}^{+\infty} B(v) \cos(2\pi v \delta) \, dv \tag{3.7}$$

where $B(v)$ gives the intensity of the source, that is the spectrum. Fourier transform yields to

$$B(v) = \int_{-\infty}^{+\infty} I(\delta) \cos(2\pi v \delta) \, d\delta \tag{3.8}$$

Because $I(\delta)$ is an even function, eqn. 3.8 can be rewritten

$$B(v) = 2 \int_{0}^{+\infty} I(\delta) \cos(2\pi v \delta) \, d\delta \tag{3.9}$$

Eqn. 3.7 indicates that the spectrum can be measured over the entire spectral range that is from $0 cm^{-1}$ to ∞, with an infinitely high resolution. From eqn. 3.9, such an intension needs to move the mirror for an infinitely long distance. Additionally, the digitizing of the interferogram has to be done at infinitely small steps. Both are not possible in practice. However, the limitation of an endless moveable mirror can be mathematically handled by the inclusion of a width function $D(\delta)$ into eqn. 3.8, [16]

$$B(v) = \int_{-\infty}^{+\infty} I(\delta) D(\delta) \cos(2\pi v \delta) \, d\delta \tag{3.10}$$

The function $D(\delta)$ is called apodization function. The limited mirror movement is then regarded using

$$\begin{aligned} D(\delta) &= 1 \quad \text{if} \quad -\delta_{max} \leq \delta \leq +\delta_{max} \\ D(\delta) &= 0 \quad \text{if} \quad \delta > |\delta_{max}| \end{aligned} \tag{3.11}$$

where δ_{max} indicates the maximum path length difference δ. The apodization function described by eqn. 3.11 is called boxcar function and is the simplest function, i.e. no apodization at all. For a spectroscopist, the choice of the apodization function has to be considered since it determines the appearance of the spectra. The boxcar function leads to spectra with the highest possible resolution, i.e. $1/\delta_{max}$, but can include distortions especially in the case of a line resolved spectra. Several other apodization functions have been tested of their influence to the spectra appearance. An overview is given in for example [16]. All of them lead to a less disturbed spectrum but cause a reduced resolution. Nevertheless, the spectra have been measured with the same parameters which have been used for the PNNL database in order to ensure the same spectra appearance. A reference, or background, spectrum I_0 and a sample spectrum I are given

in fig. 3.4, from which the transmittance spectrum TR, fig. 3.5, has been calculated using [13]

$$\text{transmittance} = \text{TR} = \frac{\text{sample spectrum}}{\text{reference spectrum}} = \frac{I}{I_0} \tag{3.12}$$
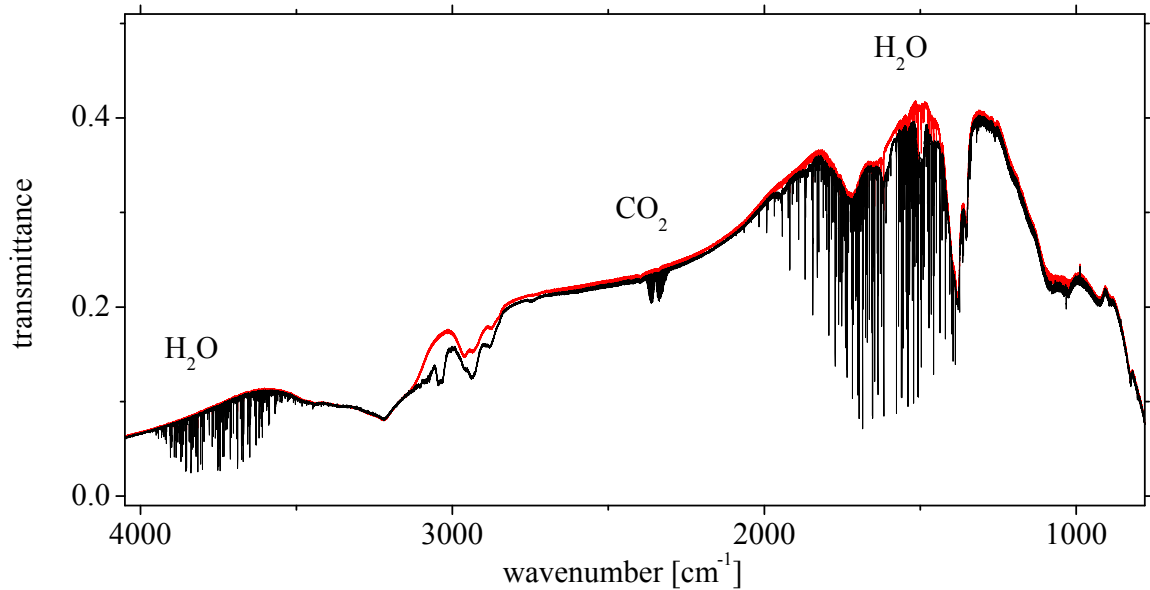

Figure 3.4: Measured reference I_0 (red) and sample I (black) spectrum of toluene between $4000 cm^{-1}$ and $800 cm^{-1}$. The spectra are also show H_2O and CO_2 absorptions. From these two spectra, the transmittance TR, fig. 3.5, has been calculated.

Throughout this thesis, the FTIR system has been used to study the gas composition produced by an atmospheric plasma discharge. The spectra obtained can consist of several overlapping absorption structures. See for example chapter 4. The identification of the absorbing species has been done by comparing the measured spectra with those listed in the PNNL database. For the quantification, the transmittance spectrum is converted to absorbance using [13]

$$\text{absorbance} = \text{AB} = -\log\left(\frac{I}{I_0}\right) \tag{3.13}$$

where I denotes the transmittance spectrum and I_0 indicates the baseline. Both can be seen in fig. 3.6. Here, the "base-10" logarithm has to be used in order to fit to the PNNL database. The quantification can be done by two different methods: For the first method, the integrated absorption band strength is calculated from the spectrum of the database. This has to be done for several species concentrations. The relation between the concentration and the integrated absorption band strength should follow a linear function. From this calibration function, the concentration corresponding to the integrated absorption band strength of the measured spec-
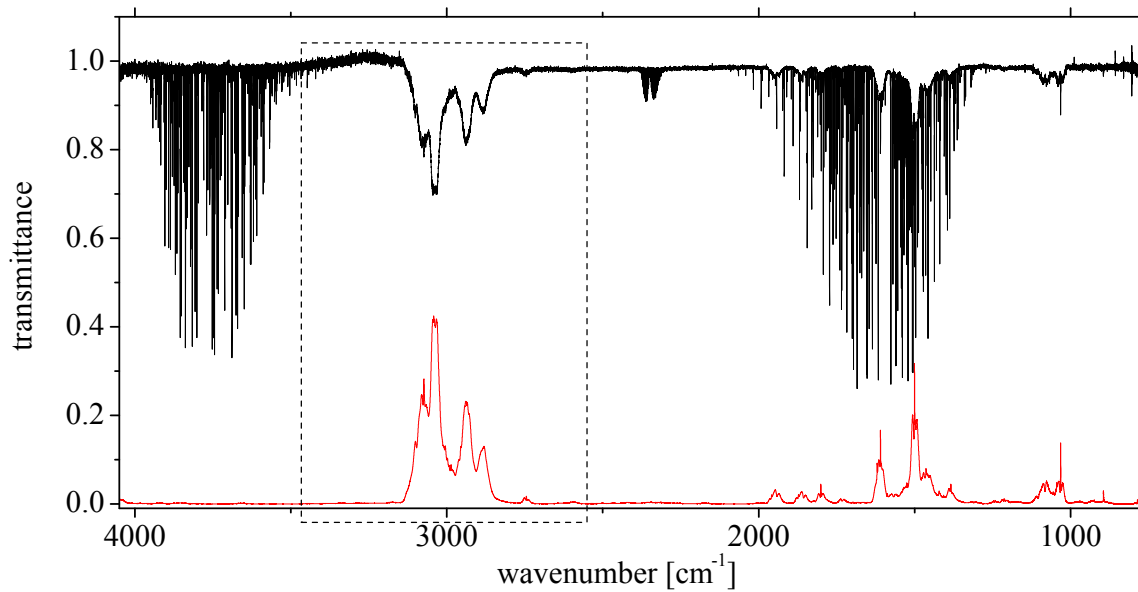
Figure 3.5: Transmittance spectrum TR of toluene (black) between $4000cm^{-1}$ and $800cm^{-1}$. Clearly visible are the strong bands at around $3000cm^{-1}$ and in the finger print region. The spectrum contains also water and CO_2. For a better comparability, the toluene absorbance spectrum for $200ppm$ taken from the PNNL [13] database is given at the bottom (red). The dashed box is zoomed out in fig. 3.6.

trum can be calculated. This method can be used in case no absorption structures do influence or overlap each other. If one can make sure that there are no influences reproducibilities better than 2% can be obtained. The second method takes into account that the absorption structures, especially for a multi component gas mixture, can be overlapped. By integration, one can not distinguish between two absorption structures from two species and, therefore, significant errors can occur. The measured absorbance spectrum is given in fig. 3.7. The quantification is done by varying the concentration C, eqn. 3.14, as long as the measured spectrum fits the database spectrum. The PNNL database is made in units of $ppm^{-1}m^{-1}$. Consequently, corrections have to be applied regarding possible differences in absorption length and gas pressure. The modified absorbance spectrum AB_{quant} is

$$AB_{quant} = AB_{PNNL} \cdot L \cdot \frac{p}{p_{PNNL}} \cdot C \tag{3.14}$$

and is given in fig. 3.7. In eqn. 3.14, AB_{PNNL} is the absorbance spectrum taken from the PNNL database, L is the absorption length, p is the pressure in the gas cell of the FTIR spectrometer, p_{PNNL} is the pressure used for the PNNL database and C is the concentration of the species, which has to be determined. The PNNL database is made with a gas pressure of $p_{PNNL} = 1000mbar$. Pressure broadening effects can be neglected since the pressure induced

line broadening effects are less than the resolution of the FTIR spectrometer. The concentration
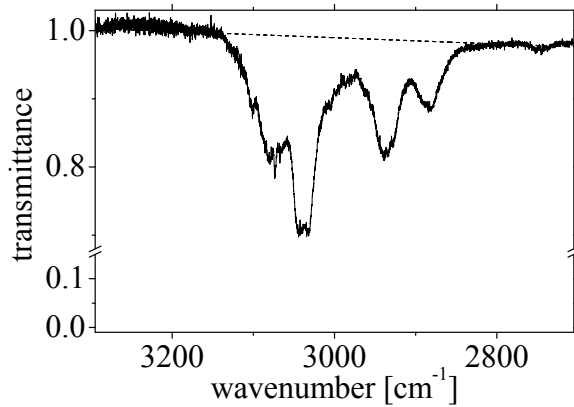
Figure 3.6: Zoomed transmittance spectrum *I* of toluene (solid) and the baseline I_0 (dashed).
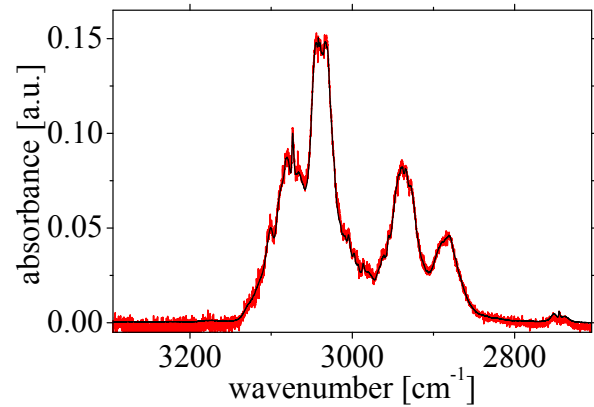
Figure 3.7: Measured absorbance spectrum *AB* (red) and the absorbance spectrum AB_{quant} (black) calculated from the PNNL [13] database for $71\,ppm$ as an example using eqn. 3.14.

C is directly obtained in units of *ppm*. The absolute number density of a component of the gas mixture is equal to the product of the concentration *C* (in *ppm*) times the total number density in the discharge device.

3.4   Quantum Cascade Laser Absorption Spectroscopy

Quantum Cascade Laser Absorption Spectroscopy (QCLAS) uses Quantum Cascade Laser (QCL) as the light source. These types of lasers are based on an idea of Kazarinov and Suris [18] and have been realised by Faist [19]. They became commercially available in the last decade. Fig. 3.8 shows a photograph of an open designed QCL. They work in the mid-infrared (MIR) region operating near room temperature emitting narrow line width radiation. The relatively high output power, tens of *mW*, makes it possible to use thermoelectrically cooled infrared detectors. These features allow the realisation of compact liquid nitrogen free spectrometers, e.g. Q-MACS [20]. A QCL consists of a stack of *nm* thick semiconductor layers [11]. Each layer is a semiconductor alloy. The alternating composition of the single layers leads to confined quantum states. Laser radiation is caused by electrodes travelling between the quantum states of the conduction band, fig. 3.9. The wavelength of the emitted radiation is determined by the separation of the energy levels. Since the thickness of the layer can by controlled during the production of the QCL, the wavelength of the emitted radiation can be designed too. The QCLs used for the present studies have been specified for pulsed operation only. Two types of pulsed operation are possible *Inter Pulse Mode* and *Intra Pulse Mode*. For both, the duty cycle specified by the manufacture must not be exceeded, which is usually 2% [21]. In the *Inter Pulse Mode*, the QCL is operated with pulse lengths of view *ns*. In the *Intra Pulse Mode*, pulses of
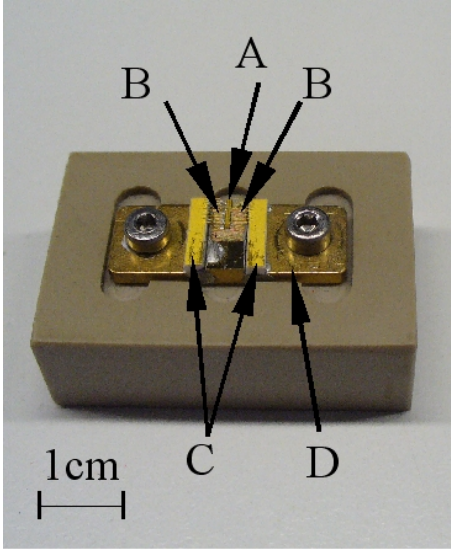
Figure 3.8: Photograph of a QCL mounted in a carrier case. The electric connection is enabled by the gold bonding. The QCL itself is the little black rod in the middle, A. B: bonding, C: electrical connections, D: cooling body.
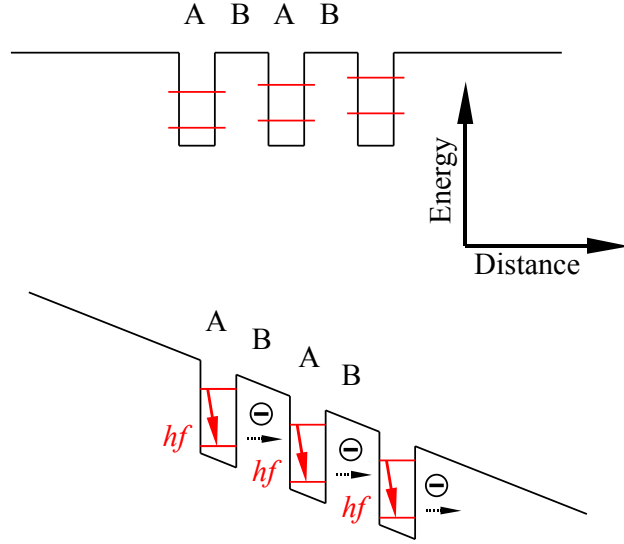
Figure 3.9: Band diagram of a potential well, upper, without bias. The letter A indicates confined quantum states of the active states and B the tunnelling barrier respectively. In the lower, a biased band diagram is shown indicating radiative transition (A) and resonant tunnelling (B) [11].

several $100ns$ can be applied. Because of the internal heating of the QCL during the pulse, a slightly thermal expansion of the laser crystal is caused leading to a tuning of the emitted laser radiation towards lower wave numbers. Tuning rates in the order of $5 \times 10^{-3} cm^{-1} ns^{-1}$ are possible. This in principal is also the case for short pulses. In the *InterPulseMode*, the temporal change of the spectral emission is not resolved. Therefore, the detector integrates over the entire spectrum of the laser pulse. Because of the tuning during the pulse, an effective laser line width has to be defined which is more than the laser line width itself. For short pulses, the effective laser line width ν_{laser} can be estimated by

$$\nu_{laser} = \eta \cdot \tau \tag{3.15}$$

where η indicates the tuning rate and τ is the pulse duration assuming an ideal rectangular pulse. In the *Intra Pulse Mode*, a fast detector with a rise time in the order of several *ns* has to be used. This setup allows resolving the entire spectrum during the laser pulse. As an example, fig. 3.10 shows a NO spectrum at around $1900.4 cm^{-1}$. For this specific laser, a laser pulse of $150ns$ leads to a spectrum over $0.5 cm^{-1}$. Clearly visible are the two absorption features of NO, $1900.52 cm^{-1}$ and $1900.08 cm^{-1}$. A typical spectrum recorded with a QCL laser working in the pulsed mode is shown in fig. 3.10. As a consequence of the high tuning rate, the absorption structure, especially a line spectrum recorded at low pressure, shows an effect known as *rapid passage effect*. This can be seen by the positive over flap very next to an
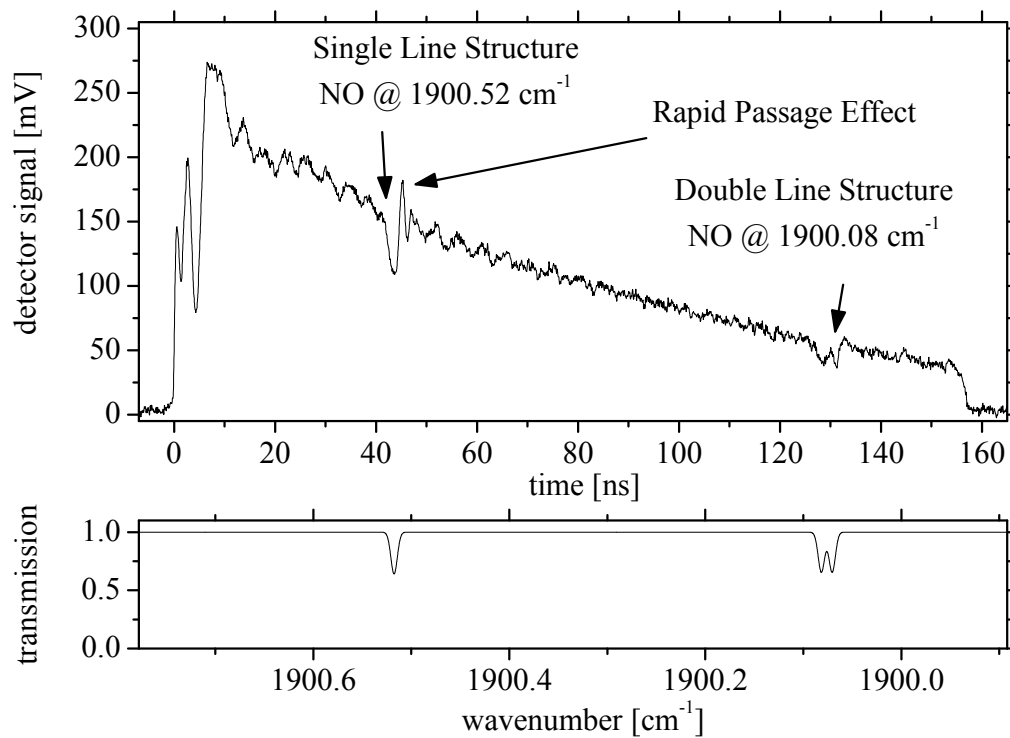
Figure 3.10: Example of a NO spectrum taken with a QCL working in the *Intra Pulse Mode* with a pulse length of $150ns$. The spectral tuning during the pulse for this specific QCL is in the order of $3 \times 10^{-3} cm^{-1} ns^{-1}$. The distortion, the *rapid passage effect*, of the absorption appearance is marked by the arrow. A corresponding spectrum simulation is shown below.

absorption line. The reason for that has been part of several studies [11, 22–24] but is not fully understood. Because of this distortion of the absorption line, eqn. 3.4, $K(T) = n \cdot S(T)$, can not be applied directly and a calibration has to be done in order to determine an effective line strength S_{eff} [24, 25]. As an example for a calibration, the three laser spectrometer used for the measurements shown in chapter 5 had to be calibrated. For this purpose, a gas mixture of known concentration at known pressure, leading to a known number density inside the recipient, did serve for the determination of the effective line strength S_{eff}. As an example, fig. 3.11 shows the measured calibration curves for three species, N_2O, NO and NO_2. They have been detected by the three channel spectrometer described in chapter 5. For all three nitric oxides, the calibration function shows a linear behaviour for low concentrations. That one for N_2O shows a non-linear increasing starting at a K-value around $0.75 cm^{-1} s$ corresponding to a concentration of about $10^{14} molecules\, cm^{-3}$. The non-linear behaviour is caused by a beginning saturation effect of the detector element. Using these calibration curves, the number density can be obtained from measured quantities, e.g. the absorption line of the corresponding species.
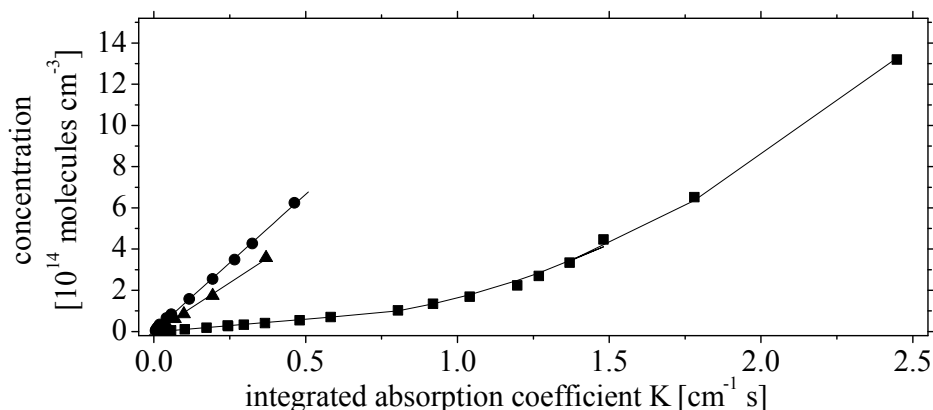
Figure 3.11: The graph shows as an example the obtained calibration function for all three QCL used for the three channel spectrometer described in chapter 5. The integrated absorption coefficient K has been calculated following eqn. 3.4. The concentration has been calculated following the ideal gas law from the known mixing ratio at a known pressure. N_2O: squares, NO: triangles, NO_2: circles. The fitted functions (solid) are used to guide the eyes. With these functions, the species concentration can be calculated from measured spectra.

3.5   Measurement of the gas temperature of the admixed NO by QCLAS

3.5.1   Motivation

The determination of the gas temperature is an essential requirement in the study of gas phase and plasma kinetics. The broad application of plasma technology in fundamental research and industry requires cheap and compact systems. Considering the law of Arrhenius, the temperature influences the rate of chemical reactions and can, therefore, control the entire chemistry. Especially in the studies of plasma surface interaction, the temperature influences the diffusion [26] of the neutrals and ions in the gas volume. Therefore, the interaction between the species and the surface can be governed by the temperature. This can be important in e.g. the study of heterogeneous catalyses between solid state catalyst and transient fragments and radicals created in the active plasma volume.

Laser absorption spectroscopy, applied to gas phase diagnostics, is of special importance since it is a non-invasive method. This is usually performed using tuneable diode laser (TDL) absorption spectroscopy (AS). However, these devices need complex and power consuming cryogenic cooling installations. In laboratory scale, TDLAS, however, has been proven to be suitable for temperature measurements both by Doppler broadening [15, 27] of an absorption line and by a line ratio method [9]. The line ratio method uses the temperature dependency of the line strength of two absorption structures. The gas temperature can be calculated from the intensity ratio of a pair of the absorption lines [9], determined by the line strength. The line strength as well as other molecular parameters of several atmospheric constitutions are tabulated in databases like

HITRAN [12, 13]. However, the parameters are calculated for thermal equilibrium. Thus the thermal distribution of the vibrational and rotational levels is valid for thermal equilibrium. In non-thermal plasmas, however, the thermal distribution especially of the vibration levels can differ from thermal equilibrium conditions. Therefore, special care is required in order to obtain correct measurements since the thermal distribution has been included to calculate the line strength in these databases. The influence of the population density of the vibrational levels can be neglected in case both absorption lines are from the same vibrational transition. Thus in the example discussed in this work, both absorption lines correspond to the excitation of the molecules from the vibrational ground state into the first vibrational state. Therefore, the population density of the vibrational states has no influence. The influence of the population density of the rotational levels has to be considered too. The rotational relaxation occurs within the ns scale. Therefore, the distribution of the rotational levels does not differ from the thermal distribution of the rotational levels for thermal equilibrium, as accounted in the HITRAN database. Therefore, the line ratio method, as described in this work, can be applied even to the diagnostics of non-thermal plasmas. In the following, the adaption of the line ratio method to the QCL absorption spectroscopy working in the *Intra Pulse Mode* is shown. These measurements causes highly distorted absorption structure especially in the low pressure range. The temporal evolution of the temperature during a dc plasma pulse has been measured.

3.5.2   Theoretical background of the line ratio method

Following chapter 3.2, in eqn. 3.4, the species concentration can be determined from the ratio between the integrated absorption coefficient K and the line strength of the particular transition. The line strength, generally, depends on the temperature. For room temperature, the lines strength can be found in data bases like HITRAN [12]. With eqn. 3.4, one is able to calculate the number density corresponding to an absorption line. The temperature dependence of the line strength requires a correction in order to obtain the correct number density at other (than room) temperatures. Therefore, the equation for S at a temperature T [28]

$$S\left(T\right) = S\left(T_{ref}\right) \cdot \frac{Q\left(T_{ref}\right)}{Q\left(T\right)} \cdot \frac{\exp\left(-\frac{hcE}{kT}\right)}{\exp\left(-\frac{hcE}{kT_{ref}}\right)} \cdot \frac{\left[1 - \exp\left(-\frac{hcE}{kT}\right)\right]}{\left[1 - \exp\left(-\frac{hcE}{kT_{ref}}\right)\right]} \tag{3.16}$$

has to be applied where h denotes Planck's constant, c the velocity of light, k denotes Boltzmann's constant, E the lower state energy, ν spectral line transition frequency, Q the total internal partition sum all at the reference temperature T_{ref} (= $296K$, room temperature). The last term in square brackets accounts for the effect of stimulated emission, which is usually neglected for temperature below $2500K$ [9]. In fact, the influence is less than 10% at $1000K$. The temperature dependency of the line strength, on the other hand, can be used to deduce the temperature from a spectroscopic measurement. For this purpose, the ratio of two absorption

structures can be used. The ratio R of the line strength becomes a function of the temperature [9]

$$
\begin{aligned}
R &= \frac{S_1(T)}{S_2(T)} = \frac{K_1 \cdot n_2}{n_1 \cdot K_2} \\
&= \frac{S_1(T_{ref})}{S_2(T_{ref})} \cdot \exp\left(\frac{hc\Delta E}{k} \cdot \frac{T - T_{ref}}{T \cdot T_{ref}}\right) \cdot \left[\frac{1 - \exp\left(-\frac{hcv_1}{kT}\right)}{1 - \exp\left(-\frac{hcv_2}{kT}\right)} \cdot \frac{1 - \exp\left(-\frac{hcv_2}{kT_{ref}}\right)}{1 - \exp\left(-\frac{hcv_1}{kT_{ref}}\right)}\right]
\end{aligned} \tag{3.17}
$$

where the indices 1, 2 are used to separate two different absorption structures and $\Delta E = E_1 - E_2$ is the energy separation of the absorbing states. Again, the term in the square brackets accounts for the stimulated emission and can be neglected for temperatures below $1000K$. Eqn. 3.17 shows that the temperature sensitivity of the ratio depends on the line strength and the energy difference of the two absorption structures transition. The second part of eqn. 3.17, $K_1 \cdot n_2 / n_1 \cdot K_2$, has been obtained using the relation $n_i \cdot S_i = K_i$ from eqn. 3.4. Taking into account that $n_1 = n_2$, by definition, the ratio can be expressed by measured quantities; these are the integrated absorption coefficients K_i taken from the absorbance spectrum.

$$
R(T) = \frac{K_1(T)}{K_2(T)} \tag{3.18}
$$

With eqn. 3.18, the temperature of a gas can be determined from the measured spectrum. Using the temperature, the number density can be calculated from one or both absorption structures.

3.5.3   Experimental Setup

The applied line ratio method is exemplarily illustrated for the temporal evolution of the gas temperature during DC plasma pulses ignited in a NO / N_2 / O_2 gas mixture at low pressure. The experiments have been carried out in a Pyrex tube reactor with an inner diameter of $20mm$ and a length of $60cm$. The ends of the tube were closed with Kalium Bromide (KBr) windows, 3.12. The gas mixture was 0.8% NO diluted in air at an initial pressure of $1.33mbar$. The experiments have been done under static gas conditions in a closed reactor. The electrodes were connected in a T-shaped holder in order to work in the homogeneous part of the dc discharge. The discharge was driven by a self made power supply consisting of a DC high voltage supply, a capacitance bank and a solid state HV switch (Behlke). This setup creates HV pulses with a rise time in the $kV/\mu s$ range. The HV pulses have been applied for $5ms$. The applied high voltage was varied in order to obtain several mean plasma currents, ranging from $25mA$, to $150mA$. The consumed electrical power was in the order of $1.5J$. The high voltage was measured with a HV probe (P6015A, Tektronix). The current has been detected by the current proportional voltage drop over a measurement resistor. Both signals have been detected by an oscilloscope (LeCroy, $500MHz$, $1GS/s$). The quantification of the probe gas, NO, has been done by QCLAS working in the *Intra Pulse Mode*. A commercially available Q-MACS system [20] has been used with a three pass alignment. The laser pulses have been detected by a fast detector with a rise time of $3ns$ (neoplas control, IRDM600A). The pulse duration of the QCL was $150ns$ with a pulse repetition frequency of $30kHz$. The internal thermal expansion of the QCL leads to a slightly tuning of the emitted laser light. This allows a scan over the spectral range of interest. An example of the detected spectrum can be seen in fig. 3.10. It shows a single line absorption

structure at $1900.52 cm^{-1}$, $NO(X_{3/2}, v = 0) \rightarrow NO(X_{3/2}, v = 1)$: R6.5, and a double line absorption structure at $1900.08 cm^{-1}$, $NO(X_{1/2}, v = 0) \rightarrow NO(X_{1/2}, v = 1)$: R6.5, of 0.8% NO in air at $1.33 mbar$ with an absorption length of $L = 180 cm$. Thus, the detection limit was about $4 \times 10^{13} molecules cm^{-3}$.
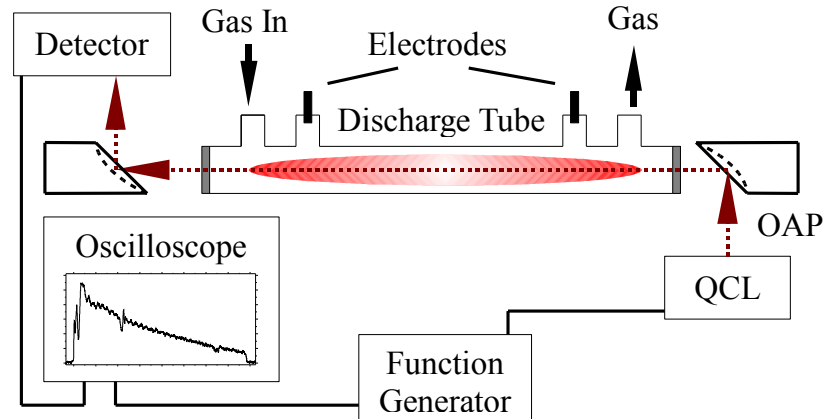
Figure 3.12: Principal sketch of the optical setup. The Pyrex tube has been passed three times by the QCLAS system. The tube was $60 cm$ in length with an inner diameter of $20 mm$. The experiments have been done under static gas conditions, $p_{initial} = 1.33 mbar$ [29].

In fig. 3.12, the spectrum consists of two absorption structures, the single line structure and the double line structure. Both phenomena are distorted by non-linear absorption effects. This is stronger pronounced for the single line structure and indicated by the peak, faced upwards very next to the absorption line. It is this non-linear absorption effect which prevents the direct calculation of the temperature from the line ratio because of the fact that the integrated absorption coefficient K can be distorted differently for each absorption line. The next chapter describes how this phenomenon can be adequate considered.

3.5.4 Line Ratio Method

The spectrum shown in fig. 3.10, shows a single line structure and a double line structure. The theory discussed in chapter 3.2 can be directly applied to those spectra in case each of these absorptions consists of a single transition. However, the HITRAN database lists several transitions for each absorption structure. Strictly speaking each absorption line of the spectrum shown in fig. 3.10 consists of several transitions. Even the single line structure consists of several transitions. The expression for the line strength correction, eqn. 3.16, therefore, has to be summed over all lines located within the absorption structures of the spectrum shown in fig. 3.10, i.e. summed over all transitions less separated than the laser line width. Consequently, the line strength S_1 and S_2 in eqn. 3.17 have to be summed over the significant transitions listed in

the HITRAN database. This can be expressed by

$$S_{1/2} = \sum_j (S_{1/2}) \qquad (3.19)$$

where the index j counts the corresponding transitions listed in the HITRAN database. The resulting expression for the line ratio, eqn. 3.19, can become very complex and has, therefore, been evaluated numerically. The line ratio method has been applied in 3 steps. First, the spectral range covered by the laser has been simulated using the commercial available software package HT-Tool [20] for the temperatures $296K$, $300K$, $350K$, . . ., $650K$, $700K$. Fig. 3.13 shows these absorbance AB spectra calculated for 0.8% NO in air. The measurements have been done in a closed tube reactor. Therefore, following ideal gas law, the pressure increases in the same way as the temperature does. This adapted pressure has been included into the simulation software. The absorption length L was $180cm$. For both absorption structures, the spectrum shows that the intensity decreases as the temperature increases. The integrated absorption coefficient K of each line structure has been calculated following eqn. 3.4. The resulting line ratio, eqn. 3.18, for each temperature as a function of the gas temperature is given in fig. 3.16. The performance of
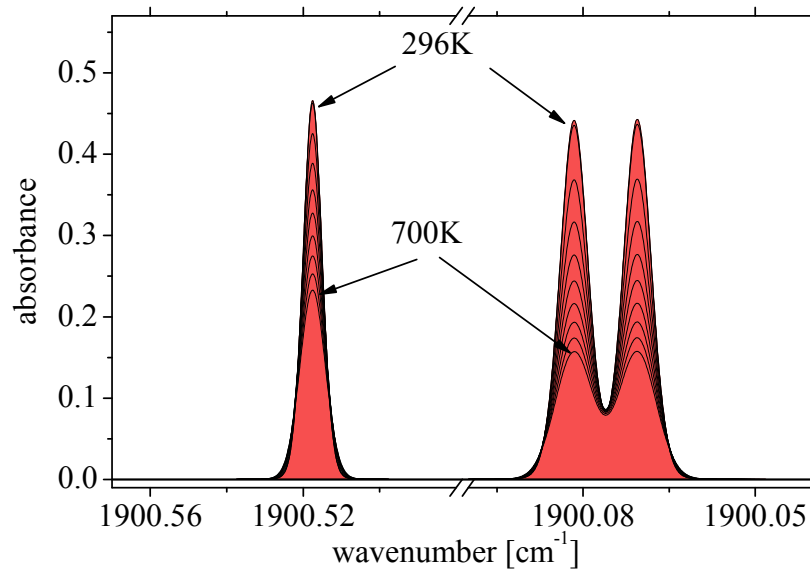
Figure 3.13: Simulated absorbance spectrum of NO at around $1900cm^{-1}$ calculated for several temperatures. For the line ratio method, the integrated absorption coefficient K (red area for $296K$) has been used.

the software package has been checked by the calculation of the line ratio following eqn. 3.17. The parameters have been taken from the HITRAN database. HITRAN lists several lines for each absorption structure. Only those lines are included into the calculation which are within three orders of magnitude starting by the strongest. There are 10 lines for each absorption structure included. Tab. 3.1 lists the transitions used for the single line structure and for the double line structure of the NO example. The temperature dependence of each listed line has
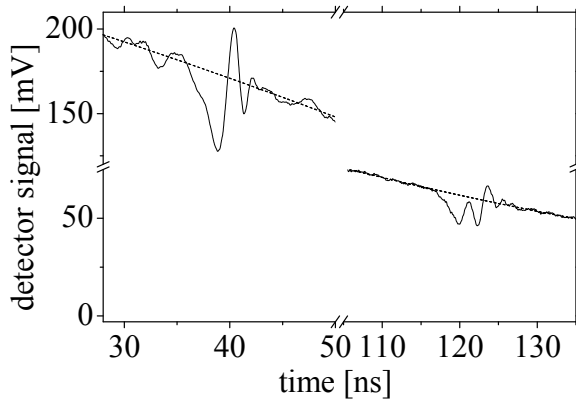
Figure 3.14: Zoomed view into the single line structure and the double line structure of the NO absorption spectrum (solid line) and the corresponding baseline (dashed line). The figure shows a 20 times averaging of the NO spectrum shown in fig. 3.10.
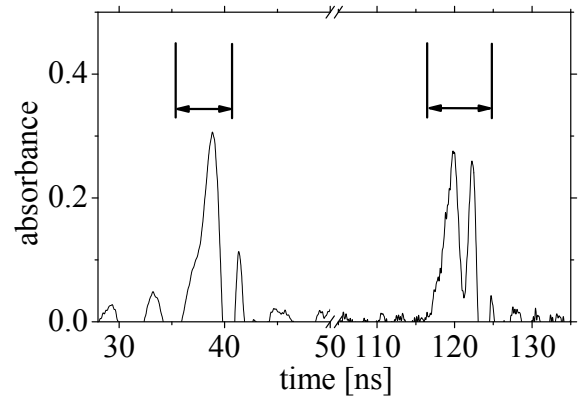
Figure 3.15: Calculated absorbance AB of the NO spectrum. The ranges marked by the arrows indicate the integration area used for the calculation of the integrated absorption coefficient K.

been calculated separately. The line strength implemented in eqn. 3.19 is therefore the sum of all listed lines covered by the laser line width. The differences between both ratio calculations, using HT-Tools and using eqn. 3.17, have been found to be always less than 1%. Second, the measured NO spectra shown in fig. 3.10, zoomed view can be seen in fig. 3.14, has been converted into absorbance AB, fig. 3.15, using the relation $AB = \ln(I_0/I)$. The example given in fig. 3.10 shows the spectrum taken at room temperature. Third, calibration of the line ratio. The temperature has been plotted as a function of the line ratio LR obtained from the simulated spectra, fig. 3.11. An exponential function

$$f_{Temp} = 245.11K + 86122K \cdot \exp(-LR/0.25) \tag{3.20}$$

has been used to approximate the data points. Therefore, this compensation curve describes the relation between the temperature and the line ratio of the simulated spectra. From this compensation curve, the line ratio of the simulated absorption structures, fig. 3.13, at $296K$ has been found to be 1.89. The line ratio of the absorptions of the measured spectrum at room temperature has been found to be 1.68. However, these two line ratios should be equal since they belong to the same transitions studied under the same conditions. The discrepancy can be caused by the influence of the non-linear absorption effects, e.g. rapid passage effect or saturation effects. Therefore, the simulated curve has to be corrected in order to reproduce room temperature at the measured line ratio. In this work, the correction is incorporated simply by a correction factor F_c. This takes into account that the influence of the non-linear absorption effects does not depend on the temperature. Such a dependency has not seen by a test experiment using a conventionally heated reference gas cell. The correction factor F_c is the quotient of the

Table 3.1: Transition position and corresponding transition intensity, line strength S, as they are listed in the HITRAN database. These lines are included into the calculation of the single line structure as well as of the double line structure, eqn. 3.19.

No.	Single Line Structure		Double Line Structure	
	Wavenumber $\left[cm^{-1}\right]$	Line Strength $\left[10^{-20}\frac{cm^{-1}}{molecules\ cm^{-2}}\right]$	Wavenumber $\left[cm^{-1}\right]$	Line Strength $\left[10^{-20}\frac{cm^{-1}}{molecules\ cm^{-2}}\right]$
1	1900.516783	0.01956	1900.070578	2.028
2	1900.516903	0.01956	1900.070593	2.322
3	1900.517093	1.238	1900.070596	1.770
4	1900.517196	1.080	1900.072052	0.03670
5	1900.517276	0.9429	1900.072147	0.03670
6	1900.517453	0.01956	1900.079250	0.03669
7	1900.517688	0.01956	1900.079550	0.03669
8	1900.517870	1.238	1900.081594	2.322
9	1900.517956	1.080	1900.081628	1.769
10	1900.518033	0.9429	1900.081636	2.027

two line ratios. That is

$$F_c = \left(\frac{Line\ Ratio\ Simulated\ Spectrum}{Line\ Ratio\ Measured\ Spectrum}\right)_{Room\ Temperature} = \frac{1.89}{1.68} = 1.125 \qquad (3.21)$$

The simulated curve in fig. 3.16 has to be shifted with this correction factor F_c in order to obtain a calibrated curve for the temperature. With F_c, the calibrated relation between temperature and measured line ratio leads to the corrected calibration curve

$$f_{Temp} = 245.11K + 86122K \cdot \exp\left(-\frac{F_c \cdot LR}{0.25}\right) \qquad (3.22)$$

With eqn. 3.22, one is able to calculate the temperature from the measured line ratio LR of the two NO absorption lines. Fig. 3.16 shows the calibration curve, temperature versus line ratio of the measured spectrum.

The line ratio for other absorption structures or other gases can differ from the example discussed here. Therefore, the correction factor as well as the fitting function and fitting parameters might be re determined for other experimental conditions. Fig. 3.16 shows the calibration curve, temperature versus line ratio of the measured spectrum. With this curve, the NO gas temperature can be determined.

3.5.5   Test of the method

The line ratio method has been tested using a conventionally heated reference gas cell. A standard reference gas cell of the length $l_{cell} = 150mm$, outer diameter of $d_{out} = 55mm$, inner
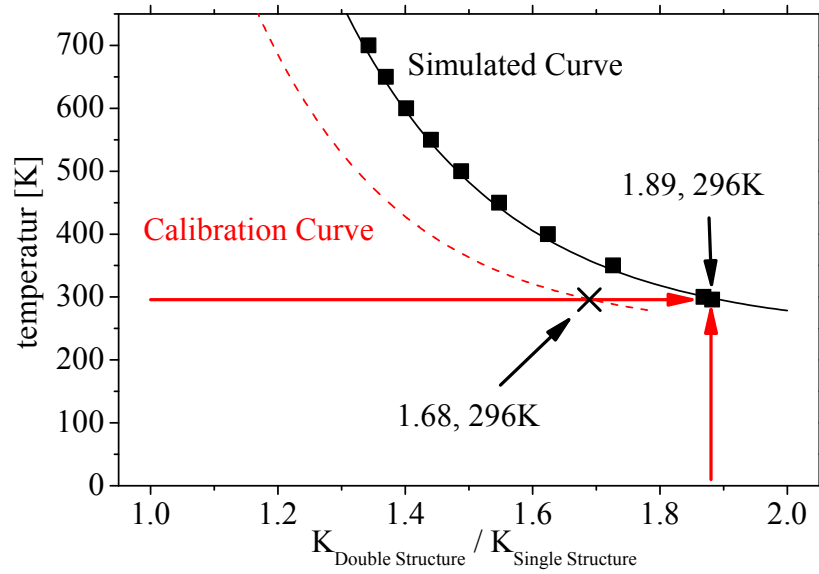
Figure 3.16: Plot of the temperature depending on the line ratio calculated from the simulated spectrum (squares). The line ratio for room temperature is 1.89. An exponential fit, f_{Temp}, (solid) has been used to approximate the data. The line ratio for room temperature calculated from the measured spectrum is 1.68. Because both line ratios have to be the same for room temperature, the discrepancy has been corrected by a correction factor F_c, eqn. 3.21. The dashed curve represents the corrected calibration.

diameter d_{in} = 44mm was filled with pure NO up to a total pressure of p = 3$mbar$. A Teflon sealed valve has been used for filling the cell. The ends were closed with KBr windows. The entire cell, except the windows, was covered by a heating tape (Horst, HT24N250) and heated up to 207°C. The temperature was measured using a PT100 meter fixed in the middle of the cell between the outer glass tube and the heating tape. Because of the simplicity of the cell the measured temperature might not be the averaged temperature as it would by measured by a spectroscopic determination of the line ratio of NO lines. This can be understood, because the windows, for example, are not fully heated by the tape in order to allow transparency. Additionally, the heating tape has not been in contact with the entire outer face of the cell. For example, the filling connection does not allow fully coverage. To estimate the true averaged inner temperature of the cell, the cell has been modelled using the software package Comsol 3.2, Heat Transfer Module [30]. The cell was modelled using 5 cylinder segments made of silica glass with a thermal conductivity k = 1.38$Wm^{-1}K^{-1}$, a density of ρ = 2.203$kgcm^{-3}$ and a heat capacity of 703$Jkg^{-1}K^{-1}$. The KBr windows were simulated with the parameter [31]: thermal conductivity k = 4.816$Wm^{-1}K^{-1}$, a density of ρ = 2.753$kgcm^{-3}$ and a heat capacity of 435$Jkg^{-1}K^{-1}$. The gas filling has been simulated by pure N$_2$ at a pressure of 3$mbar$ with the parameters: thermal conductivity k = 0.026$Wm^{-1}K^{-1}$ [32], a density of ρ = 1.25gcm^{-3} and a heat capacity of 1038$Jkg^{-1}K^{-1}$. The modelling of the gas temperature has been done for the temperatures 296K, 300K, 350K, ..., 650K, 700K. For each temperature, the outer surface of

the cell has been separated into two different heating zones, fig. 3.17. The zone A was set to the temperature 296K, 300K, 350K, ..., 650K, 700K whereas the zone B was set 2% colder than zone A. This ensures the non-homogenous covering of the heating tape. The windows were not heated. Therefore, they were assigned to have a heat flux to the ambient air. The parameters needed to put into the software package are: heat transfer coefficient $h = 10Wm^{-2}K^{-1}$ [33], external temperature $T_{inf} = 296K$, radiation type: Surface-to-ambient, surface emissivity $\varepsilon = 0.2$, ambient temperature $T = 296K$, surface radiosity expression $J_0 = 1000Wm^{-2}$. The surface emissivity was estimated to be 0.2. In fact, the averaged temperature along the line of sight varies less than 1% between $\varepsilon = 0.1$ and $\varepsilon = 0.9$. This estimation was necessary because of the lack of a reference for the emissivity of KBr. In fig. 3.17 exemplarily, a colour coded image of a temperature layer located in the centre axis of the cell is shown. The temperature in zone A was 600K. To calculate a steady-state temperature profile of the gas filling inside the reference
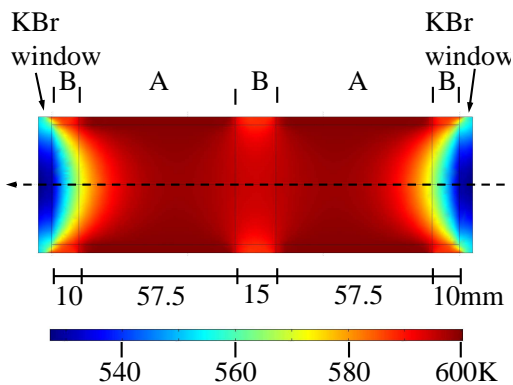
Figure 3.17: Colour coded temperature profile of a layer lying in the axial centre of the reference gas cell. The dotted arrow indicates the beam path of the laser. Using heating tape, the heating zone B was hold 2% colder than the heating zone A. This corresponds to a non-homogenously heating of the cell surface.
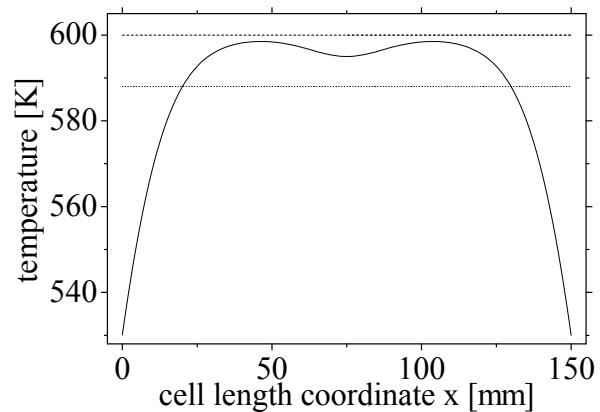
Figure 3.18: Temperature profile along the line of sight trough the reference gas cell (solid line) for a temperature of 600K (dashed line) as an example. The averaged temperature, T_{avg}, measured by the absorption spectroscopy is 492K (dotted line).

gas cell, the software meshes the geometry and solves the heat equitation numerically for each element of the mesh. From the result list, the temperature profile of a layer in the centre of the cell can be calculated and is shown in fig. 3.18. The temperature, as expected, shows a radial and axial gradient. Axially, the temperature ranges from 530K close to the windows up to 599K in the middle of the cell. This non-homogenous temperature profile will be averaged by the applied spectroscopy. Therefore, the temperature profile along the line of sight of the laser was extracted from the modelling and is shown in fig. 3.18. The averaged temperature can be calculated from the curve in fig. 3.18 using $T_{avg} = (1/l_{cell}) \cdot \int T \cdot dx$. For the example of the modelling shown in fig. 3.17 and 3.18 the temperature of the outer cell surface was 600K, whereas the averaged temperature $T_{avg} = 587K$ along the line of sight in the cell is 13K less. Although, this difference is quit small, the temperature measured by the PT100 meter has been

corrected.

For the line ratio calculation, the integrated absorption coefficients K_i have been calculated from the transmission spectrum, fig. 3.14, using eqn. 3.4. These two values where used to calculate the line ratio. Details can be found in chapter 3.6.3. Fig. 3.19 contains the line ratios calculated from the simulated spectra as well as from the measured spectra. The measured absorption structures are highly disturbed by non-linear effects, for example rapid passage effect. Because of this distortion, the line ratio calculated from the measured spectrum at room temperature is 2.3. On the other hand, the line ratio calculated from the simulated spectrum for room temperature is 1.89. In order to compensate the influence of the distortion seen in the measured spectra, the line ratios calculated from the measured spectra have been multiplied by a correction factor, i.e. 1.89/2.3 = 0.82. The application of such a correction factor assumes that the influence of the spectral distortion does not depend on the temperature. As one can see in fig. 3.19, the corrected line ratio of the measured spectra follows the line ratios calculated from the simulated spectra within an error of 10%. Therefore, from fig. 3.19, the application of a correction factor can be made for temperatures below $600K$ and confirms the assumption that a constant correction factor can be used. The NO spectra discussed here have been measured
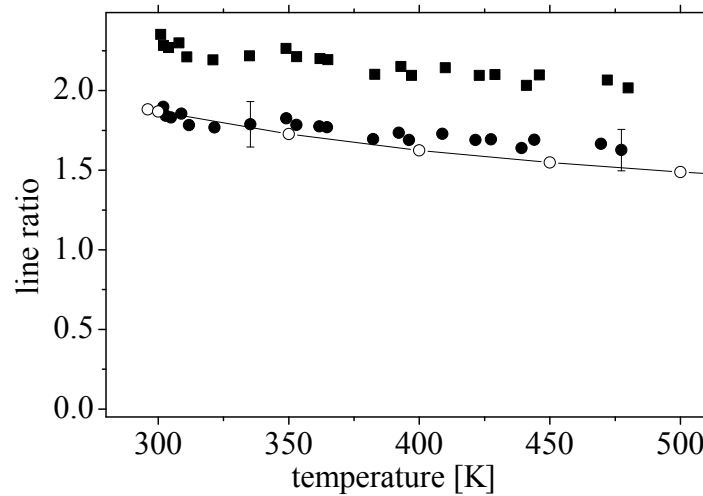
Figure 3.19: Line ratio of the two absorption lines for the measured (squares) and simulated (open symbol) spectrum. The influence of the distortion of the absorption lines has been removed by a calibrated curve (closed circles). The line ratio calculated from the measured spectrum of the reference gas cell is 2.3 at room temperature. From the errors, a comparison between the calibrated and simulated line ratio shows good agreements for temperature below $600K$.

under two conditions, (i) 0.8% NO inside the discharge tube at $1.33mbar$ with an absorption length of $180cm$ and (ii) pure NO in the reference gas cell at $3mbar$ with an absorption length of $15cm$. Both at room temperature without a discharge ignited. The line ratio calculated from the room temperature spectra were 1.68 for (i) and 2.3 for (ii). This discrepancy corresponds to the pressure dependence of the absorption structure and therefore to the line ratio too. This pres-

sure dependency requires the calculation of another correction factor F_c for other experimental conditions e.g. pressure. Strictly speaking, for other measurements under other conditions, the calibration factor F_c might be different and has to be recalculated. It should be noted, that the NO concentration was higher than in the tube reactor. Therefore, saturation might play an increasing role. Despite increasing saturation, the line ratio of the measured spectrum reproduces the line ratio of the simulated spectrum.

3.5.6   Estimation of the temperature kinetics

The procedure to estimate the gas temperature is exemplarily illustrated for experiments used to study the N_xO_y formation / destruction kinetics in a low pressure N_2 / O_2 dc plasma with small N_xO_y admixtures. These experiments have been done in a Pyrex tube under conditions as described in chapter 5. Several combinations of N_2 / O_2 admixed with N_xO_y have been studied. However, significant changes of the absorption structures, relevant for the estimation of the temperature, have only been resolved for the case of 0.8% NO, 79.2% N_2 and 20% O_2 initial gas mixture at a total flow of $12.5 sccm$ and at a total pressure of $1.3 mbar$. High voltage pulses of $5ms$ and $10ms$ duration were applied to the discharge tube $8ms$ after the start of the spectral measurements. The QCL were working in the *Intra Pulse Mode* with a pulse repetition frequency $f_{rep} = 30kHz$ leading to one spectrum each $33.3\mu s$. An example of the spectrum can be found in fig. 3.10. More details about the experimental setup and the set of parameters are given in chapter 5. The averaged NO temperature was determined using a line ratio method as described above. Therefore, the integrated absorption coefficients $K(T)$ was calculated for the single line structure K_{SL} and for the double line structure K_{DL} as described in chapter 3.6.3. Afterwards, the line ratio $LR = K_{DL}/K_{SL}$ of them has been calculated and multiplied with the correction factor F_C. This value was calculated from the line ratio calculated for the first $8ms$ since this time range can be used to calculate the line ratio at room temperature. For the example shown above, this value was calculated to 1.89. Therefore, the correction factor F_C was equal to 1.89. Finally, the calibrated line ratio was multiplied by the temperature function given in fig. 3.16. In fig. 3.20, one can see, as an example, measured curves for K_{SL} and K_{DL} as a function of time for a $10ms$ dc plasma pulse with a mean current of $150mA$. For a better impression, fig. 3.20 shows smoothed curves, too. Fig. 3.20 and 3.21 show the temperature curve which has been created for $150mA$ mean plasma current. Beside this, it has been possible to estimate the temperature evolution for further currents. Tab. 3.2 lists all experiments for which the temperature has been estimated. For this example, it is seen from fig. 3.21 that the temperature increases during the pulse up to about $470K$. The limiting factor of this method is that not only a minimum of the NO concentration is needed but also a minimum change in the line ratio that is a minimum of gas heating. This is mainly determined by the line strength or concentration and the dependency of the line strength on the temperature of the lines accessible with the laser. The error of the results, fig. 3.22, can be determined to be not better than $\pm 80K$. Therefore, the temperature obtained here is treated as an estimation. For further analyses, especially for the correction of the line strength, an exponential interpolation of the temperature curve was used, see fig. 3.22. These temperature measurements done for the first time using QCLAS are very noisy. The signal to noise ratio can be improved by a higher NO density. However, the gas mix-
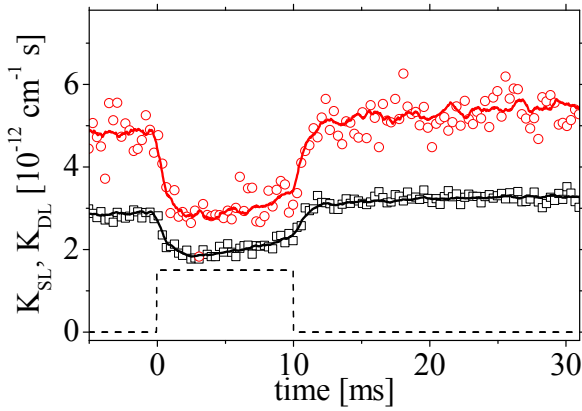
Figure 3.20: Measured time evolution of the values for the integrated absorption coefficient *K* of the single line structure (square) and the double line structure (circles). The solid curves show a smoothing whereas the dashed line indicates the plasma pulse. For clarity, only each ten point is plotted.
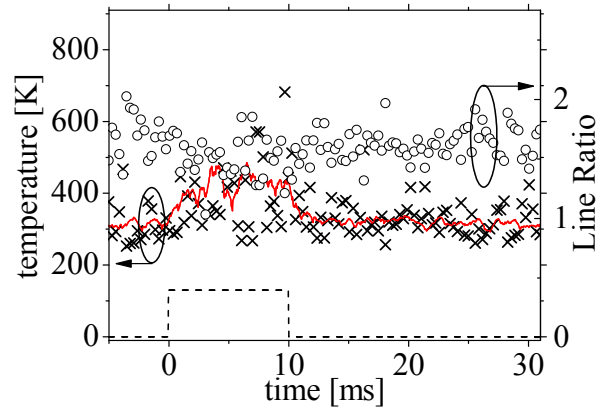
Figure 3.21: Obtained line ratio as a function of time (dotted). The corresponding temperature (crosses) and the smoothed temperature evolution (solid line). The dashed line indicates the plasma pulse. For clarity, only each ten point is plotted.

Table 3.2: Experimental parameter for which the temperature evolution has been estimated. The column *NO Temperature* lists the NO temperature at the end of the plasma pulse whereas the column *Mean Current* contains the averaged plasma current during the pulse.

Mean Current [mA]	NO temperature [K]
25	349
50	375
100	472
150	480

ture, NO in air, was a pre mixture. Also, in increased pressure did not allow the plasma ignition.

Because of the relatively high uncertainty, only a maximum pulse temperature has been determined. Fig. 3.23 indicates the ranges chosen for the line ratio method. The line ratio corresponding to room temperature has been taken from the first $8ms$ indicated by t_1. The change of the temperature has been determined within the first ms of the plasma pulse, t_2. The mean pulse temperature has been calculated from the time range t_3 ranging between $2ms$ and $5ms$. The temperature ranges from room temperature up to $382K$ for the $150mA$ current pulse. On the other hand absorption spectroscopy integrates along the line of sight. Consequently, the temperature obtained by absorption spectroscopy is an averaged temperature. The three pass alignment might strengthen these phenomena. The laser beam passes through hot areas, in the centre of the tube, as well as cold areas, close to the tube walls and the windows. Therefore, the
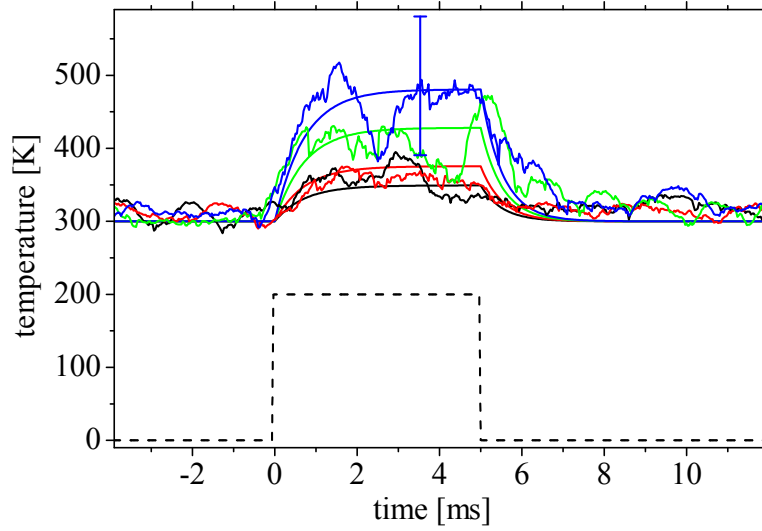
Figure 3.22: Calculated temperature evolution of NO arising during a 5*ms* plasma pulse. Here, the initial gas mixture has been 0.8% NO in air. The dashed line indicates the plasma pulse. From bottom to top: 25*mA*, 50*mA*, 100*mA* and 150*mA* averaged discharge current. The solid lines represent the estimated temperature evolution.

measured temperature might be underestimated than the true gas temperature. Nevertheless, it could be shown that the QCLAS can be adapted to the measurement of the gas temperature especially for low pressure conditions where the spectra are highly distorted by non-linear effects. The temperature determined can be used to obtain the number density either of the probe gas, like NO in this example, or of other gas components. For this purpose, the line strength can be corrected in order to obtain temperature independent measurements. The rise of the temperature considered within the first ms, t_1 in fig. 3.23, leads to specific heating in the order of 280K/mJs, dashed line in fig. 3.23. Only the energy deposited within the first ms is included.

As an example to show the performance, the measured temperature has been used to estimate the efficiency of the gas heating. Because of the closed system, isochoric changes are considered. The heat energy Q deposited in the gas is $Q = c_v \cdot m \cdot \left(T - T_{ref}\right)$, where c_v is the specific heat capacity at constant volume, air: $0.717 kJ\,kg^{-1}\,K^{-1}$ [32], m is the mass of the gas, T is the temperature and $T_{ref} = 296K$ is the room temperature. For simplicity, the energy deposited in the discharge tube was calculated by integrating the electrical power over the pulse duration. The efficiency is defined to be the ratio between the heat energy Q and the electrical energy normalised to 100%. Fig. 3.25 shows the relative part of the total energy deposited into the gas heating as a function of the total energy. As one can see, the efficiency decreases as the total energy increases. This could have two reasons. First, a higher electrical energy causes a higher expansion pressure creating a stronger radial gas flow towards the wall. This leads to an increased gas cooling because the wall is considered to have room temperature even during the plasma pulse. Second, the main process exciting inner degrees of freedom is the electron impact excitation. Further energy coupling, vibration-vibration VV or vibration-translation VT,
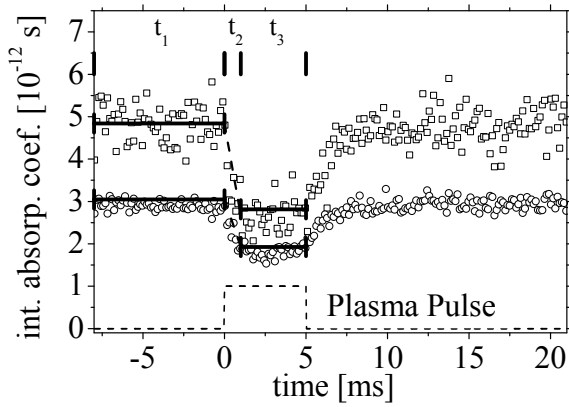
Figure 3.23: Integrated absorption coefficients K for the single line structure (circles) and for the double line structure (squares) for a 5ms dc plasma pulse. The mean current was 150mA. The initial pressure of 0.8% NO in air was 1.33$mbar$. The marked ranges, t_1, t_2, t_3, have been averaged and used for the temperature measurement, see above this figure. For clarity, only each 5th data point is plotted.
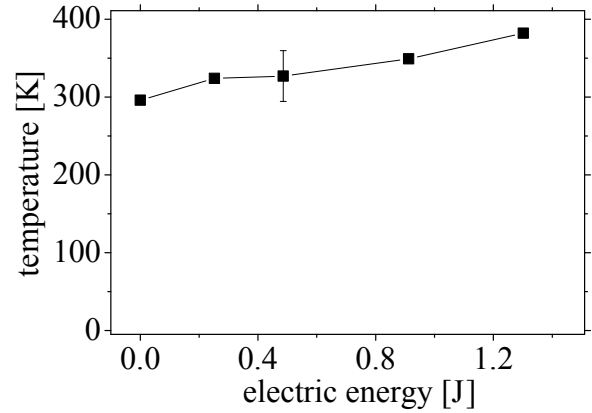
Figure 3.24: Calculated pulse temperatures as a function of the mean plasma current calculated from the absorption measurement (squares) and from emission spectroscopy (circles). The power was calculated from the electric measurement. The initial pressure was 1.33$mbar$ initial of 0.8% NO in air.

can also occur.
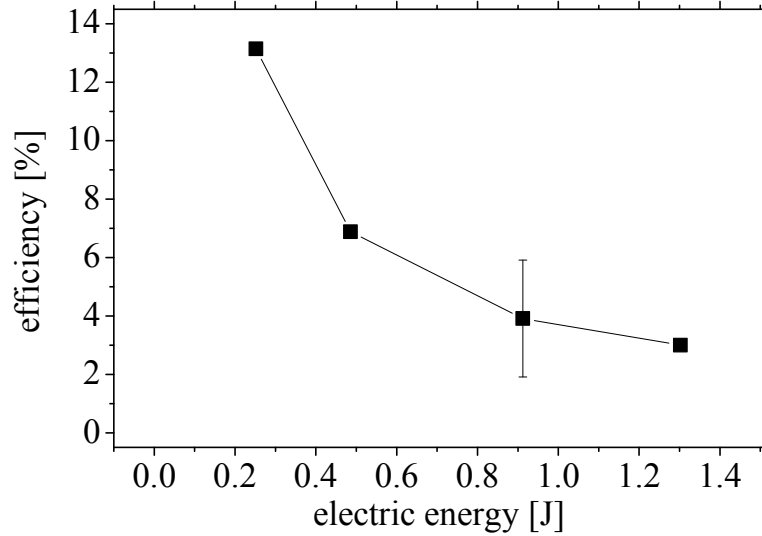
Figure 3.25: Efficiency of the gas heating as a function of the electrical energy obtained from the line ratio method (squares). The efficiency is defined as the ratio between the heat energy of the gas and the electrical energy calculated from the voltage current behaviour. The gas heating becomes less effective for higher energies.

3.5.7   Correction of the line strength

The concentration n of a species determined by absorption spectroscopy is usually calculated by applying the relation $K(T) = n \cdot S(T)$. $S(T)$ is the line strength and $K(T)$ is the integrated absorption coefficient which can be extracted from the measured spectrum, see also chapter 3.2. The line strength $S(T)$ belongs to a certain inter-molecular transition and is listed in databases like HITRAN. These values are usually valid for a certain reference temperature T_{ref}. Consequently, the line strength has to be corrected in order to obtain the correct species concentration when gas heating has to be taken into account. The QCLAS system, applied in this study, provides a laser pulse of about $150ns$. As a consequence, the spectral position of the emitted laser light is tuned slightly which results into a scan over the spectral range of interest. Therefore, the detected signal represents the intensity as a function of time. Fig. 3.26 displays a typical plot, *intensity* vs. *time*, for the etalon signal, the raw spectrum and the calibration function f needed to convert the time axis into a wavenumber scale. The spectral position of the absorption lines
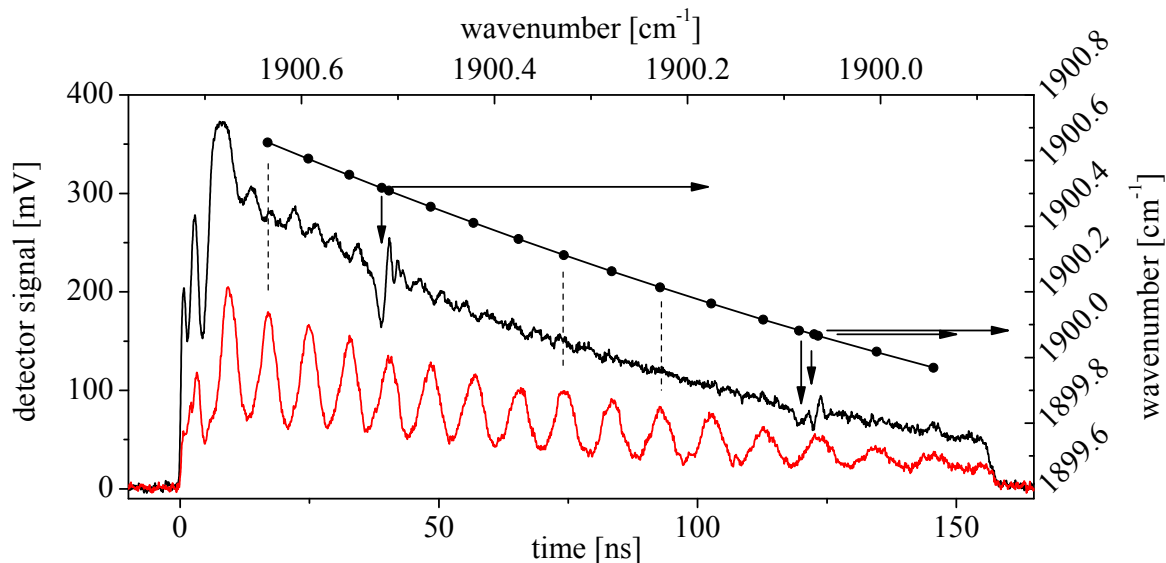
Figure 3.26: Typical plot of *intensity* vs. *time* for a $150ns$ QCL pulse at an example above. The curve at the bottom shows the etalon spectrum, free spectral range FSR = $0.049cm^{-1}$, caused by the continuous wavenumber tuning of the laser. The curve in the middle shows the spectrum of NO as a function of time, $p_{NO} = 0.013mbar$, L = $180cm$. The topmost curve illustrates the calibration curve f used to convert the time scale obtained by detector oscilloscope unit into a wavenumber scale. The black circles indicate the maxima of the etalon spectrum, see also vertical dashed lines.

are known from e.g. databases and so the distance between them, too. The etalon allows the absolute conversion of the spectra from the time domain into a wavenumber scale. This is done by recording the fringes of the germanium etalon with a free spectral range recalculated from

the line distance, fig. 3.26. A second order polynomial fit has been applied to describe this calibration function f, that is:

$$f = a_0 + a_1 \cdot t + a_2 \cdot t^2 \qquad (3.23)$$

where

$$
\begin{aligned}
a_0 &= 1900.769 cm^{-1} s^{-1} \\
a_1 &= -6.853 \times 10^6 cm^{-1} s^{-2} \\
a_2 &= 9.347 \times 10^{12} cm^{-1} s^{-3}
\end{aligned}
\qquad (3.24)
$$

This calibration converts the detected signal from a voltage / time into a voltage / wavenumber quantity. The nearly linear behaviour within an absorption structure allows the usage of a constant tuning rate, one for each absorption structure. For practical calculation, the tuning rate τ has been used instead of applying a wavenumber calibration to all measured spectra. The tuning rates τ have been calculated by evaluating the first derivative of the calibration function f at the time the lines appear, that is

$$
\begin{aligned}
\tau_{SL} &= \left.\frac{df}{dt}\right|_{\text{line1}(1900.5 cm^{-1})\text{ at } 39\,ns} = -6.13 \times 10^6 cm^{-1} s^{-1} \\[2mm]
\tau_{DL} &= \left.\frac{df}{dt}\right|_{\text{line2}(1900.1 cm^{-1})\text{ at } 120\,ns} = -4.62 \times 10^6 cm^{-1} s^{-1}
\end{aligned}
\qquad (3.25)
$$

where τ_{SL} and τ_{DL} are the tuning rates for the single line and the double line absorption structure, respectively. The negative sign accounts for the tuning direction only, and is set positive always. The calibration function shows a decreasing of the tuning rate over the pulse duration which is also illustrated by the increasing of the free spectral range of the etalon. This effect is mainly caused by the internal heating of the laser crystal and leads also to a decreased intensity at the end of the pulse. Although, the calibration function f looks nearly linear, the usage of one linear calibration function applied to both absorption structures would cause an error of about 25%. From the measured spectra, fig. 3.26, the integrated absorption coefficient K can be calculated in two different manner, see also chapter 3.2. First, a K value can be calculated from the voltage / time domain, leading to K_t. Second, the K value can be calculated from the converted voltage / wavenumber domain, leading to K_v. For practical calculations, it is convenient to calculate K_t times the tuning rate τ of the corresponding absorption structure. This gives $K_{meas} = \tau \cdot K_t = K_v$ which is of the same dimension as in the HITRAN database. From the simulated spectrum, fig. 3.13, the integrated absorption coefficient has been calculated, leading to K_{sim}. The integrated absorption coefficients, both K_{sim} and K_{meas}, have been calculated for different number densities n, again for the number densities taken from the calibration curves, n_{meas}, and taken from the mixing ratio used for the spectrum simulation, n_{sim}. These K values have been plotted versus the number density, fig. 3.27. As one can see, the data points can be approximated by a linear function. A linear function, expressed in its general form $y = m \cdot x + b$ (where m and b are the fitted coefficients), was chosen to approximate the obtained relation $K = K(n)$ shown in fig. 3.27. The method of least squares has been applied to find the best fitting coefficients and to appraise the quality of the fit. From absorption theory, the integrated absorption coefficient K is expressed by the product of the line strength S times the number density n, $K = n \cdot S$. The

slope m of a linear function represents the line strength S. Here, the intercept is zero that is the function has to pass the origin of the diagram, as required by the theory. In order to find the best parameter, the fit was done twice, with and without the inclusion of the b term that is with and without a forced intercept equal to zero. It has been found, that for the simulated K-values, K_{sim}, the inclusion of the b term improves the fit by a factor less than 1%. Therefore, the relation has been fitted directly. On the contrary, it has been found that for the measured K-values, K_{meas}, the inclusion of the b term improves the fit by a factor of about 3. Therefore, a relation $K = n \cdot S + b$ has been fitted to the measured data, but only S has been used for further analyses. The reason for a non-zero intercept could be manifold. One reason could be that the influence of the non-linear absorption phenomenon changes for lower concentration. However, such an effect was not observed in the calibration. A second reason might be that the signal to noise ratio (SNR) decreases for lower concentrations. Whatever the reason might be, the line strength which minimises the fit is used for further investigations since the validation of different line strength is only shown for the mentioned concentration range. The obtained values for the line strengths are listen in tab. 3.3 and have been used to calculate the correction factors valid at room temperature. From fig. 3.27 and tab. 3.3, the correction factor for the single line structure, C_{corr}^{SL}, and for the double line structure, C_{corr}^{DL}, can be calculated

$$C_{corr}^{SL} \quad = \quad \frac{S_{sim}}{S_{meas}}\bigg|_{\text{single line}} \quad = \quad 0.96$$

$$C_{corr}^{DL} \quad = \quad \frac{S_{sim}}{S_{meas}}\bigg|_{\text{double line}} \quad = \quad 1.43$$

(3.26)

Using these corrections, the line strengths evaluated from the measured spectra are corrected by multiplying the line strength obtained from the simulation with the correction factor. This assumes that the non linear effects of the absorption structure do not change by heating. This assumption can be made because such an effect has not been seen by the testing experiment, chapter 3.5.5. Fig. 3.28 shows the line strengths taken from the simulation and the corrected ones using $S_{corr} = S_{sim}/C_{SL/DL}$, both for the single line structure and for the double line structure. For the purpose of the temperature correction done later in this work, the single line

Table 3.3: Resulting line strength and tuning rate obtained by both, simulation and measurement for the single line and double line absorption structure. The error of the last digit is given in the brackets.

Line Structure	Spectral Position $\left[cm^{-1}\right]$	Line Strength at 296 K $\left[10^{-20}\frac{cm^{-1}}{molecules\ cm^{-2}}\right]$	Tuning rate $\left[10^{6}cm^{-1}\ s^{-1}\right]$	
Single	1900.52	6.11(5)	——	Simulation
		6.31(2)	6.13	Measurement
Double	1900.07	11.50(9)	——	Simulation
		8.05(3)	4.62	Measurement

absorption structure has been chosen, although, the double line structure shows a stronger temperature dependency compared to the single line one. The reason is, that the line strength is bigger and, therefore, the detection limit is smaller. Finally, the absolute number density n of
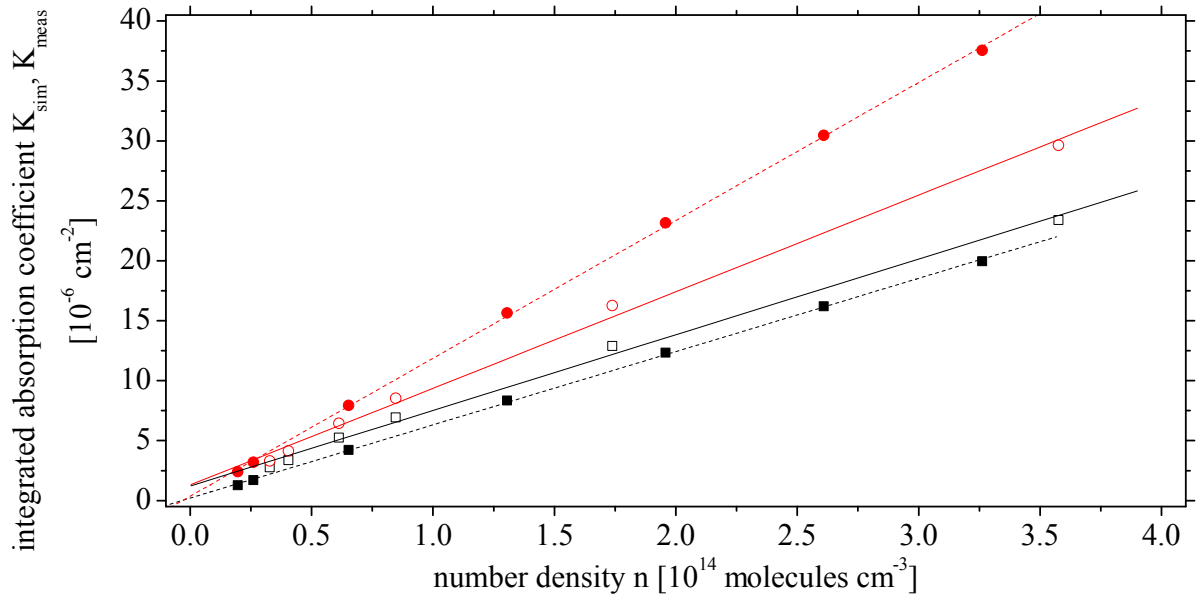
Figure 3.27: Measured (open symbol, solid line) and simulated (closed symbol, dashed line) integrated absorption coefficient $K = K(T = 296K)$ versus the number density of NO for the single (square) and double (circles) line structure at the reference temperature $T_{ref} = 296K$. The linear function represent the fitted curves whereas the slope corresponds to the line strength S.

the particle can be expressed by

$$n = \frac{K_{meas}}{S_{meas}(T)} = \frac{\tau \cdot K_t \cdot C_{corr}}{S_{sim}(T)} = \frac{\tau \cdot K_t \cdot C_{corr}}{\left[\frac{S_{sim}(T)}{S_{sim}(T_{ref})}\right] \cdot S_{sim}(T_{ref})} \tag{3.27}$$

The expression $S_{sim}(T)/S_{sim}(T_{ref})$ is called correction factor, C_{norm}, and represents the normalised line strength. Fig. 3.29 shows the correction factor C_{norm} as a function of the temperature. Fig. 3.30 shows for comparison the corrected and the uncorrected evolution of the absolute number densities n of NO. The usage of both, the single line and the double line absorption structure lead to the same absolute number density within the error bars. The discrepancies especially during the plasma pulse may be caused by the fact, that the temperature curve is estimation only.
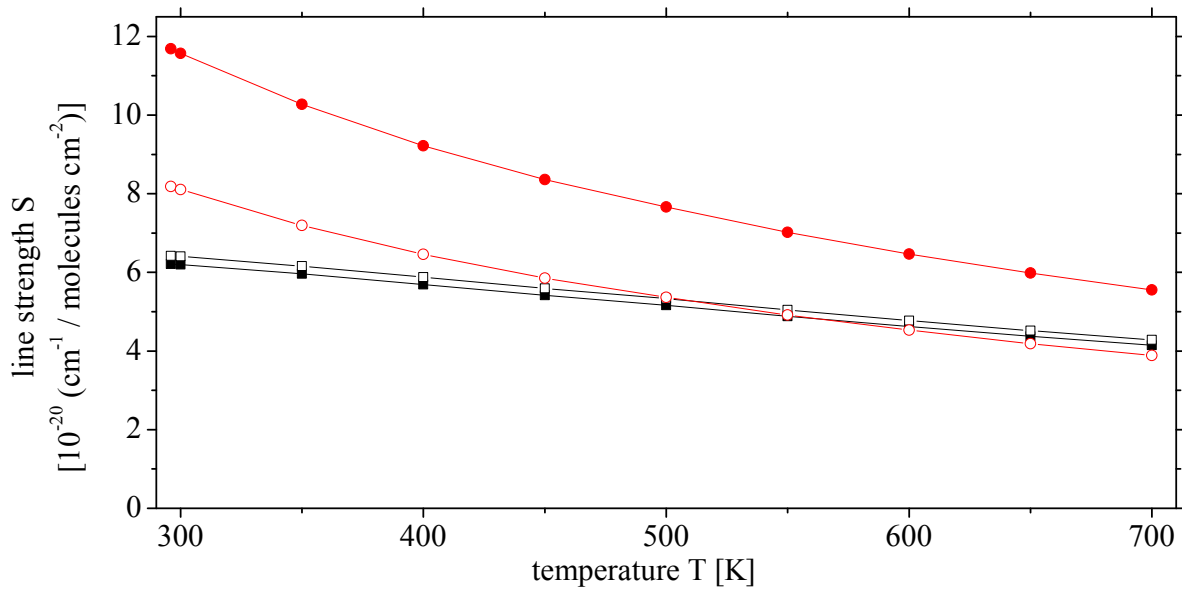
Figure 3.28: Temperature depending decay of the line strength $S(T)$ for the single (square) and double (circles) line absorption structure resulted by simulation (closed symbol). The corrected line strengths (open symbol) have been calculated using a correction factor $C_{corr}^{SL/DL}$ obtained by the investigation of simulated, temperature dependent spectra.
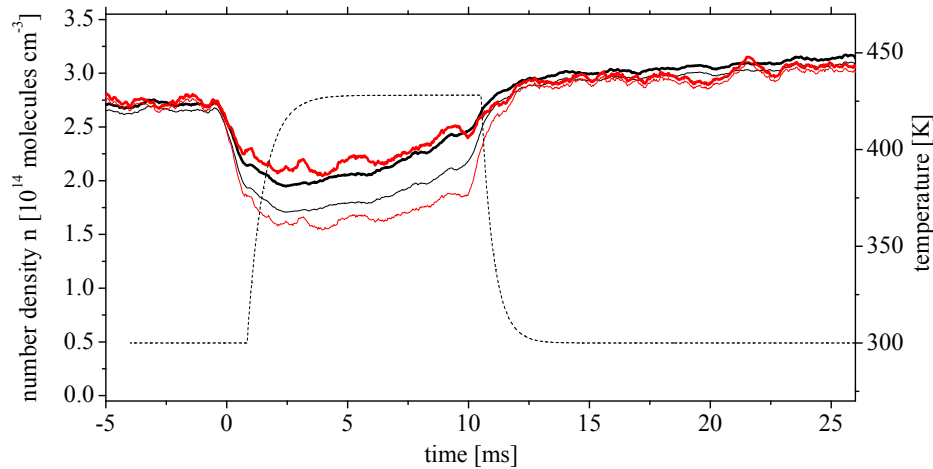
Figure 3.30: Corrected (bold line) and uncorrected (thin line) absolute number density n of NO for the single line (black) and double line (red) absorption structure calculated by eqn. 3.27. The usage of either the single line structure or the double line structure lead both to the same number density n within the error bars. The discrepancies may be caused by the fact that the temperature curve is an estimation only. Experimental parameters: 0.8% NO in air at $p_{total} = 1.33mbar$, duration: $10ms$ dc plasma pulse, mean current: $150mA$. The evolution of the temperature (dashed line) has been taken from fig. 3.22.
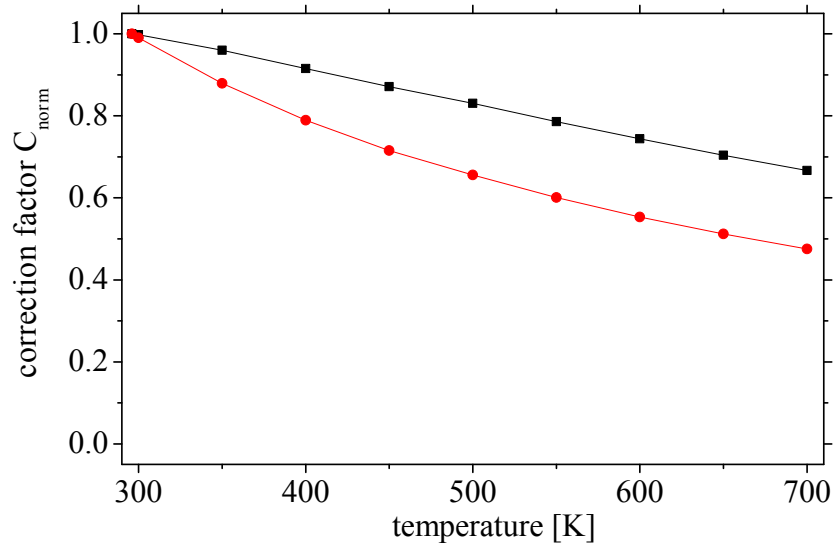
Figure 3.29: Correction factor for the single line (squares) and for the double line (circles) structure. These curves represent the normalised line strength as a function of the temperature and have been used to calculate the correct line strength as it changes with temperature.

For practical calculation, the measured integrated absorption coefficient K_{meas} has been multiplied by the correction factor directly. This can be understood by the fact, that the number density n does not change principally when gas heating is applied. Therefore, the relation $K(T) = n \cdot S(T)$ should not be depend on the temperature.

$$n = \frac{K(T)}{S(T)} = \frac{K(T_{ref})}{S(T_{ref})} \Rightarrow \frac{K_t(T)}{K_t(T_{ref})} = \frac{S_{sim}(T)}{S_{sim}(T_{ref})} \overset{!}{=} C_{corr} \qquad (3.28)$$

3.6 Triple Q: A three channel quantum cascade laser absorption spectrometer

3.6.1 Introduction and Motivation

Over the last two decades chemical sensing using laser absorption spectroscopy (LAS) in the molecular fingerprint region from 3 to $20\mu m$ has been established as a powerful in situ diagnostic tool for molecular plasmas [34–38]. The non-intrusive, selective and time resolved detection and quantification of transient and stable molecular species provides important information on the gas phase composition and chemistry of complex gas mixtures in electric discharges. Molecular plasmas are increasingly being used not only for basic research but also, due to their favourable properties, for materials processing technology. These fields of application have stimulated the development of infrared spectroscopic techniques for industrial requirements. In order to exploit the capabilities of mid-infrared (IR) tunable diode laser absorption spectroscopy (TDLAS) for effective and reliable on-line plasma diagnostics and process control in research and industry, transportable tunable infrared multi-component acquisition systems (IRMA, TOBI) have been developed [39, 40]. An infrared multi-component acquisition system (IRMA) may be equipped with up to four different diode lasers which are operated simultaneously. In this way a time resolution as short as ten milliseconds has been achieved [40]. Further progress in fast multi-species detection was reported for the two laser beam infrared (TOBI) system using two multiplexed tunable diode lasers at the same time. In comparison to the IRMA system the TOBI spectrometer was especially designed for higher detection speed. Rapid scan software enables transient plasma conditions to be investigated on time scales of tens of microseconds. The control software combines direct absorption with sweep integration to measure the absolute concentrations of several molecular species and provides continuous digital output, which might be used for process control. The optical system thereby supports both in-situ measurements in a plasma reactor and ex-situ diagnostics of gas phase samples extracted into a multi-pass cell [39]. The essential cryogenic cooling of lead salt diode lasers (and also of the detectors), that are typically operated at temperatures below $100K$, remains the main drawback of mid-IR TDLAS. Hence, systems based upon lead salt diode lasers are large in size since they require complementary equipment such as closed cycle refrigerators and / or cryogens like liquid nitrogen. The recent development and commercial availability of quantum cascade lasers (QCLs) for wavelengths longer than $3.4\mu m$ and inter-band cascade lasers (ICLs) for shorter wavelength offer an attractive new option for mid-IR LAS. In conjunction with integrated distributed feedback (DFB) gratings the emission wavelength of this new class of thermoelectrically (TE) cooled semiconductor lasers can be custom-tailored over a wide range throughout the molecular fingerprint region. DFB-QCLs provide continuous mode-hop free wavelength tuning. Their total emission range is typically limited to less than $7cm^{-1}$ (for a heat sink temperature between $\pm30°C$). Compared with an (incomplete) coverage of hundreds of wavenumbers in the case of temperature tuned multi-mode lead salt TDLs, it is clear that the application of DFB-QCLs requires a relatively precise selection of the laser. Recently tunability over much broader spectral ranges than with a typical DFB-QCL has been achieved using external cavity (EC) configurations. Nowadays EC-QCL, which are available in pulsed or con-

tinuous wave working mode, can be tuned over more than $100 cm^{-1}$ and provide mode hope free tuning ranges in the order of $60 cm^{-1}$ [41]. Meanwhile the variety of QCLs and ICLs are considered as substitutes for lead salt TDLs which has led to a rapid development of IR LAS from a niche position to a standard diagnostic technique [42]. For a better understanding of molecular processes in non-equilibrium plasmas mid-IR LAS is a valuable tool since it directly provides number densities of molecular species. Particularly under non-stationary excitation conditions time-resolved techniques combining both high sensitivity and high speed data acquisition are essential. In this respect the fast frequency chirp of pulsed QCLs, which is in the range of about tens of *MHz* per *ns* (i.e. $\approx 0.001 cm^{-1} ns^{-1}$), known as *intra pulse mode* [43, 44], offers advantages for chemical sensing: entire absorption spectra of up to $\approx 1 cm^{-1} (30 GHz)$ are recorded during a few hundred nanoseconds pulse width which fits very well to highly time resolved measurements of rapidly changing chemical processes. Studies under turbulent gas phase conditions have become feasible, because the data acquisition time is shorter than random fluctuations in the sub-millisecond range [22]. An ideal spectrometer that facilitates the investigation of transient phenomena in molecular plasmas should therefore combine high time-resolution with high sensitivity to detect key species in the gas phase and the potential of (simultaneous) multi-species monitoring. Although in-situ experiments tackling all these three criteria are still challenging, a significant improvement of existing spectrometers has become feasible due to the aforementioned progress in mid-IR laser technology. Therefore this chapter concerns a compact and transportable three channel QCL system (TRIPLE Q) developed for highly time-resolved plasma diagnostics. A photograph of the optical board can be seen in fig. 3.31. The TRIPLE Q spectrometer encompasses three different QCLs which can be used for gas phase chemical sensing in general or, particularly, for plasma diagnostics of molecular species. All three QCLs are operated in the intra pulse mode with typical pulse lengths of the order of 100 to $200 ns$. Using a multiplexed detection regime a (total) time resolution below $1s$ can be achieved to study kinetic processes of multiple infrared active compounds in plasmas. A special data processing and analysis technique considers time jitter effects of the infrared emission of the QCLs. The article gives a survey of the optical subsystem, the data processing, and the data analysis technique. The performance of the TRIPLE Q system has been assessed in pulsed direct current DC plasmas in N_2O-air and NO_2-air gas mixtures. The accuracy and sensitivity limits of the system are discussed based on the identification of main noise sources and uncertainties. One single QCL covers, depending on the pulse width and tuning rate, a spectral range in the order of about $0.5 cm^{-1}$. This range can be shifted within about $7 cm^{-1}$ tuning the temperature usually between $\pm 30°C$. This narrow range limits the spectroscopic detection mostly to one single species, although it is sometimes possible to cover several lines from several species. However, to cover several lines, these are usually not the strongest transition of a band. Therefore, compromises concerning the sensitivity have to be made. Recently, a new source of QCL came available on the market. These EC-QCL cover a spectral range of about $60 cm^{-1}$ to $100 cm^{-1}$. However, the tuning rate is in the order of $2 cm^{-1} s^{-1}$. Therefore, a whole scan over the entire spectrum takes several seconds. Consequently, high time resolved wide range measurements are very difficult. Additionally, these devices are relatively new and, therefore, reliability might be a critical issue. The limitations in spectral coverage can be overtaken by the combination of several QCL sensitive to several species. Two benefits can be mentioned. First, the spectral

range can be expanded and second, the huge time resolution obtained by pulsed QCLs can be sustained. Generally for a laser combining geometry, the intensity should not decrease and second, all single beams should be co-axial in order to pass the same volume. One approach might be realised by the application of several beam combiner. This might be quite simple to realise but can cause several problems. First, the intensity of the beams is reduced depending on the reflection / transition ratio. Second, the beam combiner can cause interferences leading to fringes in the spectrum. Third, the availability of wide range beam combiners might be problematic and fourth, this method becomes more difficult when more lasers have to be made combined. Compared to this, an alternative solution has been applied. Several lasers can be combined to one single laser beam using Off Axis Parabolic (OAP) mirrors. A beam map can be seen in fig. 3.33. The advantage of this solution, compared to the beam combiner approach, is a much less reduction of the intensity of the combined laser radiation. While the beam combiner method allows bringing all single lasers exactly on the same path, the OAP geometry creates a final laser beam where all single beams are close together but not overlapping each other. This can be an issue for spatially resolved measurements.
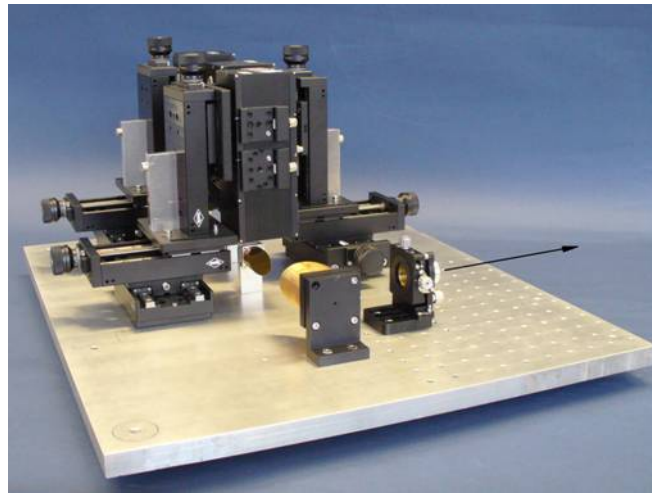
Figure 3.31: Photograph of the optical board of the three QCLs spectrometer. In the foreground, the telescope made of a 2-inch OAP and a lens can be seen. The combined laser beam is indicated by the black arrow, see chapter 3.6.2.

3.6.2   Optical subsystem

In fig. 3.32 the schematic diagram of the TRIPLE Q spectrometer connected to a pulsed dc discharge tube is shown. Fig. 3.33 provides details of the optical subsystem. The three QCLs are separately housed in temperature-stabilised laser heads and are individually operated by its corresponding pulsed laser driver (Q-MACS Basic, neoplas control, [20]). The divergent radiation of each QCL is collimated using an off-axis parabolic (OAP) mirror, $d = 25.4mm$, focal length $= 40mm$) and guided to a shared OAP of bigger diameter ($d = 50.8mm$, focal length $= 125mm$). Each laser illuminates a part of the shared OAP which re-focuses the individual beams on an IR

transparent lens ($d = 8mm$, $f = 0.4cm$) to create a single collimated (multi-wavelength) laser beam, that covers the three different QCL centre wavelengths. Strictly speaking, the shared OAP and the lens form an optical telescope to reduce the beam diameter to about $4mm$. This multi-wavelength beam is directed through the DC discharge tube and finally focused onto the fast detector (IRDM-600, neoplas control, [20]) using an OAP of $40mm$ focal length ($d = 25.4mm$). The detector module contains a temperature controller which is specifically adjusted to the fast detector element (VIGO, PDI-2TE-10/12), a fast pre-amplifier (bandwidth: $600MHz$, rise time: $2ns$) and a non-switched temperature controller. These parts are included into a nickel plated aluminium box to shield external noise sources. The pre-amplified detector signal is acquired with an oscilloscope (SDA735Zi, LeCroy, bandwith: $3.5GHz$, sample rate: $40GS/s$). A computer records the data from the oscilloscope and performs the data analysis as detailed below. A function generator (33120A, Hewlett Packard) and a delay generator (DG535, Stanford Research Systems) provide an appropriate trigger regime for multiplexing the radiation of the QCLs, fig. 3.32.
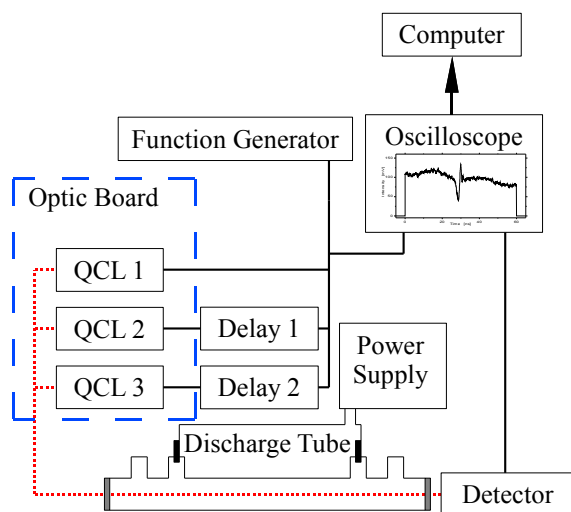
Figure 3.32: Principle arrangement of the TRIPLE Q system connected to a pulsed dc discharge in air [45].
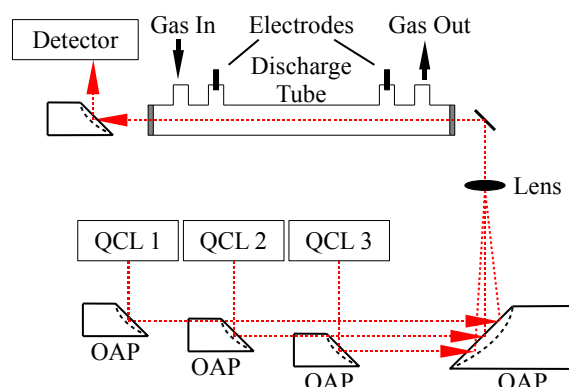
Figure 3.33: Optical subsystem combining the radiation of 3 independently controlled QCLs by means of an optical telescope formed by a shared OAP and a lens. The multi-wavelength beam is used for time resolved studies of molecular components in a discharge tube [45].

3.6.3 Data processing and analysis technique

Fig. 3.34 shows an entire spectrum as recorded by the oscilloscope. The three laser pulses centred around $2207cm^{-1}$, $1900cm^{-1}$ and $1615cm^{-1}$ along with corresponding absorption features of N_2O, NO and NO_2 can be clearly seen. Begin and end of the laser pulses are typically

characterised by a fast increase and decrease of the emission. The leading edge is often followed by damped transient oscillations (e.g. QCL-1). Strictly speaking, the emission follows the behaviour of the QCL current as detailed in [46]. The QCL current in turn follows from the match or slight mismatch between the QCL impedance and the laser driver. The response of a QCL to the same driver electronics can therefore be significantly different as can be seen for QCL1-3 in fig. 3.34. Note that the response of the laser also affects the end of the pulse. Hence, at least $20ns$ around the onset and the end of the laser emission are omitted for the spectral analysis. From fig. 3.34 it is obvious, that information about the concentration of all three molecular species can be gained in less than $800ns$. This, however, requires proper selection and adjustment of the individual laser pulse length in conjunction with the trigger regime. Note that single absorption features are observed in less than $10ns$. In case of ultra-fast periodic events, this might be considered as lower limit time-resolution of this method. For single, non-periodic events a burst mode can be applied, which acquires entire spectra after receiving a trigger pulse for a limited time period, typically only part of a second, see chapter 3.6.4. This implies an inherent time-resolution which is as short as the repetition frequency of the laser pulses. It should be pointed out that in this case all spectra are acquired without any signal averaging. In case of reduced laser pulse widths of about $50ns$, a repetition rate of up to $400kHz$ may be applied corresponding to a minimum time-resolution of $2.5s$. This mode of operation fits to the 2% duty cycle limit specified by the laser manufacturer, AlpesLaser [21]. As one can see from fig. 3.34, the line width of an absorption feature is of the order of several ns. To measure an absorption line correctly the sample rate of the oscilloscope should be - depending on the tuning rate of the QCL - at least 10 Giga samples per second. The acquisition of all three spectra along with the required high sample rate leads to a significant number of data points, i.e. of the order of several 10000 data points. Therefore an on-line data treatment becomes difficult within the available time frame of the plasma pulse(s). In general, the spectra were first subsequently acquired and stored on a standard PC hard drive whereas the data treatment was performed afterwards. The detection of a sequence of several QCL pulses on one detector requires a careful trigger regime for the individual lasers and, additionally, the consideration of uncertainties in timing with respect to the master trigger. In the case when only one QCL pulse is present such phenomena are less important. Fluctuations, usually called jitter, are inherent to the laser and are therefore inevitable. In what follows two terms are distinguished fig. 3.35, (i) pulse jitter J_1: variation of the time between the master trigger and the rising edge of the laser emission and (ii) line jitter J_2: variation of the time between the rising edge of the light signal and the absorption line. J_1 is mainly caused by the response of the laser driver to the master trigger while J_2 is directly linked to the response of the laser to the applied current pulse, i.e. influenced by ohmic heating and impedance matching. For a characterisation of these two jitter phenomena, the pulse jitters as well as the line jitters of all three lasers were established separately. For this purpose 1000 spectra of static gas compositions were analysed. It transpires that both jitter effects form a distribution which can be approximated by a fit function. The lower panel of fig. 3.34 shows two typical examples of the time distribution of J_1 and J_2 respectively. The specific distribution functions of all three QCLs used in these experiments are shown in fig. 3.36 and fig. 3.37.It is clear that the width of the distribution of the pulse jitter, J_1, is of the order of a few ns, whereas the width of the distribution of the line jitter, J_2, is about
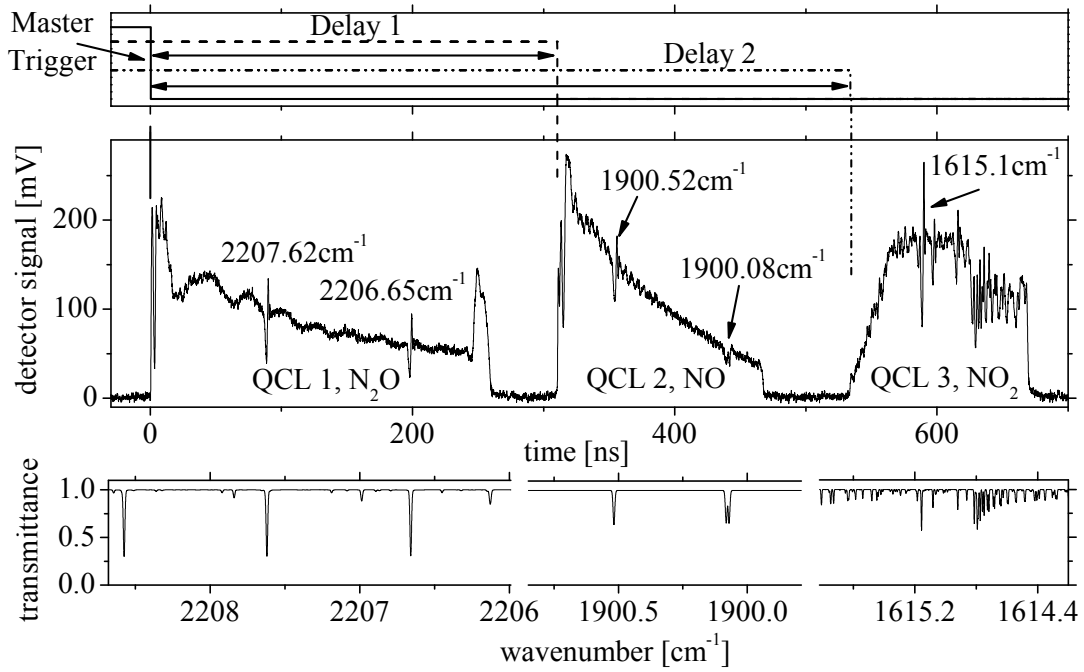
Figure 3.34: Example of single, multiplexed absorption spectra of N_2O, NO and NO_2 measured with the TRIPLE Q system (middle) and calculated spectra for the specific emission range of the three QCLs (bottom). The applied trigger regime is given above [45].

one order of a magnitude smaller. From fig. 3.36 and fig. 3.37 it is quite obvious, that QCL 3 (NO_2, at $1615 cm^{-1}$) behaves entirely different concerning its jitter distributions compared to QCL1 and 2 (N_2O and NO, at 2207 and $1900 cm^{-1}$). Particularly the pulse jitter phenomenon prevents the direct application of constant limits for the baseline fitting routine as well as for the calculation of the integrated absorption coefficient $K(T_{eff})$. Hence, at first, the position of the rising edge of each pulse is identified by means of a software algorithm. The first data point of each pulse which exceeds 10% of the pulse maximum served to define the edge of the laser emission. Once, this point is determined the main process of the algorithm continues as follows:

Calculate Baseline I_0:
The baseline I_0 has been calculated by fitting a second order polynomial function to the spectrum. Only the ranges of the spectrum which are marked in fig. 3.38 have been taken into account for the fitting routine.

Calculate Absorbance:
The absorbance AB has been calculated from the baseline (I_0) and the pulse spectrum (I) using $AB = \ln(I_0/I)$. An example is given in fig. 3.39. Subsequently, all values of the absorbance AB which turned out to be smaller than zero have been set equal to zero, fig. 3.39.

Calculate integrated absorption coefficient K:
The integrated absorption coefficient $K(T_{eff})$ is calculated from absorbance AB using eqn. 3.4 within the limits of integration given in fig. 3.39. It has been validated that the line jitter of
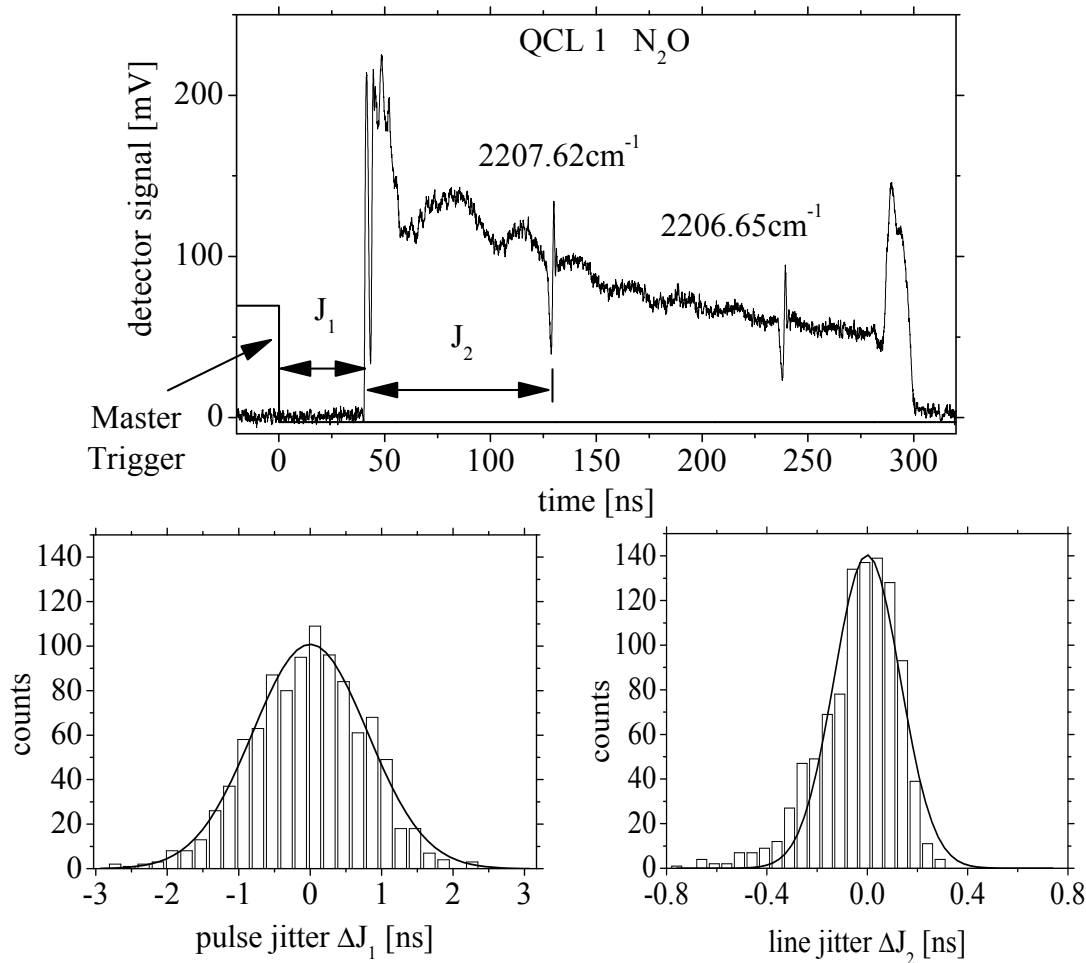
Figure 3.35: The measurement of the pulse jitter J_1 and of the line jitter J_2 (upper panel) and principle of the determination of the jitter time distribution (lower panel) [45].

about $0.5 ns$ falls always within these limits. It has, therefore, no influence on the calculation of $K(T_{eff})$.

The integrated absorption coefficient $K(T_{eff})$ is usually considered to be directly proportional to the line strength $S(T_{eff})$ documented in e.g. HITRAN, [13]. It should be mentioned that this is not the case for these experiments, since the absorption line is strongly affected by non-linear effects, e.g. rapid passage or saturation effects [42]. Therefore the relation requires a correction and a calibration function has to be determined [24, 25]. For this purpose a gas mixture of 1% of N_xO_y diluted in N_2 was filled in the discharge tube at different pressures [47]. The calibration experiments also enable the detection limits of the species of interest to be determined. For the experiments performed in the present study, the detection limits of NO, NO_2 and N_2O were found to be 4, 3.4 and $0.5 \times 10^{13} molecules cm^{-3}$, respectively.
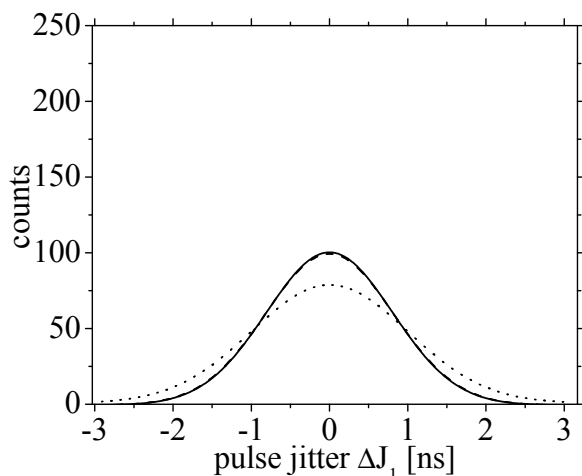
Figure 3.36: Distribution of the pulse jitter of the three QCLs used in the TRIPLE Q system. (solid: QCL 1, N_2O, at $2207cm^{-1}$; dashed: QCL 2, NO, at $1900cm^{-1}$ and dotted: QCL 3, NO_2, at $1605cm^{-1}$) [45].
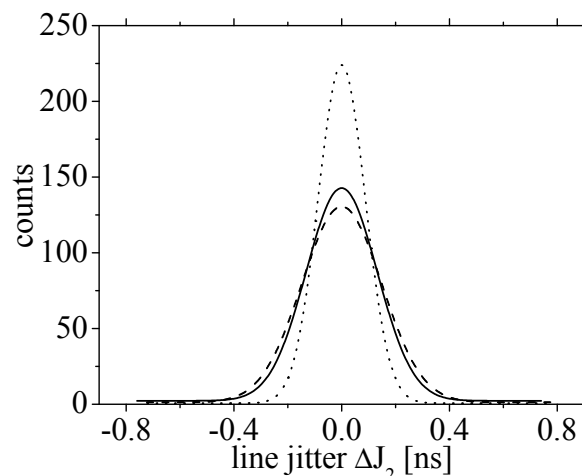
Figure 3.37: Distribution of the line jitter of the three QCLs used in the TRIPLE Q system. (solid: QCL 1, N_2O, at $2207cm^{-1}$; dashed: QCL 2, NO, at $1900cm^{-1}$ and dotted: QCL 3, NO_2, at $1605cm^{-1}$) [45].
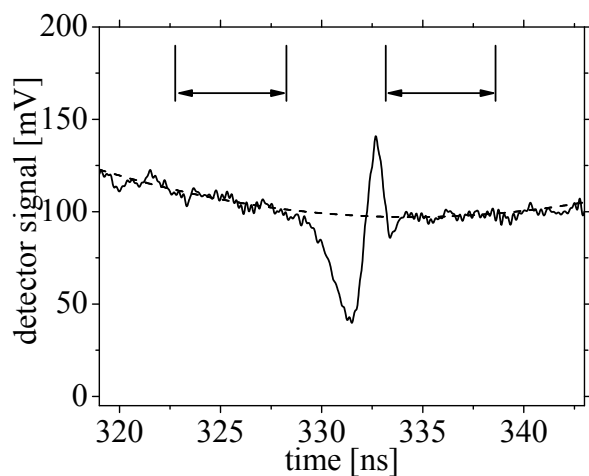
Figure 3.38: Detailed view of an absorption feature of N_2O at $2207.62cm^{-1}$. For the fit of the baseline (dashed line) the indicated signal ranges have been used [45].
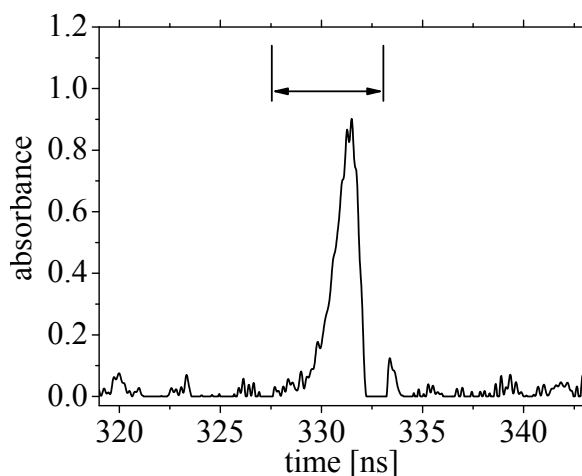
Figure 3.39: Calculated absorbance of the absorption feature of N_2O at $2207.62cm^{-1}$, fig. 3.38. The range for the integration over the area of the absorbance signal is indicated [45].

3.6.4   Validation of the system performance

The performance of the multi-channel spectrometer was validated by absorption spectroscopy measurements of N_2/O_2 plasmas with admixes of 0.8% N_xO_y. Such fundamental investigations are important to improve the understanding of the chemistry of plasma induced pollution abatement and to verify modelled species concentrations. Therefore, the fast detection of the concentration is of increasing interest for the study of the temporal evolution of key molecules and their total concentration. The low-pressure discharge chosen for the performance test here was ignited in a Pyrex tube with an inner diameter of 20*mm* and a total length of 60*cm*. A detailed description of the geometry and equipment can be found in Ref. [48]. The sensitivity limits have been improved by a multi-pass alignment of the laser. Using a set of mirrors outside of the vacuum tube the laser radiation could pass the plasma three times. The lasers were operated in the burst mode of the system, fig. 3.40, applying a pulse repetition frequency of $f_{Rep} = 20kHz$. In other words, after 50*μs* a new full spectrum, consisting of the three laser pulses, could be detected. The spectra were recorded into the internal memory of the oscilloscope. The memory size allowed saving up to 3000 spectra. From the repetition frequency f_{Rep} and the number of
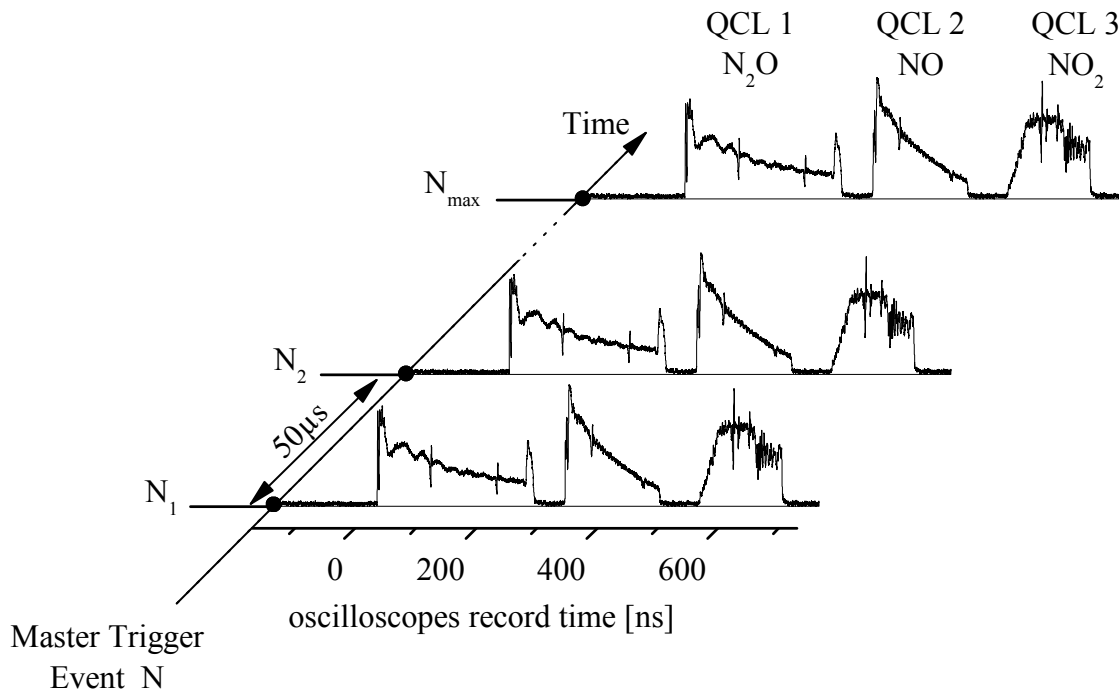
Figure 3.40: Schematic diagram of the burst mode applied to record the temporal evolution of N_xO_y absorption spectra in pulsed DC plasmas: the spectra of all 3 QCLs are recorded at once after a master trigger event; where N (max. 3000) of such combined spectra are stored in the memory of the oscilloscope; master trigger pulses are separated by 50*μs* ($f_{Rep} = 20kHz$) [45].

spectra recorded, the total duration of the spectroscopic measurement was 150*ms*. From the

saved spectra, the species concentration was calculated as described above. No additional spectral averaging was applied. In fig. 3.41 and fig. 3.42 two examples of the temporal evolution of the concentration of N_xO_y molecules in low-pressure pulsed air plasmas ($p = 1.33mbar$) are shown. The discharges were ignited with an initial concentration of 0.8% N_2O, fig. 3.41 and 0.8% NO_2, fig. 3.42 admixed to the dry air. The plasma was ignited 8ms after the spectroscopic measurements, i.e. the first burst was started. In this way molecular concentrations are available before, during and after the plasma pulse. In both discharges NO is formed as reaction product. Two pronounced steps are detected during the formation of NO. In both examples, fig. 3.41 and fig. 3.42, the NO density during the plasma pulse levels off at about 50% of the value that is measured in the afterglow phase. After a rapid depletion of the precursor molecules, N_2O and NO_2, within about 1ms these densities remain constant throughout the plasma pulse. In the afterglow a relatively fast increase in the N_2O and NO_2 ground state densities can be observed within 3ms. The temperature dependency on the line strength has been taken into account too. For this purpose, a correction factor has been determined following Ref. [49].
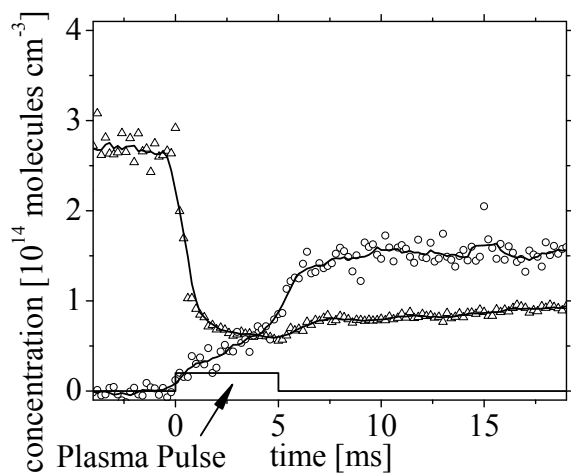
Figure 3.41: Time dependence of the N_2O (triangles) and NO (circles) concentrations before, during and after a single plasma pulse of 5ms length corresponding to an energy of 1.23J in a N_2O / air DC discharge ($p = $ 1.33$mbar$). A data point smoothing is applied to guide the eyes (solid lines) [45].
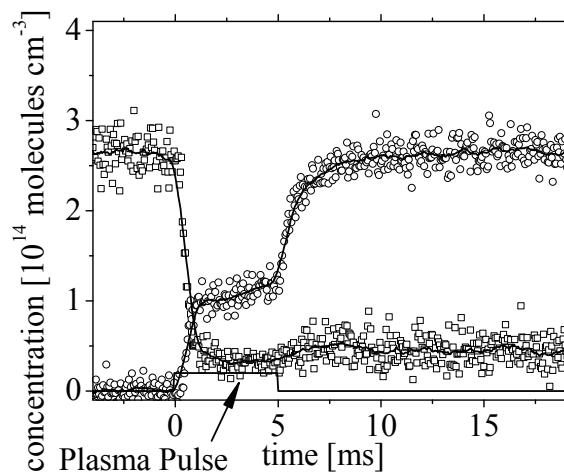
Figure 3.42: Time dependence of the NO_2 (squares) and NO (circles) concentrations before, during and after a single plasma pulse of 5ms length corresponding to an energy of 1.23J in a NO_2/air DC discharge ($p = $ 1.33$mbar$). A data point smoothing is applied to guide the eyes (solid line) [45].

3.6.5 Accuracy and limitations

In general, molecular densities obtained by QCL spectrometers applying the intra pulse mode under low pressure conditions are affected by the uncertainties of the calibration routine and by a variety of noise sources. The main error sources are summarized here briefly: First, instabilities of the laser emission, among them the stability of the output power and the tuning rate, the stability of the spectral properties (single or multimode emission) and the stability of the spectral

position of the emission (i.e. the line jitter mentioned above), increase the uncertainties. Second, the design of the optical subsystem may induce etalon effects which complicates the analysis of the baseline. Third, the stability and linearity of the detector module and digitising equipment has to be carefully checked: the noise level of the pre-amplifier, local variations in the sensitivity of the detector element and possibly saturation effects of the detector element can reduce the general sensitivity of the system. Additionally, the entire system can be sensitive to mechanical vibrations which can also cause a modulation of the detector signal. Finally, for the examples shown above, a reference gas mixture with a specified N_xO_y mixing ratio was injected to the tube reactor and controlled by mass flow controllers. Usually, these devices have an accuracy of about 2%. Since it is quite difficult to estimate the influence of a single parameter, the total error of the system was determined. For that reason, the same spectra used for scrutinising the jitter phenomena were analysed again. The integrated absorption coefficient K_{eff} of N_2O at line $2207.62 cm^{-1}$, NO at line $1900.52 cm^{-1}$ and NO_2 at line $1615.15 cm^{-1}$ were calculated for static gas conditions. The spectra were taken at a repetition frequency of $f_{Rep} = 5 kHz$. This analysis yields total relative errors for each molecule, i.e. 15% for N_2O and NO as well as 10% for NO_2.

3.7   Conclusion

In this chapter, the diagnostics which have been used for the experiments are described. Starting with a general and short review of absorption spectroscopy, the main techniques, Fourier Transform Infrared, FTIR, spectroscopy and quantum cascade laser absorption spectroscopy, QCLAS, are summarised. Both methods have been used to identify and quantify the species detected.

The FTIR spectrometer was used for the identification and quantification of the exhaust gas mixture produced by multi stage packed bed reactor with the help of the PNNL infrared database.

The QCLAS method was used mainly to quantify the concentration of either N_2O, NO and NO_2 with the help of the HITRAN database. These N_xO_y have been produced in a tube reactor, chapter 5.

Additionally, the line ratio method as a possibility to measure the gas temperature has been adapted to the QCLAS method. The highly distorted absorption spectra, especially in the low pressure range, have been handled by a sufficient calibration routine.

The experiences working with QCLAS and the need for a fast, multi component sensitive spectrometer has resulted into the development of a new, fast and compact spectrometer. This three channel TRIPLE Q system is based on pulsed QCLs. The system is able to work without complex cryogenic installations. The high power output of the laser allows a nitrogen free detector.

Overall, it has been shown, that QCLAS is a suitable technology for fast and sensitive measurement of species concentration.

Bibliography

[1] F. Hempel. *Absorption Spectroscopy Studies In Low Pressure Non Equilibirium Molecular Plasmas Using Tunable Infrared Diode Lasers*. Logos Berlin, (2003).

[2] I. Langmuir. The pressure effect and other phenomena in gaseous discharges. *Journal of the Franklin Institute*, **196**, (1923).

[3] J. E. Allen, R. L. F. Boyd, and P. Reynolds. The collection of positive ions by a probe immersed in a plasma. *Proceedings of the Physical Society of London Section B*, **70**:297, (1957).

[4] W. Rödel and G. Wölm. *Grundlagen der Gaschromatographie*. (1982).

[5] M. Schmidt, R. Foest, and R. Basner. *Mass spectrometric diagnostics*. Low Temperature Plasma Physics. 2th edition, (2008).

[6] J. W. Coburn and M. Chen. Optical-emission spectroscopy of reactive plasmas - a method for correlating emission intensities to reactive particle density. *Journal of Applied Physics*, **51**:3134, (1980).

[7] J. W. Coburn and M. Chen. Dependence of F-atom density on pressure and flow-rate in CF_4 glow-discharges as determined by emission-spectroscopy. *Journal of Vacuum Science & Technology*, **18**:353, (1981).

[8] J. Röpcke, P. B. Davies, F. Hempel, and B. P. Lavrov. *Emission and absorption spectroscopy*. Low Temperature Plasma Physics. 2th edition, (2008).

[9] M. G. Allen. Diode laser absorption sensors for gas-dynamic and combustion flows. *Measurement Science & Technology*, **9**:545, (1998).

[10] S. S. Penner. *Quantitative Molecular Spectroscopy and gas Emissivities*. Pergamon Press, London-Paris, (1959).

[11] S. Welzel. *New Enhanced Sensitivity Infrared Laser Spectroscopy Techniques Applied to Reactive Plasmas and Trace Gas Detection*. Logos Berlin, (2009).

[12] HITRAN. Hitran, http://www.cfa.harvard.edu/hitran/, (2011).

[13] S. W. Sharpe, T. J. Johnson, R. L. Sams, P. M. Chu, G. C. Rhoderick, and P. A. Johnson. Gas-phase databases for quantitative infrared spectroscopy. *Applied Spectroscopy*, **58**:1452, (2004).

[14] P. B. Davies. An introduction to high-resolution molecular spectroscopy, 2000.

[15] M. Haverlag, E. Stoffels, W. W. Stoffels, G. M. W. Kroesen, and F. J. deHoog. Measurement of the gas temperature in fluorocarbon radio frequency discharges using infrared absorption spectroscopy. *Journal of Vacuum Science & Technology a-Vacuum Surfaces and Films*, **14**:380, (1996).

[16] P. R. Griffiths and J. A. De Haseth. *Fourier transform infrared spectrometry*. Chemical analysis v. 171. Wiley-Interscience, 2nd edition, (2007).

[17] J. M. Hollas. *Modern spectroscopy*. J. Wiley, 3rd edition, (1996).

[18] R. F. Kazarino and R. A. Suris. Possibility of amplication of electromagnetic waves in a semiconductor with a superlattice. *Soviet Physics Semiconductors-USSR*, **5**:707, (1971).

[19] J. Faist, F. Capasso, D. L. Sivco, C. Sirtori, A. L. Hutchinson, and A. Y. Cho. Quantum cascade laser. *Science*, **264**:553, (1994).

[20] NPC. Neoplas control, http://www.neoplas-control.de/, (2011).

[21] AlpesLaser. Alpeslaser, http://www.alpeslasers.ch/, 2011.

[22] G. Duxbury, N. Langford, M. T. McCulloch, and S. Wright. Quantum cascade semiconductor infrared and far-infrared lasers: from trace gas sensing to non-linear optics. *Chemical Society Reviews*, **34**:921, (2005).

[23] N. Tasinato, K. G. Hay, N. Langford, G. Duxbury, and D. Wilson. Time dependent measurements of nitrous oxide and carbon dioxide collisional relaxation processes by a frequency down-chirped quantum cascade laser: Rapid passage signals and the time dependence of collisional processes. *Journal of Chemical Physics*, **132**, (2010).

[24] J. H. van Helden, S. J. Horrocks, and G. A. D. Ritchie. Application of quantum cascade lasers in studies of low-pressure plasmas: Characterization of rapid passage effects on density and temperature measurements. *Applied Physics Letters*, **92**, (2008).

[25] S. Welzel, L. Gatilova, J. Röpcke, and A. Rousseau. Time-resolved study of a pulsed dc discharge using quantum cascade laser absorption spectroscopy: NO and gas temperature kinetics. *Plasma Sources Science & Technology*, **16**:822, (2007).

[26] M. Capitelli, C. M. Ferreira, B. F. Gordiets, and A. I. Osipov. *Plasma Kinetics in Atmospheric Gases*. Springer Series on Atomic, Optical, and Plasma Physics. (2000).

[27] B. P. Lavrov, M. Osiac, A. V. Pipa, and J. Röpcke. On the spectroscopic detection of neutral species in a low-pressure plasma containing boron and hydrogen. *Plasma Sources Science & Technology*, **12**:576, (2003).

[28] L. S. Rothman, D. Jacquemart, A. Barbe, D. C. Benner, M. Birk, L. R. Brown, M. R. Carleer, C. Chackerian, K. Chance, L. H. Coudert, V. Dana, V. M. Devi, J. M. Flaud, R. R. Gamache, A. Goldman, J. M. Hartmann, K. W. Jucks, A. G. Maki, J. Y. Mandin, S. T. Massie, J. Orphal, A. Perrin, C. P. Rinsland, M. A. H. Smith, J. Tennyson, R. N. Tolchenov, R. A. Toth, J. Vander Auwera, P. Varanasi, and G. Wagner. The hitran 2004 molecular spectroscopic database. *Journal of Quantitative Spectroscopy & Radiative Transfer*, **96**:139, (2005).

[29] M. Hübner, D. Marinov, O. Guaitella, A. Rousseau, and J. Röpcke. A method for gas temperature measurements in a dc plasma pulse using quantum cascade laser absorption spectroscopy. *xxx*, (2012).

[30] Comsol. Comsol, http://www.comsol.com/, 2011.

[31] Korth. Korth Kristalle gmbh, http://www.korth.de/, 2011.

[32] H. Kuchling. *Taschenbuch der Physik*. Carl Hanser Verlag, 16 edition, (1999).

[33] engineeringtoolbox. The engineering tool box, http://www.engineeringtoolbox.com/, 2010.

[34] R. F. Curl and F. K. Tittel. Tunable infrared laser spectroscopy. *Annual Reports Section "C" (Physical Chemistry)*, **98**:219, (2002).

[35] P. B. Davies. Diode laser absorption spectroscopy of free radicals, ions and transient molecules. *Spectrochimica Acta Part A: Molecular and Biomolecular Spectroscopy*, **55**:1987, (1999).

[36] E. Hirota and K. Kawaguchi. High-resolution infrared studies of molecular-dynamics. *Annual Review of Physical Chemistry*, **36**:53, (1985).

[37] M. Lackner. Tunable diode laser absorption spectroscopy (TDLAS) in the process industries - a review. *Reviews in Chemical Engineering*, **23**:65, (2007).

[38] J. Röpcke, G. Lombardi, A. Rousseau, and P. B. Davies. Application of mid-infrared tuneable diode laser absorption spectroscopy to plasma diagnostics: a review. *Plasma Sources Science & Technology*, **15**:S148, (2006).

[39] J. B. McManus, D. Nelson, M. Zahniser, L. Mechold, M. Osiac, J. Röpcke, and A. Rousseau. Tobi: A two-laser beam infrared system for time-resolved plasma diagnostics of infrared active compounds. *Review of Scientific Instruments*, **74**:2709, (2003).

[40] J. Röpcke, L. Mechold, M. Kaning, J. Anders, F. G. Wienhold, D. Nelson, and M. Zahniser. IRMA: A tunable infrared multicomponent acquisition system for plasma diagnostics. *Review of Scientific Instruments*, **71**:3706, (2000).

[41] R. F. Curl, F. Capasso, C. Gmachl, A. A. Kosterev, B. McManus, R. Lewicki, M. Pusharsky, G. Wysocki, and F. K. Tittel. Quantum cascade lasers in chemical physics. *Chemical Physics Letters*, **487**:1, (2010).

[42] S. Welzel, F. Hempel, M. Hübner, N. Lang, P. B. Davies, and J. Röpcke. Quantum cascade laser absorption spectroscopy as a plasma diagnostic tool: An overview. *Sensors*, **10**:6861, (2010).

[43] T. Beyer, M. Braun, and A. Lambrecht. Fast gas spectroscopy using pulsed quantum cascade lasers. *Journal of Applied Physics*, **93**:3158, (2003).

[44] E. Normand, M. McCulloch, G. Duxbury, and N. Langford. Fast, real-time spectrometer based on a pulsed quantum-cascade laser. *Optics Letters*, **28**:16, (2003).

[45] M. Hübner, S. Welzel, D. Marinov, O. Guaitella, S. Glitsch, A. Rousseau, and J. Röpcke. TRIPLE Q: A three channel quantum cascade laser absorption spectrometer for fast multiple species concentration measurements. *Rev. Sci. Instrum.*, **82**:093102, (2011).

[46] E. Normand, G. Duxbury, and N. Langford. Characterisation of the spectral behaviour of pulsed quantum cascade lasers using a high resolution fourier transform infrared spectrometer. *Optics Communications*, **197**:115, (2001).

[47] S. Welzel, O. Guaitella, C. Lazzaroni, C. D. Pintassilgo, A. Rousseau, and J. Röpcke. NO kinetics in pulsed low-pressure plasmas studied by time-resolved quantum cascade laser absorption spectroscopy. *Plasma Sources Science & Technology*, **20**, (2011).

[48] O. Guaitella, M. Hübner, S. Welzel, D. Marinov, J. Röpcke, and A. Rousseau. Evidence for surface oxidation on pyrex of NO into NO_2 by adsorbed o atoms. *Plasma Sources Science & Technology*, **19**, (2010).

[49] M. Hübner, D. Marinov, O. Guaitella, A. Rousseau, and J. Röpcke. A method for gas temperature measurements in a dc plasma pulse using quantum cascade laser absorption spectroscopy, (2012).

Chapter 4

Destruction of volatile organic compounds in a packed bed reactor

4.1 Introduction

The application of a backed-bed reactor for the destruction of pollutions like volatile organic compounds (VOC) is an alternative technology in the field of environment protection from harmful species. There is a plenty of literature dealing with the destruction of pollutions admixed into an air stream. A short overview of the different types of a packed-bed reactor, its dimensions, the packing material and the harmful gases treated by this method is given in chapter 2. This amount of literature illustrates the large scientific interests since this concept allows the combination of catalytic active material, heterogenic catalysis with plasma technology approaches. This combination has promising potential for the improvement of plasma technology applied to the pollution destruction. The catalyst can be placed either directly into the active region of the plasma, packed-bed, or might be used for further treatment of the products positioning the catalytic material in the afterglow region. This might have influence to the selectivity as well as the efficiency of species treatment.

The focus of this chapter, however, lies on the description of experiments on the serial combination of several identical packed-bed reactors, in the following named stages. That means the serial arrangement of several stages is studied rather than a single stage varying parameters like frequency, gas flow, species, packed material or initial concentration etc. Of special interest is the influence of another identical stage to the gas composition of one stage. Over the last decade, such a combination of several identical stages has been of interest. Several groups have been published their experimental results. All about the destruction of poison species from an air stream at atmospheric pressure can be found in Ref. [1–4]. The focus of the research has been the retreatment of the exhaust gas mixture by another identical stage. For example, the by products such as OH or O_3 formed in one stage may react with the toxic species in the afterglow. This may lead to an additional destruction channel before the gas mixture enters the next stage. Some references are summarised here.

A pulsed corona treatment of an air stream contaminated with toluene [2] is an example. The corona discharge has been created in a stacked disk configuration. In total, the destruction

combining up to four different lengths of such a stacked configuration has been studied. The destruction of 10s of ppm of toluene admixed in synthetic air for different gas flows has been studied. The authors found that the toluene destruction depends linear on the number of stages. A multistage gliding arc discharge has been studied by Sreethawong et al. [3]. Two blank electrodes are placed vies-a-vie establishing a smooth increasing of the distance. They were studying the partial oxidation of CH_4 optimising the production of syngas. The influence of the flow rate, the frequency of the applied sinusoidal voltage, the amplitude of the applied voltage and the distance of the electrodes has been investigated. They found for all parameter variations that the species formation depends linear on the number of stages.

The reduction of NO_x in synthetic diesel exhaust has been studied by Tonkyn [4]. They used a two stage approach. Here, one stage consists of a tube array reactor combined with catalytic material placed afterwards. This serial combination of identical packed-bed reactors has been studied by Whitehead and co-workers [1]. The most important effect reported is a non-linear increase of the destruction rate of ethylene and toluene as a function of the number of active stages. However, the total power needed for the destruction scales linear. This is an interesting phenomenon especially when cost reduction is an important issue. This effect has been named "synergistic effect" and describes that a serial arrangement of several stages leads to a more efficient pollution destruction compared to a parallel one. This synergistic effect has been in the focus of this chapter.

First, the chapter starts with a description of experiments done to study the influence of the number of active stages to the destruction efficiency. Starting with the experimental setup, the chapter describes the destruction of ethylene and toluene admixed in an air gas flow as it has been reported in [1]. The experimental parameters used in [1] like gas flow, water concentration or voltage / power have been extended in order to reproduce the results on a broader basis. Special care has been paid to the gas flow conditions in order to avoid unwanted changes in the gas flow. This becomes an important fact since the experiments have been done at a flow rate of about $1 slm$. At such relatively low flow rate, the influences of components slowing down the gas flow have to be considered and might influence the residence time of the gas in one stage.

For each studied species, toluene and ethylene, the by products are identified and quantified but not further discussed here, because of the fact that the synergistic effect has been in the focus of interest rather than the chemical processes inside the stages. The last part of this chapter provides a link to the next chapter. It shows pictures from single micro discharges appearing above the packing material. They were taken by an ICCD camera with a gate of $20\mu s$. This illustrates that the micro discharges appear not only above the surface of the packing material but also exist between different packing particles. This shows that packed-bed reactors can be separated into a volume and a surface description of the species transformation. This becomes important in case catalytic material has to be used. For this purpose, it is crucial that the fragments produced in the discharge are able to reach the surface before they are reacting in the volume. This idea requires that the active volume should be in the order of the mean free path length present under atmospheric conditions.

The results are presented in a manner: physical quantity as a function of the totally consumed power. The curves in the diagrams, for showing destruction or species concentration, consist of four data points where the first point represents an empty reactor, no stages mounted at all,

and illustrates the initial condition, destruction and / or species concentration. The second, third and fourth points represent the data for conditions where 1 stage, 2 stages or 3 stages have been used simultaneously. Fig. 4.1 shows an example.
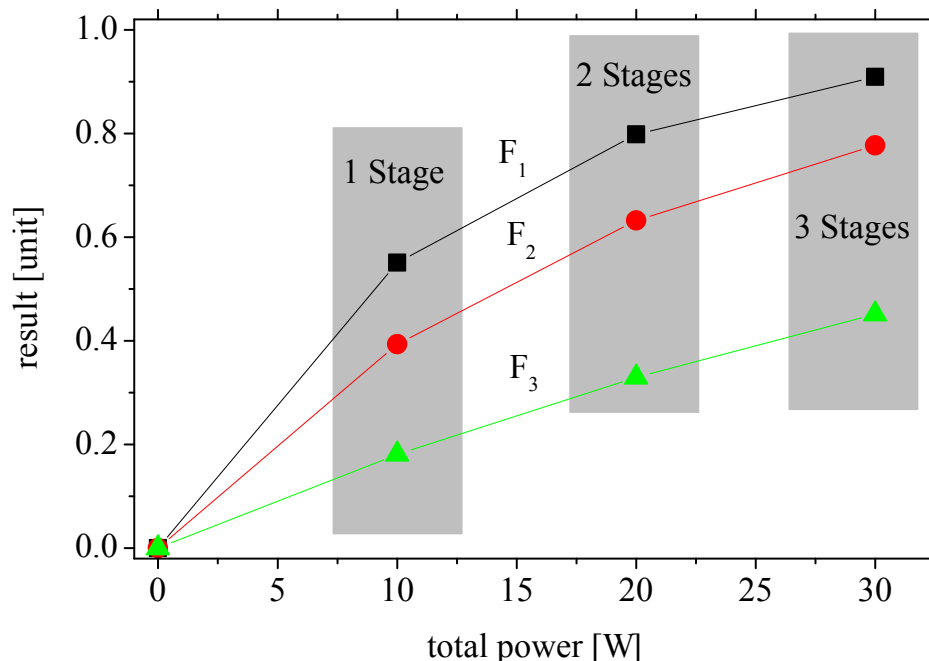

Figure 4.1: The diagram illustrates the graphical representation of the results for the toluene experiments. The data points belong to the results obtained for an experiment with 1, 2 or 3 stages used simultaneously. The total power is the power consumed by all active stages. The solid lines are used to guide the eye.

The results for ethylene are presented using the notification shown in fig. 4.24, since the data are overlapping.

4.2   Experimental Setup

The experiments to study the synergistic effect have been carried out in a Plexiglas reactor. Fig. 4.2 shows a photograph of the reactor. The dimensions of it are: length 90*cm*, width 15*cm* and height 15*cm*. The top cover is fixt by screws for an easy access. It has 10 equidistance slots in order to mount the different stages. One stage consists of two stainless steel electrodes. Both have a dimension of 120*mm* × 120*mm* and 1.2*mm* in thickness. Each of them has equidistance square holes, 4*mm*×4*mm*, distributed along the entire electrode. The electrodes are blank metal. The distance between them is about 4*mm* or 18*mm* and filled with glass beads with a diameter of 6*mm* (Merck KGaA). The electrodes and the packing material are hold together by a plastic frame. Fig. 4.3 shows a scheme of one stage. Each stage is mounted in one slot. The gas mixture under treatment flows perpendicular though the stages.
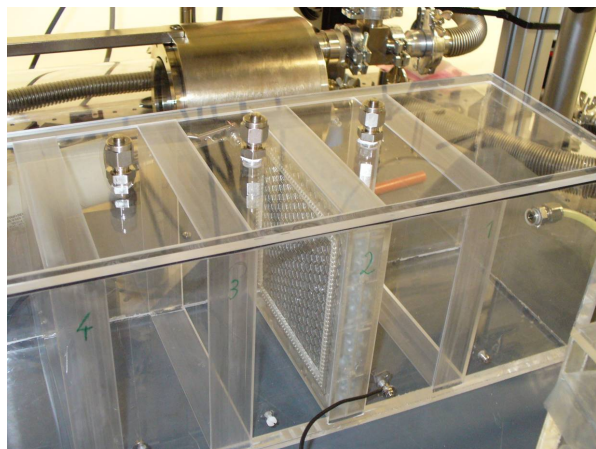
Figure 4.2: Photograph of the multi stage packed-bed reactor. Visible are the different slots. Here, one stage is mounted in slot 2 of the reactor.
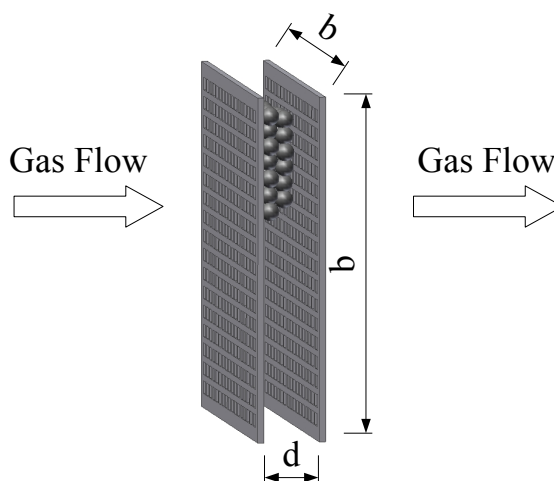
Figure 4.3: Principal sketch of one stage made of two uncovered electrodes filled with glass beads. For clarity, only a part of the stage is filled with the glass beads. The diameter of the beads is 6mm. Depending on the stages used; the distance d has been either 4mm or 18mm, respectively. The width b has been either 11cm or 12cm.

The gas input and output connections have been realised by Swagelok, 6mm, mounted at the side walls of the reactor. The used air has been supplied by a gas generator (TOC Gas Generator TG 3000, cmc GmbH) which ensures the usage of dry air, $H_2O < 1ppm$, $CO_2 < 1ppm$. The input gas flow has been controlled by mass flow controllers (MKS). The composition of the output gas mixture has been identified and quantified by an FTIR spectrometer (IFS 66v/S, Bruker) combined with an optical long path cell with 37.5m absorption length. The long path cell has been connected to the reactor using a needle valve. Inside the long path cell, the pressure has been controlled by a butter fly valve (MKS). The needle valve has been used to set the flow. All mounted stages have been driven in parallel by a high voltage power amplifier (AL-1400-HF-A, Ampline) which converted the sinus signal of a function generator (HP) into the high voltage range. The electric circuit is given in fig. 4.4. A match capacitor has been used to fulfil the resonance condition. The voltage has been measured by a high voltage probe (P6015A, Tektronix). The current was measured by the current proportional voltage drop over a measurement resistor, one for each stage. All voltage and current signals were digitalised by an oscilloscope (TDS 754C, Tektronix) and saved to a hard drive. From these signals, the consumed power has been calculated. Fig. 4.6 shows a typical voltage current behaviour.
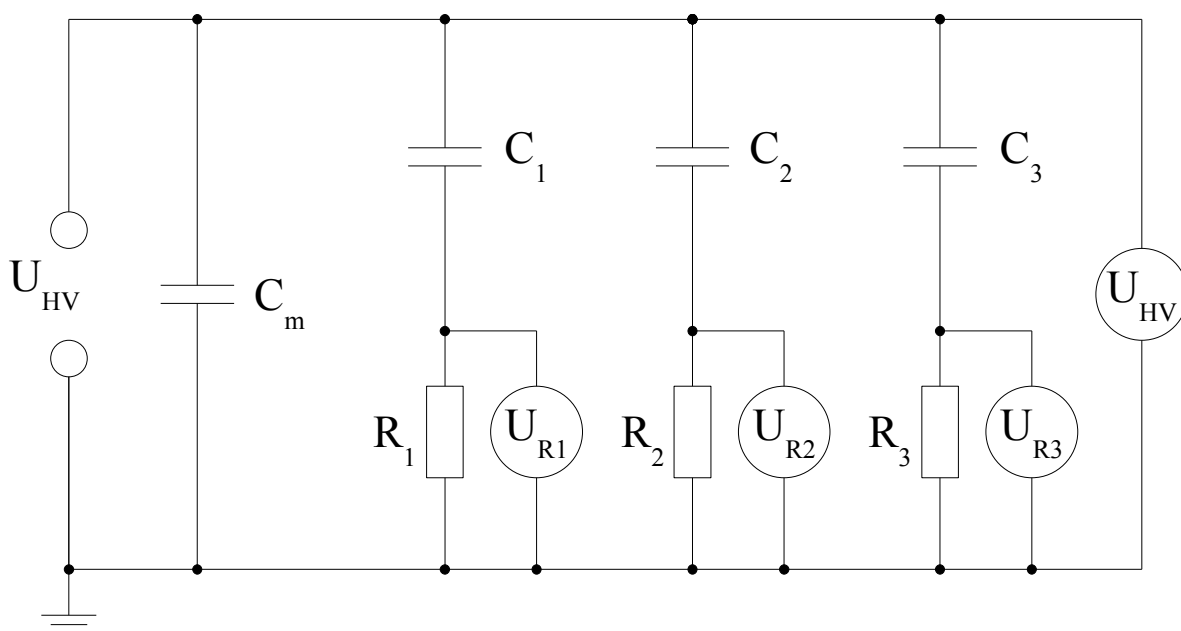
Figure 4.4: Electrical circuit of the multi stage experiment. The stages are represented by C_i, whereas the measurement resistors are marked by R_i. The capacitance Cm has been used to match the system to the resonance condition for the frequency used here.
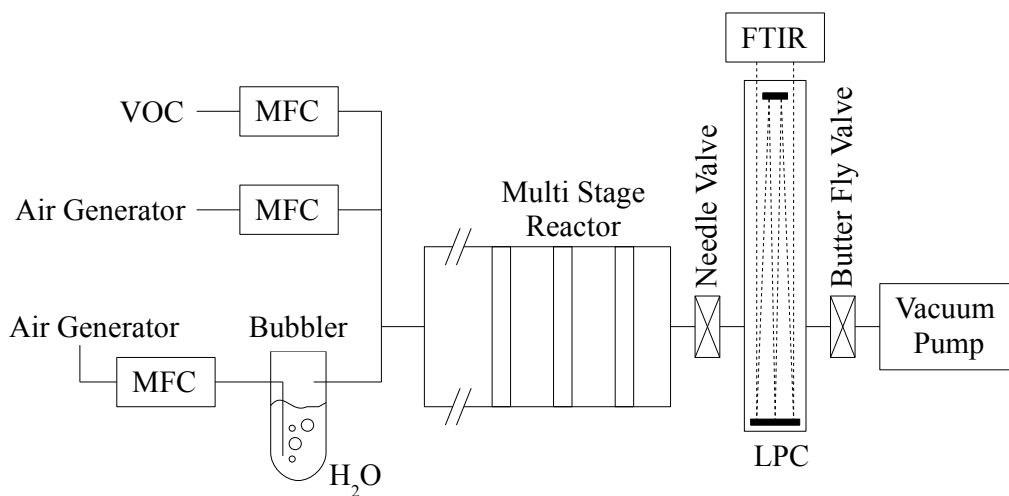
Figure 4.5: Principal sketch of the gas handling setup. The pressure inside the long path cell LPC has been controlled by a butter fly valve. The output flow was kept constant by the needle valve. The input flow was controlled by mass flow controllers (MFC).

With this setup, the destruction of one aliphatic, ethylene C_2H_4, and one aromatic, toluene C_7H_8, VOC have been tested. Ethylene was added directly into the incoming gas stream. To add toluene an open bottle was situated inside the reactor in front of the first stage. The vapour pressure has been used to obtain a sufficient toluene concentration. The detection limit reached by the FTIR system depends on the species but has been in the order of $1ppm$. The quantification has been done with the help of the PNNL [5] database. Details are given in chapter 3. The error of the method is in the order of 10%.
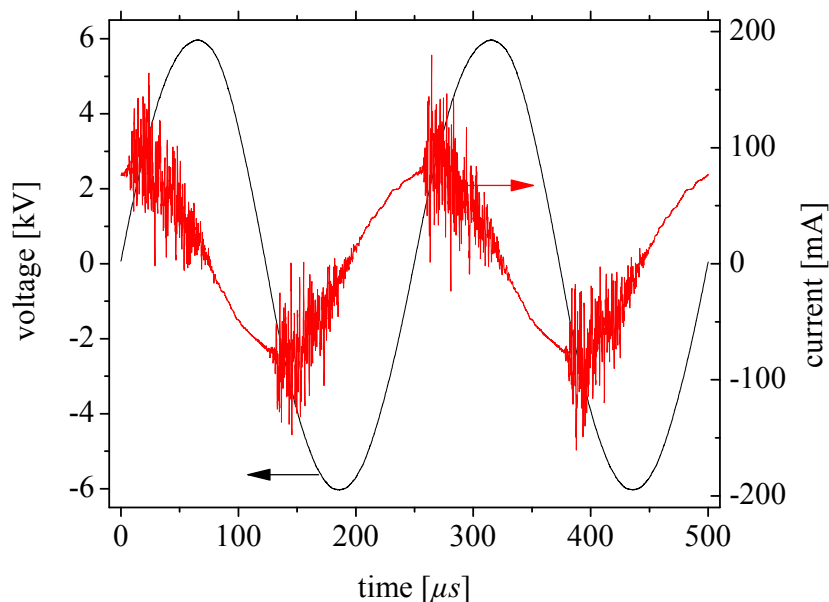
Figure 4.6: Typical voltage current behaviour. The applied voltage causes the displacement current superimposed with the current peaks. These peaks are caused by the micro discharges appearing in the stages. These curves are for one active stage at $U_{PP} = 12kV$. The gas mixture has been $1000ppm$ ethylene and $3500ppm$ humidity in synthetic air.

4.3   Destruction of Toluene

The study of the destruction of toluene has been done varying several parameters, as the gas flow, humidity level and the applied voltage which corresponds to the consumed power. The initial toluene concentration has been about $70ppm$.

4.3.1   Destruction in dry air

The toluene destruction at $1slm$ in dry air, about $85ppm$ humidity, can be seen in fig. 4.7. These experiments have been done for 1, 2 or 3 stages running at the same time for three different applied voltages, $U_{PP} = 20kV$, $21kV$, $22kV$. It turned out that voltages below $20kV$ do not lead to a significant destruction and voltages above $22kV$ where also tested, but led to arcing and destroyed the stage.
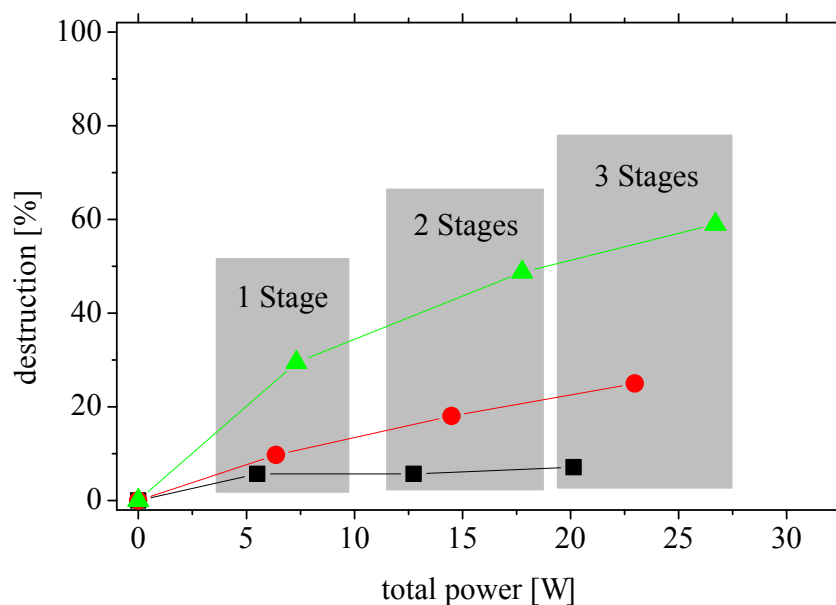
Figure 4.7: Destruction of toluene at an initial concentration of $70\,ppm$ in air as a function of the active stages. The gas flow has been $1\,slm$. For these experiments, about $85\,ppm$ humidity have been left in the gas mixture. The applied voltage has been $20\,kV$ (■), $21\,kV$ (●), and $22\,kV$ (▲).

Fig. 4.7 shows that the toluene concentration using just 1 stage leads to a destruction of about 6%, 10%, 29% for $20\,kV$, $21\,kV$, $22\,kV$ applied voltage. Two stages lead to a total destruction of 6%, 18%, 49% and three stages cause a total destruction of 7%, 25%, 58%, respectively.
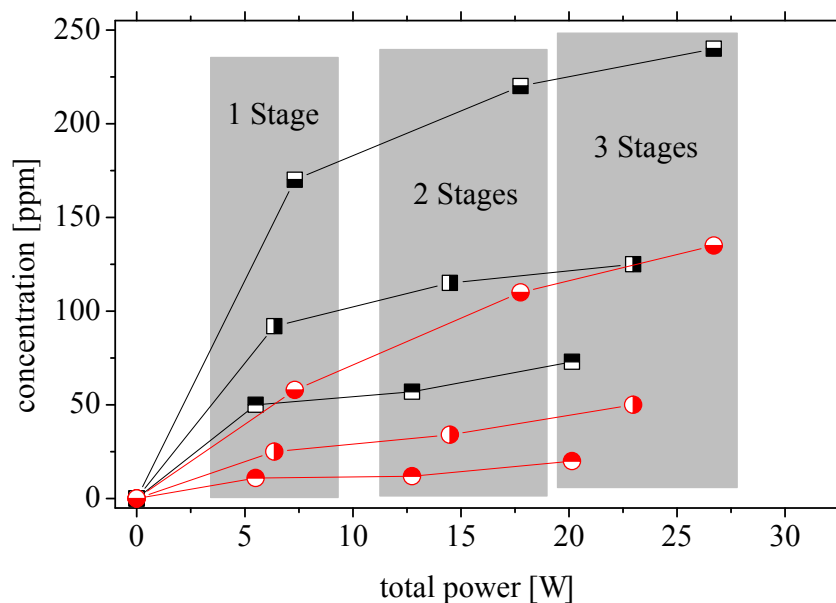
Figure 4.8: Produced ozone ($\square$) and CO_2 ($\bigcirc$) as a function of the active stages. The applied voltage has been $20kV$ ($\blacksquare$, $\ominus$), $21kV$ ($\blacksquare$, $\bullet$) and $22kV$ ($\blacksquare$, $\ominus$).
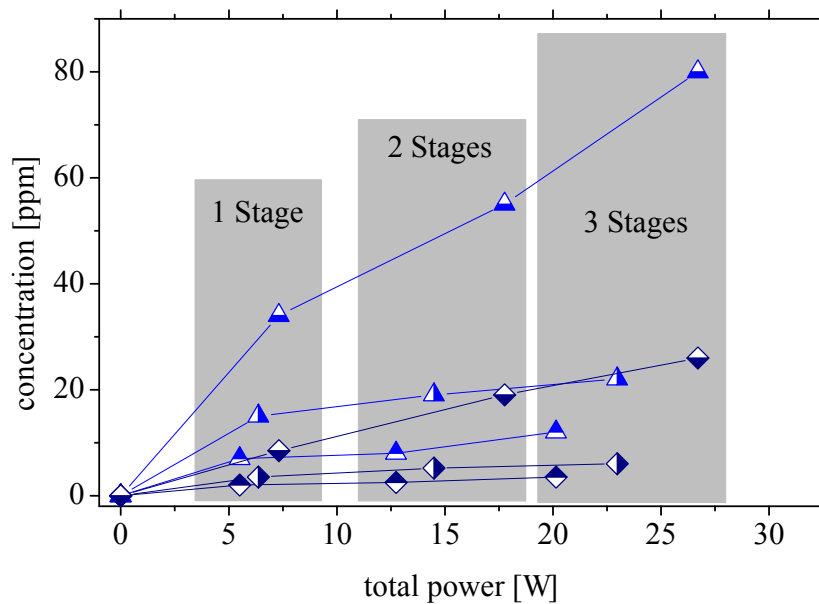
Figure 4.9: Produced CO ($\triangle$) and HNO_3 ($\diamondsuit$) as a function of the active stages. The applied voltage has been $20kV$ ($\blacktriangle$, $\blacklozenge$), $21kV$ ($\blacktriangle$, $\blacklozenge$) and $22kV$ ($\blacktriangle$, $\blacklozenge$).
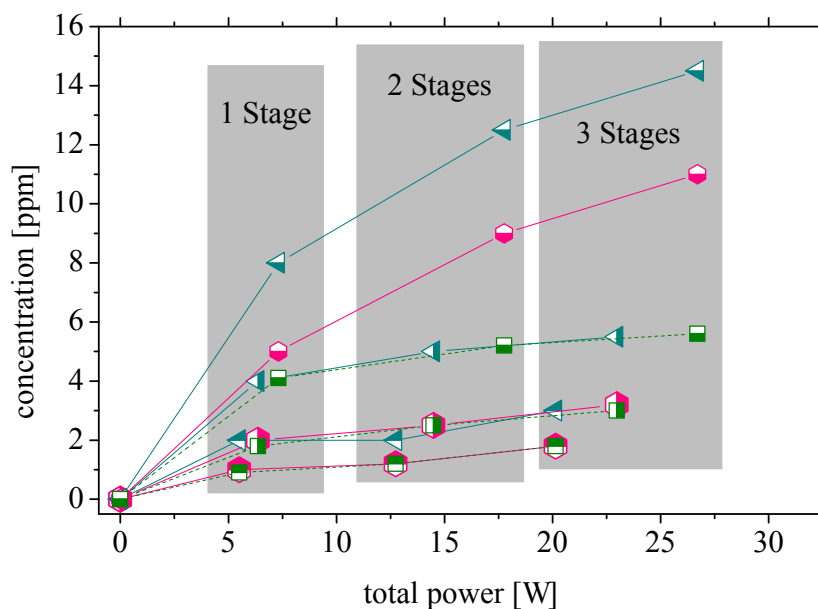
Figure 4.10: Produced N_2O ($\triangleleft$), FACID ($\ocircle$) and HCHO ($\cdots\square\cdots$) as a function of the active stages. The applied voltage has been $20kV$ ($\blacktriangleleft$, $\ominus$, $\blacksquare$), $21kV$ ($\blacktriangleleft$, $\bullet$, $\blacksquare$) and $22kV$ ($\blacktriangleleft$, $\ominus$, $\blacksquare$).

4.3.2 Destruction in humidified air

The destruction of toluene has been tested in humidified air with an initial water concentration of about $3600ppm$ in order to study ambient air conditions. This was done by splitting the air flow into $0.9slm$ main flow into the reactor and $0.1slm$ of the flow was send through the water filled bubbler see fig. 4.5. Again, three different voltages have been applied, $20kV$, $21kV$ and $22kV$. The destruction is given in fig. 4.11. As one can see, the destruction with 1 active stage is 11%, 20%, 26% for $20kV$, $21kV$ and $22kV$ applied voltage respectively. For 2 stages, the destruction is about 20%, 25%, 50% and 14%, 25%, 56% for 3 stages, respectively.
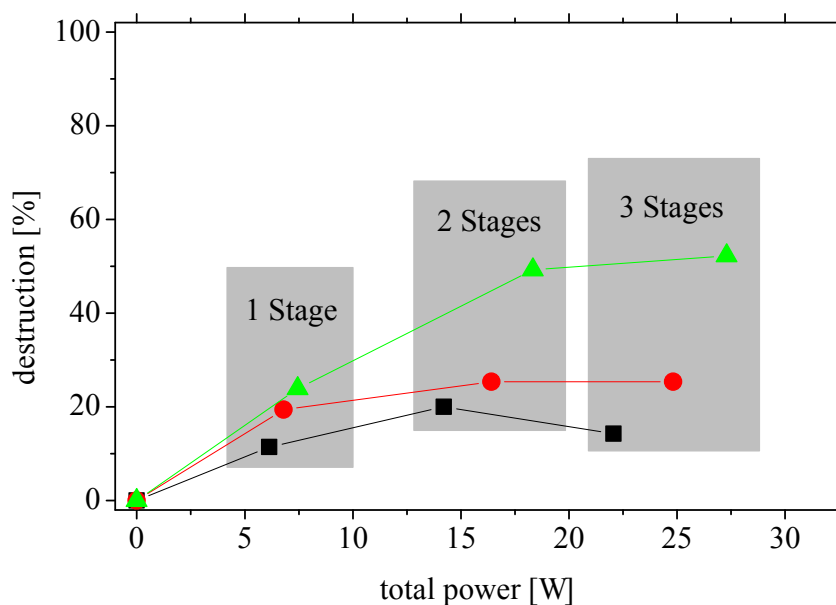
Figure 4.11: Destruction of toluene at an initial concentration of $70 ppm$ in air as a function of the active stages. The gas flow has been $1 slm$. For these experiments, about $3600 ppm$ humidity has been admixed in the gas mixture. The applied voltage has been $20 kV$ (■), $21 kV$ (●) and $22 kV$ (▲).
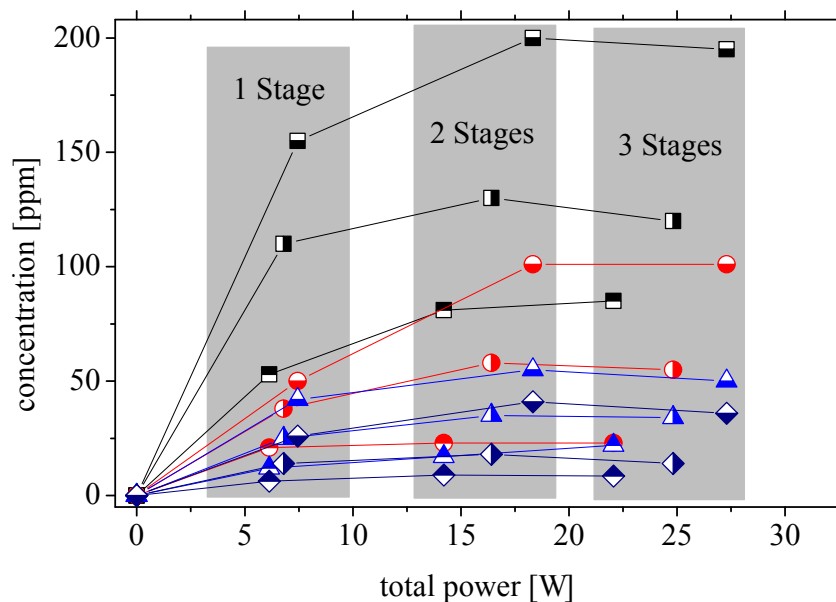
Figure 4.12: Produced O_3 (□), CO_2 (○), CO (△) and HNO_3 (◇) as a function of the active stages. The applied voltage has been $20 kV$ (⬓, ⬓, ▲, ◆), $21 kV$ (◧, ◑, ▲, ◆) and $22 kV$ (◩, ●, ▲, ◆).
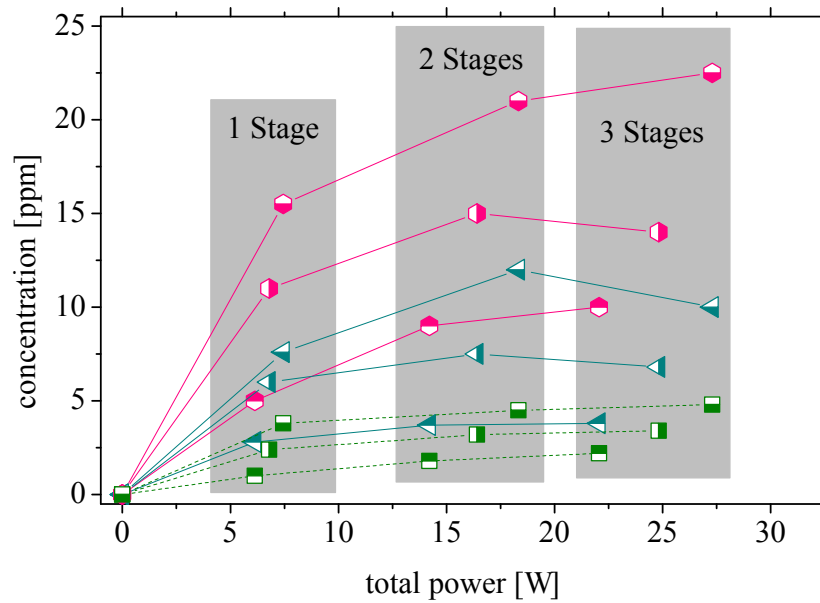
Figure 4.13: Produced N$_2$O ($\triangleleft$), FACID ($\varhexagon$) and HCHO ($\cdots\square\cdots$) as a function of the active stages. The applied voltage has been 20kV ($\blacktriangleleft$, $\varhexagon$, $\blacksquare$), 21kV ($\blacktriangleleft$, $\varhexagon$, $\blacksquare$) and 22kV ($\blacktriangleleft$, $\varhexagon$, $\blacksquare$).

4.3.3   Destruction at different gas flows

The influence of the gas flow to the destruction of toluene has also been investigated. Three different gas flows have been used. These are 1*slm*, 3*slm* and 5*slm*, all at 21*kV* applied voltage. The ambient laboratory air has been used as input gas. The initial water concentration was about 5300*ppm* for all three gas flows. This humidity level serves as an example for ambient air conditions. Fig. 4.14 shows the destruction as a function of the number of the applied stages. For the three different applied gas flows of 1*slm*, 3*slm* and 5*slm*, the destruction has been 24%, 17%, 10% for 1 stage, 33%, 28% and 21% for 2 stages and 34%, 34% and 26% for 3 stages, respectively.
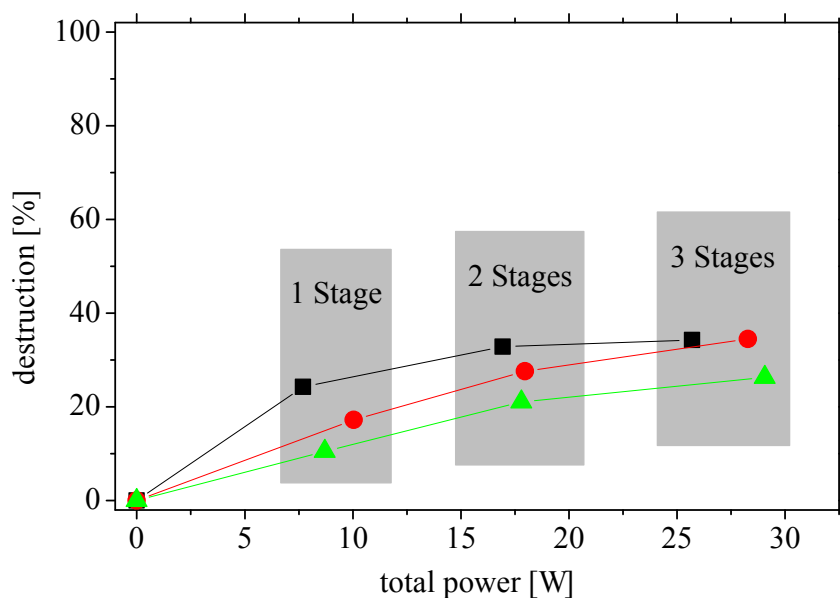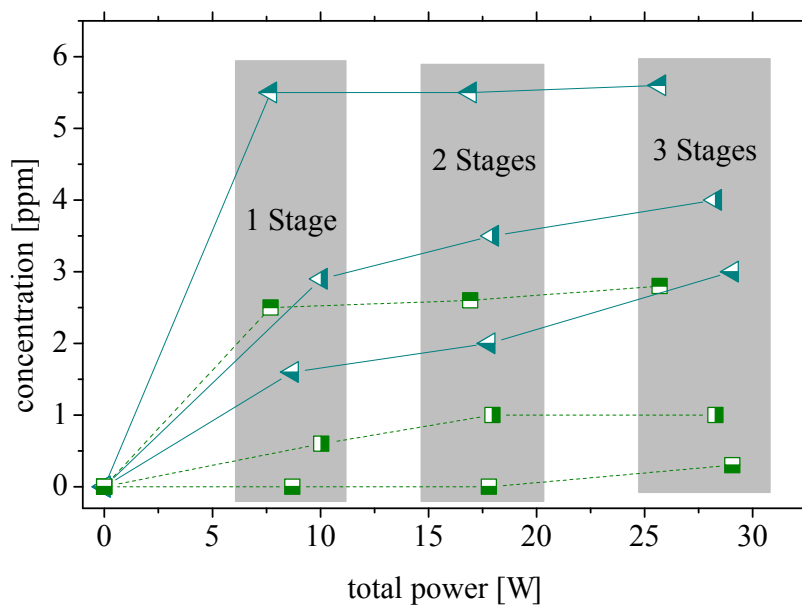
Figure 4.14: Destruction of toluene at an initial concentration of $70 ppm$ in air as a function of the active stages. The applied voltage was $21 kV$. For these experiments, about $5300 ppm$ humidity has been admixed in the gas mixture. The different gas flows have been $1 slm$ (■), $3 slm$ (●) and $5 slm$ (▲).
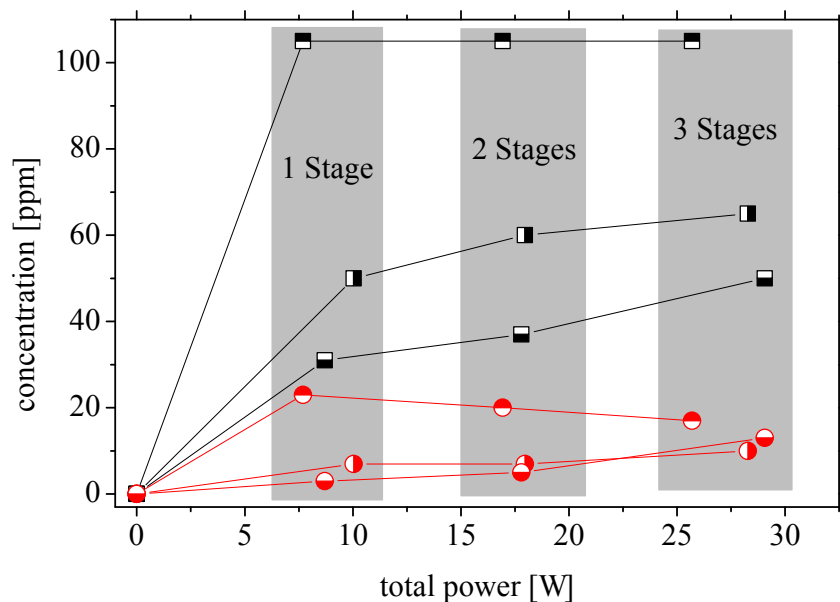
Figure 4.15: Produced O_3 (□) and CO_2 (○) as a function of the active stages. The different gas flows have been $1 slm$ (▤ , ◓), $3 slm$ (◧ , ◑) and $5 slm$ (▤ , ◒).
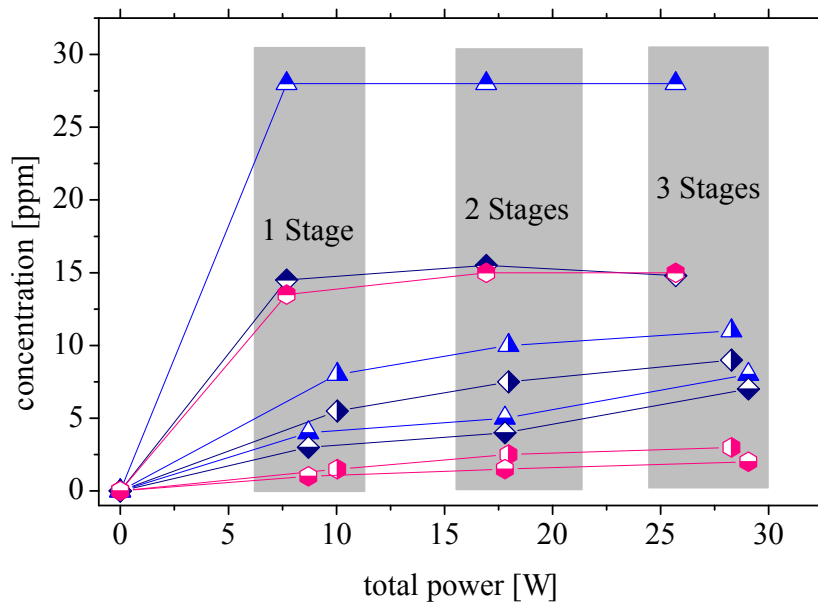
Figure 4.16: Produced CO ($\triangle$), HNO$_3$ ($\diamondsuit$) and FACID ($\ominus$) as a function of the active stages. The different gas flows have been 1 *slm* ($\blacktriangle$, $\blacklozenge$, $\ominus$), 3 *slm* ($\blacktriangle$, $\blacklozenge$, $\mathbb{O}$) and 5 *slm* ($\blacktriangle$, $\blacklozenge$, $\ominus$).


Figure 4.17: Produced N$_2$O ($\triangleleft$) and HCHO ($\cdots\square$) as a function of the active stages. The different gas flows have been 1 *slm* ($\blacktriangleleft$, $\blacksquare$), 3 *slm* ($\blacktriangleleft$, $\blacksquare$) and 5 *slm* ($\blacktriangle$, $\blacksquare$).

### 4.3.4 Destruction for different humidity levels

The influence of the toluene destruction on the initial water concentration is shown in fig. 4.18. In total, four different water concentrations have been tested, $80ppm$, $3500ppm$, $4400ppm$, $5300ppm$ at an applied voltage of $21kV$. The gas mixture has been humidified by the bubble. The water concentration has been adjusted by choosing a sufficient gas stream passing the bubbler. The total gas flow has always been $1slm$. For these four water concentrations, the destruction has been 10%, 20%, 22%, 24% for 1 stage, 18%, 25%, 29%, 33% for 2 stages and 25%, 25%, 32%, 34% for 3 stages, respectively.
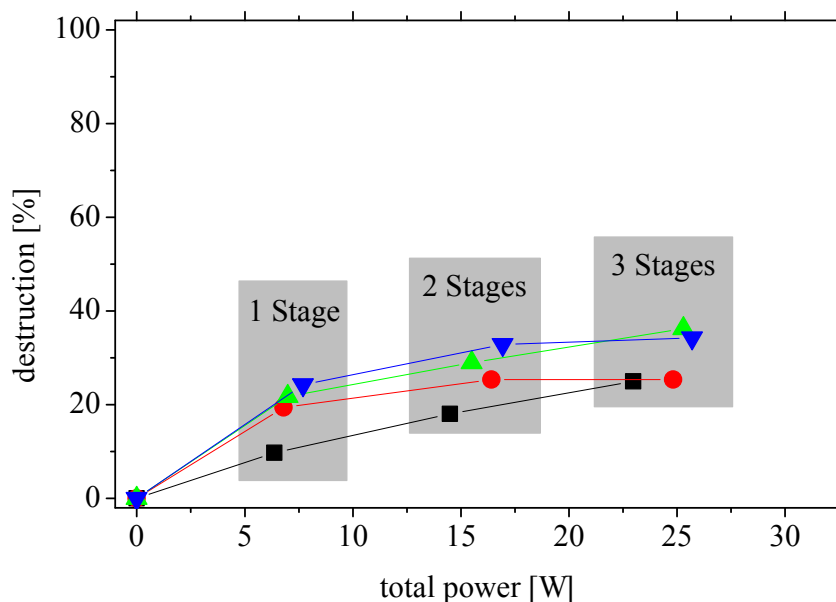

Figure 4.18: Destruction of toluene at an initial concentration of $70ppm$ in air as a function of the active stages. The gas flow has been $1slm$. For these experiments, about $3600ppm$ humidity has been admixed in the gas mixture. The different humidity's have been $80ppm$ (■), $3500ppm$ (●), $4400ppm$ (▲) and $5300ppm$ (▼).
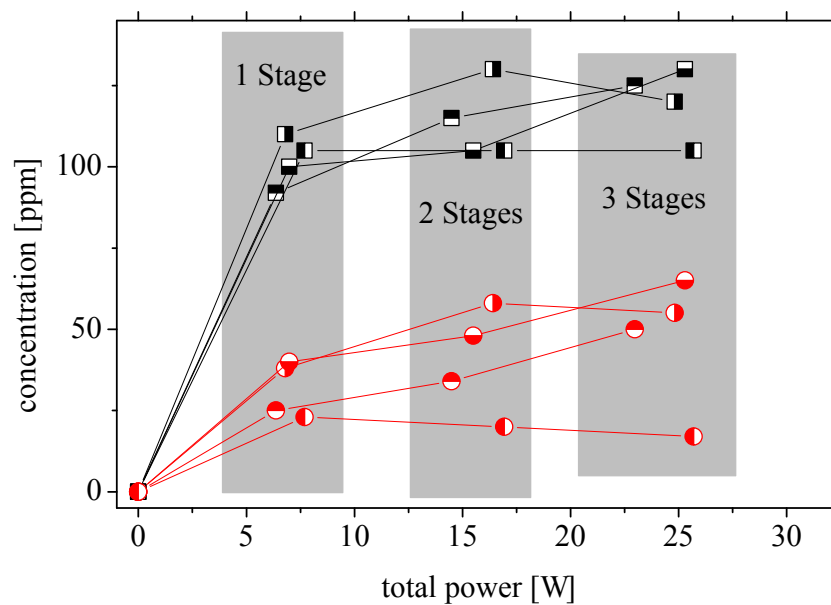
Figure 4.19: Produced O_3 (□) and CO_2 (○) as a function of the active stages. The different humidity's levels have been $80ppm$ (▣ , ◖), $3500ppm$ (◧ , ◑), $4400ppm$ (▤ , ◒) and $5300ppm$ (◪ , ◉).
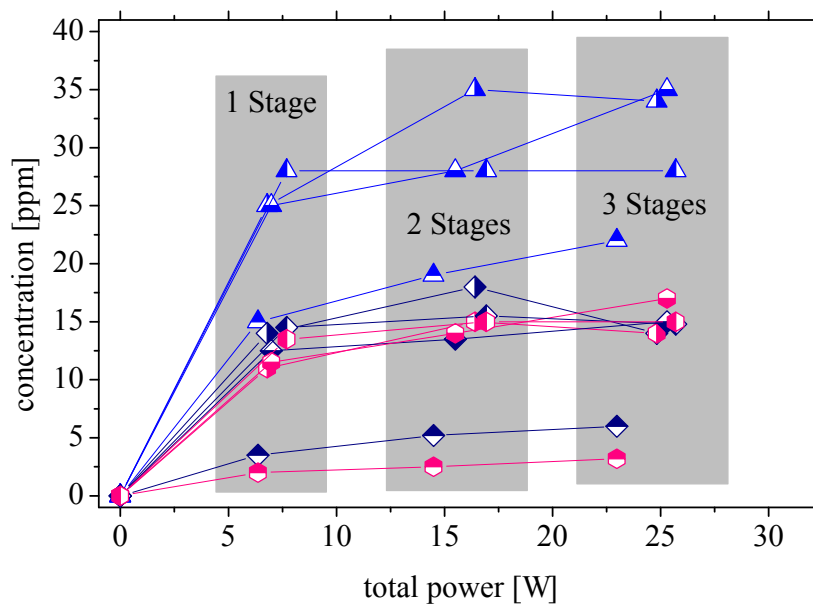
Figure 4.20: Produced CO (△), HNO_3 (◇) and FACID (⬡) as a function of the active stages. The different humidity's levels have been $80ppm$ (▲ , ◆ , ⬡), $3500ppm$ (▲ , ◆ , ◑), $4400ppm$ (◭ , ◆ , ⬡) and $5300ppm$ (◪ , ◆ , ◉).
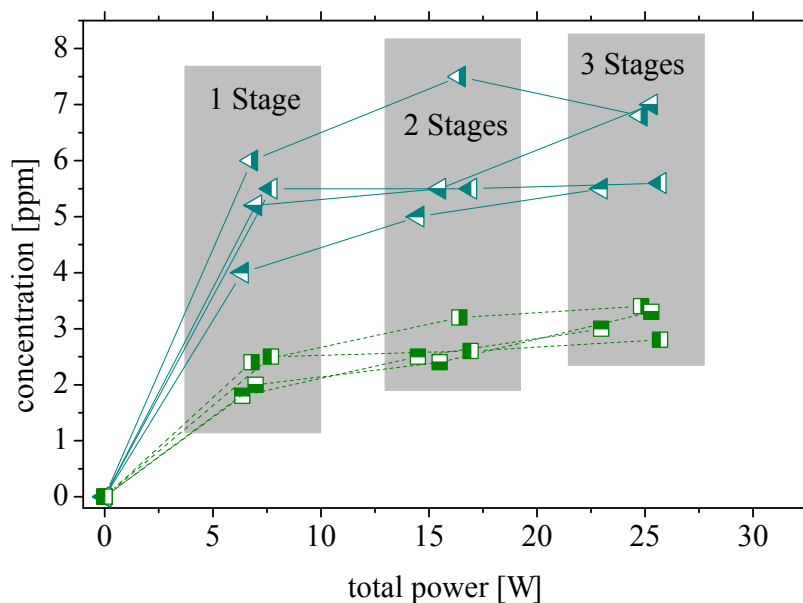
Figure 4.21: Produced N_2O ($\triangleleft$) and HCHO ($\cdots\square\cdots$) as a function of the active stages. The different humidity's levels have been $80ppm$ ($\blacktriangleleft$, $\blacksquare$), $3500ppm$ ($\blacktriangleleft$, $\blacksquare$), $4400ppm$ ($\blacktriangleleft$, $\blacksquare$) and $5300ppm$ ($\blacktriangleleft$, $\blacksquare$).

4.3.5   Discussion Toluene destruction

The experiments show, that the destruction of toluene increases as the applied voltage is increased independently on all other experimental parameters. The strongest destruction is achieved under dry air conditions, $85ppm$ humidity. A destruction of about 58% has been found for $22kV$ applied voltage and three stages in use, chapter 4.3.1. A comparable value, 56% destruction, has been measured for $3500ppm$ admixed humidity, under the same conditions, chapter 4.3.2. The destruction depending on the water concentration has been studied further. The destruction at four humidity levels measured with $21kV$ applied voltage is given in chapter 4.3.4. For example, using three stages with $21kV$ applied voltage; the destruction has been found to be 25% for $85ppm$ humidity and reaches 34% for $5300ppm$ humidity. The water dependency suggests that, during the discharge, water is dissociated into an OH radical and H atom by electron impact. The hydroxyl radical may react later in the downstream with toluene which leads to additional toluene destruction. The dependency of the destruction on the gas flow has been studied too. The variation of the gas flow leads to a decreased destruction as the flow increases, see chapter 4.3.3. For example, the destruction for three active stages decreases from 34% at $1slm$ to 26% at $5slm$ both for $21kV$ applied voltage, about $27W$ consumed power. This dependency can be explained by the fact that the residence time of the gas is reduced for higher gas velocities and so the time the gas is treated by the plasma too. The mean speed of the gas inside the stages is about $7cm\,min^{-1}$, $20cm\,min^{-1}$ and $35cm\,min^{-1}$ for $1slm$, $3slm$ and $5slm$, respectively. Therefore, the corresponding residence time of the gas within one stage is $15s$, $5.2s$ and $3.1s$ for $1slm$, $3slm$ and $5slm$, respectively. The described experiments are compared with those shown in

Ref. [1]. In tab. 4.3.5, the results from Ref. [1] and from this work are given. For a generalised comparability of different types of discharges, the destruction efficiency usually is expressed by the β-value

$$\beta = \frac{-E}{\ln{(X/X_0)}} \tag{4.1}$$

where E is the density of the deposited energy, specific energy (input electrical energy / gas flow rate; JL^{-1}), X_0 is the initial toluene concentration and X is the toluene concentration after the reactions.

Table 4.1: The results shown here have been done earlier and are published in [1]. The table lists the reported results and the results obtained in this work.

| Number of stages	Stages	Results from [1]			This Work		
		total power [W]	toluene destruction [%]	β [JL^{-1}]	total power [W]	toluene destruction [%]	β [JL^{-1}]
1	A	13	0.1	8×10^5	7	29	357
2	A+B	23	5	27080	18	48	1476
3	A+B+C	48	72	2000	27	58	3026
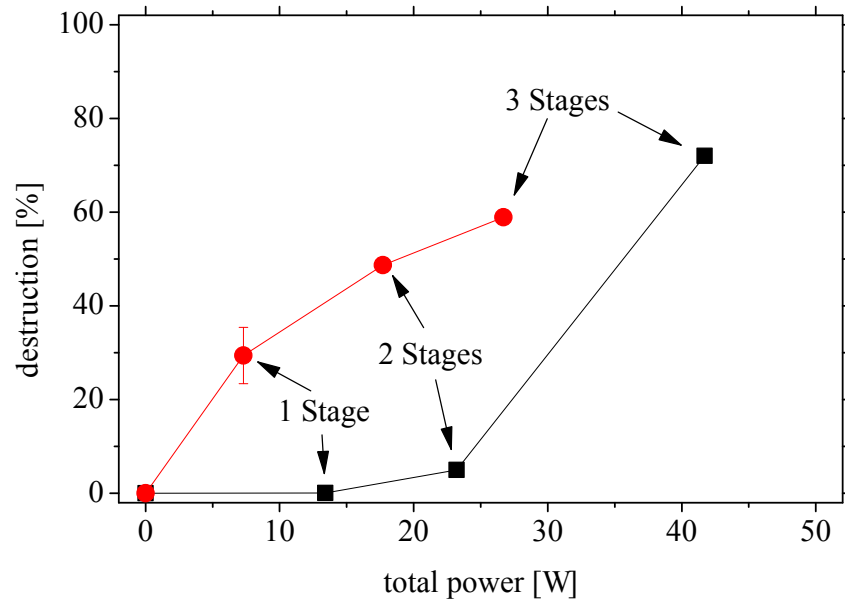
Figure 4.22: Comparison of the destruction of toluene for experiments reported in [1] (■) and for those obtained in this work (●).

Fig. 4.22 shows strong discrepancies between the destruction of toluene reported in Ref. [1] and those measured in this work. The results were taken for dry air, fig. 4.7 at $22kV$ applied voltage. The differences are not only found in the absolute values but also the general behaviour is

different. As one can see, the destruction reported in [1] shows a progressive behaviour, whereas the destruction measured in this work shows a degressive one. The total power consumed by both experiments is of the same order, e.g. $23W$ [1] and $18W$, this work, both for 2 active stages. However, the consumed power is tendencially higher for the experiments described in Ref. [1] compared with those obtained in this work. The power in Ref. [1] has been measured including the power supply. That means load depending, varying efficiency of the power supplies are influencing the power measurement. However, the reason for the discrepancies might be not dominated by the power measurement / coupling. When the first experiments have been made, it has been found that the valve at the output has been filled with a white wax over the time, roughly $1mm^3\,3h^{-1}$ at $1\,slm$ and $70ppm$ initial toluene concentration. These depositions narrowed the tube diameter. As a consequence with the setup used here, the flow and therefore the residence time has been reduced. This leads to improved toluene destruction, see chapter 4.3.3. Since this has been discovered, the flow has been controlled manually. Instead of using a mass flow controller at the output, the bulbs in the bubbler have been counted. With this information, the output valve has been controlled ensuring a constant number of bulbs per unit time. The discrepancy shown in fig. 4.22 might be explained by the fact that the output valve used in Ref. [1] has been narrowed in the same way. Consequently, the residence time of the gas in the stages decreased and the toluene destruction might be stronger at lower gas speed. The influence of the toluene concentration shows no influence to the power consumption of the entire system. The specific energy as a function of the number of stages can be seen in fig. 4.23. The power consumption shows a linear behaviour for all three applied voltages for an initial toluene concentration of $70ppm$ admixed to synthetic air with $3500ppm$ humidity. Therefore, the linearity of the power consumption shows equality of the stages and indicates that the admixture of trace gas in the *ppm* range does not influence the power consumption at all. The diagrams, specific energy as a function of the number of stages, for the other parameter variation, see also chapter 4.3.1 or chapter 4.3.4, etc are given in appendix A.
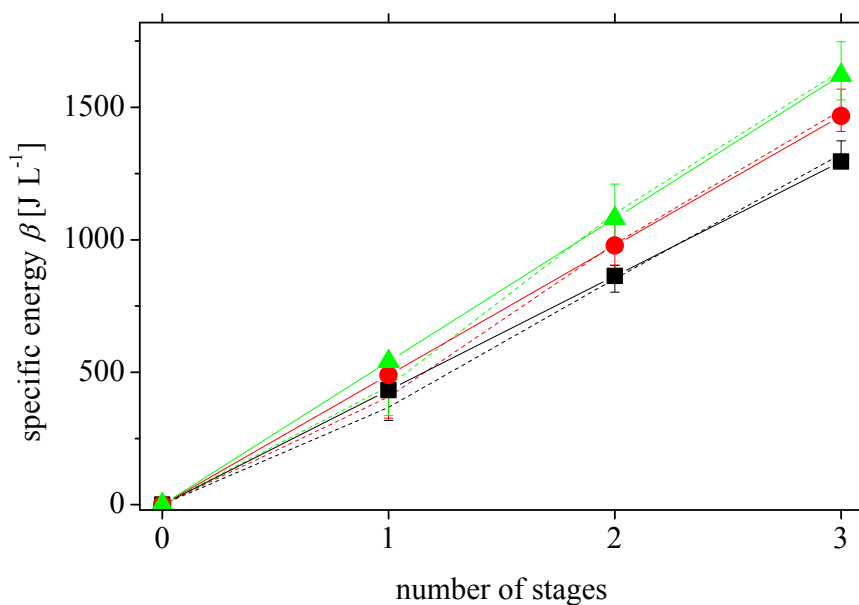
Figure 4.23: Specific energy as a function of the active stages for UPP = $20kV$ (■), $21kV$ (●) and $22kV$ (▲) applied sinusoidal voltage. The initial gas mixture has been $70ppm$ Toluene, $3500ppm$ humidity in synthetic air at atmospheric pressure.

In general, the destruction of toluene in a multi stage packed-bed reactor shows no synergistic effect.

4.4   Destruction of Ethylene

### 4.4.1   Destruction in humidified air

The study of the destruction of ethylene has been done using stages which are conceptually the same as they have been used for the toluene destruction, see chapter 4.3. However, in order to couple sufficient power, the distance of the electrodes has been d = $4mm$, fig. 4.3. Therefore, only one layer of glass beads has been used as a packing material. The used power supply, Chroma 61604 connected to a high voltage transformer, supplied a sinusoidal voltage of $1kHz$. For the destruction experiments, several voltages have been tested, i.e. U_{PP} = $9kV$, $10kV$, $11kV$ and $12kV$ each for 1, 2 or 3 active stages. The initial ethylene concentration has been $1000ppm$ admixed to a gas flow of $1slm$ synthetic air. About $0.1slm$ of the synthetic air have been guided through a water bubbler leading to about $1200ppm$ humidity admixed to the gas stream. The resulting destruction of ethylene is given in fig. 4.24. No ethylene destruction below $9kV$ has been detected. On the other hand, voltages greater than $12kV$ lead to an arcing. The curves in fig. 4.24 consist of four points. The zeroth point, zero destruction at zero power, is used to guide the eye. The other points correspond to the number of active stages as explained for U_{PP} = $9kV$ in fig. 4.24.
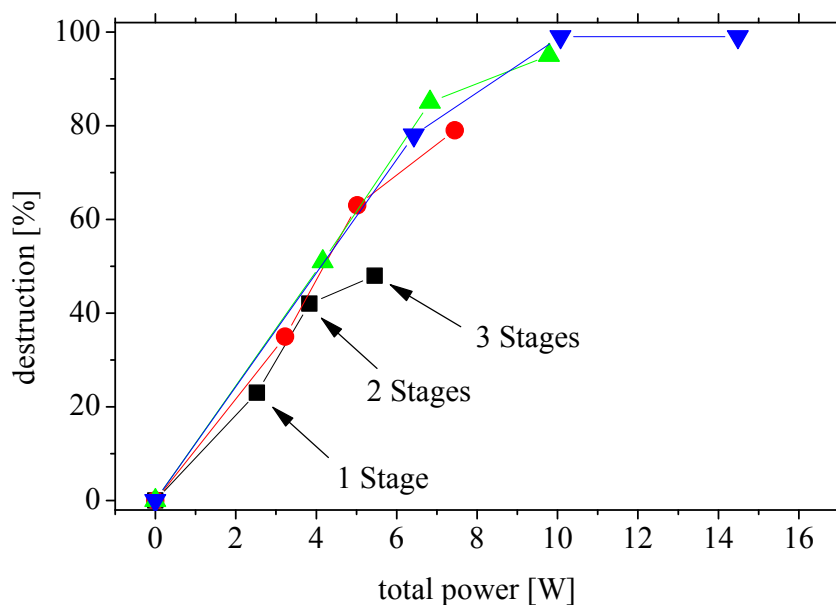
Figure 4.24: Destruction of Ethylene as a function of the total power. The initial gas mixture has been: $1000 ppm$ C_2H_4, $1200 ppm$ H_2O in synthetic air. The applied sinusoidal voltage has been: $9kV$ (■), $10kV$ (●), $11kV$ (▲) and $12kV$ (▼), respectively. As exemplarily shown for $9kV$, the single symbols of each curve, from left to right, correspond to the number of stages in use.
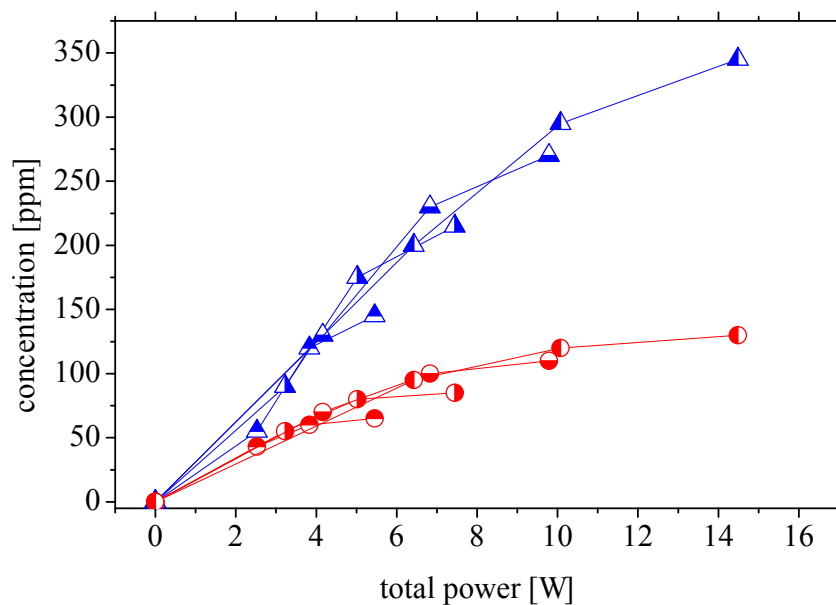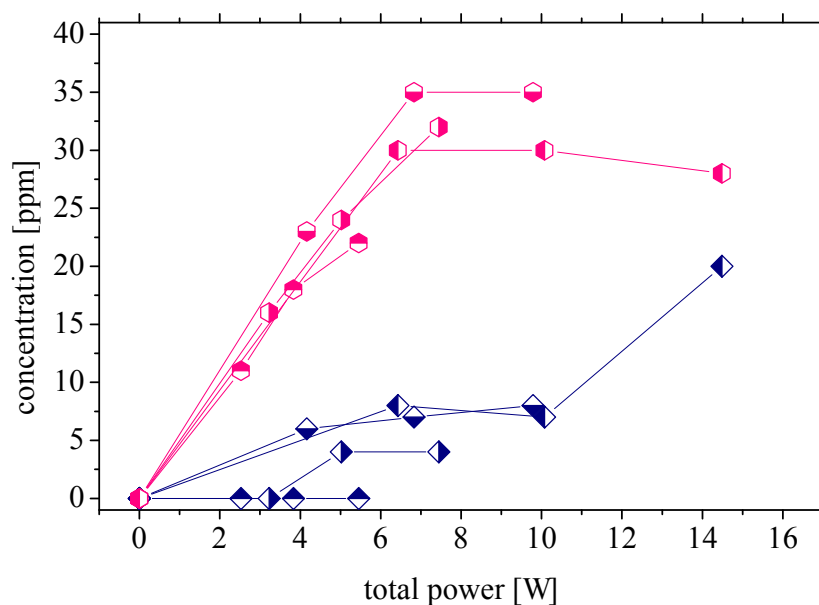

Figure 4.25: Produced CO_2 (△) and CO (○) as a function of the active stages. The applied voltage has been: $9kV$ (▲ , ◕), $10kV$ (▲ , ◑), $11kV$ (▲ , ◒) and $12kV$ (▲ , ◐). The single symbols of each curve correspond to the number of stages in use, see fig. 4.24.
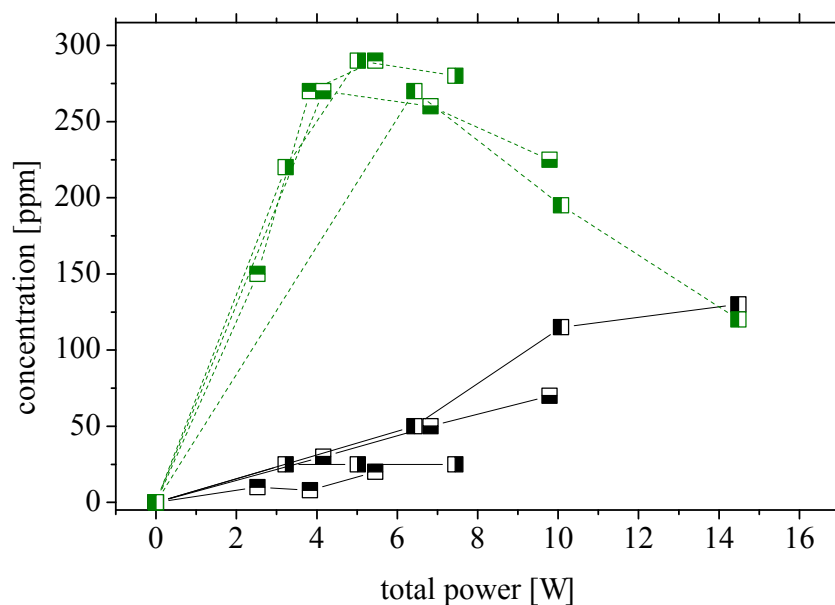
Figure 4.26: Produced O_3 ($\square$) and HCHO ($\cdots\square\cdots$) as a function of the active stages. The applied voltage has been: $9kV$ ($\blacksquare$, $\cdots\blacksquare\cdots$), $10kV$ ($\blacksquare$, $\cdots\blacksquare\cdots$), $11kV$ ($\blacksquare$, $\cdots\blacksquare\cdots$) and $12kV$ ($\blacksquare$, $\cdots\blacksquare\cdots$). The single symbols of each curve correspond to the number of stages in use, see fig. 4.24.
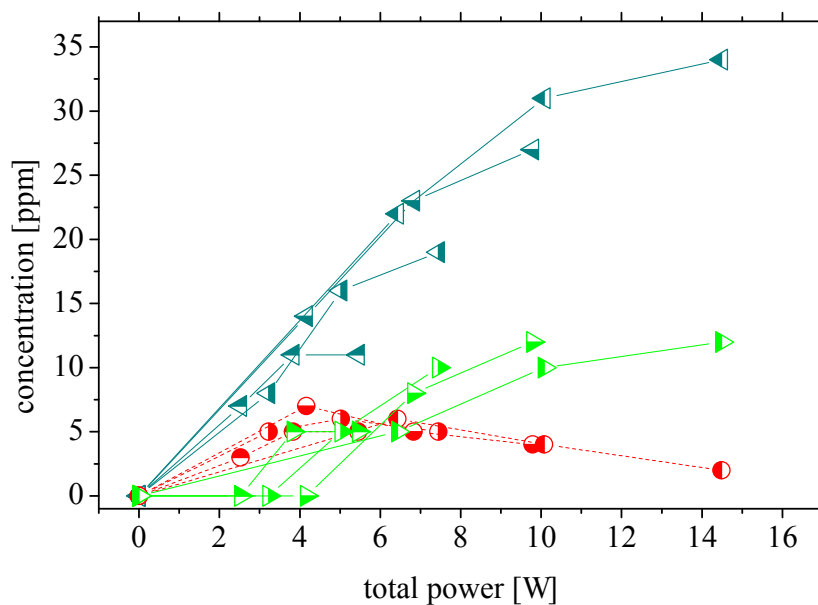
Figure 4.27: Produced N_2O ($\triangleleft$), NO_2 ($\cdots\bigcirc\cdots$) and HCN ($\triangleright$) as a function of the active stages. The applied voltage has been: $9kV$ ($\blacktriangleleft$, $\cdots\ominus\cdots$, $\blacktriangleright$), $10kV$ ($\blacktriangleleft$, $\cdots\bullet\cdots$, $\blacktriangleright$), $11kV$ ($\blacktriangleleft$, $\cdots\ominus\cdots$, $\blacktriangleright$) and $12kV$ ($\blacktriangleleft$, $\cdots\bullet\cdots$, $\blacktriangleright$). The single symbols of each curve correspond to the number of stages in use, see fig. 4.24.

Figure 4.28: Produced FACID ($\bigcirc$) and HNO$_3$ ($\diamondsuit$) as a function of the active stages. The applied voltage has been: $9kV$ ($\ominus$, $\blacklozenge$), $10kV$ ($\oplus$, $\blacklozenge$), $11kV$ ($\ominus$, $\diamondsuit$) and $12kV$ ($\oplus$, $\blacklozenge$). The single symbols of each curve correspond to the number of stages in use, see fig. 4.24.

4.4.2   Discussion Ethylene destruction

The experiments about the ethylene destruction have been done at a gas flow of $1slm$ using $1000ppm$ ethylene, $1200ppm$ water admixed to synthetic air. The distance of the electrodes has been $4mm$. Therefore, the gas flow of $1slm$ leads to a residence time of $3.5s$ of the gas inside the stages. As one can see from fig. 4.24, the ethylene destruction depends nearly linear on the total power independently on the number of active stages. For higher destructions, the dependency of the destruction on the power deviates from a linear function. The reason might be the reduced destruction efficiency at lower concentrations. Such a discharge device can be characterised by the β-value. Tab. 4.4.2 gives these values for the different applied voltages. The influence of

Table 4.2: For comparison of different destruction devises, the table gives the β-values for the different applied voltages. For one voltage, the β-value is averaged of the beta value for a 1, 2 and 3 stage experiment.

Voltage UPP $[JV]$	Beta $[JL^{-1}]$
9	500
10	346
11	254
12	191

the concentration of ethylene to the power consumption has been investigated too. The specific

energy as a function of the active stages is given in fig. 4.29. As one can see, there is a linear dependency. This is even the case when the concentration has been reduced. For example, it is the case for three stages with $12kV$ applied voltage. Compare also fig. 4.24. Such behaviour indicates that the concentration does not change the power consumption. Additionally, from fig. 4.29, it can be seen that the stages are equal corresponding to the amount of power for a certain applied voltage.
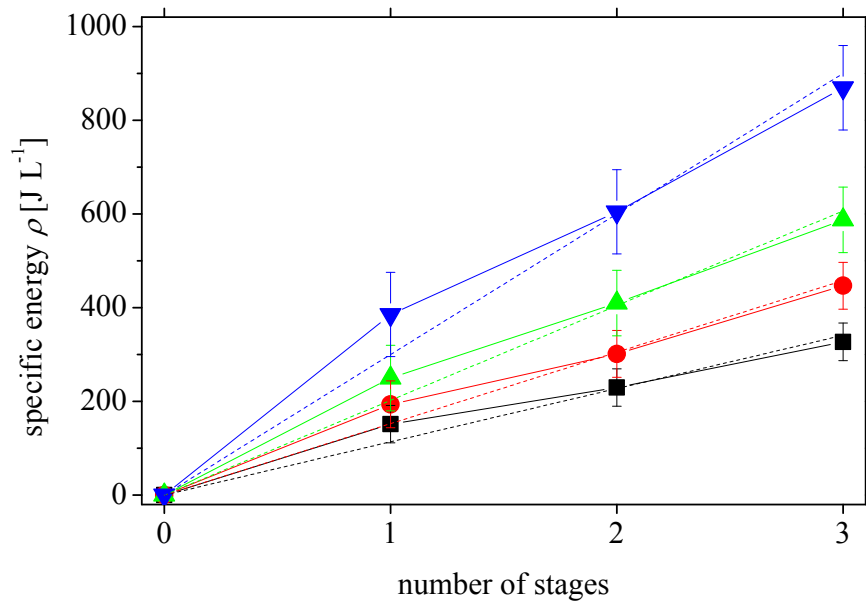
Figure 4.29: Specific energy as a function of the active stages for $U_{PP} = 9kV$ (■), $10kV$ (●), $11kV$ (▲) and $12kV$ (▼) applied sinusoidal voltage. The initial gas mixture has been $1000ppm$ ethylene, $3500ppm$ humidity in synthetic air at atmospheric pressure.

4.5 Discussion of the by product formation

For all experiments, not only the destruction of toluene and ethylene has been investigated but also the formation of by-products. The following table lists the species and the detection limit of the used FTIR system. For the destruction of toluene, the following by-products have been identified, CO_2, CO, O_3, CH_2O, N_2O, FACID and HNO_3. In the experiments, no NO, NO_2, HCN have been detected. For the destruction of ethylene, the following main by-products have been identified CO_2, CO, O_3, CH_2O, N_2O, NO_2, HCN, FACID and HNO_3. In the experiments, no NO has been detected. A indication of the experiments is the carbon balance which is defined as the ratio of the amout of input carbon devided by the amout of output carbon times 100%. That is

$$C_{Balance} = \frac{\sum [C]_{out}}{[C]_{in}} \cdot 100\% \tag{4.2}$$

The carbon balance of the experiments for the toluene destruction in dry air, chapter 4.3.1, is given in fig. 4.30. Within the error bars, the amount of carbon start to be not balanced for the

Table 4.3: By-products identified in the destruction experiments for both toluene and ethylene. The species and the detection limit are listed.

Name	Sum formula	Detection limit [ppm]]
carbon dioxide	CO_2	2
carbon monoxide	CO	3
ozone	O_3	10
nitric oxide	NO	30
nitrogen dioxide	NO_2	2
nitrous oxide	N_2O	3
nitric acid	HNO_3	0.5
hydrogen cyanide	HCN	1
formaldehyde	CH_2O	0.1
formic acid	FACID, CH_2O_2	0.5

$22kV$ applied voltage. The carbon balances for the other experiments are given in appendix A.
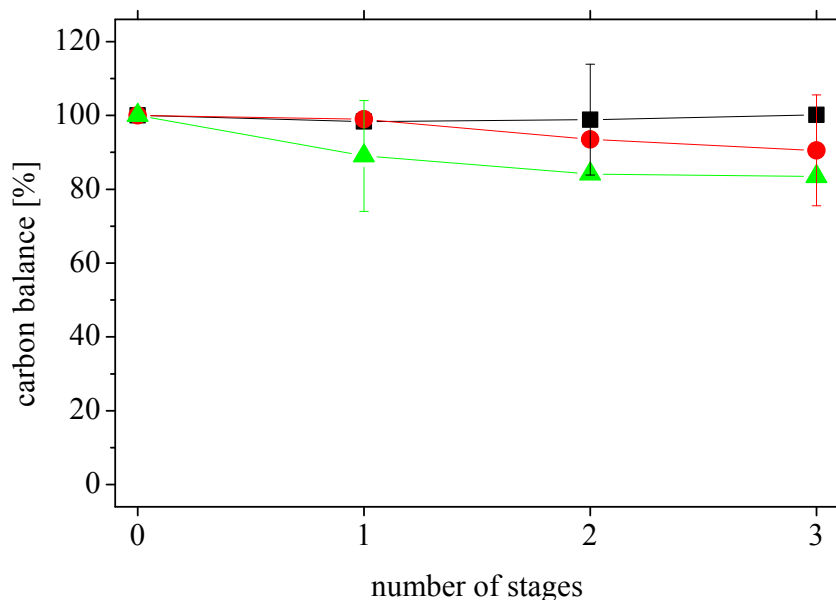
Figure 4.30: Carbon balance of the experiments for toluene destruction in dry air, see chapter 4.3.1. The balance is the ratio of the input carbon divided by the output carbon times 100%. The gas flow has been 1slm. For these experiments, about 85ppm humidity has been left in the gas mixture. The applied voltage has been 20kV (■), 21kV (●) and 22kV (▲).

The difference may be explained by several reaction channels. First, the deposition of the white wax could lead to the carbon discrepancy. Second, species may be created which are not detected by the FTIR system. Either, they are not IR active or they are below the detection

limit. Third, a deposition of a carbon film on the electrode may cause an unbalanced carbon concentration. However, such a deposition has never been observed. Fourth, chemical reaction at the walls may happen.

4.6 Characterisation of the discharge, phenomenological approach

4.6.1 Power consumption at pre discharge voltages

The power measurement has been shown, that some parts of the power are consumed without plasma ignition. Fig. 4.31 and fig. 4.32 show the electrical power as a function of the effective value of the applied sinusoidal voltage. As one can see, there is some power consumed before plasma ignition. A similar effect has been shown in [6] for a frequency of the applied voltage of $50Hz$. This power consumption may have two reasons. First, the power is caused by heat losses during polarisation of the dielectric material, Ppolarisation. Second, since there are blank electrodes, the power may be caused be a current flowing above the surface, Psurface. The current probably flows through a water film. Consequently, the total power Ptot consumed at pre discharge voltages can be expressed by

$$P_{tot} = P_{polarisation} + P_{surface} \tag{4.3}$$

Losses caused by polarisation effects may estimated in the following way [7, 8]. The energy stored in a capacitance is given by $W = \frac{1}{2} \cdot C \cdot U^2$, where C is the capacity of the capacitance and U is the effective value of the applied sinusoidal voltage, $U = \sqrt{\frac{1}{2} \int_0^T u(t)^2 \, dt}$, where T is the period time and $u(t)$ is the time dependent voltage. The capacity is given by $C = \varepsilon_0 \cdot \varepsilon_r \cdot \frac{F}{d}$ with the dielectric constant $\varepsilon_0 = 8.854 \cdot 10^{-14} \frac{As}{Vcm}$, $\varepsilon_r = 3$ for glass, F the area of the electrodes and d is the distance between them. Assuming that all energy stored due to polarisation is loss in the stage, ohmic heating of the dielectric material, the power is given by

$$P_{polarisation} = \frac{W}{T} = W \cdot f = \frac{1}{2} \cdot \varepsilon_0 \cdot \varepsilon_r \cdot \frac{F}{d} \cdot f \cdot C_{filling} \cdot U^2 = X_{polarisation} \cdot U^2 \tag{4.4}$$

where f is the frequency, $X_{polarisation}$ is the conductivity and $C_{filling}$ is a correction factor which takes into account that the space between the electrodes is not completely filled with the dielectric material. Since regular beads are used here, $C_{filling}$ is set to be 0.74 adopted from the 74% filling calculated for a hexagonal closed-packed arrangement known from crystallography. Power losses caused by a current flowing over the surface, $P_{surface}$, can be expressed by

$$P_{surface} = \frac{1}{R} U^2 = X_{surface} \cdot U^2 \tag{4.5}$$
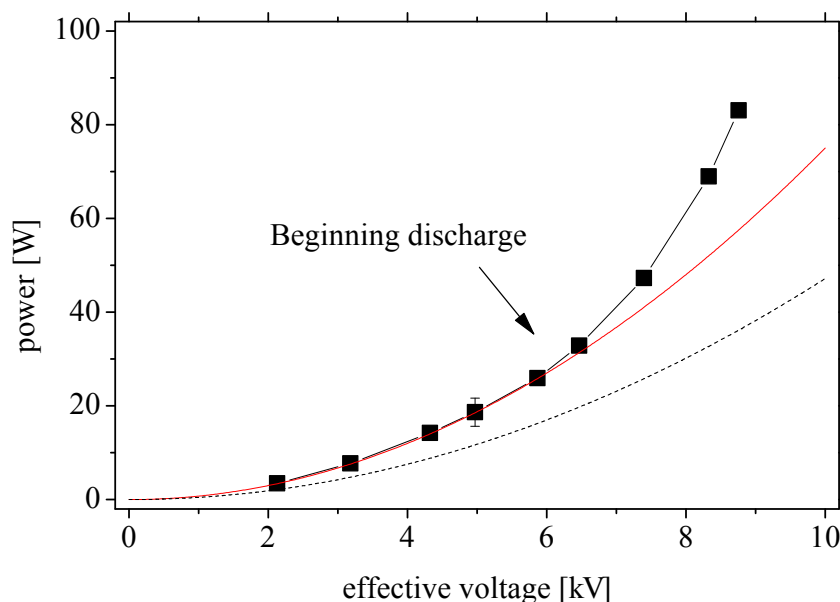
Figure 4.31: Consumed power before plasma ignition takes place. The dimension of the stage were, see fig. 4.3, d = 1.8*cm* and b = 12*cm* at a frequency of 60*kHz*. The measured power (■) has been fitted (solid). The dashed line gives the power assumed to be loss due to polarisation effects, eqn. 4.4.
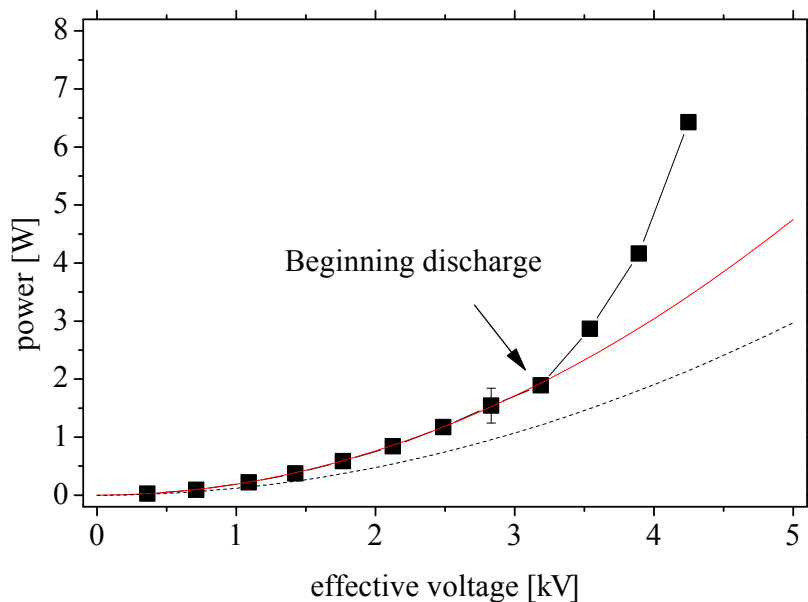
Figure 4.32: Consumed power before plasma ignition takes place. The dimension of the stage were, see fig. 4.3, d = 0.4*cm* and b = 11*cm* at a frequency of 4*kHz*. The measured power (■) has been fitted (solid). The dashed line gives the power assumed to be loss due to polarisation effects, eqn. 4.4.

where R is the resistor which can be assign to the surface and $X_{surface}$ is the conductivity of the surface. From the Rsurface in table 4.4, the specific surface resistance can be calculated. For

Table 4.4: Conductivities deduced from the measurement, fig. 4.31 and fig. 4.32 and estimated from eqn. 4.4. These values have been used to estimate the lower resistivity of the surface of the packing material.

|	Stage	
	d = 1.8 cm, fig. 4.31	d = 0.4 cm, fig. 4.32
X_{tot}, solid line in fig. 4.31 and fig. 4.32 $X_{polarisation}$, dashed line in fig. 4.31 and fig. 4.32	$471 \cdot 10^{-9} A/V$	$118 \cdot 10^{-9} A/V$
$X_{surface} = X_{tot} - X_{polarisation}$	$279 \cdot 10^{-9} A/V$	$72 \cdot 10^{-9} A/V$
$R_{surface} = 1/X_{surface}$	$4 M\Omega$	$14 M\Omega$

the stage with d = 0.4cm, the specific surface resistance is about $35 M\Omega cm^{-1}$ and for the stage with d = 1.8cm the specific surface resistance is about $2 M\Omega cm^{-1}$. It should be noted that these two resistivity are a lower limit, since the influence of dielectric losses are not clear yet. The differences of the two resistivity for both stages, may be caused by a different humidity or can be caused by a different packing density of the dielectric material especially for the stage with d = 0.4cm.

4.6.2 Spatial appearance of the discharge

In this chapter, the spatial appearance of the discharge between the packing material and in the volume close to the electrodes has been studied by taking photographs. A special holder, fig. 4.33, has been designed in order to hold one or two glass beads. This arrangement replicates the condition in a packed-bed stage as it has been used in this study. In fig. 4.33, the experimental condition is shown. Two stainless steel rods serve as the electrodes. The experiments were done for 1kHz applied sinusoidal voltage with $U_{PP} = 12kV$ for the single bead and $U_{PP} = 18kHz$ for the double bead configuration. The pictures were taken with a standard photo camera (DMC-LZ2, Panasonic). Pictures with a 8s exposure time were taken. The spatial appearance of the plasma around a single bead can be seen in fig. 4.35. The discharge appearance around a double bead configuration can be seen in fig. 4.37. The view direction of the camera for both experiments is given in fig. 4.34 for the single bead and in fig. 4.36 for the double bead arrangement.
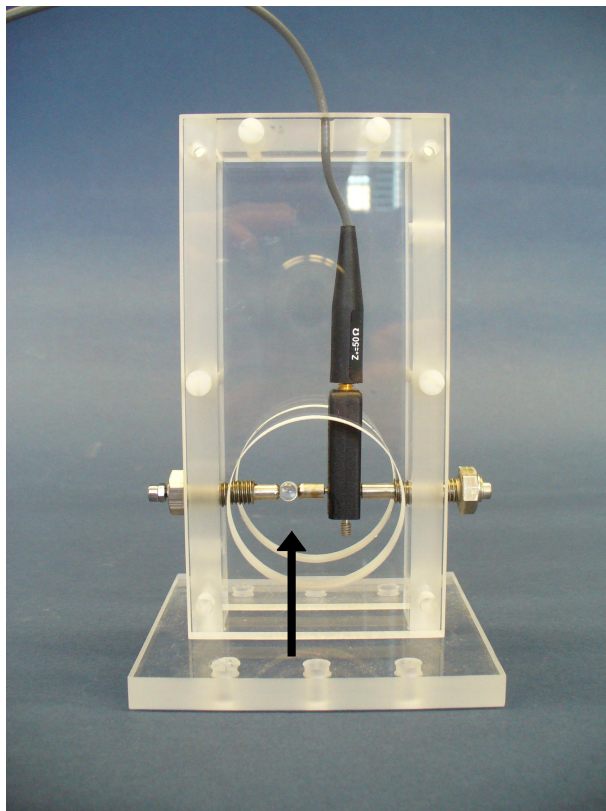
Figure 4.33: Holder for the investigation of the spatial appearance of the active plasma volume. The picture shows one glass bead hold between the electrodes. The current was measured using a current monitor (Tektronix, CT 1, rise time: $350ps$) mounted in the ground path. The arrow indicates the view direction. The pictures in the following have been taken with a $8s$ exposure time of the camera. The frequency of the applied sinousadial voltage has been $1kHz$ with $U_{PP} = 12kV$, single bead, and $U_{PP} = 18kV$, double bead.
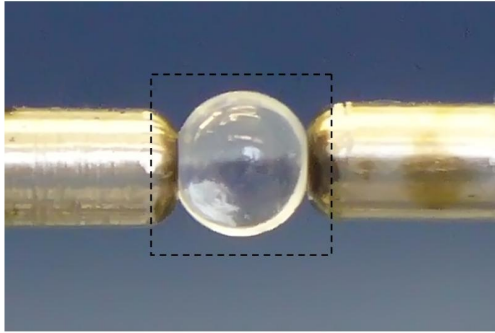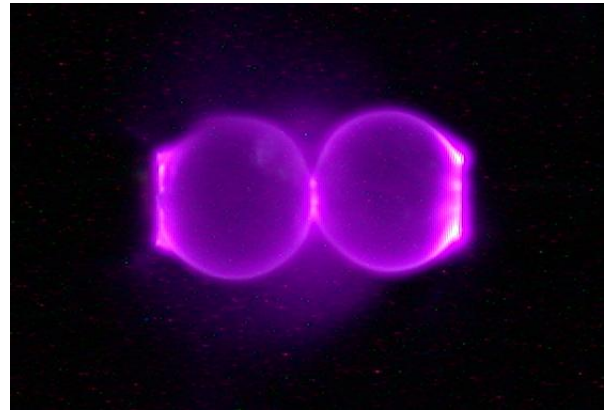
Figure 4.34: Two semi spherical electrodes holding one glass bead. The diameter of the bead is 6*mm*. The rectangle indicates the position fig. 4.40 has been taken.
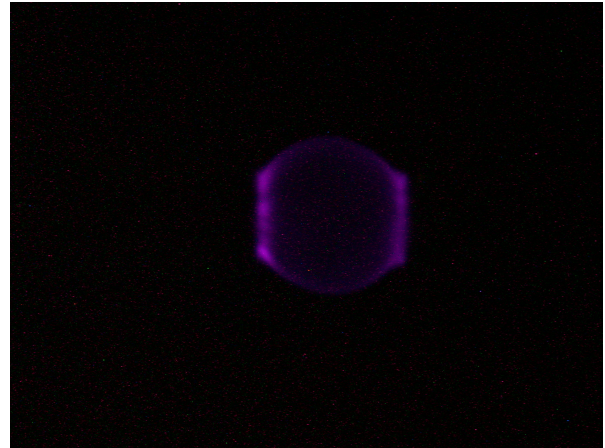
Figure 4.35: Corresponding plasma appearance for $12kV_{PP}$ applied voltage at 1 kHz. The gate of the camera has been 8*s*.
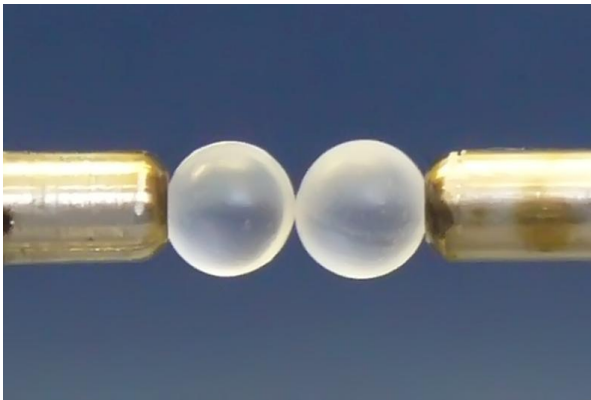

Figure 4.36: Two glass beads are fixed in the single glass beads holder.


Figure 4.37: Discharge appearance around two glass beads taken with a 8*s* exposure time. Visible is a relatively big glow between the two glass beads.

From fig. 4.35, the single bead picture, one can see that the brightest light emission comes from an area around the electrodes. The active volume is then spread over the bead surface. A similar appearance can be seen from fig. 4.37, the double beads configuration. Close to the electrodes, the active volume creates a ring around the electrodes and the glass beads and is again spread out over the surface of the glass beads. Additionally, a corona like plasma can be seen in the volume between the two beads. For the single bead arrangement, a typical voltage current behaviour can bee seen in fig. 4.38. In the positive and negative half wave, short current pulses can be seen representing the filamented structure of the plasma. As one can see, two

groups of current peaks, and therefore of micro discharges, can be distinguished. They differ in the amplitude. Small current peaks, marked with arrows in fig. 4.38, and bigger current peaks. For those, amplitudes up to 50*A* in the pulse are possible. Fig. 4.39 shows a zoom into one single current peak. As one can see, these small current peaks are followed by the bigger one. Fig. 4.40 shows a picture taken with an ICCD camera (Dicam-Pro 25-SVGA grey) with the gate specified in fig. 4.38. The figure shows that the small current peaks appear to belong to the plasma channels marked by arrows in fig. 4.40. On the other hand, the bigger current peaks correspond to the discharge channels going over the glass bead, as can be seen in fig. 4.40.
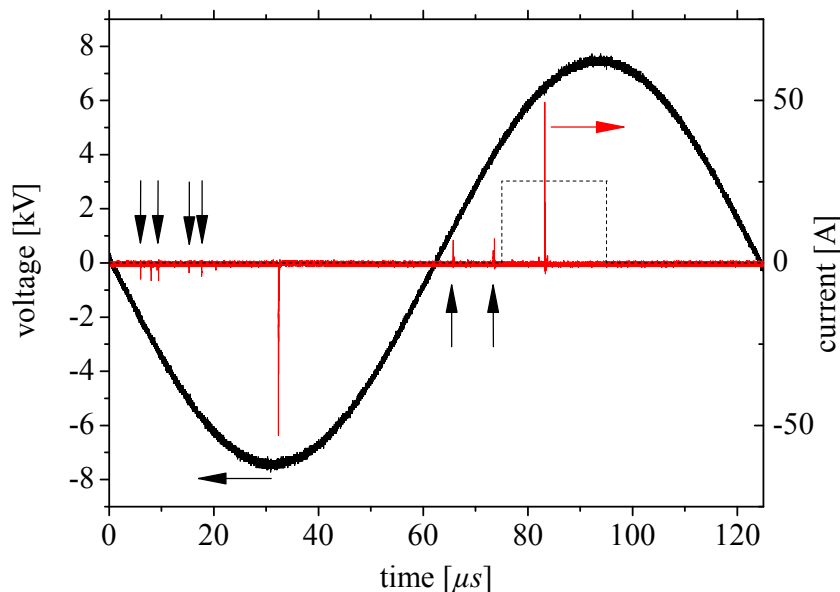
Figure 4.38: Example of a voltage current behaviour applied to the single beads holder. Single micro discharges are indicated by short current pulses. The dashed TTL signal shows the cameras gate the fig. 4.40 has been taken.
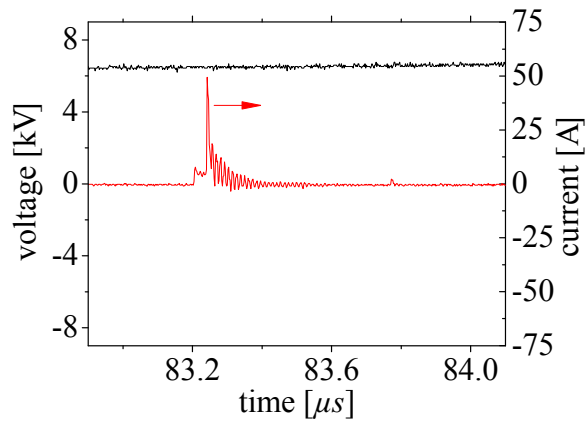
Figure 4.39: Zoomed view into the current pulses. The bigger current peak follows a small one after about 30 ns.
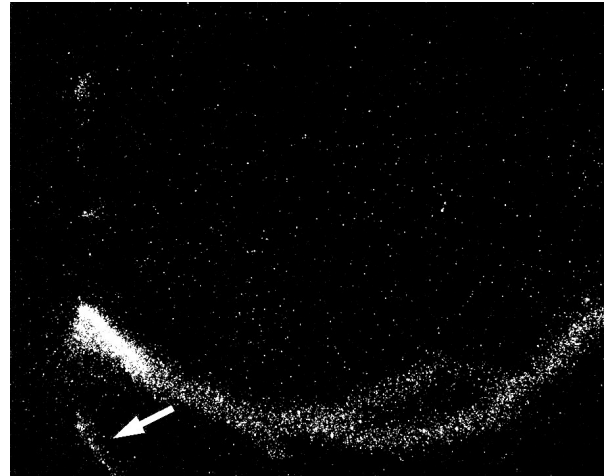
Figure 4.40: ICCD image of the micro discharge above the single bead surface. The picture belongs to the current behaviour given in fig. 4.39. The arrow marks a micro discharge belonging to a small current peak. For clarity, the gray scale has been modified.

Bibliography

[1] A. M. Harling, D. J. Glover, J. C. Whitehead, and K. Zhang. Novel method for enhancing the destruction of environmental pollutants by the combination of multiple plasma discharges. *Environmental Science & Technology*, **42**:4546, (2008).

[2] R. McAdams. Pulsed corona treatment of gases: system scaling and efficiency. *Plasma Sources Science & Technology*, **16**:703, (2007).

[3] T. Sreethawong, P. Thakonpatthanakun, and S. Chavadej. Partial oxidation of methane with air for synthesis gas production in a multistage gliding arc discharge system. *International Journal of Hydrogen Energy*, **32**:1067, (2007).

[4] R. G. Tonkyn, S. E. Barlow, and J. W. Hoard. Reduction of NO_x in synthetic diesel exhaust via two-step plasma-catalysis treatment. *Applied Catalysis B-Environmental*, **40**:207, (2003).

[5] S. W. Sharpe, T. J. Johnson, R. L. Sams, P. M. Chu, G. C. Rhoderick, and P. A. Johnson. Gas-phase databases for quantitative infrared spectroscopy. *Applied Spectroscopy*, **58**:1452, (2004).

[6] A. Ogata, N. Shintani, K. Mizuno, S. Kushiyama, and T. Yamamoto. Decomposition of benzene using a nonthermal plasma reactor packed with ferroelectric pellets. *IEEE Transactions on Industry Applications*, **35**:753, (1999).

[7] G. Hagmann. *Grundlagen der Elektrotechnik*. AULA-Verlag, (2000).

[8] W. Nolting. *Elektrodynamik*. Grundkurs Theoretische Physik. Spinger, (2002).

Chapter 5

Formation / destruction kinetics of N_xO_y in a low pressure tube reactor

5.1 Introduction / Motivation

The increasing regulations of air quality have raised scientific studies in pollution abatement from a gas stream. As it is described in the chapters above and exemplarily demonstrated in chapter 4, the application of electric discharges is a promising technique for the pollution abatement from an exhaust gas stream, especially when these gases are at low concentration [1–6]. Plasma based pollution control might have the potential to be an alternative or addition to conventional techniques e.g. adsorption on active charcoal, catalysis, scrubbers or combustion by a carrier gas. Over the last years, the synergy between plasma and catalyst has been studied in the low and atmospheric pressure region by adding catalytic active material either directly into the discharge volume or near behind [7–11]. However, the combination of plasma and catalyst remains a technical and scientific challenge. The most interesting phenomena are the interaction between the plasma and the dielectric material, especially the processes involved in the destruction and production of molecules on the wall. These effects are mostly unknown. The loss probability of atomic oxygen on a silica surface has been measured using a pulsed fluorescence technique using a pulsed DC discharge [12]. They found that the loss probability of O atoms at the surface is higher under plasma exposure than it is just after discharge extinction. The loss probability of O atoms on the surface of different materials has been measured by emission spectroscopy [13]. It was found that on the TiO_2 surface O atoms were stored without any recombination and could be desorbed into the gas phase by a strong electric field. At the wall, radicals may recombine but they could also be involved in other chemical reactions such as the production of NO_x species in air plasmas. There is a wealth of literature dealing with the NO_x problem but only a few examples are directly related to the study of the interaction of these species with surfaces. The production of NO in a pulsed DC discharge was shown to be proportional to the energy density injected into the gas, independently from both pulse duration and plasma pulse repetition frequency [14]. This NO formation was well fitted by kinetic modelling [15] of the gas phase for high energy densities but small discrepancies were obtained for lower energy values. These discrepancies might be explained by surface processes which

cold play a dominant role when the injected power becomes low enough [16]. Alternatively, the discrepancies can be caused by breakdown instabilities, which relatively increases as the pulse duration shortens [15]. Recently the importance of surface reactions for the formation of molecules by recombination in a N_2/O_2 plasma has been demonstrated [17, 18]. The experiments for studying the interaction between the plasma and the inner surface have been carried out in a capacitively coupled RF plasma reactor with ultra-high vacuum connections. This experiment allows studying the amount of oxygen atoms deposited on the surface by following the time resolved conversion of NO into NO_2. NO was diluted in either N2 or in Ar and initially fed to the reactor, chapter 5.3. Generally, the kinetics in a N_2/O_2 plasmas is of over all interest because of their importance for many applications. A lot of investigations [19–26] have been done to improve the understanding of their complexity. For example, Ref. [15] needs 3 full page tables to list all reactions taken into account in the model including also the coupling between vibrational and chemical kinetics. Because of their complexity, however, modelling seems to be the most promising approach to obtain a most comprehensive set of information about the different reactions and processes. On the other hand, the positive column of a DC discharge provides a relatively homogeneous structure. Such a discharge has been the subject for several modelling efforts. Starting at an ab initio model, the code has been developed further supplemented by different experimental investigations [14, 16, 27, 28]. Recently, the modelling has been extended now including some NO_2 reaction paths. Efforts where done to use the modelling to predict also the afterglow evolution of NO [29]. This, however, has been possible only for the very beginning of the afterglow period. For later afterglow, the modelled NO concentration decreases down to zero where in experiments it remains constant at a level existing right after the extinction of the discharge pulse. To extend the knowledge of the N_2/O_2 plasma kinetics, the kinetics of nitrous oxides initially present in the discharge volume is of increasing interest. The time resolved development before, during and after a DC plasma pulse might help to improve the kinetic model further. For this reasons, the TRIPLE Q system described above has been used to detect the nitrous oxides, N_2O, NO and NO_2 simultaneously. Details are given in chapter 5.4. The main intentions of this chapter are therefore:

1. Results are presented of experiments to study the plasma wall interaction. Especially the ability of a discharge to deposit oxygen on the surface for potentially later VOC treatment is considered.

2. Presenting high time resolved detection of the species concentration especially the formation during a short plasma pulse. This helps to access the different reaction rates for improved kinetic modelling.

3. To prove the functionality of a multi channel QCLAS system. Its ability to be sufficient for high time resolved plasma diagnostics. An automated data treatment has been successfully implemented.
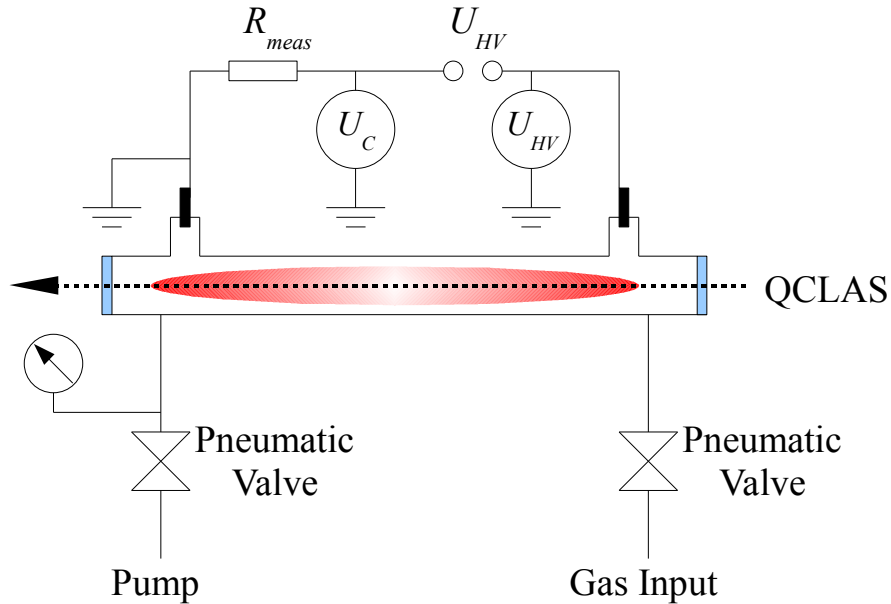
5.2 Experimental Setup

The experiments have been done in a glass tube reactor made of Pyrex with an inner radius of 0.8*cm* and a length of 60*cm* [28]. The ends of the tube were closed with high vacuum sealed Kalium Bromide (KBr) windows in order to allow infrared absorption spectroscopy to be performed. The optical height has been 11*cm*, which is the distance between the optical table and the centre of the tube. The spectroscopic quantification of the species has been done applying quantum cascade laser absorption spectroscopy, QCLAS, in the infrared region, fig. 5.1 and 5.2, respectively. The line of sight was axially orientated. This setup was adapted to two different experimental configurations.

5.2.1 DC configuration

For the DC configuration, the electrodes are necessarily inside the reactor. Therefore, the Pyrex tube was modified to have T-shaped electrode holders, fig. 5.1. On one hand, this avoids possibly disturbing parts affecting the laser beam. On the other hand, it allows to measure in the homogenous part of the positive column of the DC discharge. In order to drive the plasma, one electrode was grounded and the other electrode was set on high voltage. The high voltage (HV) was delivered by a self made high voltage DC pulse generator. The main parts are a commercial HV DC power supply, a HV capacitor bank and a fast semiconductor HV switch (Belke). This device did allow to use pulses ranging from 1*ms* up to 10*ms* duration. The amplitude could be chosen up to several thousands of volts. A typical rise time of the voltage was in the order of 420$V/\mu s$. The applied voltage has been measured by a high voltage probe (LeCroy). The current was measured using the current proportional voltage drop over a measurement resistor, R_{meas} = 18.4Ω. Both signals were digitalised by an oscilloscope (LeCroy LC584) and saved to the hard drive. The gas mixture of interest has been pre mixed by the manufacture, Air Liquid. The gas filling has been controlled by mass flow controllers (MKS). The pressure was measured by a capacitive transducer (Pfeiffer CMR 263). The spectroscopic quantification of the species has been done by a 3 channel quantum cascade laser spectrometer, chapter 3, equipped with lasers suitable for simultaneous detection of N_2O, NO and NO_2. The three pass alignment allowed a detection limit of these three species of: N_2O $5 \times 10^{12} molecules\, cm^{-3}$, NO $4 \times 10^{13} molecules\, cm^{-3}$, NO_2 $3.4 \times 10^{13} molecules\, cm^{-3}$.

5.2.2 RF configuration

For the RF configuration, the tube reactor was made of a simple Pyrex tube with the same dimensions as in the DC experiment, fig. 5.2. Again, the windows at the ends were made of kalium bromide (KBr) and high vacuum sealed. The plasma was driven by a RF generator adapted to the reactor via a match box. The power was capacitive coupled by two outside placed ring electrodes driven with a frequency of 13.56*MHz*. For the power measurement, the incident power P_in as well as the reflected power $P_{reflect}$ have been measured by an in-line power meter placed between the RF generator and the match box. Details can be found in Ref. [30]. The power loss inside the match box P_match has been considered by the assumption that this is
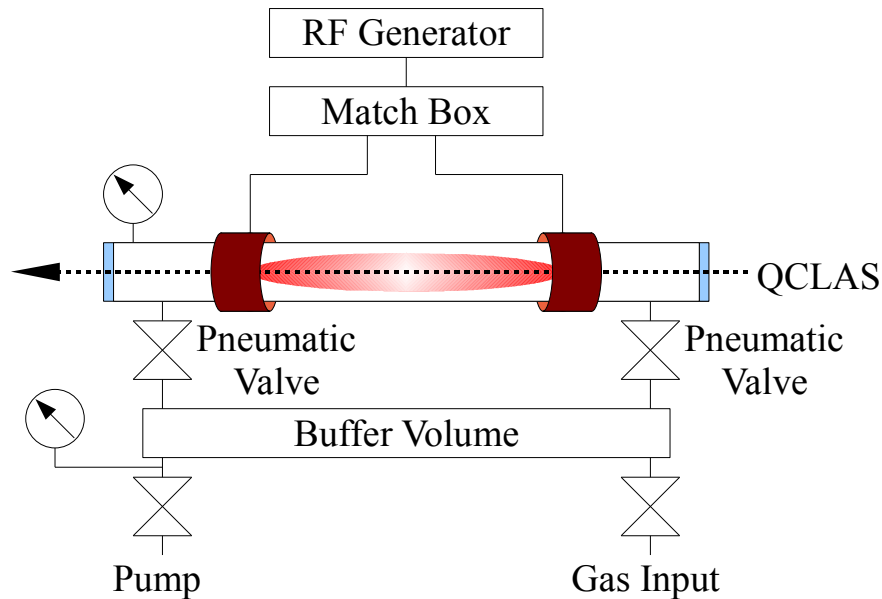
Figure 5.1: Principal sketch of the experimental setup of the DC configuration. The electrodes are represented by the two black rods inside the T-shaped holder. The discharge current was measured by the measurement resistor Rmeas. One electrode was grounded and the other one was set to high voltage. The tube reactor was made of a Pyrex tube with an inner radius of 1*cm* and a length of 60*cm*.

mainly caused by the resistance R of the coil of the match box. Therefore, the voltage on the coil of the match box with plasma U_{Plasma} and without plasma U_w has also been measured. For the latter, the ignition of the plasma has been avoided by a sufficient high pressure inside the tube. With these assumptions, the power measured under plasma condition can be expressed by (i) $P_{Plasma} = P_{in} - P_{reflect} - (U_{Plasma})^2/R$, where the last term represents the power loss in the match box. In the case that no plasma was ignited, the relation (ii) $P_{in} - P_{reflect} = (U_w)^2/R$ can be formulated assuming that the consumed power is lost in the match box only. Transposing (ii) with respect to R and substituting R in (i) leads to the relation used for the power determination. That is:

$$P_{Plasma} = \left(P_{in} - P_{reflect}\right)_{Plasma} - \left(P_{in} - P_{reflect}\right)_w \cdot (U_{Plasma}/U_w)^2 \qquad (5.1)$$

Typical values have been about 17*W* dissipated in the plasma and about 28*W* dissipated in the match box. Therefore, the power loss in the match box can not be neglected. The determination of the species concentration was done by QCLAS, too. The two lasers used for the experiments have been suitable to detect NO and NO_2 in a single pass alignment. The detection limit for both NO and NO_2, has been $5 \times 10^{13} molecules\, cm^{-3}$, respectively.

Figure 5.2: Principal sketch of the experimental setup of the RF configuration. The gas mixture was pre mixed in the buffer volume. The pneumatic valves were used to ensure a fast and synchronised filling into the evacuated tube reactor. The tube reactor was made of a Pyrex tube with an inner radius of $1cm$ and a length of $60cm$.

5.3 Plasma stimulated surface modification by a RF discharge

5.3.1 Experimental Set-up / Procedure

The experiments have been carried out in the cylindrical plasma reactor, fig. 5.2, made of Pyrex with a length of $60cm$ and an inner diameter of $20mm$. The inner surface of the tube has been pre-treated by a capacitively coupled RF plasma, $f = 13.56MHz$, for $1h$ at flowing conditions using a gas pressure of $0.53mbar$. At such a relatively high pressure, the main volume of this capacitive discharge is similar to a glow discharge. The Pyrex surface is mainly in contact with this part of the discharge. Consequently, for the purpose of this work in which the grafting of the atoms onto the surface has been considered, one can reasonably consider our discharge comparable to the positive column of a DC discharge for the same pressure and injected power. Outside the tube two metallic rings work as electrodes in order to avoid any contact between plasma and metal which could induce additional chemical reactions. The plasma has been driven with different precursor gases, namely O_2, N_2, Ar, and synthetic air (80% N_2, 20% O_2). The injected power has been $30W$. The same injected power in a DC discharge with the same reactor and pressure would typically lead to a $50mA$ discharge current and around $400K$ gas temperature in pure O_2. After the plasma pre-treatment, the tube was filled with a probing gas

of 1% NO in N_2 or in Ar at a pressure of 5.3*mbar*. The tube was then closed and NO and NO_2 densities are simultaneously measured without plasma during a period of 2*h*. Using a double quantum cascade laser measurement and control system (Q-MACS) [31], NO and NO_2 concentrations are monitored by means of absorption lines at 1897cm^{-1} and 1612cm^{-1}, respectively. To calculate absolute species concentrations, the system has been calibrated before experiment using NO and NO_2 at a known pressure and concentration. The different pre-treatment plasmas and probing gases employed for this study are summarized in tab. 5.1.
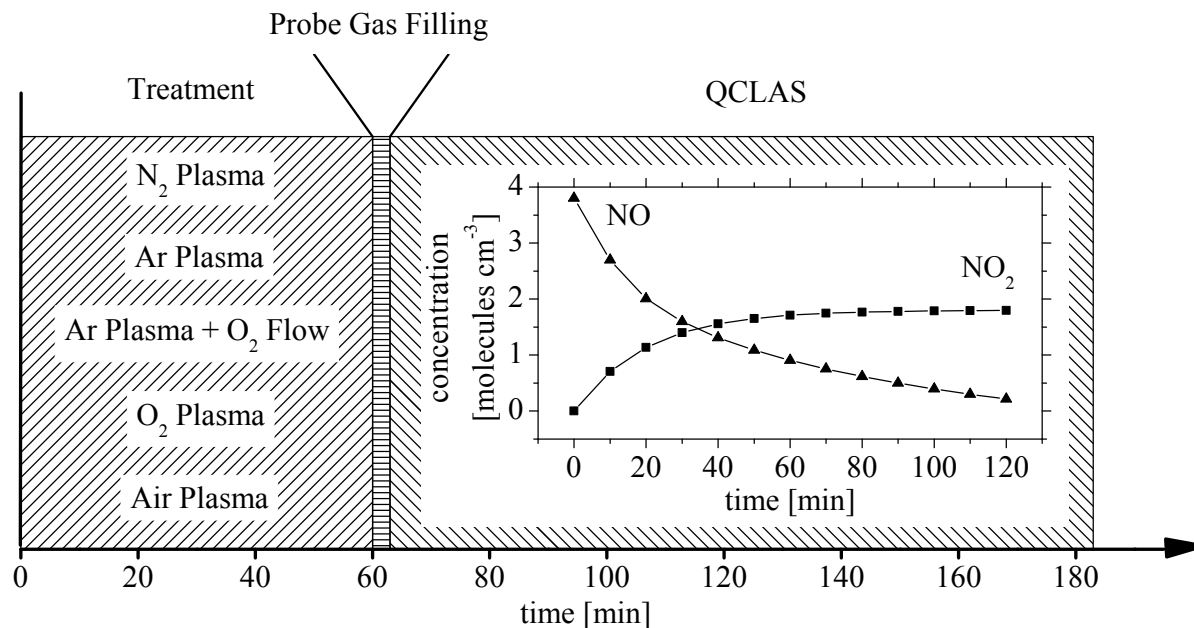
Figure 5.3: Time line of the experiment. First, treatment of the inner surface of the Pyrex tube, ▨ , by either a N_2 plasma, Ar plasma, Ar plasma followed by a O_2 flow, O_2 plasma or an air plasma, one treatment after another. Second, the Pyrex tube has been filled with the probe gas, ▤ . Third, the species transformation has been detected using QCLAS, ▧ . For one certain treatment, the species conversion has been monitored by QCLAS, before the next treatment has been applied.

5.3.2   Results and discussion

Pre-treatment with Ar and N_2 plasmas (experiments A, B and C)

The Pyrex tube was exposed to Ar and N_2 plasmas (experiments A and B). This plasma cleaning without any O atom containing species allows to check if ion bombardment is able to create free adsorption sites for NO on the Pyrex surface. In both cases no significant decrease in the NO concentration was observed, fig. 5.4. Thus, it is assumed that under these conditions, NO is

Table 5.1: Overview of the different experiments, the corresponding surface pre-treatment RF plasmas and the probing gases used in this study. The species detected by the double QCLAS system are given in the right column [16].

Experiment	Pre-treatment plasmas $P = 30W$, ($p = 0.53mbar$)	Probing gas 1% NO in ... ($p = 5.3mbar$)	Detected Species
A	60 min N_2	N_2	NO
B	60 min Ar	N_2	NO
C	30 min Ar plasma + 30 min O_2	N_2	NO
D	60 min O_2	N_2	NO, NO_2
E	60 min O_2	Ar	NO, NO_2
F	60 min Air	N_2	NO, NO_2

not lost on the Pyrex walls even after plasma exposure. This is in good agreement with results reported in the literature [32]. For 30*min* experiment C was performed with an Ar plasma as pre-treatment followed by a pure O_2 flow without any plasma, again for the duration of 30*min*. Similar to experiments A and B, the NO concentration remains constant over more than 80*min*. This behaviour suggests that O_2 molecules are not adsorbed at the Pyrex surface and / or the possibly adsorbed O_2 could not directly lead to an oxidation of NO at the wall.

Pre-treatment with O_2 plasma (experiments D and E)

For 60*min* a pure O_2 plasma pre-treatment was applied in order to verify if oxidation reactions occur on the surface. Fig. 5.5 shows the results for two types of probing gas (i) 1% of NO in N_2 (experiment D) and (ii) 1% of NO in Ar (experiment E). In both cases the concentration of NO decreases while NO_2 simultaneously increases. Although fig. 5.5 shows not a pure exponential decay of the NO behaviour, a first order exponential fit applied as a first estimation gives a reduction rate of $2.3 \times 10^{11} molecules\, cm^{-3}\, s^{-1}$ for NO losses for both experiments. The production rate of NO_2 has a production rate of nearly the same ($2.1 \times 10^{11} molecules\, cm^{-3}\, s^{-1}$ for experiment D in N_2 and $1.9 \times 10^{11} molecules\, cm^{-3}\, s^{-1}$ for experiment E in Ar). Therefore, it can be concluded that NO is oxidized into NO_2 by O containing species (O_2, O_2^- or O atoms) adsorbed on the Pyrex surface during the pre-treatment phase. O_2 molecules are not adsorbed and / or are not involved in the oxidation of NO under these conditions which was clearly demonstrated by experiment C. At the surface O_2^- could have been adsorbed under plasma exposure, but the amount of oxygen atoms required to produce the measured NO_2 density of $5.3 \times 10^{14} molecules\, cm^{-3}$ would induce a surface charge density as high as $20\mu\, C\, cm^{-2}$ leading to a plasma breakdown at the surface during the filling procedure. O atoms involved in the NO oxidation process can thus only originate from atomic oxygen adsorbed during the pre-treatment (designated as O_{ads} further below). These O_{ads} do not recombine to O_2 and remain at the surface during all pumping and filling procedures. Since the O_{ads} cannot be easily desorbed, NO oxidizes at the surface and not in the gas phase. The oxidation to NO_2 with O_{ads} could occur via two different mechanisms:
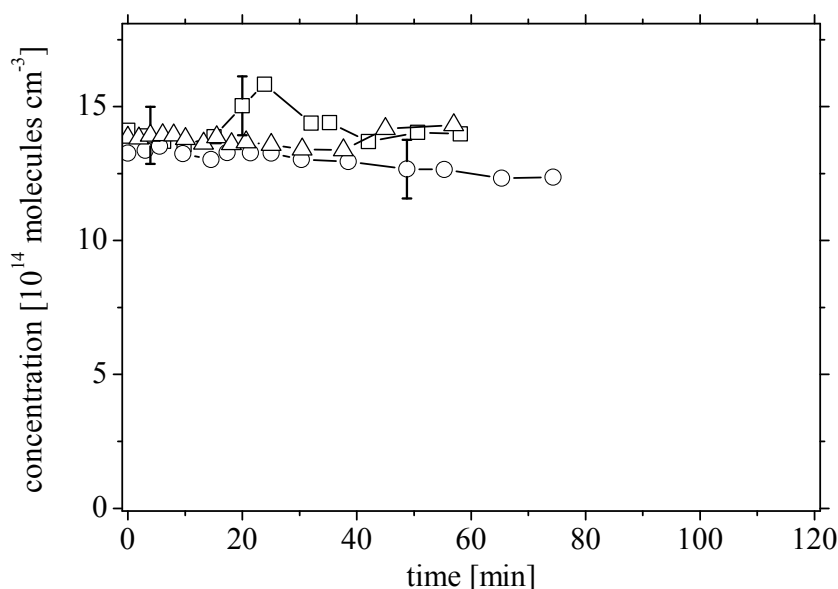
Figure 5.4: The NO concentration after an Ar pre-treatment ($\square$), N_2 pre-treatment ($\bigcirc$) and after an Ar pre-treatment followed by a O_2 gas flow ($\triangle$). From such a nearly constant behaviour, the O_2 molecules are not adsorb on the surface or the adsorb molecules do not lead oxidation of NO at the wall [16]. The initial gas concentration was 1% NO diluted in N_2 or Ar at a total gas pressure of 5.3 *mbar*. More details can be found in Ref. [16].

(i) (i) in the gas phase NO reacts directly with O_{ads} via a direct pick-up of NO from the gas phase (Eley-Rideal mechanism),

(ii) (ii) first NO is adsorbed and then reacts with O_{ads} at the surface (Langmuir-Hinshelwood mechanism).

Experiments A and B have shown that Ar or N_2 plasmas are not able to create adsorption sites for NO at the Pyrex surface. The Langmuir-Hinshelwood mechanism could then happen only if the O_2 plasma provides a better cleaning of the surface than a N_2 or Ar plasma. Whatever the mechanism involved, the rate coefficient is relatively low compared with that one of the NO_2 production at the same pressure in the gas phase. Here according to Atkinson et al. [33] the oxidation of NO into NO_2 is a third order reaction with a rate coefficient $k(298K)=10^{-31}cm^6\ molecule^{-2}\ s^{-1}$. Just for comparison purpose, if in the gas phase all the adsorbed O atoms used for the NO_2 production would be available and react with the 1% of initial NO at a pressure of 5.3 *mbar*, the production rate would be $6.6 \times 10^{15} molecule\ cm^{-3}\ s^{-1}$ instead of the $2.1 \times 10^{11} molecule\ cm^{-3}\ s^{-1}$ measured in experiment D. The limiting factor for the surface oxidation reaction is probably not the surface density of O_{ads}. Assuming that all the O_{ads} stored onto the surface are used to oxidize NO, an oxygen surface density of $2 \times 10^{14}cm^{-2}$ can be estimated by considering a smooth surface at the pre-treated tube. The surface coverage could be estimated by considering only the part of SiO_2 of Pyrex. The length of the Si-O bond is 183 *pm* in Pyrex. Therefore, each tetrahedral mesh has a size of about $5 \times 10^{-16}cm^2$ leading to about
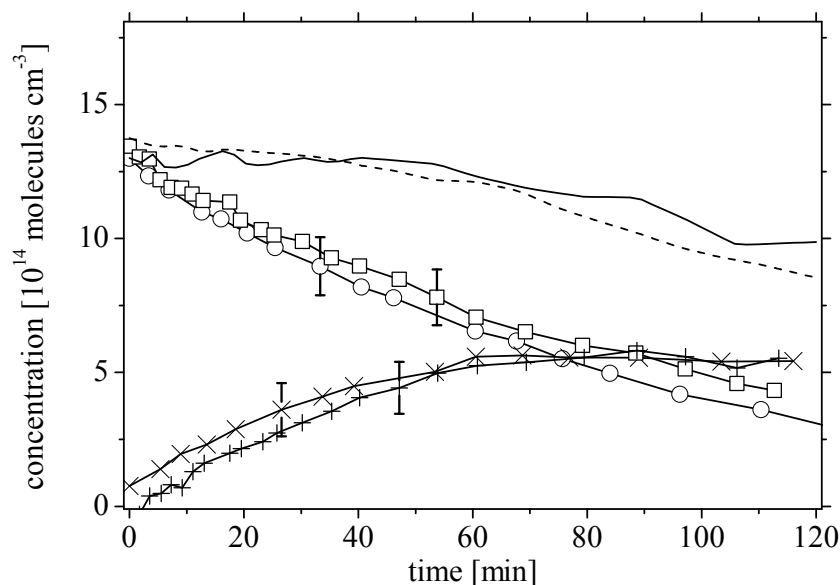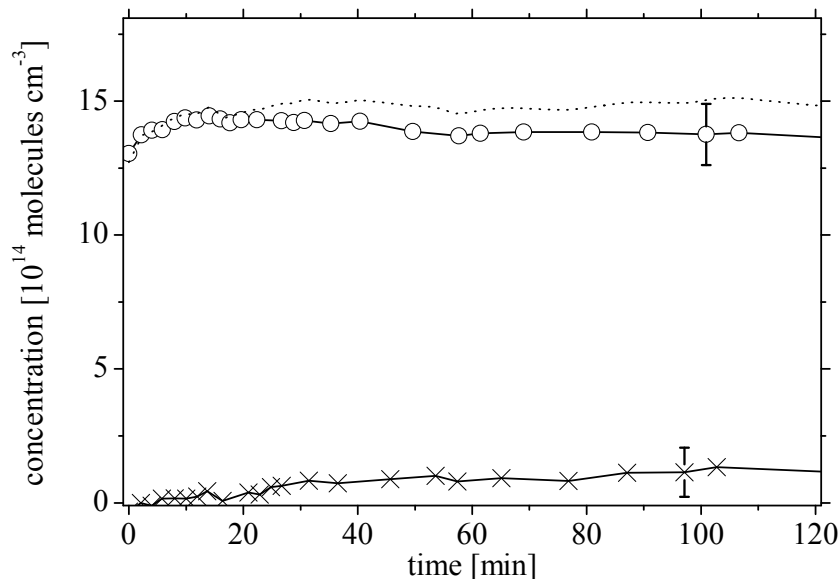
Figure 5.5: Time dependence of the NO and NO_2 concentrations after a $1h$ oxygen plasma pre-treatment of the Pyrex tube. Probing gas: (i) N_2 + 1% NO (NO: ○ , NO_2: ×), (ii) Ar + 1% NO (NO: □ , NO_2: +), p=5.3*mbar*. Upper curves show the sum of the NO and NO_2 concentrations (solid line for N_2 + 1% NO, dotted for Ar + 1% NO) [16].

10% of Si atoms occupied by adsorbed O atoms after the pre-treatment. This corresponds to a highly saturated surface [34]. However, 10% is an upper limit because the roughness of the surface has to be taken into account. Experiments D and E with NO in N_2 or in Ar as probing gas give the same kinetics for NO and NO_2, fig. 5.5. The relatively low production rate of NO_2 is thus not limited by a competition between NO and N_2 for adsorption processes and / or direct reactions of N_2 with adsorbed O atoms. The NO_2 desorption from the surface is not either the slowest process because the production rate of NO_2 is about equal to the reduction rate of NO ($2.1 \times 10^{11} molecule\, cm^{-3}\, s^{-1}$ for NO and of $2.3 \times 10^{11} molecule\, cm^{-3}\, s^{-1}$, respectively). However, in the gas phase the sum of the NO and NO_2 concentrations decreases slightly with time. The NO_2 concentration shows saturation at $5.3 \times 10^{14} cm^{-3}$. After 120 min about 30% of the N atoms originating from NO have not been detected as NO or NO_2 in the gas phase. On a longer time scale NO could be partly adsorbed or NO_2 has been also converted into other oxygen containing compounds such as N_2O, NO_3 and N_2O_3. Therefore, for future studies it would be worthwhile monitoring also the concentrations of these compounds, e.g. using a third laser in the experimental set-up. The Pyrex surface highly saturated with O_{ads}, the similarity between experiments D and E and the almost impossible adsorption of NO (as for experiments A and B) strongly suggest an oxidation of NO with O_{ads} by the Eley-Rideal mechanism. At the Pyrex surface the relatively low effective rate of the NO oxidation may have several explanations: for instance, a part of NO_2 could react with O_{ads} atoms to form NO. The possible catalytic role of B, Al and Na atoms present in Pyrex could also lower the NO_2 production if the O atoms need to reach these specific catalytic sites for the oxidation of NO.

Pre-treatment with air plasma (experiment F)

Fig. 5.6 shows the NO and NO_2 concentrations after an air plasma pre-treatment and the sub-sequent filling with 1% NO in N_2. A small increase in the NO concentration occurs during the first 10*min* then the NO concentration decreases slightly. The concentration of NO_2 increases from the beginning of the measurement and reaches a value which is five times lower than after the pure O_2 pre-treatment (experiments D and E).

Figure 5.6: Time dependence of the NO ($\bigcirc$) and NO_2 ($\times$) concentrations after a 1*h* air plasma treatment of the Pyrex tube. The dotted curve shows the sum of both concentrations. Probing gas: N_2 + 1% NO, p=5.3*mbar* [16].

The previously discussed experiments of an Ar, N_2 or O_2 plasma pre-treatment show that NO is not strongly adsorbed. Therefore, the differences between experiments D and F considering the NO losses are not a consequence of a weaker adsorption of NO because of a lack of free adsorption sites caused by the adsorption of other species produced by the air plasma. Two main reasons are responsible for the differences obtained after an air or an O_2 plasma pre-treatment: (i) the losses of NO are balanced by the production of NO, (ii) the amount of O_{ads} remaining on the surface is lower after the air plasma pre-treatment. Further, the following should be noted: (i) As in the experimental conditions NO molecules are not strongly adsorbed on the Pyrex surface: within the first 10*min* a small increase in the NO concentration suggests that NO is produced at the surface. After the O_2 pre-treatment this phenomenon has not been observed. Therefore, N atoms are probably involved in this NO formation at the wall. It was shown in Ref. [17] that N atoms play a key role in the NO formation at the wall after a pre-treatment by a N_2 plasma. However, the main difference between experiment D and F is certainly the remaining amount of O_{ads} on the Pyrex surface. (ii) After the air pre-treatment the NO_2 production is five times lower than after the pure O_2 pre-treatment, which is the same ratio as that one of O_2 in

air. In both pre-treatment plasmas the O atom density has not been measured but this density is obviously lower in air. Moreover, at the surface the NO oxidation observed in experiments D and E is probably the consuming part of the O_{ads} during the air plasma pre-treatment itself. In air a $30W$ plasma produces larger amounts of NO. Unfortunately, for the air plasma pre-treatment the NO and NO_2 concentrations were below the detection limit of the setup (about $5 \times 10^{13} molecules\, cm^{-3}$ for both species). This means that efficient mechanisms which could consume O_{ads} destroy NO and NO_2. A lower production rate of O atoms, the consumption of O_{ads} during the pre-treatment and the possible adsorption of other species like N atoms instead of O atoms lead to a less pronounced decay of NO and to the production of NO_2 after an air plasma pre-treatment.

5.3.3 Kinetic Surface Modelling

The results given above clearly show that the surface interaction can play a significant role in species conversion. For an improved understanding, the results have been fitted by a simple surface model [35, 36]. The key steps are given here. The model used therein is based on an analytic model presented in [17]. This model was developed to describe the heterogeneous recombination of single atomic species on silicalike surfaces. It provides expressions for the surface atomic recombination probability obtained as a function of surface characteristics such as the densities of adsorption sites and the activation energies for the different elementary surface processes. The model includes physisorption, chemisorption, thermal desorption, surface diffusion, and both Eley-Rideal and Langmuir-Hinshelwood recombination mechanism. For the model, the surface is considered to be fully covered with adsorption sites. They can hold atoms or molecules either due to physisorption or due to chemisorption. Here, it is assumed that the recombination takes place at the active adsorption sites. The simplest surface kinetic scheme describing the conversion of NO into NO_2 takes into account only two surface reactions [35, 36],

$$NO + O_S \rightarrow NO_2 \tag{5.2}$$

$$NO + S_V \rightarrow (NO)_S \tag{5.3}$$

where O_S indicates a chemisorbed oxygen atom, $(NO)_S$ a chemisorbed NO molecule, S_V a vacant chemisoption site and NO and NO_2 the gas phase molecules. The solution of the following coupled system of equations has been used to calculate the time development of the corresponding concentration:

$$\frac{d\,[NO]}{dt} = \frac{2}{R_t}\left(-r_1\Theta_S^O - r_2\left(1 - \Theta_S^O - \Theta_S^{NO}\right)\right)[S] \tag{5.4}$$

$$\frac{d\,[NO_2]}{dt} = \frac{2}{R_t}\Theta_S^O r_1\,[S] \tag{5.5}$$

$$\frac{d\left[\Theta_S^O\right]}{dt} = -\Theta_S^O r_1 \tag{5.6}$$

$$\frac{d\left[\Theta_S^{NO}\right]}{dt} = r_2\left(1 - \Theta_S^O - \Theta_S^{NO}\right) \tag{5.7}$$

where [S] denotes the surface density of chemisorptions sites and $\Theta_S^M = [M_S]\,/\,[S]$ is the fractional coverage of chemisorption sites covered from species M. As given in [17], the (time dependent) reaction rates r_1 and r_2 are:

$$r_1 = \frac{\Phi_{NO}}{[S]}\varphi k_1^0 \exp\left(-\frac{E_1}{RT_W}\right) \tag{5.8}$$

$$r_2 = \frac{\Phi_{NO}}{[S]}\varphi k_2^0 \exp\left(-\frac{E_2}{RT_W}\right) \tag{5.9}$$

where Φ_{NO} stands for the flow of gas phase molecules of NO to the wall, T_W is the wall temperature, R is the gas constant, E_1 is the activation energy for recombination, E_2 is the activation energy for chemisorption and the k_i^0 $(i = 1, 2)$ values are related to elementary sticking coefficient on the adsorption sites (occupied or vacant) and correct the formulas for directional effects and other unknown phenomena. The calculated evolution of the NO and NO_2 density have been compared with the measured data, fig. 5.7 and 5.8. For the calculation, a density of physisorption sites $[F] = 1.5 \times 10^{15} cm^{-2}$ was chosen. The other values are: $\varphi 1.1 \times 10^{-1}$, $E_1 = 24 kJ/mol$, $E_2 = 0 kJ/mol$, $k_1^0 = 10^{-3}$, $k_2^0 = 2 \times 10^{-8}$, $T_g = T_W = 298 K$. The initial concentration of NO was equal to the partial pressure of $0.01 \cdot 5.3 mbar$. The values for [F], E_1 and E_2 are considered to be typical in recombination studies, compare [17]. On the other hand, φ is larger than in [17] but close to the one given in [37]. The factor $k_1^0 = 10^{-3}$ is much lower than in [17] where it was 1. In comparison with [38] the value of 1.5×10^{-2} has been used for a similar reaction of CO: $CO + O_S \rightarrow CO_2 + S_V$. In fig. 5.7, one can see the modelled time evolution of the NO and NO_2 concentration including only reaction 5.2. Both show a good agreement for the first $2000 s$. For a longer time period, the modelled NO concentration shows an increasing discrepancy whereas the NO_2 concentration is already in a good agreement. As mentioned in [16], a slow loss of N-containing species can be present. This has been included into the current modelling by the quite slow reaction 5.3. The small value for k_2^0 indicates a not very efficient chemisorption of NO on the wall. However, the inclusion of reaction 5.3 is just an effective way to describe the loss sequence. Principally, the adsorption of NO_2 or even more complex sequences of reaction might have to be regarded in future investigations. Fig. 5.8, shows the fractional coverage of chemisorption sites. It indicates a progressive replacement of O_S by chemisorbed NO molecules. Future modelling can be improved by the inclusion of additional reactions e.g. NO_2 adsorption, physisorption, diffusion and Langmuir-Hinshelwood recombination.

5.3.4   Conclusions

It has been shown that at a Pyrex surface NO is oxidized to NO_2 after an oxygen containing plasma treatment of the surface. The O atoms produced by a pure O_2 or an air plasma are adsorbed at the inner surface and remain available for oxidation reactions at a medium pressure
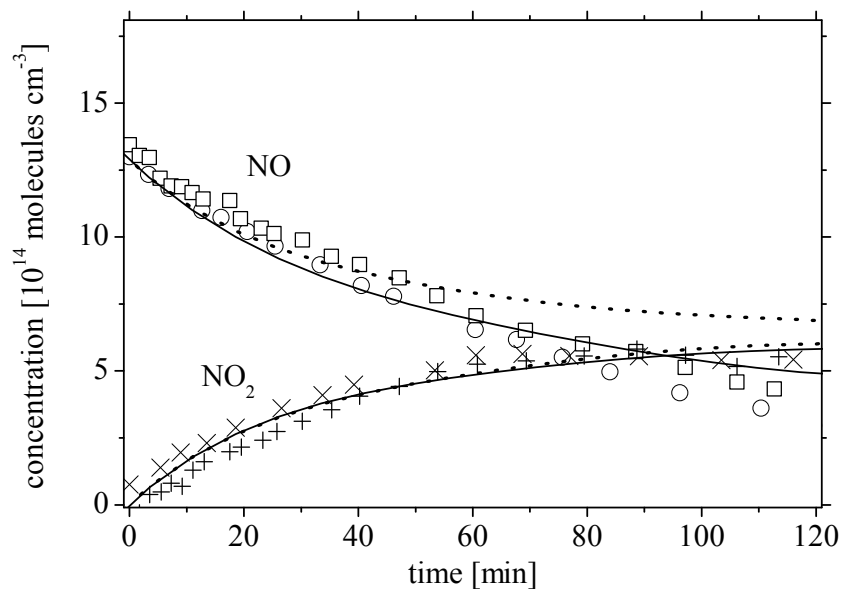
Figure 5.7: Experimental (points) and calculated (lines) concentrations of NO and NO_2 as a function of time, using reaction 5.2 only (dotted) or reactions 5.2 and 5.3 simultaneously (solid). Curves are extracted from [35].
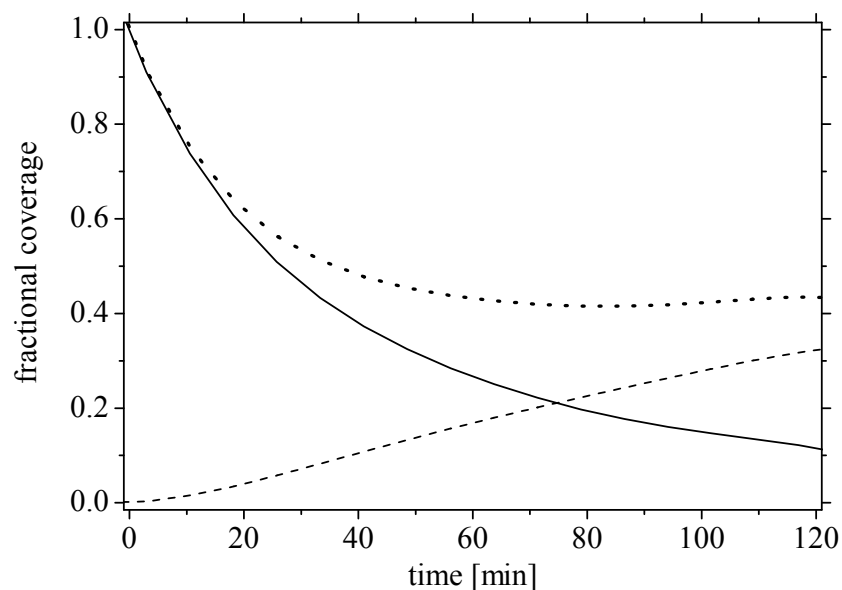
Figure 5.8: Fractional coverage of adsorption sites with O atoms (Θ_S^O, solid), NO molecules (Θ_S^{NO}, dashed) and total ($\Theta_S = \Theta_S^O + \Theta_S^{NO}$, dotted). Curves are extracted from [35].

range of a few millibars over several tens of minutes. A pure O_2 plasma treatment of the Pyrex material leads to a surface highly saturated with O atoms. Under the experimental conditions NO is probably oxidized to NO_2 via the Eley-Rideal mechanism. An effective reduction rate of $2.3 \times molecules\, s^{-1}$ has been determined. An Ar or N_2 plasma treatment of the Pyrex surface has not led to considerable numbers of adsorption sites for NO [16]. In air plasmas the surface reactions appear to be crucial to understand the NO kinetics at least in the *mbar* pressure range. Additional experiments are now planned to be performed using pure silica surfaces in order to identify the adsorption sites involved in these surface oxidation reactions. The developed simple surface model accords well with the experimental results. In the model a fraction of the surface is considered to be covered with chemisorption sites where atoms and molecules can be adsorbed, whereas they can be removed only by recombination. In particular, after about 30*min* the fractional coverage of adsorption sites with NO molecules is non-negligible and may partially explain the loss of N containing species in the gas phase.

5.4　Study of the formation and destruction of N_xO_y in a pulsed DC discharge

5.4.1　Experimental setup and procedure

For the experiments reported here, the DC configuration of the setup has been used. The experiments have been carried out as follows:

- First, preparation, the inner side of a brand new Pyrex tube has been exposed to an Ar plasma for several hours in order to clean the surface. This was done for several hours at a total gas flow of 12.5*sccm* and at a pressure of 1.33*mbar*.

- Second, filling, the reactor was evacuated down to $10^{-3}mbar$. Afterwards, a constant flow of the gas mixture of interest at a flow of 12.5*sccm* was established holding a pressure of 1.33*mbar*. The reactor was closed quickly by simultaneously closing the input and output pneumatic valve. A 1*min* break has been applied in order to stabilise potential species surface interactions.

- Third, plasma ignition and species detection, a DC current pulse has been feed to the electrodes.

Fig. 5.9 illustrates the experimental procedure, the applied trigger regime and the species concentration measurement. The experimental procedure shown in fig. 5.9 has been done using different mean currents that are: 25*mA*, 50*mA*, 100*mA* and 150*mA*. The voltages leading to the mean current values have been determined in the very beginning that is before the preparation phase. The pulse duration τ was also varied ranging from 1*ms* up to 10*ms*. The species concentration has been detected by a 3 channel quantum cascade laser system, TRIPLE Q, working in the *Intra Pulse Mode* using different pulse repetition frequencies, see chapter 3 and Ref. [39]. Each measurement itself started with a manually established main trigger event, fig.
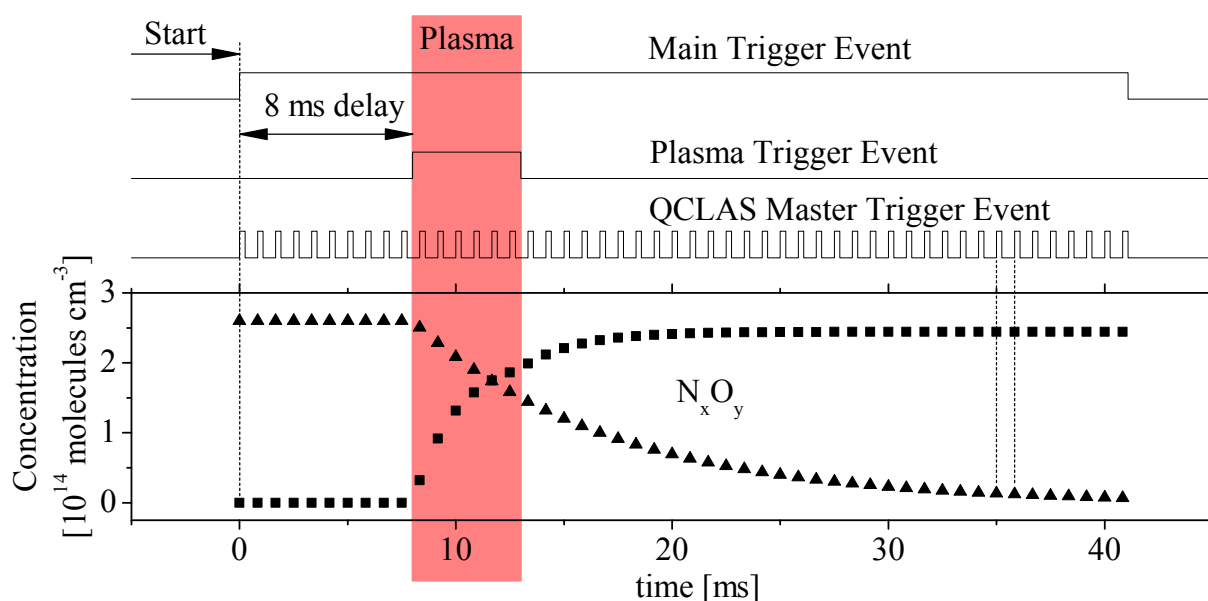
Figure 5.9: Timeline of the experimental procedure. After the gas filling, the experiments have been started by a manually initialised trigger event, Main Trigger Event. This triggers the QCLAS as well as a delay generator. After a fixed delay of 8*ms*, the plasma pulse has been ignited. The species concentration has been measured before, during and after the plasma pulse. At each QCLAS trigger event, an entire spectrum was taken, 3000 in total always. Depending on the pulse repetition frequency of the QCLAS system, different resolutions and, therefore, different total durations of the measurement have been used, tab. 5.2 shows more details.

5.9, which was triggering the QCLAS system and a delay generator. A 8*ms* time delay was applied to the plasma power supply. This procedure allows the determination of the initial species concentration, too. The QCLAS system recorded 3000 entire spectra which were analysed afterwards. The total duration of the spectroscopic detection did, therefore, depend on the pulse repetition frequency of the QCLAS system. Several repetition frequencies of the QCLAS system have been used. The pulse repetition frequency, the corresponding time distance between two spectra and the total duration of the spectroscopic detection are listed in tab. 5.2. The pulse repetition frequency was chosen to be 5*kHz* for the first experiments. Since the operator has to become familiar with the properties and response of the laser, the frequency has been increased for latter experiments. The frequency has also been influenced by the species concentration itself. Some concentration evolutions showed a longer time constant. Consequently, to cover all effects, the frequency has been chosen depending on former measurements. Beside this, not all lasers are suitable to a higher frequency operation. Therefore, the fastest pulse repetition frequency applied, 30*kHz* tab. 5.2, has been applied to one laser. On the other hand, a higher frequency demands a higher memory size of the detecting oscilloscope. The supply of the high voltage was done by a home made power supply as described in chapter 5.2.1. Fig. 5.10 shows a typical voltage and current vs. time plot for a 5*ms* plasma pulse. The current shows a rise time

of about $100ns$ (about $2MA\ s^{-1}$). The voltage riches a stable steady state level within $200\mu s$. The energy consumed by the plasma pulse has been calculated by $W = \int_{Pulse} U \cdot I dt$ and was found to be in the range between $0.2J$ and about $3J$. In some experiments, the ignition of the plasma showed a little delay compared to the rising voltage. This ignition phenomenon has been neglected so far. This effect is automatically regarded by the energy calculation since there is no current before the ignition. A typical evolution obtained by the QCLAS system is shown in
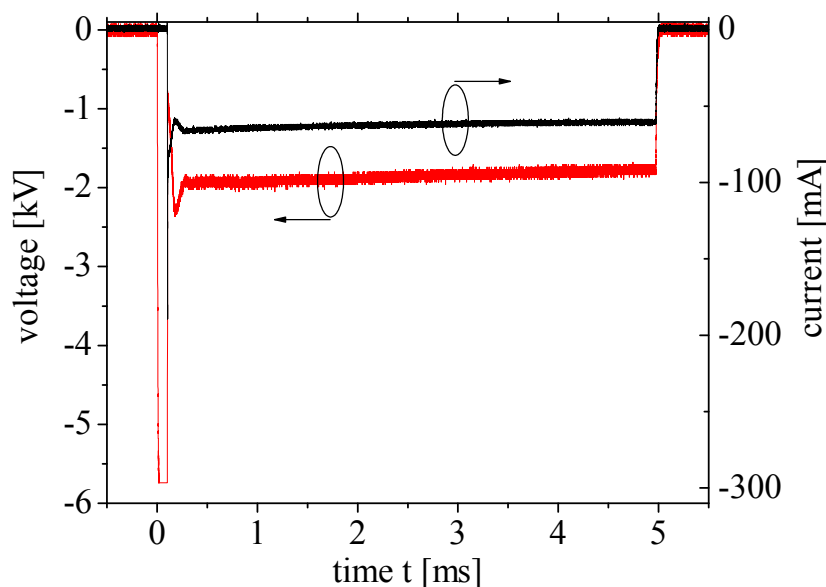
Figure 5.10: Example of a typical voltage and current behaviour for a $5ms$ plasma pulse creating an average current of about $50mA$. The gas mixture has been 80% N_2 and 20% O_2 at a pressure of $1.33mbar$.

Table 5.2: The table lists the applied pulse repetition frequency of the QCLAS system and the corresponding resolution as well as the total measurement time.

Repetition Frequency [kHz]	Resolution [μs]	Total Duration [ms]
5	200	600
10	100	300
20	50	150
30	33.3	100

fig. 5.11. The example shows the result of a $10ms$ plasma pulse with a mean current of $100mA$ fed to the reactor. The curve represents the integrated absorption coefficient K calibrated with the calibration function, see also chapter 3. As one can see in fig. 5.11 and fig. 5.12 the curves can be separated into 3 main parts. The first part represents the initial concentration that is $8ms$ before the plasma pulse ignition. A second part can be defined ranging from the beginning of

the plasma pulse up to a little behind. The third part is defined to be the stable steady state at the end of the measurements. Several effects can be described in fig. 5.11 and fig. 5.12. The first effect described here is about the total dissociation of the initial N_xO_y concentration. The physical quantity obtained by the QCLAS system is the integrated absorption coefficient K. This has been corrected by the calibration function, chapter 3. However, this function has been determined for thermal equilibrium at room temperature. Consequently, the calibration can not lead to the right concentration since additional effects can influence the spectroscopic measurements caused by the plasma. That means that the integrated absorption coefficient K might be strongly influenced by the temperature dependency of the line strength or by a vibrational excitation of the N_xO_y molecule. Principally, competing temporally production and dissociation of the detected molecule might also influence the measurement both, during the plasma pulse as well as in the afterglow period. To avoid the influence of any disturbing effect, the total dissociation has been measured between the initial concentration and the stabilised steady state of the concentration at the end of the measurement. These two parts fulfil the conditions present for the calibration procedure. Both levels are marked in fig. 5.11 and 5.12. Furthermore, the mea-
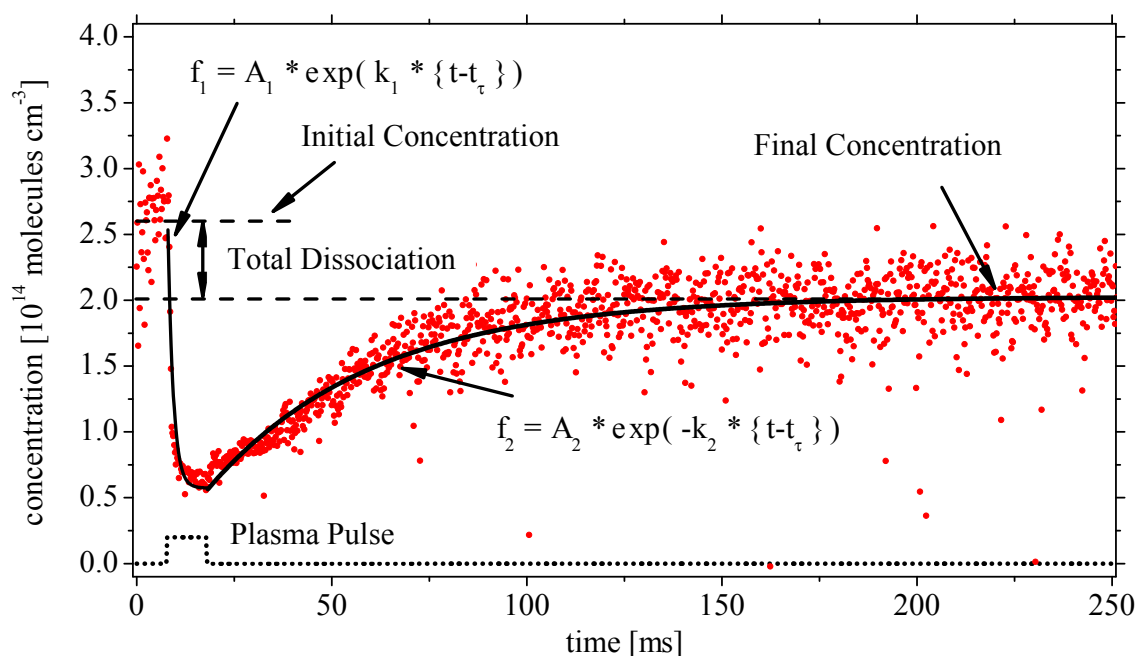
Figure 5.11: Typical evolution of N_xO_y, N_2O shown as an example, detected by the QCLAS system (dotted). These values have been calculated from the integrated absorption coefficient K times the calibration curve. Thus, no heating or vibrational excitation phenomena, affecting K, are regarded yet. The solid lines represent an exponential fit to the measured points during the plasma pulse and in the afterglow. The total value of dissociation is calculated between the initial and final signal.
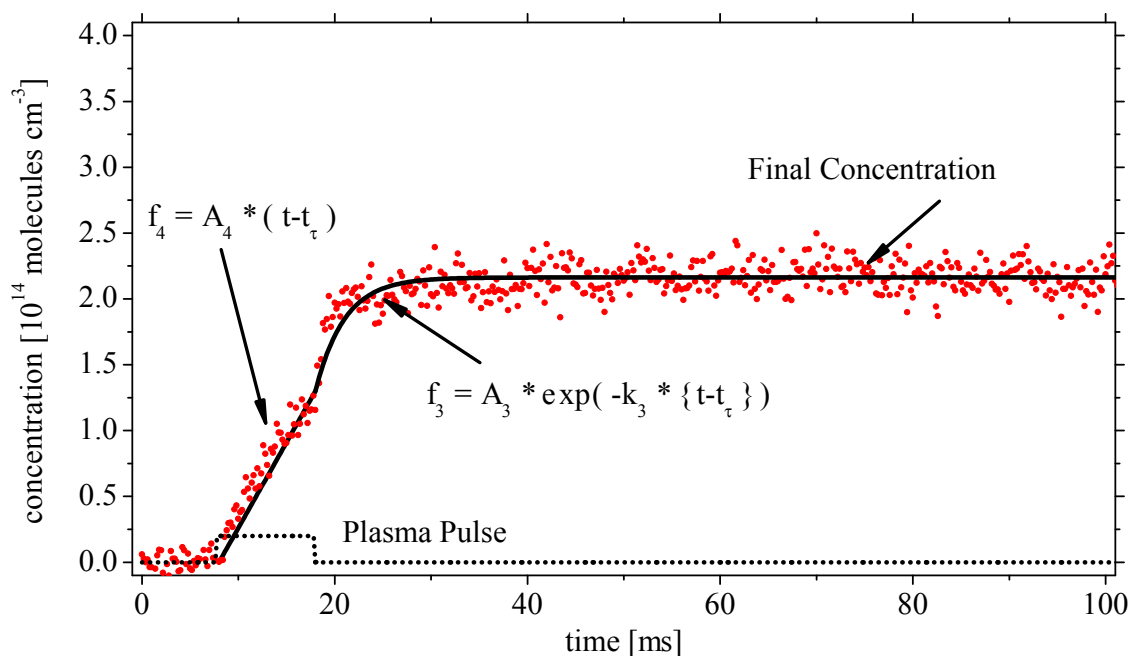
Figure 5.12: Typical temporally development of N_xO_y. The production during the pulse has been fitted to a linear function. The afterglow evolution has been fitted to an exponential growing function. For a better understanding, the NO production has been separately approximated by f_3.

sured species evolution decreases during the plasma pulse depending on the deposited energy. The measured concentration decreases never below a value of about $0.6 molecules\, cm^{-3}$. This corresponds to the size of the tubes death volume close to the windows. These are the parts of the tube left and right next to the T-shaped tube junction. From this, the tube region not treated by the plasma can be estimated to have a length $6 - 7cm$ at each side. For some experiments, it was possible to fit an exponential decaying function to the falling measured concentration right after the ignition. Directly after the end of the pulse, the measured evolution increases again or shows a constant value up to the end of the spectroscopic measurement. This depends on the initial gas mixture. In case of an increase of the measured concentration, it has been possible to fit an exponential growing function to the afterglow evolution. This function usually reaches a steady state within the measurements. Depending on the initial gas mixture, some experiments show the production of NO. An example is given in fig. 5.12. During the plasma pulse, the production usually followed a linear function (compare also Ref. [14]) starting at the beginning of the plasma pulse up to the end and has been fitted to a linear function. For the afterglow evolution, the measured concentration stays constant or undergoes an exponential grow. This, again, depends on the initial gas composition and is discussed later. The totally produced concentration has been measured in the steady state at the end of the measurement. The afterglow evolution in fig. 5.11 and in fig. 5.12 has been fitted to an exponential function representing

a reaction of the first order. From this, the first order rate coefficient k_i of the exponential fit function, defined in fig. 5.11 and 5.12, have been determined.

5.4.2 Degree of dissociation

The first results presented here are the degree of dissociation caused during the plasma pulse inside the tube reactor. For this purpose, the experiments have been done with an initial gas mixture of 1% N_xO_y in N_2 or 0.8% N_xO_y in air ($N_xO_y = N_2O$, NO or NO_2). The differences of the initial concentrations are because of the available mass flow controllers and do not play a crucial role in the study of the dissociation effects. Fig. 5.13 and fig. 5.14 show typical examples of the concentration evolution of the initial species. The steady states in the beginning and at the end serve as an indicator for stable conditions and are used to calculate the total dissociation independently of the highly time dependent processes during and right after the plasma pulse.
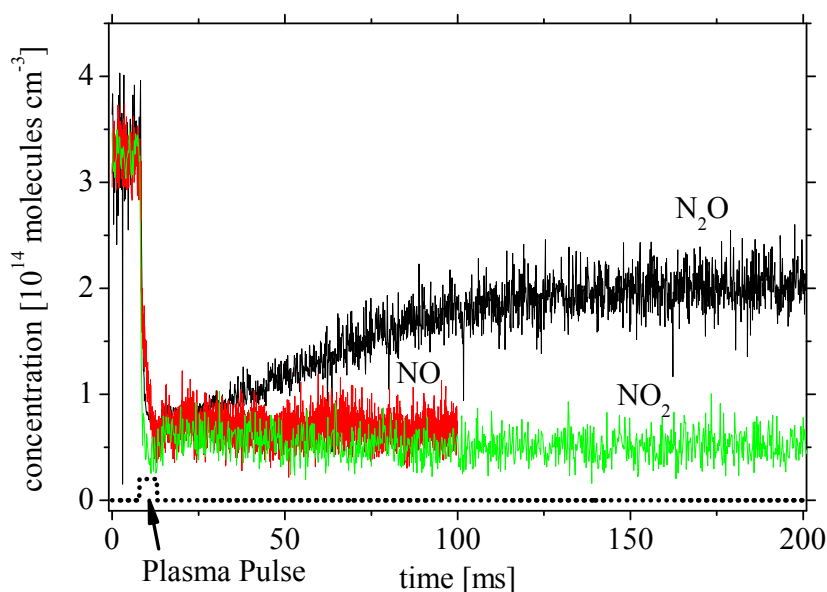
Figure 5.13: Typical example of the total dissociation of 1% N_xO_y in N_2. Here, the mean current has been $100mA$ for $5ms$ plasma pulse duration.

Several mean plasma currents ($25mA$, $50mA$, $100mA$ and $150mA$) have been used for different plasma pulse durations τ ($1ms$, $5ms$ and $10ms$). The important quantity for efficient pollution control is the energy consumed by the devices. Therefore, the energy has been calculated from the electrical circuit for each combination of the plasma pulse duration and the mean current. Fig. 5.15 and fig. 5.16 show the dissociation for all experiments as a function of the consumed energy for all used N_xO_y. The highest possible dissociation reached for all three nitrous oxides is about 80%. This is because of the limited active plasma volume. The first nitrous oxide, N_2O, is destroyed partly in both, N_2 and air. In N_2, the dissociation goes up to 40% for the conditions used here. In air, the total dissociation is less pronounced and reaches only about 20% for the same energy. The examples in fig. 5.13 and fig. 5.14 did consume energy of
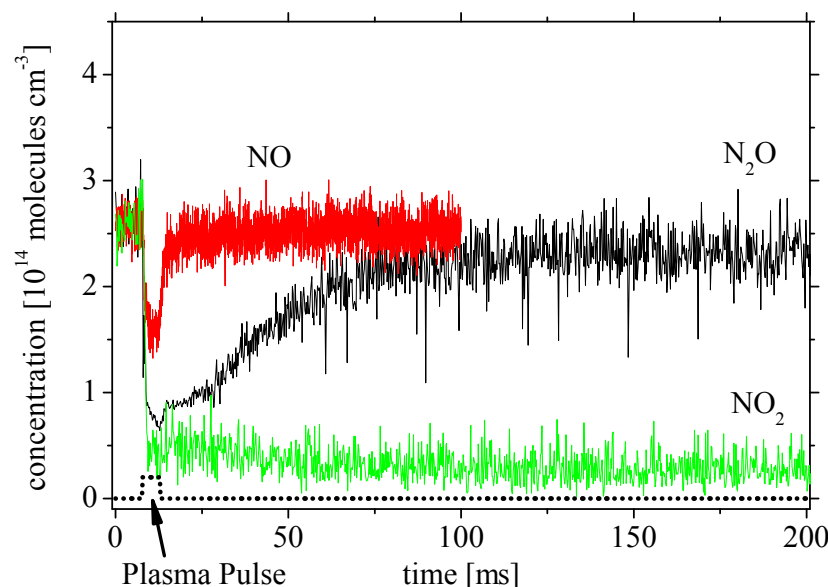
Figure 5.14: Typical example of the total dissociation of 0.8% N_xO_y in air. Here, the mean current has been $100mA$ for $5ms$ plasma pulse duration.

about $0.84J$ for N_2 and of about $0.89J$ for air. The second nitrous oxide, NO is destroyed almost completely at the highest consumed energy in N_2 that is about $0.84J$ for N_2. The total dissociation shows a saturation effect for higher energies. This corresponds to the fact that the active volume is cleaned from NO. Therefore, no increase of the dissociation can be detected. In air, NO shows no effective dissociation. This is mainly because of a re-production of NO during the plasma pulse in oxygen containing gas mixtures. The third nitrous oxide, NO_2 shows the highest dissociation. It is completely destroyed in both, N_2 and air. The high dissociation is reached even at much lower energy that is about $0.3J$ in N_2 and about $0.2J$ in air.

5.4.3   NO production in air like mixtures

The efficiency and profitability of a device used for pollution destruction is not only determined by the destruction of the pollution but also by the amount of species produced both in the active plasma region as well as in the afterglow. For a better characterization of the species production, the amount of the three nitrous oxides, N_2O, NO and NO_2, has been checked. These results are also used to verify modelling. The production of N_2O and NO_2 has not been seen in a pure N_2/O_2 gas mixture. That means the concentration has been below the detection limit of $5 \times 10^{12} molecules\, cm^{-3}$ for N_2O and $3.4 \times 10^{13} molecules\, cm^{-3}$ for NO_2, respectively. For NO, it has been possible to measure the ground state concentration, NO(X), during as well as in the afterglow. Fig. 5.12 shows a typical evolution. The first quantity determined is the totally produced amount of NO. This is calculated from the steady state of the concentration at the end of the measurement, since the gas is at room temperature. The NO production has been measured for three gas mixtures, namely 80% N_2 + 20% O_2, 50% N_2 + 50% O_2 and
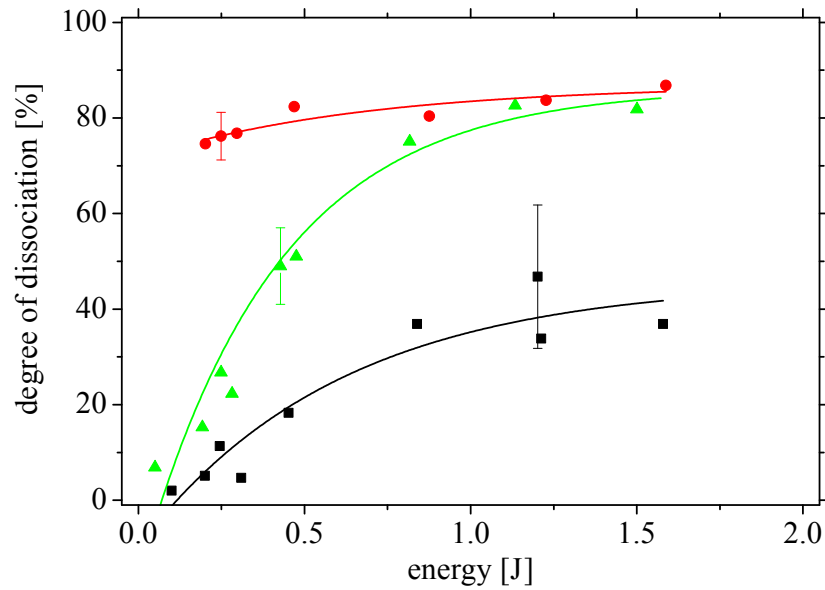
Figure 5.15: Degree of dissociation of the initial gas mixture (1% N_xO_y in N_2) as a function of the total energy, N_2O ($\blacksquare$, black), NO ($\blacktriangle$, green) and NO_2 ($\bullet$, red). The strongest dissociation has been found for NO_2. The solid lines are given to guide the eyes. The initial pressure has been 1.33*mbar*.

20% N_2 + 80% O_2 initial gas mixture. The pressure has been 1.3*mbar*. Tab. 5.3 lists the different parameters applied. A plot of produced NO depending on the consumed energy is given in fig. 5.17. Fig. 5.17 shows the NO production as a function of the consumed energy for three different N_2/O_2 mixing ratios. The production in air shows a linear relation with a slope of $0.99 \times 10^{14} molecules\, cm^{-3}\, J^{-1}$. The points ordered from left to right like they are listed from top to bottom in tab. 5.3. As one can see from fig. 5.17, the production depends linear on the overall consumed energy independently of the pulse duration or the plasma mean current. For the other air like mixtures, 50% N_2 + 50% O_2 and 20% N_2 + 80% O_2 a liner fit passing the origin leads to a NO(X) production of $1.17 \times 10^{14} molecules\, cm^{-3}\, J^{-1}$ and $0.71 \times 10^{14} molecules\, cm^{-3}\, J^{-1}$, respectively. The total amount of NO production is in good agreement with results reported in [14]. The authors were studying the NO formation in a similar reactor of similar dimensions at comparable plasma power and pressure for air. They reported that the NO production depends only on the product *mean current* times *pulse duration*. For example, they showed that a mean current of 80*mA* applied for 1*ms* and a mean current of 40*ms* applied for 2*ms* lead to the same NO concentration. These studies were done to investigate the influence of the vibrationally exited nitrogen to the NO concentration: N_2 (X, $v > 12$) + O $\rightarrow$ NO + N, proposed e.g. in [22]. From their discussion, the process N_2 (X, $v > 12$) + O $\rightarrow$ NO + N is fully balanced by the reverse process N + NO $\rightarrow$ N2 + O as long as this process is the main nitrogen loss mechanism. A simulation suggest that the NO concentration is mainly driven by the N_2^* (A) density. They concluded that NO is produced during the plasma pulse and in the early afterglow where the density of N_2^* (A) is still high enough. The time resolution of them has been
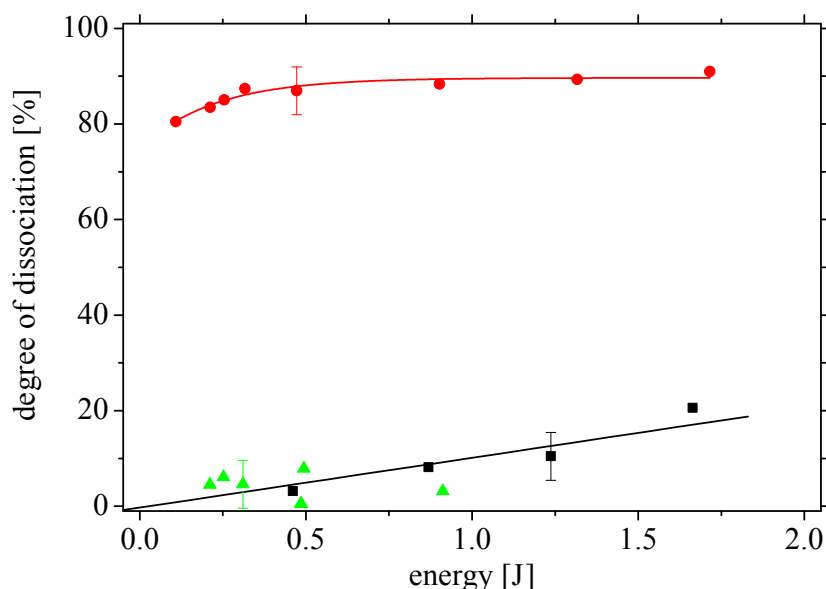
Figure 5.16: Degree of dissociation of the initial gas mixture (0.8% N_xO_y in air) as a function of the total energy, N2O (■ , black), NO (▲ , green) and NO_2 (● , red). Again, the strongest dissociation has been found for NO_2. The solid lines are given to guide the eyes. The initial pressure has been 1.33*mbar*.

about 14*ms*. Therefore, it has not been possible to follow the NO production during the plasma pulse. This limitation has been overtaken by the new developed TRIPLE Q system. The pulse repetition frequency of the QCLs used here has been f_{Rep} = 30*kHz*, leading to a whole spectra about each 34*μs*. The resulting time evolution of the NO concentration shows an almost linear production of NO during the plasma pulse. It has been possible to fit a linear function to the measurement. The production rate is given in tab. 5.4. The total amount of NO produced during the plasma pulse is equal to the product of the production times the pulse duration. These values are also given in tab. 5.4. From tab. 5.4, one can see that the NO production depends on both the mean current and the N_2/O_2 mixing ratio. For a 20% N_2 + 80% O_2 gas mixture, the NO production is almost independent on the mean current at about $0.83 \times 10^{16} molecules\,s^{-1}$. For a 50% N_2 + 50% O_2 mixing ratio and air (80% N_2 + 20% O_2) the NO production shows a clear dependency on the mean current. In general, one can conclude the greater the mean current the higher the NO production. In [14] the results have been also modelled using the software package 'Bolsig' [40] for an air mixture at 1.33*mbar* and a mean current of 55*mA*. For such parameters, the simulation calculated a NO production of about $4 \times 10^{13} molecules\,cm^{-3}$ for a 5*ms* plasma pulse and $1.5 \times 10^{14} molecules\,cm^{-3}$. In [29] a kinetic model was used to model an air mixture at 1.33*mbar* and a mean current of 40*mA*. The authors predicted a NO concentration for a 5*ms* plasma pulse to be $3 \times 10^{13} molecules\,cm^{-3}$ and about $7 \times 10^{13} molecules\,cm^{-3}$ for a 10*ms* plasma pulse. Both were done for reactor geometries and experimental conditions as they are described in this chapter. Although, both simulations calculate a NO density similar to each other, additional modelling should be applied using the experimental parameters in order

Table 5.3: Total produced amount of NO calculated from the steady state of the spectroscopic measurement. The measurements were done for different mean currents and varied plasma pulse duration. Different N_2/O_2 gas mixtures have been tested at 1.3*mbar*.

Gas Mixture	Pulse Duration [ms]	Mean Current [mA]	Consumed Energy [J]	NO Production $\left[10^{14} molecules\, cm^{-3}\right]$
80% N_2 + 20% O_2	5	50	0.56	0.572
	5	100	0.91	1.05
	5	150	1.31	1.32
	10	100	1.8	1.72
50% N_2 + 50% O_2	5	150	1.27	1.38
	10	100	1.69	2.07
20% N_2 + 80% O_2	5	150	1.14	0.70
	10	100	1.60	1.23

Table 5.4: Total calculated amount of NO at the end of the plasma pulse. The fourth column contains the production rate during the plasma pulse when fitted by a linear function.

| Gas Mixture	Pulse Duration [ms]	Mean Current [mA]	NO production $\left[10^{16} molecules\, s^{-1}\right]$	NO (at the end of the pulse) $\left[10^{14} molecules\, cm^{-3}\right]$
80% N_2 + 20% O_2	5	50	——	——
	5	100	——	——
	5	150	1.53	0.767
	10	100	1.09	1.09
50% N_2 + 50% O_2	5	150	1.61	0.809
	10	100	1.26	1.26
20% N_2 + 80% O_2	5	150	0.83	0.416
	10	100	0.837	0.837

to allow additional conclusions concerning the NO dependency on the mean current and the N_2/O_2 mixing ratio. The afterglow evolution of the NO concentration has also been studied. From fig. 5.12, one can see that the measured concentration right at the end of the plasma pulse, that is the very first *ms* of the afterglow, differs from the one later in the afterglow, view tens of *ms* after the plasma pulse. The NO density in the late afterglow, corresponding to the total amount of produced NO, for the different experiments is given in tab. 5.3 and the NO calculated density right at the end of the plasma pulse is given in tab. 5.4, both in the last column. As one can see, the calculated amount of NO right at the end of the plasma pulse is about 60% of the total produced amount of NO, measured at the steady states. This discrepancy can have several reasons, namely virationally relaxation, production or temperature effects. The temperature dependency of the line strength of the intermolecular transition has been corrected. However, the applied temperature evolution, fig. 3.22, has been only an estimation. Therefore,
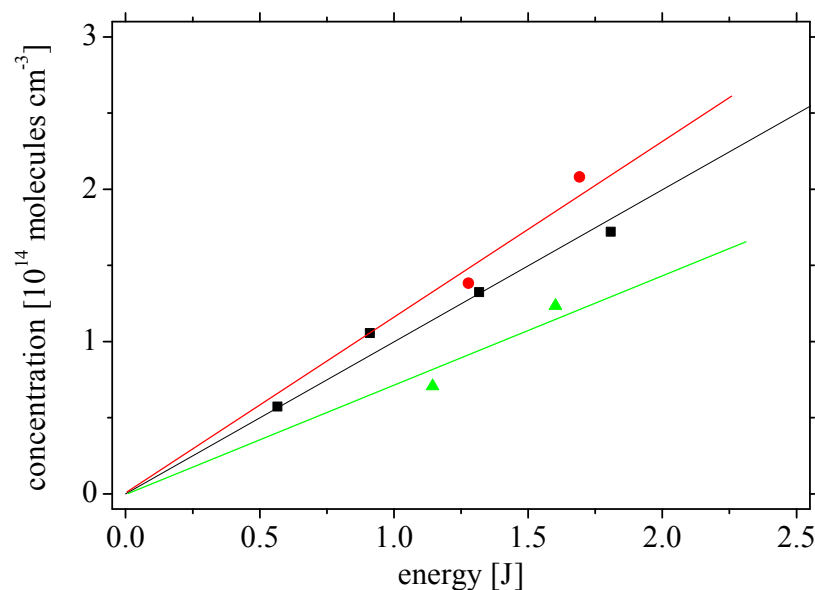
Figure 5.17: Total produced NO concentration for different N_2/O_2 mixtures depending on the total energy calculated from the steady state of the spectroscopic measurement, taken from tab. 5.3. The solid lines are presented to guide the eyes. From top to bottom: ● 50% N_2 + 50% O_2: $1.17 \times 10^{14} molecules\, cm^{-3}\, J^{-1}$, ■ 80% N_2 + 20% O_2: $0.99 \times 10^{14} molecules\, cm^{-3}\, J^{-1}$, ▲ 20% N_2 + 80% O_2: $0.71 \times 10^{14} molecules\, cm^{-3}\, J^{-1}$. Initial pressure: $1.3 mbar$.

this correction is further discussed. The temperature dependency of the line strength has to be regarded in case the gas temperature changes significantly since the population density of the ground state is influenced. In chapter 3, it has been shown that the temperature is in the order of $500K$. The corresponding line strength decreases down to about 80% compared to room temperature, fig. 5.18. The relaxation time of the gas temperature for such a geometry heated by a plasma pulse was calculated in [28] and found to be in the order of $3ms$ [27]. That means the gas would need about $3ms$ to reach room temperature. This is comparable with the time of the increase of the measured NO density in the very beginning of the afterglow period. However, the size of the abrupt increase may be considered. Therefore, to avoid any influence of the correction to the rough data, the time evolution of the integrated absorption coefficient K is considered here. Assuming that the temperature dependency of the line strength may be the only effect responsible for the abrupt increase of the measured NO density right after the plasma was switched off, the line intensity would have been dropped down to 60% of its room temperature value. Such a strong decrease corresponds to a gas temperature of about $750K$, fig. 5.18. Such a high temperature has never been measured neither in chapter 3 nor in [28]. This may become even more clear when one considers that such a high temperature as the mean temperature along the line of sight. Since absorption spectroscopy averages the influence of temperature effects along the line of sight, the temperature in the active volume would even be higher, about $830K$, assuming a trapezoidal temperature profile. A constant temperature between the electrode and a liner decrease to room temperature towards the windows is assumed. Therefore, one can
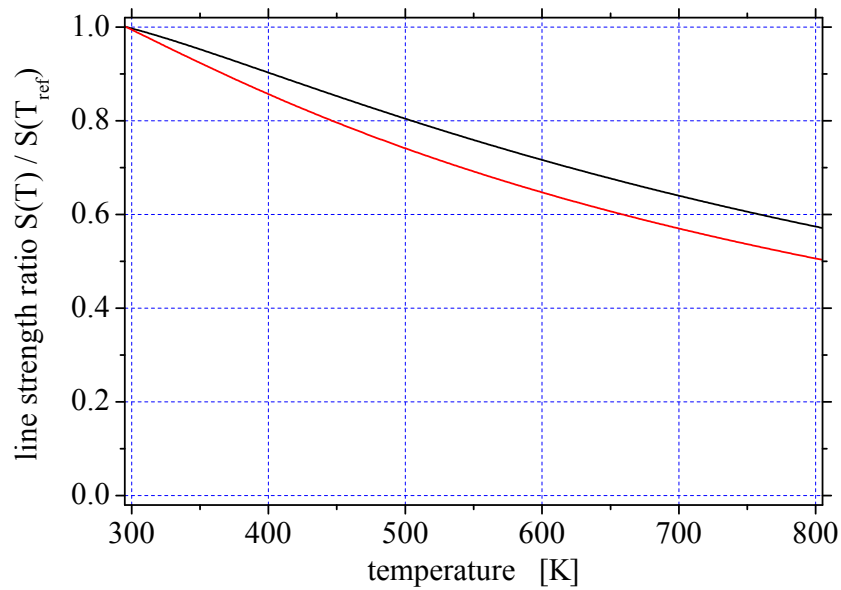
Figure 5.18: Correction factor for the line strength of NO at $1900.517cm^{-1}$, $NO\,(X_{3/2}, v_1 \leftarrow v_0 : R6.5)$, top. For comparison, the correction factor of the NO line at $1894.151cm^{-1}$, $NO\,(X_{3/2}, v_1 \leftarrow v_0 : R4.5)$, bottom, used in former experiments [27, 28] is given, too.

conclude that the temperature dependency of the line strength is not the only effect causing the abrupt increase in the measured NO concentration. Unfortunately, from the experiments done so far it is not possible to distinguish between the two other effects, namely vibrationally relaxation or NO production as proposed in [14]. This may be possible by repeating the same experiment with different initial NO concentrations assuming that slightly different NO concentration do not change the gas temperature significantly. Alternatively, the three pass alignment realised through a relatively small tube requires to consider the radial extend of the beam paths. That is, one beam might go close to the relatively cold tube walls another beam might go directly through the centre of the tube. Here, the temperature should be tendentially higher than close to the walls. Therefore, the measured decrease of the NO concentration right after the end of the plasma pulse might be caused by an averaging effect.

5.4.4 N_2O destruction during a single plasma pulse

For a separated study of the N_2O kinetics, a gas mixture of 1% N_2O diluted in N_2 and 0.8% N_2O diluted in air has been exposed to a DC plasma pulse. The total destruction caused by the plasma is shown in fig. 5.15 for N_2 and in fig. 5.16 for air. The time evolution given exemplarily in fig. 5.13 and 5.14 show a quite slow recovering of the $N_2O(X, v = 0)$ state. This effect could be caused either (i) by the temperature dependency of the line strength, (ii) by a production in the afterglow period or (iii) by vibrationally relaxation. Considering the temperature dependency, following HITRAN database for the line strength, would cause a correction factor less than 15%

for the considered temperature range. Additionally, the characteristic time constant of the gas cooling should be of the same order as it has been found for the temperature estimation using NO, that is $3ms$ [27, 28]. The experiments used for the NO production studies were also used to study the N_2O production. Non of these measurements showed the production of N_2O which means that the N_2O concentration has always been below $5 \times 10^{12} molecules\, cm^{-3}$. Therefore, it can be concluded that no N_2O is produced in the afterglow region and, therefore, does not contribute to the slow afterglow recovering of N_2O. At last, the long relaxation of the measured N_2O density, shown in fig. 5.13 and 5.14, approximated by f_2 in fig. 5.11, is considered to be caused by the vibrational relaxation of $N_2O(X, \nu = 0)$.

5.4.5   Hot band studies

Another indication for vibrational excitation of the N_2O molecule is discussed below. Fig. 5.19 shows a typical spectrum obtained for N_2O before the plasma pulse for 0.8% N_2O in air at $1.33mbar$. The two strong lines belong to the transition, line A: N_2O $2207.6203 cm^{-1}(00^01 - 00^00)$ P18e and line B: N_2O $2206.6588 cm^{-1}(00^01 - 00^00)$ P19e. Fig. 5.20 shows a spectrum recorded $600\mu s$ after the plasma pulse ignition. For this example, the mean plasma current has been $I_{mean} = 150mA$ and the pulse repetition frequency of the QCLAS system has been $20kHz$, leading to an entire spectrum each $50\mu s$. As one can see in fig. 5.20, new absorption structures appear. The determination of the spectral position of the new lines has been done with respect to the known spectral positions of the N_2O line A and line B using an Germanium etalon with a free spectral range, FSR, of about $0.049 cm^{-1}$, which has been recalculated for each spectrum. The new lines have been interimistically named: line G, at around $2206.6 cm^{-1}$, line F, at around $1107.4 cm^{-1}$ and line E, at around $2208.1 cm^{-1}$. The identification of the corresponding intermolecular transition has been done with the help of the HITRAN database. For that region, the transitions listed in the HITRAN database are given in tab. 5.5. For line G, only one transition is listed for that position. For the positions of line E and line F, several transitions are listed. In the following, the identification is discussed. The line strength, and therefore, the measured integrated absorption coefficient K as well, is influenced by the population density of the vibrational levels. Under plasma conditions, the distribution of the vibrational levels might differ from the thermal distribution. The true thermal distribution of the rotational levels J for a certain vibrational level ν is not known. In the following, it is assumed that the neighbour lines $J \pm 1$ of a certain line J is of similar intensity. That means, if a line with the rotational number J is detectable than the neighbour line with $J \pm 1$ will also be detectable. Vice versa, in the case a listed line with J is not seen, the lines with $J \pm 1$ will also not detectable. Following this assumption, line F can not contain line $2207.3986 cm^{-1}(03^11 - 03^10)$ R34f because the listed line at $2207.3329 cm^{-1}(03^11 - 03^10)$ R34e would clearly be resolved, which is not the case. The same idea can be used to separate line E and F. For both lines, HITRAN contains several transitions. Again in the case that line F and E contain the lines $2207.4005 cm^{-1}(01^11 - 01^10)$ Q22f and $2208.0728 cm^{-1}(01^11 - 01^10)$ Q23e, the lines $2207.585 cm^{-1}(01^11 - 01^10)$ Q21f should be detectable. As one can see from fig. 5.20, this is not the case. Therefore, the following identification of the new lines E, F, G can be assigned

   (i) line E: $2208.0929 cm^{-1}(00^02 - 00^01)$ R18e

(ii) line F: $2207.3940 cm^{-1}$ $(00^02 - 00^01)$ R17e

(iii) line G: $2206.6881 cm^{-1}$ $(00^02 - 00^01)$ R16e

Additionally, the time evolution of all the lines have been exemplary calculated and are shown in fig. 5.21. The discrepancy between line G and line E and F may be caused by the fact that line G lies very close to the stronger line B which may influence the calculation algorithm and / or the line shape itself. Therefore, in the following, line G is not considered further. Concluding, the new absorption structures have been identified to be the first hot band of N_2O $(00^02 - 00^01)$.

Table 5.5: The table contains the lines listed in the HITRAN database which are potentially overlapped in the spectra shown in fig. 5.20. The quantum numbers $v_1v_2l_2v_3$ indicated as follows: v_1 NO symmetric stretch vibration, v_2 bend vibration, l_2 contribution of the bending mode to the angular rotation and v_3 NN asymmetric stretch vibration [41, 42]. The marked lines are the identified ones appearing strongest during the plasma pulse.

Line G	Line F	Line E
$2206.6881 cm^{-1}$ $(00^02 - 00^01)$ R16e	$2207.3889 cm^{-1}$ $(01^11 - 01^10)$ Q28e	$2208.0728 cm^{-1}$ $(01^11 - 01^10)$ Q23e
	$2207.3940 cm^{-1}$ $(00^02 - 00^01)$ R17e	$2208.0888 cm^{-1}$ $(01^11 - 01^10)$ Q18f
	$2207.3986 cm^{-1}$ $(03^11 - 03^10)$ R34f	$2208.0929 cm^{-1}$ $(00^02 - 00^01)$ R18e
	$2207.4005 cm^{-1}$ $(01^11 - 01^10)$ Q22f	

Since the new absorption structures have been identified to belong to the first hot band of N_2O, extended vibrational studies have been possible. For this, a gas mixture of 1% N_2O in N_2 and 0.8% N_2O in air has been exposed to a plasma pulse. Different pulse durations, $1ms - 10ms$, with different mean plasma currents, $25mA - 150mA$, have been applied. Principally, independent on the mean current or the plasma pulse duration, the integrated absorption coefficient K of line E and line F, fig. 5.21 and fig. 5.22, increases very fast within the first $0.5ms$ of the plasma pulse. Afterwards, depending on the mean current, the signal decreases. Ones the plasma pulse has been switched off, the signal increases shortly and decreases to the zero level, usually before $300ms$, fig. 5.21. Fig. 5.23 and fig. 5.24 contain the evolution of the integrated absorption coefficients K of line F and line B for experiments using different mean plasma currents for a $5ms$ pulse duration ignited in 1% N_2O in N_2 at $1.33mbar$ and 0.8% N_2O in air at $1.33mbar$, respectively. From fig. 5.13 and fig. 5.14, it can be seen that the N_2O density decreases within $1ms$ which means that the ground state of N_2O is depopulated. On the other hand, fig. 5.23 and fig. 5.24 show that the first hot band is exited within less than $1ms$. The evolution of the integrated absorption coefficient K of line B, fig. 5.23 and fig. 5.24 has been fitted to an exponential function f_1 as it is defined in fig. 5.11. Only data values during the plasma
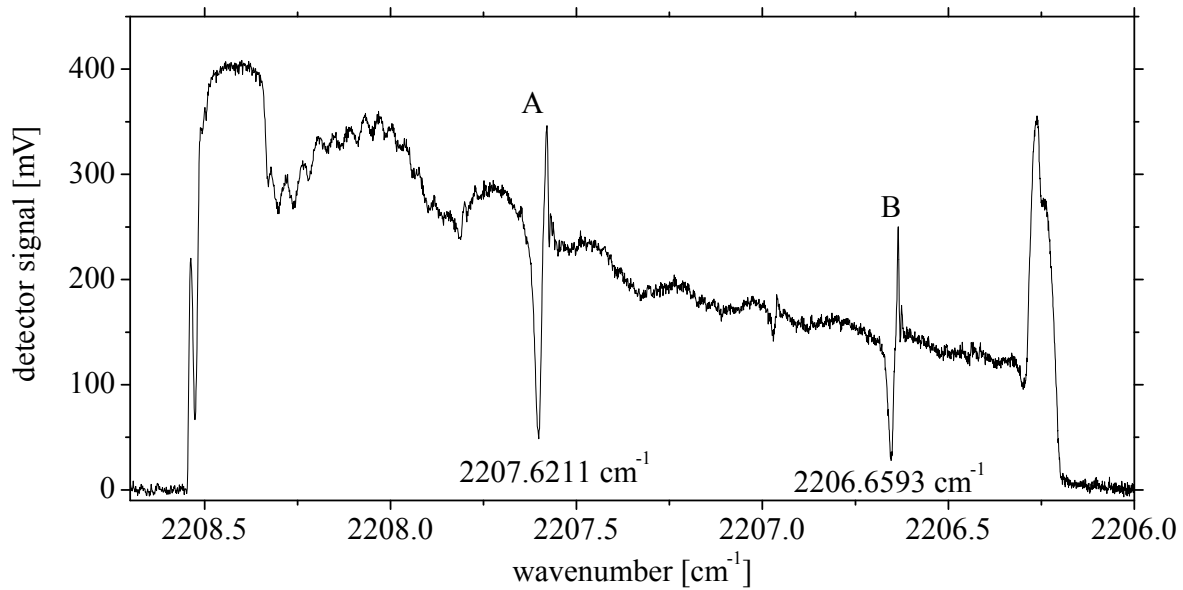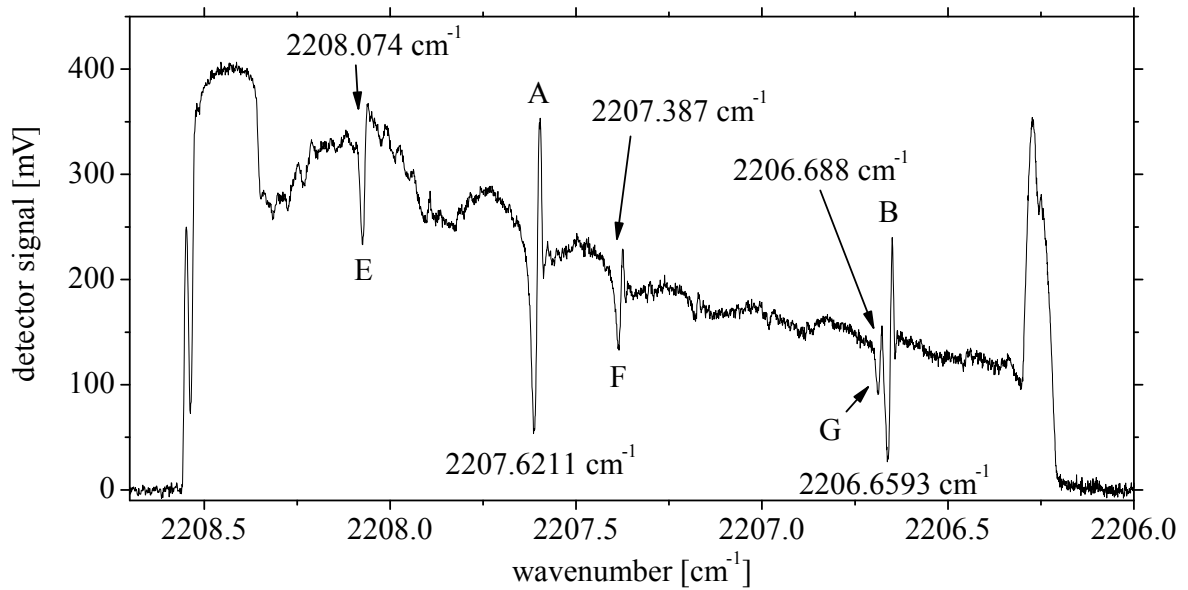
Figure 5.19: Spectrum of N_2O before the plasma pulse ignition at 1.33*mbar* for room temperature. The two lines belong to the transition: line A: N_2O 2207.6203cm^{-1} $\left(00^01 - 00^00\right)$ P18e, and line B: N_2O 2206.6588cm^{-1} $\left(00^01 - 0000\right)$ P19e.

pulse have been included in the fitting routine. The resulting reaction rate constant k_1 for each experiment as a function of the mean plasma current is given in fig. 5.25. As one can see from fig. 5.25, the reaction rate constant k_1 can be approximated by a linear function of the mean plasma current. The slope is about $13 \times 10^3 s^{-1} mA^{-1}$, for N_2O in N_2 and about $10 \times 10^3 s^{-1} mA^{-1}$ for N_2O in air. That means, the depopulation of the N_2O (X, $v = 0$) state tends to be slower in air than in N_2. Additionally, fig. 5.23 and fig. 5.24 show also the evolution of the integrated absorption coefficient K of line F. The evolution within the plasma pulse can be described by a production process in the very beginning of the pulse and by a destruction process. Both have been done by an exponential function. Consequently, the whole approximation function can be formulated:

$$f_{\text{approx}} = \text{Const.} + \text{Production} + \text{Destruction} \qquad (5.10)$$

$$f_{\text{approx}} = \text{Const.} + A_1 \cdot \exp\left(-k_1 \cdot t\right) + A_2 \cdot \exp\left(-k_2 \cdot t\right) \qquad (5.11)$$

For the discussion following, only the reaction rate constants k_1 for the production process is considered here. The noise of the measurements avoids the determination of the other fitting parameters; these are A_1, A_2, k_2 and Const. The k_1 values as a function of the mean plasma current are given in fig. 5.26. As one can see, the reaction rate constant k_1 for N_2O in N_2 as a function of the mean plasma current is about $56 \times 10^3 s^{-1} mA^{-1}$ and about $73 \times 10^3 s^{-1} mA^{-1}$ for N_2O in air. That means, that the population of the $v = 1$ state of N_2O is much faster populated. Additionally, the population is faster in air than in N_2.   The presented investigations allow studying the vibrational excitation of N_2O. In fig. 5.21, an overview of the temporal evolution

Figure 5.20: Spectrum of N_2O recorded $600\mu s$ after the plasma pulse ignition. The new lines have been identified with the help of the HITRAN database: line E: $2208.0929cm^{-1}\left(00^02-00^01\right)$ R18e, line F: $2207.3940cm^{-1}\left(00^02-00^01\right)$ R17e, line G: $2206.6881cm^{-1}\left(00^02-00^01\right)$ R16e.

of the integrated absorption coefficients K of several absorption lines are shown. It can be seen, that the intensities of line A and line B reach a steady state after about 150ms. At the same time, the hot bands, line E and line F, reach a maximum tens of ms after the plasma pulse. Finally, they reach the detection limit after about 200ms after the plasma pulse. Fig. 5.25 and fig. 5.26 show that for both, N_2O in air as well as N_2O in N_2, cause a faster population of the $v = 1$ state than the depopulation of the $v = 0$ state. Therefore, it can be concluded that state $v = 1$ must be populated by additional reaction channels. Additionally, the experiments have also be done for several pulse durations, 1ms, 5ms, 7ms and 10ms. Fig. 5.27 shows the evolution for N_2O in N_2 for line B and line F. Fig. 5.28 shows the evolution for N_2O in air. As one can see, especially for longer pulses of 10ms, the intensity of line F reaches a steady state during the last third of the pulse duration. On the other hand, for short pulses, about 1ms, the intensity of line F exist at the similar level as at the end of the plasma pulse.
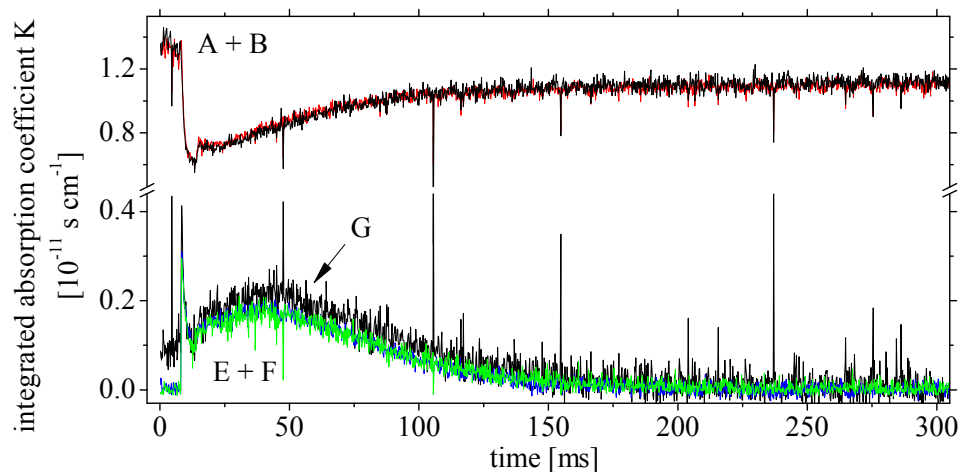
Figure 5.21: As an example, the temporally behaviour of the intensity of the absorption lines indicating the relative intensities. From top to bottom: line B: N_2O $2206.6588cm^{-1}$ $\left(00^01 - 00^00\right)$ P19e, line A: N_2O $2207.6203cm^{-1}$ $\left(00^01 - 00^00\right)$ P18e, line E: $2208.0929cm^{-1}$ $\left(00^02 - 00^01\right)$ R18e, line F: $2207.3940cm^{-1}$ $\left(00^02 - 00^01\right)$ R17e and line G: $2206.6881cm^{-1}$ $\left(00^02 - 00^01\right)$ R16e. Line E and F are coincident, whereas line G shows a disturbance and is not considered further.
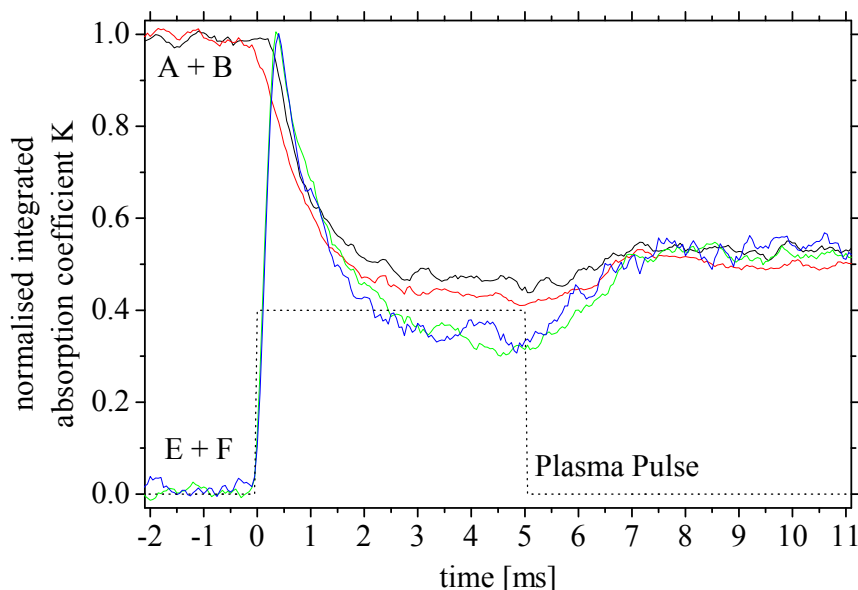

Figure 5.22: Normalised line intensities during a *5ms* plasma pulse, zoom of fig. 5.21, presented as an example. The gas mixture was 0.8% N_2O in air at 1.33*mbar*.
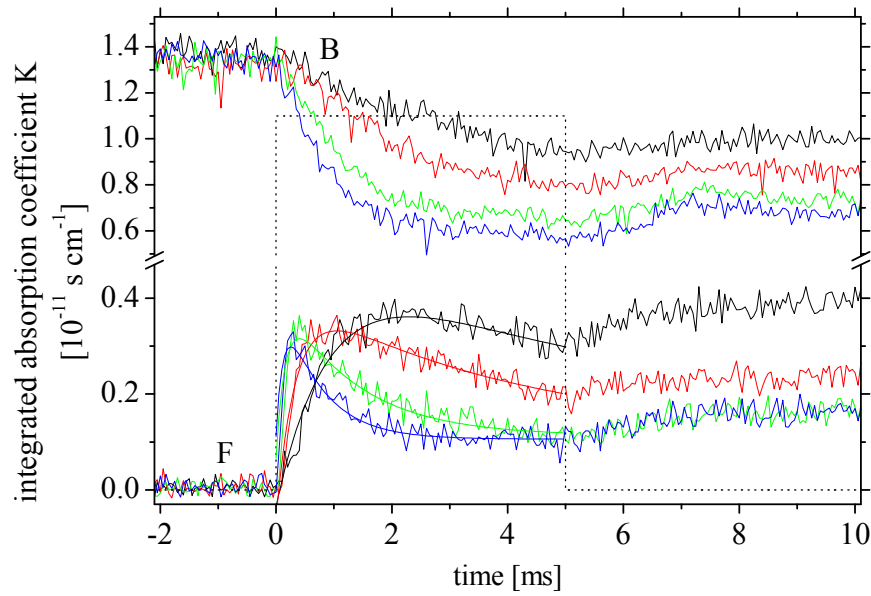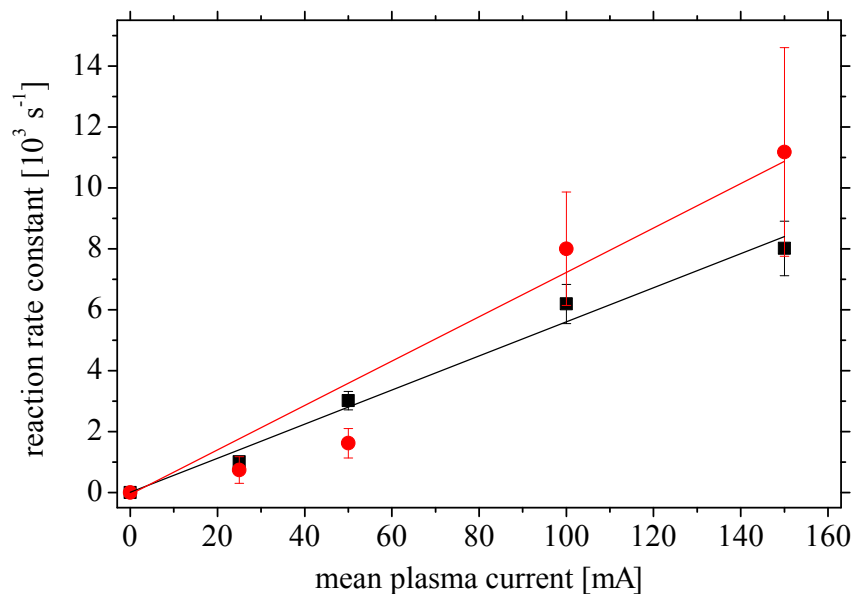
Figure 5.23: Time evolution of the intensity of line B: N_2O $2206.6588cm^{-1}$ $\left(00^01 - 00^00\right)$ P19e and of line F: $2207.3940cm^{-1}$ $\left(00^02 - 00^01\right)$ R17e for a $5ms$ plasma pulse (dotted). The mean plasma current has been: $25mA$ (black), $50mA$ (red), $100mA$ (green) and $150mA$ (blue). The initial gas mixture was 1% N_2O in N_2 at $1.33mbar$.
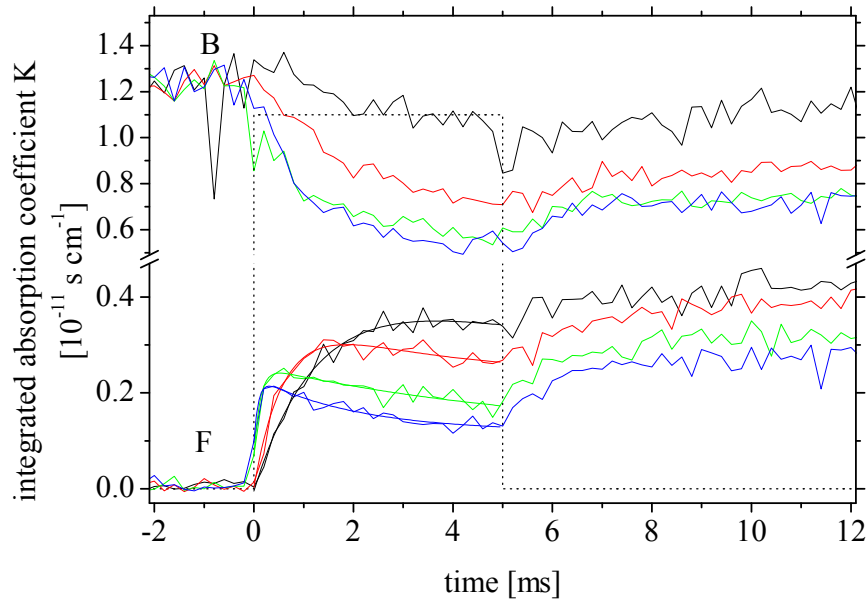
Figure 5.24: Time evolution of the intensity line B: N_2O $2206.6588cm^{-1}$ $\left(00^01 - 00^00\right)$ P19e and of line F: $2207.3940cm^{-1}$ $\left(00^02 - 00^01\right)$ R17e for a $5ms$ plasma pulse. The mean plasma current has been: $25mA$ (black), $50mA$ (red), $100mA$ (green) and $150mA$ (blue). The initial gas mixture was 0.8% N_2O in air at $1.33mbar$.
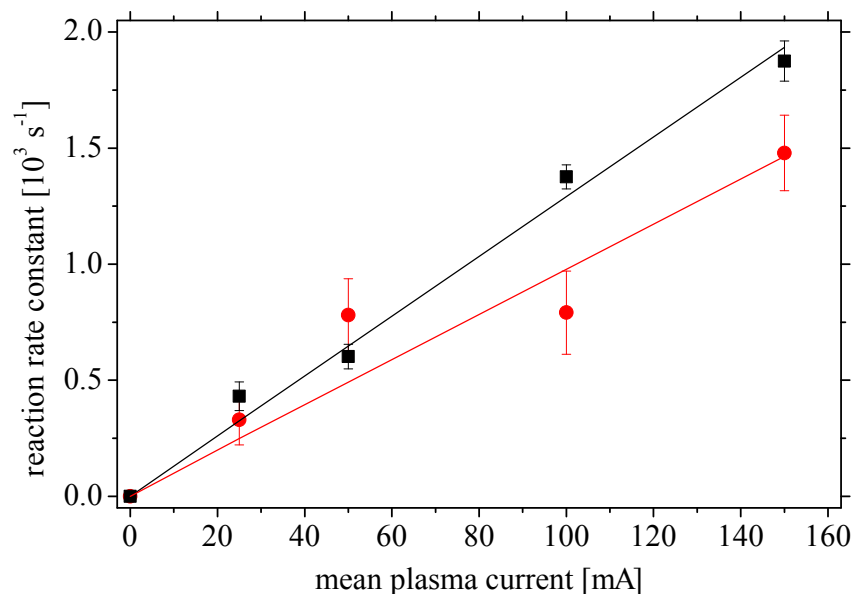
Figure 5.25: Dependency of the reaction rate constant k as a function of the mean plasma current of the integrated absorption coefficient K of the line B for a 5*ms* plasma pulse. The gas mixture has been 0.8% N_2O in air (●) and 1% N_2O in N_2 (■) at 1.33*mbar*.
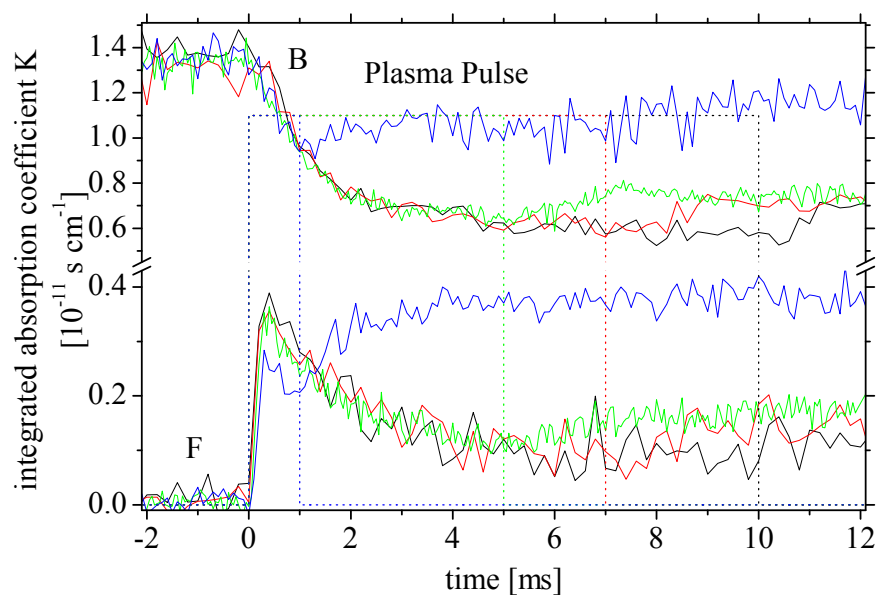

Figure 5.26: Dependency of the reaction rate constant k as a function of the mean plasma current of the integrated absorption coefficient K of the line F for a 5*ms* plasma pulse. The gas mixture has been 0.8% N_2O in air (●) and 1% N_2O in N_2 (■) at 1.33*mbar*.

Figure 5.27: Time evolution of the intensity of line F: $2207.3940 cm^{-1} \left(00^02 - 00^01\right)$ R17e for a plasma pulse of $1ms$ (blue), $5ms$ (green), $7ms$ (red) and $10ms$ (black). The mean plasma current has been $100mA$. The initial gas mixture was 1% N_2O in N_2 at $1.33mbar$.
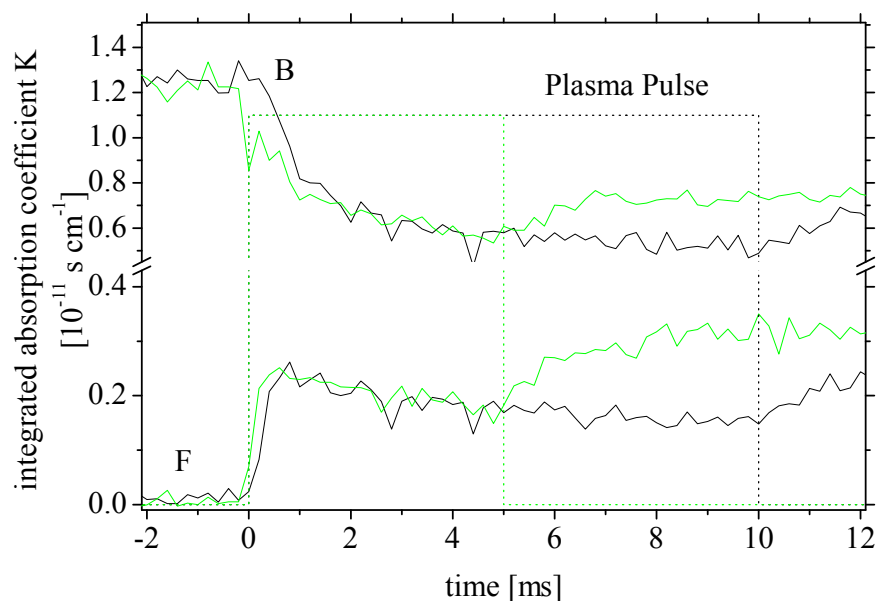

Figure 5.28: Time evolution of the intensity of line F: $2207.3940 cm^{-1} \left(00^02 - 00^01\right)$ R17e for a plasma pulse of $5ms$ (green) and $10ms$ (black). The mean plasma current has been $100mA$. The initial gas mixture was 0.8% N_2O in Air at $1.33mbar$.

5.4.6   Afterglow relaxation of N$_2$O

In the afterglow, the temporally behaviour of the N$_2$O concentration shows a relatively slow relaxation. That is, a steady state is reached after tens of *ms* after the plasma pulse. For example, the intensity of the lines of NO, fig. 5.14, reach a steady state within few *ms*. For N$_2$O, it is seen that the stable level of the concentration is reached after about 100*ms*. Fig. 5.29 and fig. 5.30 show the time evolution of the N$_2$O concentration in the afterglow period. The initial N$_2$O concentration has been again 1% N$_2$O in N$_2$ and 0.8% N$_2$O in air both at an initial pressure of 1.33*mbar*. For each gas mixture, three different mean plasma currents have been used, 50*mA*, 100*mA* and 150*mA*. In this chapter, the hypotheses is discussed that this long term effect is caused by a vibration vibration (V - V) coupling of N$_2$ to N$_2$O. From fig. 5.29 and fig. 5.30 it

Table 5.6: Reaction rate constant k_2 of an exponential fit applied to the afterglow period of the measurement. For the definition of the fitting function see fig. 5.11. As one can see, the reaction rate constant is bigger for air than for N$_2$. Additionally, the reaction rate constant is also bigger for smaller values of the mean plasma currents.

Mean Current [mA]	Reaction Rate Constant k_2 in N$_2$ $\left[s^{-1}\right]$	Reaction Rate Constant k_2 in air $\left[s^{-1}\right]$
50	28.7	40.9
100	22.1	39
150	18.2	35.7
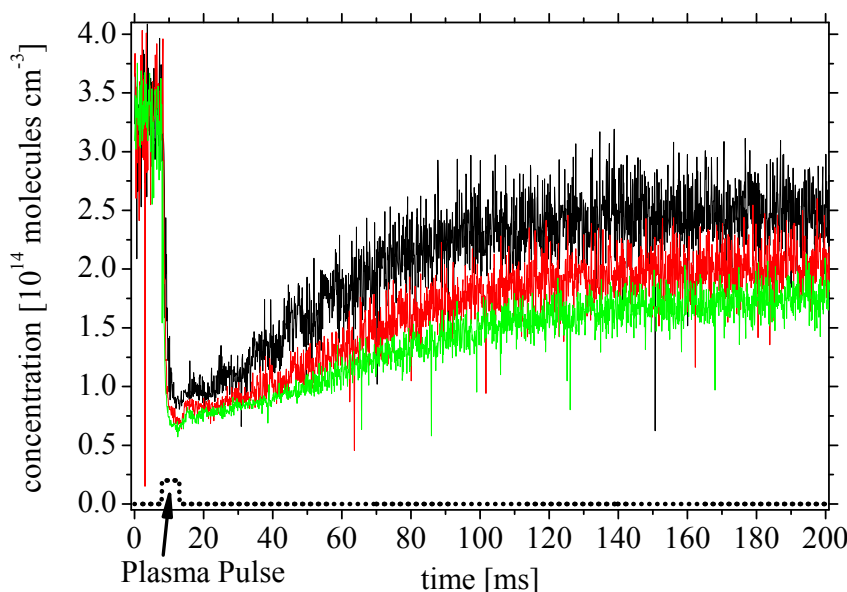
Figure 5.29: Time evolution of N$_2$O in the afterglow period for different mean currents (top: 50*mA*, middle: 100*mA*, bottom: 150*mA*). The initial concentration has been 1% N$_2$O in N$_2$ at 1.33*mbar*. The pulse duration was 5*ms*.
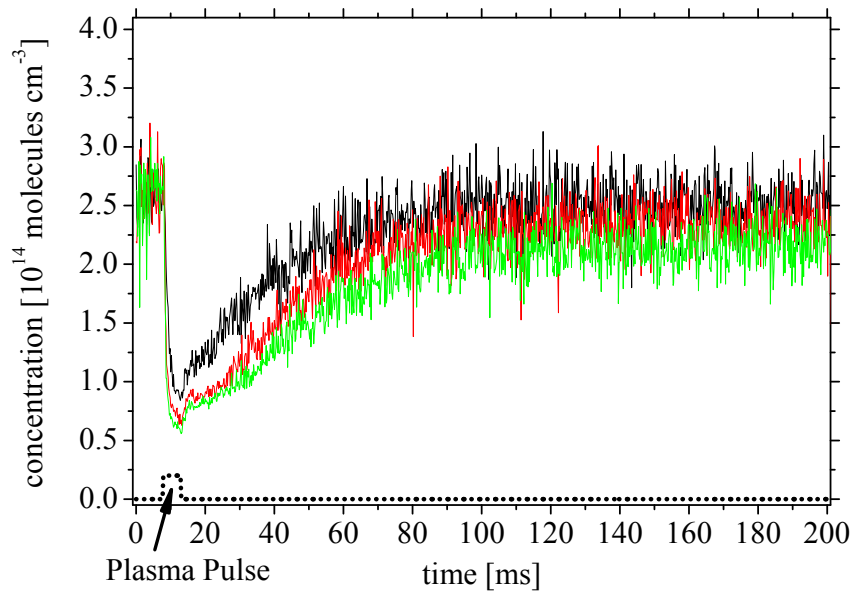
Figure 5.30: Time evolution of initially 0.8% N_2O at 1.33*mbar* in air for different mean currents, top: 50*mA*, middle: 100*mA*, bottom: 150*mA*. The pulse duration was 5*ms*.

can be seen that the total dissociation, see also fig. 5.11, is less pronounced in air than in pure N_2. Additionally, the relaxation of the measured N_2O concentration relaxes faster in air than in nitrogen, which is indicated by the reaction rate constant k_2 in tab. 5.6 5.6. To estimate the differences, an exponential fit to the afterglow period of the measured concentration of N_2O, f_2 in fig. 5.11, has been done. The corresponding reaction rate constant k_2 is given in tab. 5.6. The appearance of the hot band suggests already that the N_2O molecule is highly vibrationally excited. Their appearance, fig. 5.23 and fig. 5.24, compared with the time evolution of the fundamentals, allow to study the temporally de-excitation. In the literature, three processes are discussed on witch vibration de-excitation of the N_2O molecule can occur, [43]: (i) First, quenching is considered. These intermolecular collisions can transfer the vibrational energy into kinetic energy of the collisions partner. This conversion rate depends on the collision frequency, i.e. pressure and temperature. (ii) Second, diffusion to the wall followed by vibrational de-excitation. The vibrationally exited molecules can reach the surface of the discharge vessel and can undergo a wall induced de-excitation. This process depends not only on the diffusion velocity, i.e. pressure and temperature but also on the geometry of the discharge vessel as well as the wall-de-excitation efficiency. (iii) Third, the vibration energy can be released by radiation. The rate is given by the Einstein coefficient of spontaneous emission. The total rate of de-excitation can be reduced because of re-absorption of the surrounding molecules. This is governed by the gas pressure and the geometry of the discharge volume. In [43], a fluorescence decay method has been used to study the de-excitation. It was found that the fluorescence decay follows an exponential decay:

$$I = I_0 \cdot \exp\left(-\beta \cdot t\right) \tag{5.12}$$

where β is the relaxation constant and describes how fast the molecules do de-excite. Here β takes all three processes into account. For this reason β is the sum of the single relaxation constants of each process. Therefore, $\beta = K + \delta + \pi_P$, where K corresponds to the quenching decay (process i), δ to the wall induced decay (process ii) and π_P to the radiative decay (process iii). These three relaxation constants have been published in [43] as a function of the pressure ranging from 0.06 up to 4*mbar*. For the conditions, pressure and tube diameter, used in the studies discussed here, these parameters are: $K = 745\,s^{-1}$, $\delta = 414\,s^{-1}$, $\pi_P = 248\,s^{-1}$. The values for K and δ have been taken for 1.3*mbar* total pressure since collision and diffusion depend on the total pressure. On the other hand, π_P was taken for 0.06*mbar* because the radiative decay is influenced by the self-absorption and therefore depends on the partial pressure. The smallest listed pressure in [43], 0.06*mbar*, is five times higher than the partial pressure used in the experiments here. However, the relaxation constant for 0.013*mbar* would be even higher. Nevertheless, for further discussions the π_P value corresponding to 0.06*mbar* is used in the following. Including all these relaxation constants (K, δ, π_P) into 5.12 leads to the fact that the amount of vibrationally excited N_2O should be reduced below 1% of the initially total amount of vibrationally excited N_2O, within 3 to 4*ms*. This conclusion leads to the question: Where does the energy comes from re-exiting N_2O in the afterglow period? The hypotheses suggested here is that this energy comes from the vibration vibration transition (V - V) transfer between vibrationally excited N_2 to N_2O. This is because of the fact that the vibration energy of N_2 is close to the one for N_2O. On the other hand, the vibration energy of O_2 is much different and therefore, the V - V coupling between O_2 and N_2O is neglected here. Additionally, O_2 is much less vibrationally excited during the plasma pulse compared with N_2. Therefore, this has become a useful tool to study vibrationally exited N_2 indirectly by the investigation of N_2O.

### 5.4.7 N_2O in Air; NO production

The dissociation of N_2O can be determined from the steady state at the end of the spectroscopic measurement as it has been shown above. The main dissociation channel might be electron impact. Nitrous oxide, N_2O, is an asymmetric linear molecule with a triple bond between the two nitrogen atoms and a double bond between the oxygen atom and one of the nitrogen atoms. Principally, electron impact might lead to a dissociation of either the triple or double bond or both. Additionally, other species produced in the plasma can help the dissociation of N_2O to be happen, e.g. atomic oxygen. The corresponding chemical reactions are:

$$N_2O + e \rightarrow NO + N + e \tag{5.13}$$

$$N_2O + e \rightarrow N_2 + O + e \tag{5.14}$$

$$N_2O + O\left(^1D\right) \rightarrow 2NO \tag{5.15}$$

The influence of the different channels has been studied by comparing the NO production both in air and in air admixed with 0.8% N_2O used as a initially gas mixture. The NO density evolution during and after a 5*ms* plasma pulse with different mean currents is given in fig. 5.25 for pure air and in fig. 5.26 for air admixed with N_2O. As one can see from fig. 5.25 and fig.
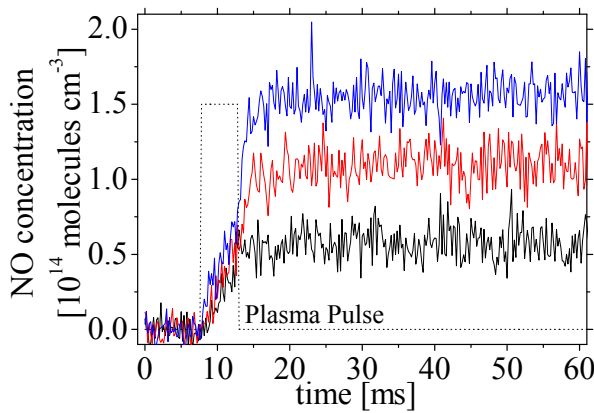
Figure 5.31: Production of NO after a 5*ms* plasma pulse. The gas mixture was 0.8% N_2O in air at 1.33*mbar*. The mean plasma current has been, from top to bottom: 150*mA*, 100*mA* and 50*mA*.
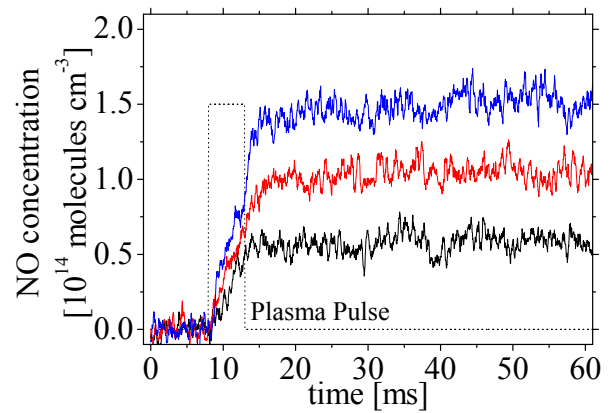
Figure 5.32: Production of NO after a 5*ms* plasma pulse. The gas mixture was air only at 1.33*mbar*. The mean plasma current has been, from top to bottom: 150*mA*, 100*mA* and 50*mA*.

5.26, the NO density is comparable. The steady state value is the same for each mean current. The conversion of N_2O into NO following the reaction channels 1 or 3 would increase the NO density. This production should be detectable even in the late afterglow. Therefore, reaction channel 1 and 3 does not play a significant role for the increase of the NO density. In [14] it is discussed that the NO production reaction $N_2 + O \rightarrow NO + N$ is fully balanced by the reverse reaction $N + NO \rightarrow N_2 + O$. It can be argued that this reaction limits the NO density in case of N_2O admixture. But, to balance reaction 1 means that the NO density is the dominating reactant. It further means that the N density is much higher than the NO density and can, therefore, be treated to be constant. In such a case, however, N exist much higher, it makes no sense to have any NO left since any NO molecules should be destroyed by the reverse reaction $N + NO \rightarrow N_2 + O$.

Bibliography

[1] E. A. Filimonova, R. H. Amirov, H. T. Kim, and I. H. Park. Comparative modelling of NO_x and SO_2 removal from pollutant gases using pulsed-corona and silent discharges. *Journal of Physics D-Applied Physics*, **33**:1716, (2000).

[2] E. A. Filimonova. Multiparametric investigation on NO_x removal from simulated diesel exhaust with hydrocarbons by pulsed corona discharge. *Journal of Physics D: Applied Physics*, **35**:2795, (2002).

[3] R. McAdams. Prospects for non-thermal atmospheric plasmas for pollution abatement. *Journal of Physics D-Applied Physics*, **34**:2810, (2001).

[4] B. M. Penetrante, S. E. Schultheis, and North Atlantic Treaty Organization. Scientific Affairs Division. *Non-thermal plasma techniques for pollution control*. NATO ASI series. Series G, Ecological sciences. Springer-Verlag, (1993).

[5] E. M. v. Veldhuizen. *Electrical discharges for environmental purposes : fundamentals and applications*. Nova Science Publishers, (2000).

[6] T. Yamamoto. VOC decomposition by nonthermal plasma processing – a new approach. *Journal of Electrostatics*, **42**:227, (1997).

[7] O. Guaitella, F. Thevenet, C. Guillard, and A. Rousseau. Dynamic of the plasma current amplitude in a barrier discharge: influence of photocatalytic material. *Journal of Physics D-Applied Physics*, **39**:2964, (2006).

[8] O. Guaitella, F. Thevenet, E. Puzenat, C. Guillard, and A. Rousseau. C2h2 oxidation by plasma/tio2 combination: Influence of the porosity, and photocatalytic mechanisms under plasma exposure. *Applied Catalysis B-Environmental*, **80**:296, (2008).

[9] F. Holzer. Oxidation von organischen Verbindungen unter Nutzung von porösen und unporösen Feststoffen im nichtthermischen Plasma, (2003).

[10] F. Thevenet, O. Guaitella, E. Puzenat, J. M. Herrmann, A. Rousseau, and C. Guillard. Oxidation of acetylene by photocatalysis coupled with dielectric barrier discharge. *Catalysis Today*, **122**:186, (2007).

[11] A. E. Wallis, J. C. Whitehead, and K. Zhang. Plasma-assisted catalysis for the destruction of CFC-12 in atmospheric pressure gas streams using TiO_2. *Catalysis Letters*, **113**:29, (2007).

[12] G. Cartry, X. Duten, and A. Rousseau. Atomic oxygen surface loss probability on silica in microwave plasmas studied by a pulsed induced fluorescence technique. *Plasma Sources Science & Technology*, **15**:479, (2006).

[13] O. Guaitella, K. Allegraud, C. Lazzaroni, and A. Rousseau. Reversible adsorption of o atoms on TiO_2 surface: an explanation for plasma/TiO_2 synergy for C_2H_2 removal. In 19th *Europhysics Conference on the Atomic and Molecular Physics of Ionized Gases*, Granada, Spain, 2008.

[14] L. V. Gatilova, K. Allegraud, J. Guillon, Y. Z. Ionikh, G. Cartry, J. Röpcke, and A. Rousseau. NO formation mechanisms studied by infrared laser absorption in a single low-pressure plasma pulse. *Plasma Sources Science & Technology*, **16**:S107, (2007).

[15] C. D. Pintassilgo, O. Guaitella, and A. Rousseau. Heavy species kinetics in low-pressure dc pulsed discharges in air. *Plasma Sources Science & Technology*, **18**, (2009).

[16] O. Guaitella, M. Hübner, S. Welzel, D. Marinov, J. Röpcke, and A. Rousseau. Evidence for surface oxidation on pyrex of NO into NO_2 by adsorbed o atoms. *Plasma Sources Science & Technology*, **19**, (2010).

[17] V. Guerra. Analytical model of heterogeneous atomic recombination on silicalike surfaces. *IEEE Transactions on Plasma Science*, **35**:1397, (2007).

[18] Y. C. Kim and M. Boudart. Recombination of O,N and H-atoms on silica - kinetics and mechanism. *Langmuir*, **7**:2999, (1991).

[19] M. Castillo, V. J. Herrero, I. Mendez, and I. Tanarro. Spectrometric and kinetic study of a modulated glow air discharge. *Plasma Sources Science & Technology*, **13**:343, (2004).

[20] M. Castillo, I. Mendez, A. M. Islyaikin, V. J. Herrero, and I. Tanarro. Low-pressure dc air plasmas. investigation of neutral and ion chemistry. *Journal of Physical Chemistry A*, **109**:6255, (2005).

[21] B. F. Gordiets, C. M. Ferreira, V. L. Guerra, J. Loureiro, J. Nahorny, D. Pagnon, M. Touzeau, and M. Vialle. Kinetic-model of a low-pressure N-2-O-2 flowing glow-discharge. *IEEE Transactions on Plasma Science*, **23**:750, (1995).

[22] V. Guerra and J. Loureiro. Nonequilibrium coupled kinetics in stationary N-2-O-2 discharges. *Journal of Physics D-Applied Physics*, **28**:1903, (1995).

[23] V. Guerra and J. Loureiro. Self-consistent electron and heavy-particle kinetics in a low-pressure N_2 O_2 glow discharge. *Plasma Sources Science & Technology*, **6**:373, (1997).

[24] I. A. Kossyi, A. Y. Kostinsky, A. A. Matveyev, and V. P. Silakov. Kinetic scheme of the non-equilibrium discharge in nitrogen-oxygen mixtures. *Plasma Sources Science & Technology*, **1**:207, (1992).

[25] J. Nahorny, C. M. Ferreira, B. Gordiets, D. Pagnon, M. Touzeau, and M. Vialle. Experimental and theoretical investigation of a N-2-O-2 dc flowing glow-discharge. *Journal of Physics D-Applied Physics*, **28**:738, (1995).

[26] C. D. Pintassilgo, J. Loureiro, and V. Guerra. Modelling of a N-2-O-2 flowing afterglow for plasma sterilization. *Journal of Physics D-Applied Physics*, **38**:417, (2005).

[27] D. Marinov, O. Guaitella, A. Rousseau, and Y. Ionikh. Production of molecules on a surface under plasma exposure: example of NO on pyrex. *Journal of Physics D-Applied Physics*, **43**:7, (2010).

[28] S. Welzel, L. Gatilova, J. Röpcke, and A. Rousseau. Time-resolved study of a pulsed dc discharge using quantum cascade laser absorption spectroscopy: NO and gas temperature kinetics. *Plasma Sources Science & Technology*, **16**:822, (2007).

[29] C. D. Pintassilgo, V. Guerra, O. Guaitella, and A. Rousseau. Modelling of an afterglow plasma in air produced by a pulsed discharge. *Plasma Sources Science & Technology*, **19**:14, (2010).

[30] V. A. Godyak, R. B. Piejak, and B. M. Alexandrovich. Electrical characteristics of parallel-plate rf discharges in argon. *IEEE Transactions on Plasma Science*, **19**:660, (1991).

[31] NPC. Neoplas control, http://www.neoplas-control.de/, (2011).

[32] K. I. Hadjiivanov. Identification of neutral and charged N_xO_y surface species by IR spectroscopy. *Catalysis Reviews-Science and Engineering*, **42**:71, (2000).

[33] R. Atkinson, D. L. Baulch, R. A. Cox, J. N. Crowley, R. F. Hampson, R. G. Hynes, M. E. Jenkin, M. J. Rossi, and J. Troe. Evaluated kinetic and photochemical data for atmospheric chemistry: Volume i - gas phase reactions of O_x, HO_x, NO_x and SO_x species. *Atmospheric Chemistry and Physics*, **4**:1461, (2004).

[34] J. H. van Helden, R. A. B. Zijlmans, D. C. Schram, and R. Engeln. Resemblance in gas composition of $Ar-N_2-O_2$ plasmas and Ar-NO plasmas. *Plasma Sources Science & Technology*, **18**:11, (2009).

[35] O. Guaitella, M. Hübner, D. Marinov, V. Guerra, C. D. Pintassilgo, S. Welzel, J. Röpcke, and A. Rousseau. Oxidation of NO into NO_2 by surface adsorbed O atoms. *Contributions to Plasma Physics*, **51**:176, (2011).

[36] V. Guerra, O. Guaitella, D. Marinov, C. D. Pintassilgo, M. Hübner, J. Röpcke, and A. Rousseau. A simple model of the surface oxidation of NO in NO_2. In 20th *European Conference on the Atomic and Molecular Physics of Ionized Gases*, Novi Sad, Serbien, 2010.

[37] G. Cartry, L. Magne, and G. Cernogora. Atomic oxygen recombination on fused silica: modelling and comparison to low-temperature experiments (300 K). *Journal of Physics D-Applied Physics*, **33**:1303, (2000).

[38] N. E. Afonina, V. G. Gromov, and V. L. Kovalev. Investigation of the influence of different heterogeneous recombination mechanisms on the heat fluxes to a catalytic surface in dissociated carbon dioxide. *Fluid Dynamics*, **37**:117, (2002).

[39] M. Hübner, S. Welzel, D. Marinov, O. Guaitella, S. Glitsch, A. Rousseau, and J. Röpcke. TRIPLE Q: A three channel quantum cascade laser absorption spectrometer for fast multiple species concentration measurements. *Rev. Sci. Instrum.*, **82**:093102, (2011).

[40] Bolsig. http://www.siglo-kinema.com/bolsig.htm, 2011.

[41] L. S. Rothman, D. Jacquemart, A. Barbe, D. C. Benner, M. Birk, L. R. Brown, M. R. Carleer, C. Chackerian, K. Chance, L. H. Coudert, V. Dana, V. M. Devi, J. M. Flaud, R. R. Gamache, A. Goldman, J. M. Hartmann, K. W. Jucks, A. G. Maki, J. Y. Mandin, S. T. Massie, J. Orphal, A. Perrin, C. P. Rinsland, M. A. H. Smith, J. Tennyson, R. N. Tolchenov, R. A. Toth, J. Vander Auwera, P. Varanasi, and G. Wagner. The hitran 2004 molecular spectroscopic database. *Journal of Quantitative Spectroscopy & Radiative Transfer*, **96**:139, (2005).

[42] NIST. NIST chemistry webbook, http://webbook.nist.gov/chemistry/, (2011).

[43] Margotti.M, Doyennet.L, and L. Henry. Relaxation of vibrational energy in CO, HCL, CO_2, and N_2O. *Applied Optics*, **10**:1768, (1971).

Chapter 6

Summary / Outlook

Increased concerns about environmental protection have led to increased scientific efforts in the field of pollution abatement from an air stream. The emission of pollutions into the atmosphere emerges in a wide area of human existence. Due to their harmfulness, the accumulation of these contaminants in the atmosphere or in the ground water has to be avoided. Apart from conventional cleaning techniques, such as flaring, adsorption or catalytic oxidation, plasma technology has proved its ability to be an alternative approach to improved pollution control. However, the energy efficiency as well as the selectivity of the reaction products remains challenging.

As a contribution to these issues, the main results in the present work can be summarised as follows:

First, as an example for pollution control, a gas flow of synthetic air in the slm-range, contaminated with one aliphatic, ethylene, or one aromatic, toluene, has been treated by a multi stage packed-bed reactor at atmospheric pressure. Both species were admixed in the ppm-range. The admixed ethylene has been nearly completely removed. The β-value, used for comparability, has been between 120 and $900 JL^{-1}$ at a total consumed power between $2W$ and $16W$. The CO_2 selectivity, indicating the destruction performance, has been about 17%. A gas mixture of initially $70 ppm$ toluene diluted in synthetic air has been treated by the multi stage packed-bed reactor as well. The maximum destruction has been about 60% for three stages in use simultaneously. The β-value has been between 300 and $1600 JL^{-1}$ at a total power between $5W$ and $27W$. In toluene destruction experiments, the CO_2 selectivity has been about 24%. Additionally, a polymerisation on the exhaust tubes has been observed. The synergistic effect, reported in the literature, has not been reproduced. As a hypothesis, the polymerisation found in the exhausted gas stream leads to a reduced tube diameter which reduces the gas flow in the reactor as well. This causes a greater residence time of the gas mixture in the stages and, therefore, can lead to increased pollution destruction. At low pollution concentration, the consumed power remains unchanged. Therefore, a graph, destruction as a function of the total power shows an increased non-linear destruction behaviour. For both contaminates, beside the target species, H_2O and CO_2, up to 8 additional reaction products have been identified. These are CO, O_3, N_2O, NO_2, HNO_3, HCN, CH_2O_2 and HCHO. None of these experiments led to the detection of NO in the

exhausted gas mixture. An imaging technique has been used to illustrate the spatial appearance of the plasma around the single packing beds. Thus, the plasma distributes along the surface as well as through the volume. Consequently, pollution control using a packed-bed reactor has to be considered as volume and surface processes.

Outlook:
Since two processes, volume and surface, are present in the packed-bed reactor, an electrode geometry has been designed which leads to a dominating surface plasma. Fig. 6.1 shows a cylindrical rod acting as an electrode. The other one is a metal plane. As one can see, no plasma channel, leaving the surface, can be observed.

Figure 6.1: Electrode geometry forcing the plasma to be distributed over the surface. Thus, volume processes are reduced.

Second, experiments at low pressure have shown that a rf plasma is able to deposit atomic oxygen on a Pyrex surface. It remains stable and can be used for selective pollution oxidation afterwards. This phenomenon has been measured indirectly studying the oxidation of NO into NO_2. Both species have been measured using quantum cascade laser absorption spectroscopy, QCLAS. The NO_2 concentration after an oxygen plasma was $5.3 \times 10^{14} molecules\, cm^{-3}$ and after an air plasma $1.2 \times 10^{14} molecules\, cm^{-3}$. These concentrations correspond to an oxygen surface density of $1.7 \times 10^{12} oxygen\, atoms\, cm^{-2}$ for an O_2 plasma and $0.4 \times 10^{12} oxygen\, atoms\, cm^{-2}$ for an air plasma. Modelling showed that the reaction $NO + O_{adsorbed} \rightarrow NO_2$ dominates the species conversion. However, other NO loss processes like the NO adsorption have to be considered for longer time scales.

Outlook:
These experiments will be repeated using CO as a probe gas. The reaction $CO + O_{adsorbed} \rightarrow CO_2$ is considered. Both reactions, $NO + O_{adsorbed} \rightarrow NO_2$ and $CO + O_{adsorbed} \rightarrow CO_2$, will be studied using a heated Pyrex tube and a Pyrex tube exposed to UV radiation. This might help to distinguish between two important surface reaction mechanism, Langmuir-Hinshelwood Reaction and Eley-Rideal Reaction.

Third, a small and compact three channel spectrometer has been developed, TRIPLE Q. It consists of three quantum cascade lasers, QCL, suitable to detect N_2O, CO, NO and NO_2. Lasers, emitting in other spectral ranges, can be mounted easily. The lasers work in the *Intra Pulse Mode* establishing a high time resolution in the μs-range for single events or in the *ns*-range for repetitive events. Therefore, the spectrometer combines the high time resolution with multi species detection abilities. Depending on the duration of a measurement, several thousand spectra can be recorded. In order to calculate absolute number densities, an algorithm has been developed and validated which automatically treats typical phenomena like pulse jitter, rapid passage effect or fluctuation of the intensity.

Forth, the degree of dissociation and the NO production in N_2 / air like plasmas at low pressure has been studied. Using the TRIPLE Q spectrometer, it has been found that all three nitrous oxides, N_2O, NO and NO_2, diluted in N_2 / air, are dissociated after few *ms* of a dc plasma pulse. The mean plasma current has been in the *mA*-range. From the destruction of N_2O, the reaction $N_2O + e \rightarrow NO + N + e$ and $N_2O + O\left(^1D\right) \rightarrow 2NO$ are found to play not an important role in the NO production.

Fifth, the quantum cascade laser absorption spectroscopy has been developed further. The gas temperature has been calculated from the measured spectra using the line ratio method. However, under low pressure conditions, the absorption spectra show huge distortions of the absorption structures leading to an incorrect line ratio. Therefore, a spectra simulation has been applied in order to compensate the influence of the spectral distortions which are caused by non-linear absorption effects. The correction of the line ratio can be done applying a constant factor which has been determined from simulated spectra. The suitability of such an approach has been validated using a heated gas cell. Using this technique, the averaged gas temperature created in pulsed dc plasma at low pressure is not higher than about $500K$.

Outlook:
The high time resolution allows one to calculate the evolution of the gas temperature in the μs-range. Combined with a very narrow beam shape, topographic measurement of the gas temperature in plasma devices might lead to improved understanding of cooling or relaxation properties of surfaces. This might help to develop e.g. better ceramics for astronautic applications or can lead to an improved study of the plasma catalyst interaction in pollution control experiments.

Sixth, using the TRIPLE Q spectrometer, hot bands ($v = 1 \rightarrow v = 2$) of the asymmetric stretch vibration of N_2O have been detected in dc pulsed low pressure experiments with a time resolution of $33\mu s$. Their appearance implies a high degree of vibrationally excited molecules. For the first time, using QCLAS, the relative population / depopulation processes of the ground and first vibration state have been studied. From the temporally development, the formation rate has been determined. The reaction rate constant has been about 2 times higher for N_2O diluted in air compared to N_2O diluted in pure N_2.

Seventh, the temporally evolution of the concentrations of N_2O, NO and NO_2 in the afterglow of a pulsed dc plasma, measured with the TRIPLE Q system, have shown differences of the relaxation rate of the three nitrous oxides. The relaxation rate of the N_2O concentration into stable conditions has been significant lower than the relaxation rate for the NO or NO_2 concentration. The discrepancy has been studied. Neither a temperature effect nor a N_2O production has been found to be responsible. The plasma under study creates significant amount of vibrationally excited N_2. Therefore, the discrepancy of the relaxation rates has been found to be due to resonant vibration-vibration coupling between vibrationally excited N_2 and N_2O. Indeed, an analogue phenomenon has been reported recently for the system N_2 / CO_2 coupling using the same experimental setup [1].

Outlook:
Item six and seven, offer the opportunity for detailed study of the plasma surface interaction. Especially the catalytic active material and its effects to the species conversion can be accessed. The possibility to detect vibrationally excited N_2 indirectly via IR active species has increased the field of commercially and industrial application of the QCLAS.

The current work has illustrated that pollution control based on plasma technology is an interesting and powerful tool and can serve as an alternative technique to conventional cleaning methods. The remaining challenge, energy efficiency and selectivity of the reaction products, can significantly improved combining catalytic active material with plasma devices. QCLAS has been proved to be a powerful tool for fast detection possibilities which makes the QCLAS highly attractive in plasma surface experiment. Time resolution in the *ns*-range allows one to study also the start phase of a plasma. This has great benefit in improving pollution control based on plasma technology.

Bibliography

[1] D. Marinov, D. Lopatik, O. Guaitella, M. Hübner, Y. Ionikh, J. Röpcke, and A. Rousseau. Surface vibrational relaxation of N_2 studied by CO_2 titration with time-resolved quantum cascade laser absorption spectroscopy. *J. Phys. D: Appl. Phys.*, **45**:XXXX, (2012).

Acronyms

ac	alternating current
dc	direct current
HITRAN	High Resolution Transmission
LEL	lower explosive limit
NIST	National Institute of Standards and Technology
OAE	off axis ellipsoid
OAP	off axis paraboloid
OES	optical emission spectroscopy
PNNL	Pacific Northwest National Library
ppb	parts per billion (10^{-9})
ppm	parts per million (10^{-6})
QCL	quantum cascade laser
QCLAS	quantum cascade laser absorption spectroscopy
rf	radio frequency
sccm	standard cubic centimetre
SNR	signal to noise ratio
slm	standard litre per minute
TDL	tuneable diode laser
TDLAS	tuneable diode laser absorption spectroscopy
TLV	threshold limit value
VOC	volatile organic compounds

Declaration / Selbständigkeitserklärung

Hiermit erkläre ich, dass diese Arbeit bisher von mir weder an der Mathematisch-Naturwissenschaftlichen Fakultät der Ernst-Moritz-Arndt-Universität Greifswald noch einer anderen wissenschaftlichen Einrichtung zum Zwecke der Promotion eingereicht wurde.

Ferner erkläre ich, daß ich diese Arbeit selbständig verfasst und keine anderen als die darin angegebenen Hilfsmittel und Hilfen benutzt und keine Textabschnitte eines Dritten ohne Kennzeichnung übernommen habe.

Unterschrift des Promovenden

Curriculum Vitae

Personal details

Name	Marko Hübner
Date of birth	29. May 1978
Place of birth	Berlin
Citizenship	German

Education

1984 - 1994	Primary school
1994 - 1997	Joiner's apprentice
1997 - 1999	Joiner
1997 - 1999	Secondary school (night school)
1999 - 2004	Student at the University of Applied Science Wildau
	Qualification: Dipl. Ing. (FH) für Physikalische Technik
2004 - 2007	Study phase of the Greifswald Graduate School of Science, GGSS at the University of Greifswald

Experience

1998 - 1999	Compulsory Civilian Service
2001 - 2002	Internship at the University Loughborough, Leicestershire, UK (6 months)
2004	Engineer at the INP Greifswald (2 months)
2008 - 2010	Continuous exchange program with Ecole Polytechnique, Palaiseau, France, (6 weeks external measurement campaigns)
2008 - 2012	Student of the International Max-Planck Research School (IMPRS)

Acknowledgement / Danksagung

Mit der Fertigstellung der vorliegenden Arbeit ist es an der Zeit, allen zu danken, die mich in den letzten Jahren begleitet und unterstützt haben.

Zunächst einmal danke ich Prof. Dr. Klaus-Dieter Weltmann für die Möglichkeit, diese Arbeit in der Arbeitsgruppe 'Plasmadiagnostik' am Leibniz-Institut für Plasmaforschung und Technologie e.V. durchführen zu können.

Besonderer Dank gilt Prof. Dr. Jürgen Röpcke für die Vergabe des sehr interessanten Themas sowie für seine wissenschaftliche Betreuung, die stets zu neuen Überlegungen ermunterte. Ich danke den Mitarbeitern der Arbeitsgruppe 'Plasmadiagnostik', die mir fortdauernd durch anregende und motivierende Diskussionen und Ratschläge unterstützend zur Seite standen. Besonderer Dank gilt Uwe Macherius, Frank Weichbrodt, Sven Glitsch, Henrik Zimmermann, und Stephan Saß für Ihre tatkräftige Unterstützung bei den Versuchsaufbauten.

Darüber hinaus danke ich der Arbeitsgruppe von Prof. Dr. Antoine Rousseau von der École Polytechnique, Palaiseau, Frankreich, insbesondere Dr. Olivier Guaitella und Daniil Marinov für die exzellente Zusammenarbeit und die hervorragenden wissenschaftlichen Diskussionen.

Abschließend danke ich meiner Familie und Freunden, insbesondere meinen Eltern für Ihre tatkräftige und geduldige Unterstützung.

Allen ehemaligen und hier nicht weiter namentlich erwähnten Mitgliedern des Leibniz-Instituts für Plasmaforschung und Technologie e.V., die mich bei der Anfertigung der vorliegenden Arbeit unterstützt haben, bin ich ebenfalls zu Dank verpflichtet.

Publications

List of Publications

[1] M. Hübner, M. Castillo, P.B. Davis, and J. Röpcke. Diode laser spectroscopy of the fundamental bands of $^{12}C^{14}N$, $^{13}C^{14}N$, $^{12}C^{15}N$, $^{13}C^{15}N$ free radicals in the ground $^2\Sigma^+$ electronic state. *Spectrochimica Acta Part A-Molecular and Biomolecular Spectroscopy*, **61:**57, (2005).

[2] M. Hübner, and J. Röpcke. On the Destruction of Volatile Organic Compounds using a Dielectric Pellet Bed Reactor. *J. Phys. Conf. Ser.*, **157:**012004,(2009)

[3] O. Guaitella, M. Hübner, S. Welzel, D. Marinov, J. Röpcke, and A. Rousseau. Evidence for surface oxidation on Pyrex of NO into NO_2 by adsorbed O atoms. *Plasma Sources Sci. Technol.*, **19:**045026, (2010)

[4] S. Welzel, F. Hempel, M. Hübner, N. Lang, P.B. Davies, and J. Röpcke. Quantum Cascade Laser Absorption Spectroscopy as a Plasma Diagnostic Tool: An Overview. *SENSORS*, **10:**6861, (2010)

[5] O. Guaitella, M. Hübner, D. Marinov, V. Guerra, C.D. Pintassilgo, S. Welzel, J. Röpcke, and A. Rousseau. Oxidation of NO into NO_2 by surface adsorbed O atoms. *Contrib. Plasma Phys.*, **51:**176, (2011)

[6] M. Hübner, S. Welzel, D. Marinov, O. Guaitella, S. Glitsch, A. Rousseau, and J. Röpcke. TRIPLE Q: A three channel quantum cascade laser absorption spectrometer for fast multiple species concentration measurements. *Rev. Sci. Instrum.*, **82:**093102, (2011)

[7] D. Marinov, D. Lopatik, O. Guaitella, M. Hübner, Y. Ionikh, J Röpcke, and A. Rousseau. Surface vibrational relaxation of N_2 studied by CO_2 titration with time-resolved quantum cascade laser absorption spectroscopy. *J. Phys. D: Appl. Phys.*, **45:**000000, (2012)

Oral Presentations

[1] M. Hübner, and J. Röpcke. IR-spektroskopische Untersuchungen zum Abbau flüchtiger organischer Substanzen (VOC) in einem mehrstufigen, geschütteten Plasmareaktor, *DPG-Frühjahrstagung*, Greifswald, Germany, (2009)

[2] M. Hübner, O. Guaitella, A. Rousseau, and J. Röpcke. Removal of volatile organic compounds using a multi stage packed bed reactor under atmospheric conditions, *DPG-Frühjahrstagung*, Hannover, Germany, (2010)

[3] M. Hübner, O. Guaitella, A. Rousseau, and J. Röpcke. Application of a multi stage packed-bed reactor for destruction of volatile organic compounds under atmospheric conditions, Hot Topic Talk, *20*[th] *ESCAMPIG*, Novi Sad, Serbia, (2010)

[4] M. Hübner, D. Marinov, O. Guaitella, V. Guerra, C.D. Pintassilgo, A. Rousseau, and J. Röpcke. Fast Simultaneous Measurement of the time evolution of NO, NO_2 and N_2O in a pulsed DC Discharge using a 3 channel QCLAS system, *IPS*, Rolduc - Kerkrade, Netherland, (2010)

[5] M. Hübner, O. Guaitella, A. Rousseau, and J. Röpcke. Pollution control using an atmospheric packed-bed reactor: Plasma surface interaction and species conversion, Topical Talk, *DPG-Frühjahrstagung*, Stuttgart, Germany, (2012)

Contributions

[1] M. Hübner, and J. Röpcke. On Destruction of Volatile Organic Compounds using a Dielectric Pellet Packed-Bed Reactor, *9*[th]*MIOMD*, Freiburg, Germany, (2008)

[2] M. Hübner, O. Guaitella, A. Rousseau, and J. Röpcke. On the deposition ability of atomic species on a Pyrex surface studied via NO destruction kinetics, *DPG-Frühjahrstagung*, Greifswald, Germany, (2009)

[3] M. Hübner, O. Guaitella, A. Rousseau, S. Welzel, and J. Röpcke. Quantum Cascade Laser Absorption Spectroscopy Study on the Influence of Plasma Stimulated Surface Adsorptions to the NO Destruction Kinetics, *8*[th]*FLTPD*,Blansko, Czech Republic, (2009)

[4] M. Hübner, S. Welzel, and J. Röpcke. Application of infrared absorption techniques to study VOC destruction in a multi stage dielectric pellet bed plasma reactor, *8*[th]*FLTPD*,Blansko, Czech Republic, (2009)

[5] M. Hübner, D. Marinov, O. Guaitella, A. Rousseau, and J. Röpcke. A 3 quantum cascade laser spectrometer for fast in situ determination of absolute number densities, *20*[th] *ESCAMPIG*, Novi Sad, Serbia, (2010)

[6] J. Röpcke, M. Hübner, O. Guaitella, and A. Rousseau. Destruction of volatile organic compounds under atmospheric conditions by usage of a multi stage packed bed reactor, *63*[rd] *GEC* and *7*[th] *ICRP*, Paris, France, (2010)

[7] D. Marinov, O. Guaitella, A. Rousseau, M. Hübner, and J. Röpcke. Kinetics of pulsed DC discharge in $N_2/O_2/N_xO_y$ mixtures studied by quantum cascade laser absorption spectroscopy, *63*[rd] *GEC* and *7*[th] *ICRP*, Paris, France, (2010)

[8] M. Hübner, O. Guaitella, A. Rousseau, and J. Röpcke. Investigation of the VOC destruction efficiency of a multi stage packed bed reactor by FTIR spectroscopy, *IPS*, Rolduc - Kerkrade, Netherland, (2010)

[9] V. Guerra, O. Guaitella, D. Marinov, C.D. Pintassilgo, M.Hübner, J. Röpcke, and A. Rousseau. A simple model of the surface oxidation of NO in NO_2, *20*[th] *ESCAMPIG*, Novi Sad, Serbia, (2010)

[10] D. Marinov, M. Hübner, O. Guaitella, J. Röpcke, and A. Rousseau. Production / conversion of molecules on catalytic surfaces under plasma exposure, *20*[th] *ESCAMPIG*, Novi Sad, Serbia, (2010)

[11] D. Marinov, O. Guaitella, A. Rousseau, M. Hübner, J. Röpcke, V. Guerra, and C. Pintassilgo. Reactivity of atoms adsorbed on catalytic surfaces under plasma exposure, *63*[rd] *GEC* and *7*[th] *ICRP*, Paris, France, (2010)

[12] J. Röpcke, M. Hübner, D. Marinov, O. Guaitella, A. Rousseau, C.D. Pintassilgo, and V. Guerra. On plasma based species deposition at a Pyrex surface studied by post plasma N_xO_y conversion, *63*[rd] *GEC* and *7*[th] *ICRP*, Paris, France, (2010)

[13] M. Hübner, D. Marinov, O. Guaitella, A. Rousseau, and J. Röpcke. Estimation of the Gas Temperature of NO during a DC Plasma Pulse using QCL-Absorption Spectroscopy, *9*[th] *FLTPD*, Zinnowitz, Germany, (2011)

[14] J. Röpcke, P.B. Davies, S. Glitsch, F. Hempel, M. Hübner, N. Lang, D. Lopatik, A. Rousseau, and S. Welzel. Applications of IR Absorption Techniques for Plasma Diagnostics in Basic Research and Industry, *FLAIR*, Murnau, Germany, (2011)

[15] D. Lopatik, D. Marinov, O. Guaitella, M. Hübner, A. Rousseau, and J. Röpcke. On plasma- and UV-induced VOC oxidation on TiO_2 surface pre-treated by plasma exposure monitored by QCLAS, *9*[th]*FLTPD*, Zinnowitz, Germany, (2011)

[16] D. Marinov, D. Lopatik, M. Hübner, O. Guaitella, J. Röpcke, and A. Rousseau. Vibrational relaxation of N_2 studied by IR titration with time-resolved Qantums Cascade Laser diagnostics, *9*[th]*FLTPD*, Zinnowitz, Germany, (2011)

[17] D. Marinov, D. Lopatik, M. Hübner, O. Guaitella, J. Röpcke, and A. Rousseau. Vibrational relaxation of N_2 studied by infrared titration, *30*[th] *ICPIG*, Belfast, Northern Ireland, UK, (2011)

[18] V. Guerra, D. Marinov, O. Guaitella, C. D. Pintassilgo, M. Hübner, J. Röpcke, and A. Rousseau. Modeling heterogeneous atomic recombination and molecule conversion, *30*[th] *ICPIG*, Belfast, Northern Ireland, UK, (2011)
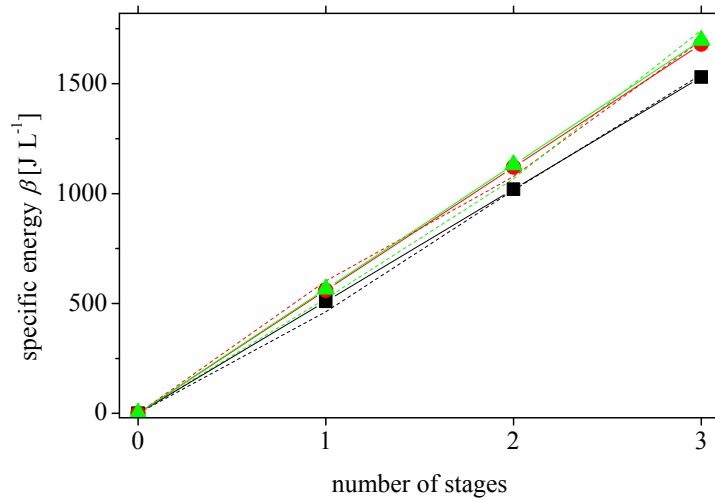
Appendix

Specific energy as a function of the active stages for the toluene destruction
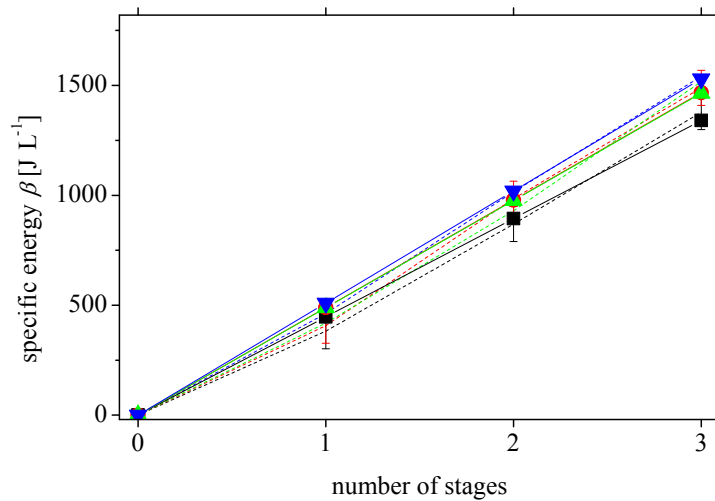
Toluene destruction in dry air:
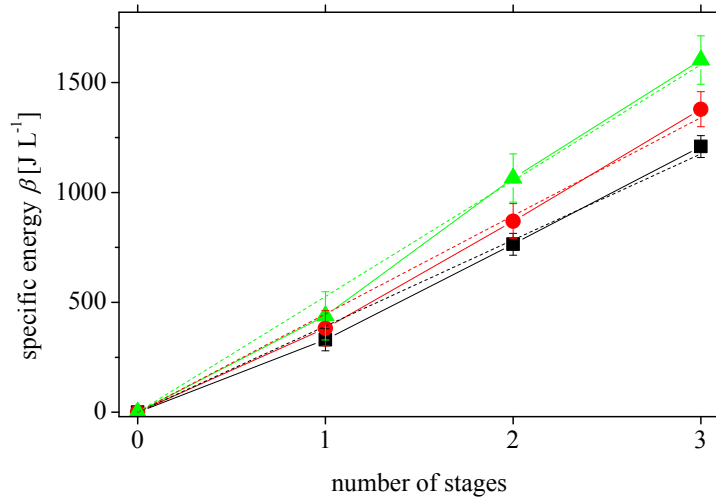
Figure A.1: Figure A.1 Specific energy β as a function of the active stages for the destruction of toluene at an initial concentration of $70ppm$ in air as a function of the active stages. The gas flow has been $1slm$. For these experiments, about $85ppm$ humidity have been left in the gas mixture. The applied voltage has been $20kV$ (■), $21kV$ (●) and $22kV$ (▲).

Toluene destruction at different gas flows:

Figure A.2: Figure A.2 Specific energy β as a function of the active stages for the destruction of toluene at an initial concentration of $70ppm$ in air as a function of the active stages. The applied voltage was $21kV$. For these experiments, about $5300ppm$ humidity has been admixed in the gas mixture. The different gas flows have been $1slm$ (■), $3slm$ (●) and $5slm$ (▲).
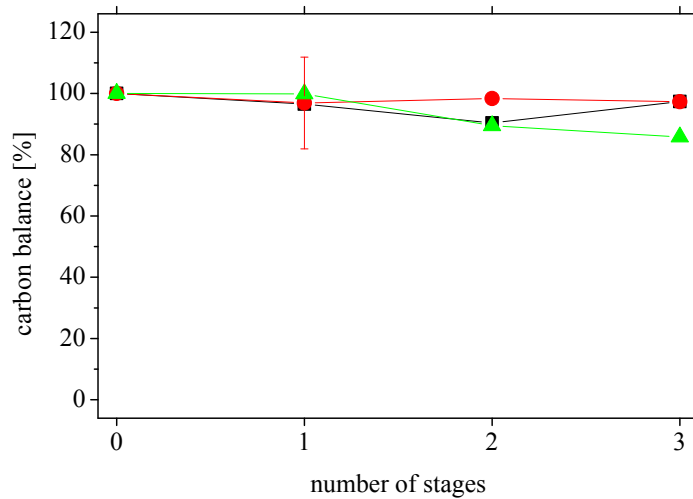
Toluene destruction for different humidity levels:

Figure A.3: Figure A.3 Specific energy β as a function of the active stages for the destruction of toluene at an initial concentration of $70ppm$ in air as a function of the active stages. The gas flow has been $1slm$. For these experiments, about $3600ppm$ humidity has been admixed in the gas mixture. The different humidity have been $80ppm$ (■), $3500ppm$ (●), $4400ppm$ (▲) and $5300ppm$ (▼).
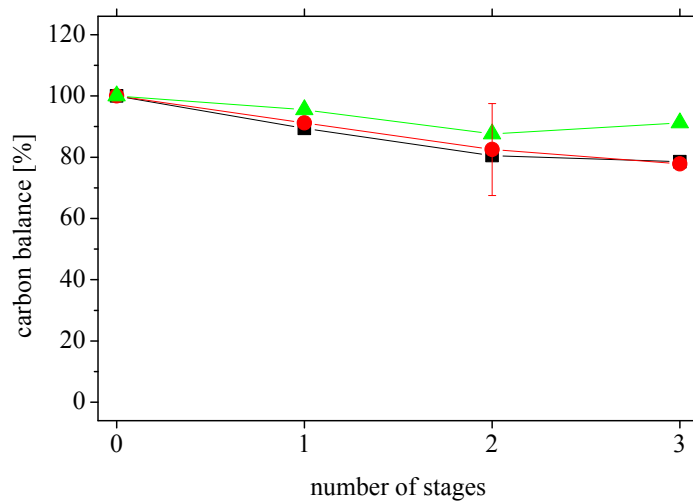
Mass balance of carbon for the toluene destruction
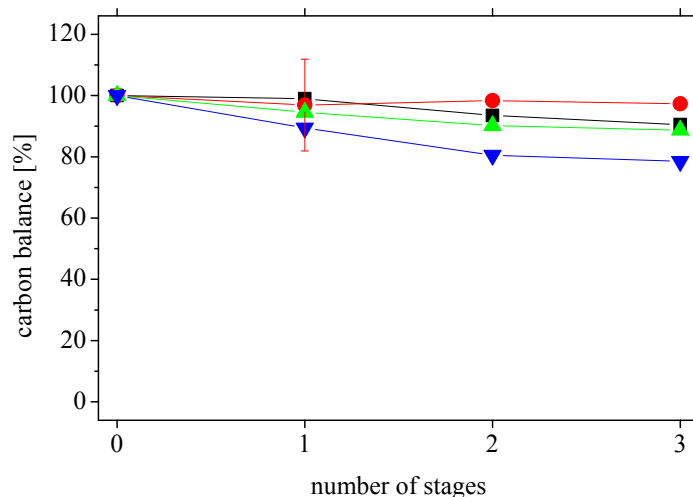
Mass balance of carbon for humidified air:

Figure A.4: Figure A.4 Mass balance of the destruction of toluene at an initial concentration of $70ppm$ in air as a function of the active stages. The gas flow has been $1slm$. For these experiments, about $3600ppm$ humidity has been admixed in the gas mixture. The applied voltage has been $20kV$ (■), $21kV$ (●) and $22kV$ (▲).

Mass balance of carbon at different gas flows:

Figure A.5: Figure A.5 Mass balance of the destruction of toluene at an initial concentration of $70ppm$ in air as a function of the active stages. The applied voltage was $21kV$. For these experiments, about $5300ppm$ humidity has been admixed in the gas mixture. The different gas flows have been $1slm$ (■), $3slm$ (●) and $5slm$ (▲).

Mass balance of carbon for different humidity levels:

Figure A.6: Figure A.6 Mass balance of the destruction of toluene at an initial concentration of $70ppm$ in air as a function of the active stages. The gas flow has been $1slm$. For these experiments, about $3600ppm$ humidity has been admixed in the gas mixture. The different humidity have been $80ppm$ (■), $3500ppm$ (●), $4400ppm$ (▲) and $5300ppm$ (▼).

Mass balance of carbon for the ethylene destruction
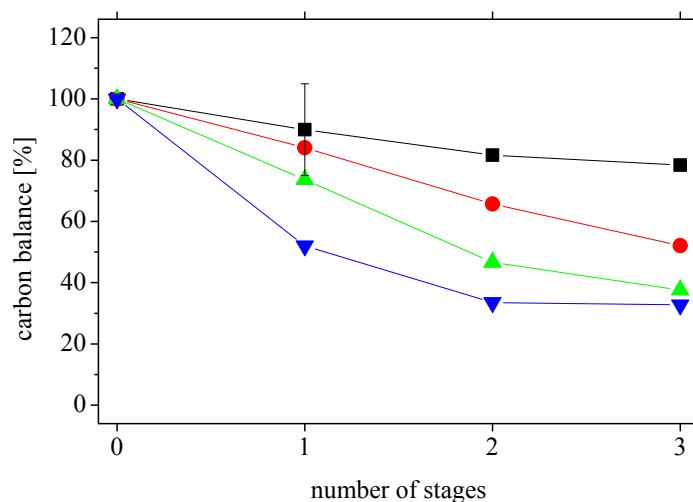
Figure A.7: Figure A.7 Mass balance Destruction of ethylene as a function of the total power. The initial gas mixture has been: $1000ppm$ C_2H_4, $1200ppm$ H_2O in synthetic air. The applied sinusoidal voltage has been: $9kV$ (■), $10kV$ (●), $11kV$ (▲) and $12kV$ (▼), respectively.